The Dissertation Committee for Mehdi Haghshenas Certifies that this is the approved version of the following dissertation:

Modeling and Remediation of Reservoir Souring

Committee:

Kamy Sepehrnoori, Supervisor

Steven L. Bryant, Co-Supervisor

Mojdeh Delshad

Chun Huh

Howard M. Liljestrand

Modeling and Remediation of Reservoir Souring

by

Mehdi Haghshenas, B.S.; M.S.

Dissertation

Presented to the Faculty of the Graduate School of

The University of Texas at Austin

in Partial Fulfillment

of the Requirements

for the Degree of

Doctor of Philosophy

The University of Texas at Austin

August 2011

I dedicate this work to my mother, to the memory of my father, and to my wonderful sisters, Mahya, Marziyeh, and Maryam.

Acknowledgements

I would like to express my sincere gratitude to my supervising professor, Dr. Kamy Sepehrnoori, for his continuous guidance, support, and encouragement through my research. What he provided was far beyond supervising and I am grateful for that. I would like to thank Dr. Steven. L. Bryant, my co-supervisor, for sharing his knowledge and for his great questions and comments. I am privileged to have an opportunity to work with him. I extend my regards to my committee members, Dr. Mojdeh Delshad, Dr. Chun Huh, and Dr. Howard M. Liljestrand for their time to serve on my committee and review my dissertation.

I would like to thank Dr. Francisco Marcondes for his help and involvement in my development work. I am thankful to my colleagues in the Reservoir Simulation research group, specially, Dr. Abdoljalil Varavei, Dr. Farhad Tarahhom, and Mahdy Shirdel for their help throughout my research. I have had valuable technical discussions with Rohollah A. Pour, Dr. Mohammad Ali Farhadinia, Javad Behseresht, Amir Frooqnia, and other colleagues and classmates during my study. I thank them all.

Special thanks to the staff of Petroleum and Geosystems Engineering Department at The University of Texas at Austin, Michelle Hewitt, Dr. Roger Terzian, Tim Guinn, Cheryl Kruzie, Frankie Hart, and Joanna Castillo for their technical and administrative support.

Modeling and Remediation of Reservoir Souring

Publication No._____

Mehdi Haghshenas, PhD

The University of Texas at Austin, 2011

Supervisors: Kamy Sepehrnoori and Steven L. Bryant

Reservoir souring refers to the increase in the concentration of hydrogen sulfide in production fluids during waterflooding. Besides health and safety issues, H_2S content reduces the value of the produced hydrocarbon. Nitrate injection is an effective method to prevent the formation of H_2S. Although the effectiveness of nitrate injection has been proven in laboratory and field applications and biology is well-understood, modeling aspect is still in its early stages. This work describes the modeling and simulation of biological reactions associated with reservoir souring and nitrate injection for souring remediation. The model is implemented in a general purpose adaptive reservoir simulator (GPAS). We also developed a physical dispersion model in GPAS to study the effect of dispersion on reservoir souring.

The basic mechanism in the biologically mediated generation of H_2S is the reaction between sulfate and organic compounds in the presence of sulfate-reducing bacteria (SRB). Several mechanisms describe the effect of nitrate injection on reservoir souring. We developed mathematical models for biological reactions to simulate each mechanism. For every biological reaction, we solve a set of ordinary differential

equations along with differential equations for the transport of chemical and biological species. Souring reactions occur in the areas of the reservoir where all of the required chemical and biological species are available. Therefore, dispersion affects the extent of reservoir souring as transport of aqueous phase components and the formation of mixing zones depends on dispersive characteristics of porous media.

We successfully simulated laboratory experiments in batch reactors and sand-packed column reactors to verify our model development. The results from simulation of laboratory experiments are used to find the input parameters for field-scale simulations. We also examined the effect of dispersion on reservoir souring for different compositions of injection and formation water. Dispersion effects are significant when injection water does not contain sufficient organic compounds and reactions occur in the mixing zone between injection water and formation water. With a comprehensive biological model and robust and accurate flow simulation capabilities, GPAS can predict the onset of reservoir souring and the effectiveness of nitrate injection and facilitate the design of the process.

Table of Contents

List of Tables

List of Figures

Chapter 1: Introduction

1.1 Reservoir Souring

Water injection is a common way to improve recovery in many oil fields. However, an unwanted side effect of water injection can be reservoir souring, which refers to the increase in concentration of hydrogen sulfide (H_2S) in production fluids. This usually occurs some time after the breakthrough of the injected water at the producing wells. Thus a reservoir that initially produces oil and gas with negligible concentrations of H_2S can later produce fluids containing significant H_2S concentrations. This situation results from waterflooding and should be distinguished from reservoirs that already contain substantial H_2S when discovered.

Reservoir souring can be very detrimental as H_2S is a highly toxic and flammable gas. The lethal concentration is 800 ppm for 50% of humans exposed for 5 minutes, poisoning several different systems in the body. Therefore, the production of H_2S raises a major health and safety concern in field operations. Corrosion is another detrimental effect of hydrogen sulfide. In the presence of moisture, H_2S can act as a catalyst in the absorption of atomic hydrogen in steel, promoting sulfide stress cracking (SSC) in high strength steels. H_2S corrosion can be found during drilling, and in production wells and surface facilities. At the onset of reservoir souring, it becomes necessary to deploy chemical scavengers or corrosion inhibitors to protect the production facilities. Hence, reservoir souring increases the operational costs of oil production, especially, when it is not predicted in the field development plan. In addition, contamination of hydrocarbon fluids with H_2S reduces the sale value of products. Lastly, the installation of chemical

sweetening systems to meet export or refinery specifications is another complexity caused by reservoir souring.

Reservoir souring is a common problem in waterflooded reservoirs worldwide. Billions of U.S. dollars (USD) are estimated as lost per year (Mueller and Nelson, 1996), proving the significance of the reservoir souring threat. It is necessary to consider the possibility of reservoir souring in the planning stages of field development. Underestimating the risk of reservoir souring can lead to the unexpected need to install equipment such as sweetening units, internally coated pipes, or chemical injectors for corrosion inhibition. The substitution of equipment is not always feasible in complex situations such as the deepwater environment. In this case, operators are forced to shut in producers with high levels of H_2S.

The prediction of the onset and severity of reservoir souring requires an understanding of reactions that produce hydrogen sulfide during waterflooding. Several biotic and abiotic mechanisms have been proposed as causing reservoir souring. It is now widely accepted that the reduction of sulfate by sulfate-reducing bacteria (SRB) is the most significant mechanism of souring in seawater-injected reservoirs (Ligthelm et al., 1991; Sunde et al., 1993). This is due to the combination of abundant electron donors (selected oil components) and electron acceptors (sulfate in the seawater).

Reducing H_2S concentration in the produced fluids is desirable to reduce corrosion and associated environmental risks. Membrane filtration of injection water to remove sulfate is effective to prevent reservoir souring (Seland et al., 1992). However, the field-scale application of this method is very expensive. Another approach is to use biocides to stop SRB activity. Besides the toxicity of biocides and the high expenses of field applications, studies show that bacteria become ever more resistant to biocides over time and continue to reproduce. The most effective method from a technical and

economical standpoint is to use nitrate for reservoir souring remediation. In this method, beneficial microbes multiply and out-compete the detrimental sulfide-generating bacteria. Nitrate stimulates nitrate-reducing sulfate-oxidizing bacteria (NR-SOB) and heterotrophic nitrate-reducing bacteria (hNRB). The injection of nitrate has emerged as a new method that considerably reduces the produced H_2S.

Nitrate is now widely used in the oil fields to prevent or reduce reservoir souring. The Coleville field in Saskatchewan, Canada, the Skjold field in the North Sea, and the Bonga field in Nigeria are examples of successful field applications of nitrate for reservoir souring control (Jenneman et al., 1997 a, and b; Larsen et al., 2002; and Kuijvenhoven et al., 2007). Although the use of nitrate to control microbial production of hydrogen sulfide is proven and the microbiology is well understood, the modeling is at the early stages. The most widely known models for reservoir souring prediction are the mixing model (Ligthelm et al., 1991), the biofilm model (Sunde et al., 1993), and the Dynamic TVS model (Eden et al., 1993). None of these models use a multi-dimensional reservoir simulator for fluid flow or species transport calculations. Evans and Dunsmore (2006) reported the development of a souring model coupled with a reservoir simulator with a one-way flow of simulation data to the souring model. The recent souring model developed at The University of Texas at Austin is implemented in an in-house reservoir simulator called UTCHEM (Farhadinia et al., 2010). UTCHEM is a three-dimensional compositional reservoir simulator (Delshad et al., 1996). UTCHEM's souring model includes the effects of physical and chemical constraints on the generation and transportation of hydrogen sulfide in porous media. Physical constraints, such as temperature, determine the initiation of the biological reactions, while chemical constraints, such as the concentrations of the electron acceptors, substrates, and nutrients, determine the rate of hydrogen sulfide generation. In this work, we

developed a biological model based on the UTCHEM biodegradation model in a General Purpose Adaptive Simulator (GPAS, Wang et al., 1999). The effect of temperature on reservoir souring is extensively studied by Farhadinia (2008) by using UTCHEM. The main focus of our study is the biological reactions and dispersion effects. To the best of our knowledge, GPAS is the first compositional field scale reservoir simulator to model nitrate injection for reservoir souring inhibition. The incorporation of a comprehensive, mechanistic model in a field-scale reservoir simulator provides the capability of optimizing reservoir souring remediation designs.

1.2 RESEARCH OBJECTIVES

Reservoir souring prediction requires modeling field cases with heterogeneities and the full physics and chemistry of multiphase flow, species transport, and energy transport. We also have to be able to perform multi-dimensional reservoir simulations for the lifetime of the reservoir. The hypothesis of whether a mathematical model can predict the actual performance of bacteria in reservoir souring will be tested in this research. Thus, we develop a biological model in a fully-implicit reservoir simulator known as GPAS (GPAS 3.5 Technical Documentation, 2005). This model is able to simulate the reactions involved in the production of H_2S and its inhibition. Experimental data in the literature are used to verify the model.

The objectives of this research are as follows:

- Modeling different mechanisms present in the souring remediation by nitrate
- Developing the biological model for GPAS
- Validating the model

- Performing field case simulations

1.3 DISSERTATION OUTLINE

We present a literature review of reservoir souring treatment by nitrate injection and proposed models for reservoir souring in Chapter 2. Chapter 3 covers the general formulation and features of GPAS. In Chapter 4, we describe the biological model of GPAS and its implementation in the simulator. Chapter 5 presents the simulation of laboratory experiments for verification of the biological model. In Chapter 6 we study the effect of dispersion on reservoir souring with analytical and numerical methods. Chapter 7 explains the development and validation of the physical dispersion model in GPAS. In Chapter 8, we present the results of field-scale simulation of reservoir souring and its remediation. Finally, Chapter 9 presents the conclusions and recommendations for future work.

Chapter 2: Literature Review

The generation of hydrogen sulfide in oil reservoirs causes numerous problems such as toxicity to humans, corrosion of production facilities, plugging of injection wells, and souring of produced oil and gas. Hydrogen sulfide could be produced by both geochemical and biological processes. The geochemically produced hydrogen sulfide is naturally present in the reservoir and the risk is posed during exploration and developmental drilling. This H_2S is produced during the deposition and later maturation of the oil in geological ages. However, reservoir souring normally refers to the generation of hydrogen sulfide as a consequence of microbial activities during waterflooding. It occurs in reservoirs with little or no amount of H_2S at the beginning of production. After the start of water injection, the concentration of H_2S increases in the producing fluids. In this chapter, we discuss the basics of reservoir souring and its remediation methods. We also review the extant work on prediction and modeling of reservoir souring.

2.1 Microbial Reservoir Souring

Water injection is the most common secondary recovery method. Water is injected to maintain pressure and to sweep the oil toward the producers. One consequence of waterflooding in many reservoirs is the generation of hydrogen sulfide after the start of water injection. It is now widely accepted that H_2S is produced as a result of microbial activities in the reservoir, referred to as reservoir souring. The microbial reservoir souring is mediated by sulfate-reducing bacteria (SRB). These

bacteria reduce the sulfate (usually present in the injected water) and generate H_2S. In many cases, the reservoir at the primary production stage is a hostile environment to microbial activities. As a result of water injection, a more favorable environment develops. This could be because of more suitable temperature distribution or availability of sulfate and nutrients. Substantial levels of fatty acids are available in many formation waters that can be used directly by sulfate-reducing bacteria. In off-shore reservoirs, seawater is injected and provides an extensive source of sulfate. There should be a good mixing of formation and injection water to have a suitable environment for SRB activity and growth. Diffusion and dispersion, reservoir heterogeneity, bypass flow due to permeability variations and so many other features of reservoirs affect the formation of mixing zones. One common practice in water injection operations is to re-inject the produced water. In this case, the injection water holds fatty acids that normally exist in the formation water and provides all the required compounds for SRB activity. Therefore, bacteria grow in an area around the wellbore and form an immobile microbial biofilm. In this situation, the reaction zone for production of H_2S is in the vicinity of injectors.

2.1.1 Sulfate-Reducing Bacteria

Bastin et al. presented the first indication of SRB activity in oil reservoirs in 1926. They observed that sulfate-reducing bacteria were common in production water. The SRB recovered from the production water of a North Sea reservoir survived, multiplied and produced H_2S in temperatures and pressures as high as 80°C and 4500 psi, respectively (Rosnes et al., 1991). This observation along with other field examples shows that microorganisms can produce hydrogen sulfide even in extreme conditions of

oil reservoirs. Researchers speculated whether the bacteria were introduced to the reservoir by injected water or if they were an indigenous microbe community. The recovery of novel species from oil fields that have never been flooded supports the indigenous origin of microbes. A wide range of microbial communities live in subsurface reservoirs. The sulfate-reducing prokaryotes comprise a diverse group of microorganisms that use sulfate as a terminal electron acceptor and generate hydrogen sulfide through anaerobic reactions. Therefore, they survive where sulfate is available. These microorganisms use organic acids such as acetate, lactate, propionate, and butyrate as sources of carbon and energy. These organic acids exist in formation waters substantially (Barth, 1991). However, sulfate is normally found at lower concentrations in reservoirs that are not flooded yet. Hence, the abundance of sulfate-reducing prokaryotes depends on the availability of sulfate.

Sulfate-reducing bacteria have different characteristics with respect to the favorable temperature, nutrients, pH, and salinity. Although biological sampling from oil reservoirs is extremely difficult, different communities of SRB are recovered and isolated from produced waters from oil fields around the world. These bacteria survive at the reservoir condition but their activity is severely affected by the change of environment during water injection. As an example, injection of cold seawater changes the temperature distribution in the reservoir, which consequently provides a more favorable environment for mesophilic bacteria.

Sulfate-reducing bacteria are classified based on their active temperature range. Mesophilic bacteria generally have growth optima in the 25-40°C temperature range. These bacteria multiply in the surface facility and in shallow low temperature reservoirs. Thermophilic SRB are active in a higher temperature range up to 80°C and are believed to be indigenous to oil reservoirs. Sampled production water from many oil fields shows

the existence of thermophilic SRB (Christensen et al., 1992; Rees et al., 1995; and Beeder et al., 1995). Hyperthermophilic sulfate-reducing Archaea grow at temperatures above 80°C are found in oil field produced waters (Beeder et al., 1994).

Sulfate-reducing bacteria are nutritionally diverse. They can use electron donors and carbon sources available in oil reservoirs such as acetate, propionate, naphthenic acids, n-alkanes, benzoate, benzene, toluene, and phenol (Widdel, 1988; Aeckersberg et al., 1991; Heider et al., 1998; Lovly et al., 1995). Acetate in particular is present in most formation waters at high concentrations; therefore, it is considered as the main substrate (or electron donor) for reservoir souring. Considering the variety of organic compounds that can act as SRB substrate, microbial activity is fairly viable in the mixing zones with favorable temperatures.

2.1.2 Souring Mechanism

Several mechanisms are suggested for reservoir souring including microbial and geochemical reactions such as release from pyrite, thermochemical sulfate reduction, and decomposition of organic sulfur (Herbert, 1987). However, sulfate reduction by SRB is believed to be the most dominant mechanism of reservoir souring during waterflooding (Ligthelm et al., 1991; Sunde et al., 1993).

SRB use various organic compounds as electron donors for sulfate reduction. Based on their metabolic capabilities, SRB fall into two groups: those that cannot oxidize acetate and those that perform complete oxidation of acetate to CO_2 (Pfenning et al., 1981). Reaction (2.1) shows the oxidation of lactate to acetate by some type of SRB that cannot oxidize acetate.

$$2CH_3CHOHCOO^- + SO_4^{2-} + 2H^+ \rightarrow 2CH_3COO^- + 2H_2O + 2CO_2 + H_2S$$

$$\Delta G=-77 \text{ KJ/(mole lactate)} \qquad (2.1)$$

Reaction (2.2) shows complete oxidation of acetate by SRB. The available energy for this reaction is less than the oxidation of lactate to acetate.

$$CH_3COO^- + SO_4^{2-} + 3H^+ \rightarrow 2H_2O + 2CO_2 + H_2S$$

$$\Delta G=-47 \text{ KJ/(mole acetate)} \qquad (2.2)$$

Studies show that SRB can use almost 100 compounds as substrates, most of them abundant in the formation water (Barton, 1995). Therefore, with a supply of sulfate in reservoir, SRB can potentially generate H_2S using organic compounds from crude oil as sources of carbon and energy.

During waterflooding, the temperature around the injectors decreases and provides better conditions for SRB growth. The water backflow samples from injectors in an oil-field in California showed that a region of high bacterial activity existed close to the injectors (McKinley et al., 1988). The backflow from injectors in the Skejold field in Norway showed the existence of viable SRB population and H_2S concentrations as high as 60 mg/L (Larsen et al., 2002). A similar study took place for the Statfjord field in the North Sea. The backflow water showed SRB activity in the vicinity of the wellbore. The low temperature (27°C) injection water reduced the reservoir temperature and made it favorable for mesophilic SRB activity (Maxwell et al., 2002).

The specific area of rock provides a wide surface for SRB growth and biofilm formation. Coreflood experiments by Vance and Brink in 1994 showed that a sphere of rock with a radius of 9.3 m could provide enough space for SRB to produce 50 Kg of H_2S

per day. Therefore, a small area around the injectors can support high volumes of hydrogen sulfide production in reservoirs.

2.1.3 H_2S Transport

Souring occurs during waterflooding as the chemical and biological species move along the water front. All issues that are associated with the transport of aqueous phase components affect reservoir souring. This includes diffusion/dispersion, adsorption on the rock, and partitioning between phases. The interactions of H_2S with the oil phase and the solid surfaces of the porous media tend to retard the migration of H_2S relative to the water. Retardation affects the concentration profile of H_2S, and hence, the onset of reservoir souring.

Reactions with iron-containing minerals scavenge the generated H_2S. Ligthelm et al. (1991) noted the role of siderite ($FeCO_3$), hematite (Fe_2O_3), and magnetite (Fe_3O_4) in adsorption of H_2S from the fluid phase. The extent of scavenging depends on availability and solubility of minerals. Hence, temperature, pressure, and pH influence the amount of adsorbed H_2S as they affect the solubility of iron-rich minerals. Sunde et al. (1993) considered adsorption in development of biofilm model for reservoir souring prediction. They concluded that the capacity of the reservoir to adsorb H_2S determines the number of pore volumes injected before souring is observed at producers.

The partitioning of H_2S from water to oil retards its movement and delays its appearance at the producers. However, the amount of hydrogen sulfide partitioned in the oil phase behind the water front is an order of magnitude less than the amount that is normally adsorbed by minerals (Vance and Thrasher, 2005). Thus, adsorption effects dominate the dissolution in residual oil phases. The movement of H_2S with water

continues toward the producers. In the wellbore and surface facilities, the highest concentration of H_2S is found in the gas phase because of temperature and pressure changes. Operators monitor the produced gas to diagnose reservoir souring and to calculate the amount of produced hydrogen sulfide. However, evaluating the H_2S concentration in the produced water and oil and the total production phase cuts provides more accurate H_2S measurement.

The main components of the souring reaction are sulfate and organic electron donors. Sulfate comes into the reservoir with the injection water. Fatty acids and other organic compounds that act as electron donors normally exist in the formation water. The reactions take place where all the required nutrients and energy sources are available. Hence, bacteria grow and generate H_2S in the mixing zone between injection water and formation water. The formation and extent of the mixing zone strongly depends on the physical dispersion of components in the aqueous phase. Therefore, dispersion greatly affects hydrogen sulfide production. We studied this effect and presented the results in Chapter 6.

2.2 Reservoir Souring Remediation Methods

The production of H_2S lowers the value of oil and gas, damages the facilities and causes many operational problems regarding health, safety, and environment. Industry has been looking for methods to overcome the problem of reservoir souring. Some methods attempt to deal with the produced hydrogen sulfide. Operators may have to shut in producers with regard to their oil production, water-oil ratio, and H_2S concentration. The economic loss because of the delay in production is inevitable. Another approach is to use H_2S scavengers on the surface. This adds a lot of cost and

complexity to the surface facility design. Sturman and Goeres (1999) used the nitrite squeeze treatment on sour producers. They injected nitrite solutions through producers for 36 to 54 hours and then started production after a hold period. They reported a significant decline in H_2S production for up to 7 months. However, it is preferred to prevent the production of hydrogen sulfide in the reservoir to avoid operational complexity and economical and environmental disadvantages.

To inhibit souring in the reservoir, we have to eliminate SRB activity. There are several ways to accomplish this objective. One way is to remove sulfate from injection water; this is achieved by the nano-filtration of injection water to remove sulfate. A second way is to kill microbes by biocides to stop reservoir souring and a final way is by nitrate injection. The latter method is a new application of biotechnology in the petroleum industry. We describe the abovementioned methods in the following sections.

2.2.1 Sulfate Nano-Filtration

Heatherly et al. (1994) report using nano-filtration membrane technology to reduce the sulfate ion concentration in injection water to eliminate sulfate scales in production systems. They reduced the sulfate concentration from 2600 mg/L in the seawater to as low as 50 mg/L. Removing sulfate from injection water effectively reduced the scale in production facilities. However, Widdel et al. (1988) show that SRB can generate H_2S from other oil field chemicals such as thiosulfate and sulfite. Hence, this method may not be quite effective if sulfate is the only compound to be removed.

Rizk et al. (1998) set up a series of experiments to show the effect of sulfate removal on reservoir souring. They suggest that nano-filtration can be effective if sulfate

concentration is reduced enough that it becomes the limiting nutrient for SRB activity in any mixture of formation water and injection water. In their experiment, the sulfate concentration is reduced to 160 mg/L after mixing the de-sulfated injection water and dilution with the syntethic formation water. This sulfate concentration produces 50 mg/L H_2S in the bioreactor. In the field application, a drop in H_2S production from 250-300 ppmv to 50-60 ppmv is expected. They speculate that with further reduction of sulfate to 13.5 mg/L the maximum H_2S in the gas would never exceed 8-10 ppmv.

The amount of sulfate required for SRB activity and growth is relatively small. Sunde et al. (1993) give a half saturation sulfate concentration of 0.1 mg/L as a typical value for SRB. Therefore, even small concentrations of sulfate can stimulate bacteria. To inhibit reservoir souring, the de-sulfation of injected water to extremely small values is necessary. The sulfate removal facilities installed for scale prevention normally reduce sulfate concentration to around 50 mg/L (Heatherly et al., 1994). This limits the maximum extent of reservoir souring but does not remediate it completely. The high capital expenditure for installation of sulfate removal facilities is another drawback of this method.

2.2.2 Biocides

Biocides are chemicals that deter or control organisms by chemical or biological means. The first application of biocides in souring treatment was at surface facilities. In Alberta and Saskatchewan oil reservoirs in Canada, diamines are used routinely to reduce souring and corrosion associated with SRB growth in surface equipments (Telang et al., 1998). Increase in temperature and pressure intensify biocide activity but cause molecular instability. Since the movement of biocides in the reservoir depends on their

stability and adsorption characteristics; it is essential to select chemicals that can migrate through the reservoir. Larsen et al. (2000) report successful application of the THPS biocide in the Skjold field in the North Sea. Batch treatment reduced the concentration of H_2S in the short-term. Pulse injection of THPS continued for further control of reservoir souring. In the Velsefrikk field in the Norwegian sector of the North Sea, glutaraldehyde was injected biweekly from 1989 to 1999. However, nitrate injection replaced these biocide treatments and proved to be more effective (Thorstenson et al., 2002).

If a large population of SRB exists around the injectors, a great amount of biocide is required to kill the bacteria. Bacteria other than SRB are also present in the biofilm. Hence, more biocide is needed because biocides do not act discriminately, which increases the operational costs. In addition, the biocide treatment should be repeated frequently to prevent SRB growth, also a costly procedure. In addition, operators have to decide whether they want to start biocide treatment from the start of water injection or after H_2S concentration has reached a certain level. Because biocides are intended to kill living organisms, they have significant effects on the environment. Due to severe and long-lasting damages of biocides to ecosystems, disposal of biocides must be considered carefully. In oil-foiled applications, a large amount of biocide should be used. Therefore, a great amount of contaminated water is produced. One way to overcome this problem is to reinject the produced water.

2.2.3 Nitrate Injection

Nitrate injection has emerged as a new technology for reservoir souring remediation. Microbial control of hydrogen sulfide production in a petroleum reservoir

involves adding nitrate to the injection water and pumping it to the oil-bearing formation. The nitrate should be consumed by nitrate-reducing bacteria (NRB) to affect the production of H_2S. Several researchers studied water samples from oil reservoirs to investigate the presence of NRB in the oil field formation waters. Eckford and Fedorak (2004) collected several results that show the existence of NRB in 15 different oil fields. In these reservoirs, the indigenous NRB can be stimulated by nitrate for reservoir souring control.

One advantage of nitrate injection method is the low cost. Nitrate injection does not require a vast capital expenditure as nitrate salts are added to the injection water. The operational costs are also competitive as nitrate salts are relatively inexpensive. Jenneman et al., (1997) compared the costs of nitrate injection to biocide treatment based on the nitrate injection data in Coleville field in Canada. They suggested that chemical costs of nitrate injection are between 0.76 and 1.19 US dollars per Kg of H_2S removed. The equivalent costs for biocide treatment based on the wastewater treatment data are 3.90 to 17.60 US dollars depending on the chemical types. Besides the cost, health and environmental factors are considered in choosing chemical treatment methods. Nitrate salts are far less toxic than biocides used for reservoir souring treatment. Nitrate is also widely used in agriculture for fertilizing; therefore, it does not pose major environmental risks. Nitrate has replaced biocide in many offshore fields and the application is growing.

Experimental results are used to propose the mechanisms by which NRB activity can control reservoir souring. Here, we listed the four main mechanisms suggested for nitrate effect on H_2S production. In Chapter 4 we explain how we model these mechanisms in GPAS.

1. **Inhibitory Action of Nitrite:** NRB reduce nitrate to nitrite as an intermediate or final reduction product. Low concentrations of nitrite inhibit SRB activity (Reinsel et al., 1996; and Myhr et al., 2002). Furthermore, the production of N_2O and NO as a result of NRB activity increases the redox potential of an aqueous environment. Hubert et al. (2007) report redox potential values as high as +150 mV when nitrate reduction happens in their packed-bed bioreactor. Even a redox potential of -100 mV is too high for SRB growth (Postgate, 1984). The alteration of redox potential inhibits hydrogen sulfide production.
2. **Bio-Competitive Exclusion:** NRB and SRB use the same substrates as sources of carbon and energy in their metabolic reactions. But nitrate reduction reaction produces more energy than sulfate reduction. Reactions (2.3) and (2.4) show the reduction of nitrate and sulfate with acetate as the electron donor. The released energy per mole of substrate for nitrate reduction is 792 KJ compared to 47 KJ for sulfate reduction.

$$CH_3COO^- + SO_4^{2-} \rightarrow 2HCO_3^- + HS^- \qquad \Delta G=-47 \text{ KJ/(mole acetate)} \qquad (2.3)$$

$$5CH_3COO^- + 8NO_3^- + 3H^+ \rightarrow 10HCO_3^- + 4N_2 + 4H_2S$$

$$\Delta G=-792 \text{ KJ/(mole acetate)} \qquad (2.4)$$

Hence, NRB outcompete SRB for substrates, thereby inhibiting SRB activity which results in less H_2S production. This mechanism is dominant when substrate availability is limited. In the oil reservoirs, formation water is normally rich with organic compounds; therefore, the competition does not stop SRB activity completely.

3. **Nitrate Utilization by SRB:** Some SRB reduce nitrate as a terminal electron acceptor (Dalsgaard and Bak, 1994). Even though nitrate reduction can produce ammonium, unlike nitrite or N_2O, the formation of ammonium is not detrimental to SRB. However, using nitrate instead of sulfate as electron acceptor reduces the generation of H_2S.
4. **Nitrate-Reducing Sulfide-Oxidizing Bacteria Stimulation:** Nitrate injection stimulates nitrate-reducing sulfide oxidizing bacteria (NR-SOB). These bacteria reduce nitrate to nitrite, thereby increasing the redox potential. Moreover, they use sulfide as an electron donor and oxidize it back to sulfate or sulfur (Jenneman et al., 1996). This mechanism removes the existing H_2S in addition to suppressing SRB activity. Greene et al. (2003) carried out experiments with NR-SOB and studied their ability of sulfide oxidization. At small initial sulfide concentrations (lower than 4.6 mM) all the sulfide was converted to sulfate. But at high initial sulfide concentrations, no additional sulfate was generated. The NR-SOB oxidized sulfide to elemental sulfur. In any case, sulfide generation by SRB was inhibited because of NR-SOB activity.

Understanding the microbiology of reservoir souring is important to design the field-scale process. A number of experiments studied the effect of nitrate injection on bacterial activity and H_2S generation. In the following sections we review the experiments and field applications of nitrate injection.

2.2.3.1 Experiments for Reservoir Souring Remediation by Nitrate

Several experiments have been performed to study the effect of nitrate on reservoir souring using core or sand columns. In this section we present the results of some notable experiments.

The first laboratory experiments which showed the efficiency of nitrate in inhibition of sulfide production in oil field waters was completed by Jenneman et al. in 1986. They investigated how variable amounts of nitrate can inhibit sulfide production by SRB. Later in 1992, McInerney et al. used formation water from a gas storage facility in Iowa, USA for nitrate remediation experiments. They used two sandstone core systems with 3.2 h and 16.7 h hydraulic retention times (HRT). They added nitrate to the injection water and observed nitrate consumption. The H_2S concentration was reduced by 40% in the core with 3.2 HRT and 98% in the core with 16.7 HRT. Their experiment supported the existence of an indigenous microbial community that used nitrate as electron acceptor and suppressed SRB activity.

Reinsel et al. (1996) performed a set of experiments on produced waters from oil fields in the North Sea and Alaska as sources of microorganisms. Nitrate injection stimulated indigenous microbes and inhibited souring at thermophilic temperatures. They used an up-flow reactor with crushed Berea sandstone as the porous medium. They showed that after using 3.6 mM nitrate to inhibit reservoir souring, a smaller concentration (0.36 mM) was needed to prevent further SRB activity. We used the results of their experiments to validate our model in GPAS. The details of the simulation results in comparison to experimental data are presented in Chapter 5.

Another work by Jenneman et al. in 1996 investigated the effect of nitrate addition to the brine from a Canadian oil field injected into a porous core. Under various

flow regimes, sulfide removal was between 87 and 100 percent. Elemental sulfur, bacteria and calcium carbonate were produced. They added phosphate and nitrate to the system as nutrients, but relied on the organic compounds present in the medium as substrates.

Complete elimination of H_2S was reported in an experiment in which 0.5 mM nitrate was added into bacteria-enriched water (Myhr et al., 2002). The inhibition of SRB was reported to be the result of produced nitrite from nitrate reduction.

Hubert et al. (2007) performed experiments on produced water from oil fields in packed-bed bioreactors. In most cases they examined, souring control required the injection of a certain amount of nitrate, irrespective of sulfate concentration.

2.2.3.2 Field Application of Nitrate Injection

Hitzman and Dennis (1997) demonstrated nitrate injection as a new technology to remediate reservoir souring. They referred to this technology as “bio-competitive exclusion” regarding the competition between SRB and NRB for substrates. They deployed this technology in several sour wells in Wyoming, Texas, and Oklahoma. They showed that the levels of sulfide can be reduced to zero and can be maintained at low levels with periodic treatments. Several other operators used nitrate for souring remediation.

Injection of nitrate and phosphate into the Coleville field in Saskatchewan, Canada resulted in a considerable decrease in sulfide concentration and a large growth in NRB population (Jennenman et al., 1997 a, and b). After the completion of nitrate injection, the abundance of NRB decreased very quickly (Telang et al., 1997).

Studies in the Skjold field in the North Sea consider the activity of both NRB and NR-SOB in nitrate injection. In this field test, a well in a highly fractured zone showed considerable reduction in H_2S. As expected, a marked increase in the number of NRB and NR-SOB was observed (Larsen et al., 2002). Thorstenson et al. (2002) reported similar results in the Veslefrikk field in the North Sea.

Sunde et al. (2004) present the results of nitrate injection in Gullfaks field in the North Sea. After changing the treatment method from biocide to nitrate, they observed a 10- to 20-fold reduction in sulfate, thereby less corrosion in pipelines. Following nitrate injection, the SRB population was replaced by an equally large NRB population in the biofilm around the injectors.

In the Halfdan field in the North Sea, nitrate was added to the injection water since the start of the injection (Larsen et al., 2004). The analysis of injector backflows and producers with water breakthrough shows the effectiveness of the nitrate injection. Larsen et al. reported a significant increase in NRB population and a one to two orders of magnitude decrease in SRB population. They did not observe any H_2S in the backflow from the injectors. They suggested that NRB-SRB competition and nitrite inhibitory action are the main mechanisms in suppressing SRB activity.

Souring prevention from the start of injection is practiced in Bonga field in Nigeria (Kuijvenhoven et al., 2007). A calcium nitrate solution is constantly injected in the reservoir. Biocides are also injected to control the bacterial growth in the surface facilities. Even though no H_2S was observed in producers, authors did not form an opinion on the effectiveness of nitrate injection. By the time the results were published (one year after the start of water injection); there was only limited water production.

Although the use of nitrate to control microbial production of hydrogen sulfide is proven and the microbiology is well-understood, there is no reported work on the field-

scale modeling of nitrate inhibition mechanisms. In this study, we present development of a biological model in GPAS which is capable of modeling several mechanisms of reservoir souring remediation by nitrate.

2.3 Modeling of Reservoir Souring

Being able to predict the onset and extent of reservoir souring is essential in preparing development and treatment plans. Operators would like to know if changes in the reservoir condition by water flooding could result in reservoir souring. The knowledge of timing, amount of souring, and the wells that are most likely to produce H_2S helps operators to plan for possible treatment options. Furthermore, the design of the remediation process benefits from modeling tools that predict the effectiveness of different strategies. The main concern in souring prediction is to accurately predict how the physical and chemical environment develops as water injection proceeds. Therefore, a reservoir souring simulator should be capable of modeling fluid flow in complex reservoirs.

Several mathematical models are proposed for prediction of reservoir souring in oil reservoirs. These models vary with respect to the concepts on which they are based to explain reservoir souring. In the following sections, we review the existing models and simulators and point out their advantages and shortcomings.

2.3.1 Mixing Model

Ligthelm et al. (1991) developed the first mathematical model for microbial reservoir souring. They assumed that reactions occur in a mixing zone between the

injection water and the formation water where all of the chemicals are available for SRB activity. Injection water is normally sulfate-rich but does not have a lot of organic compounds that SRB use as substrates. On the other hand, fatty acids and other organic compounds are abundant in the formation water because of the contact between the formation water and the oil phase. As injection water displaces the formation water, a mixing zone develops due to diffusion and dispersion. Ligthelm et al. assumed that reactions take place in a narrow region within the mixing zone which moves along the reservoir (Figure 2.1).

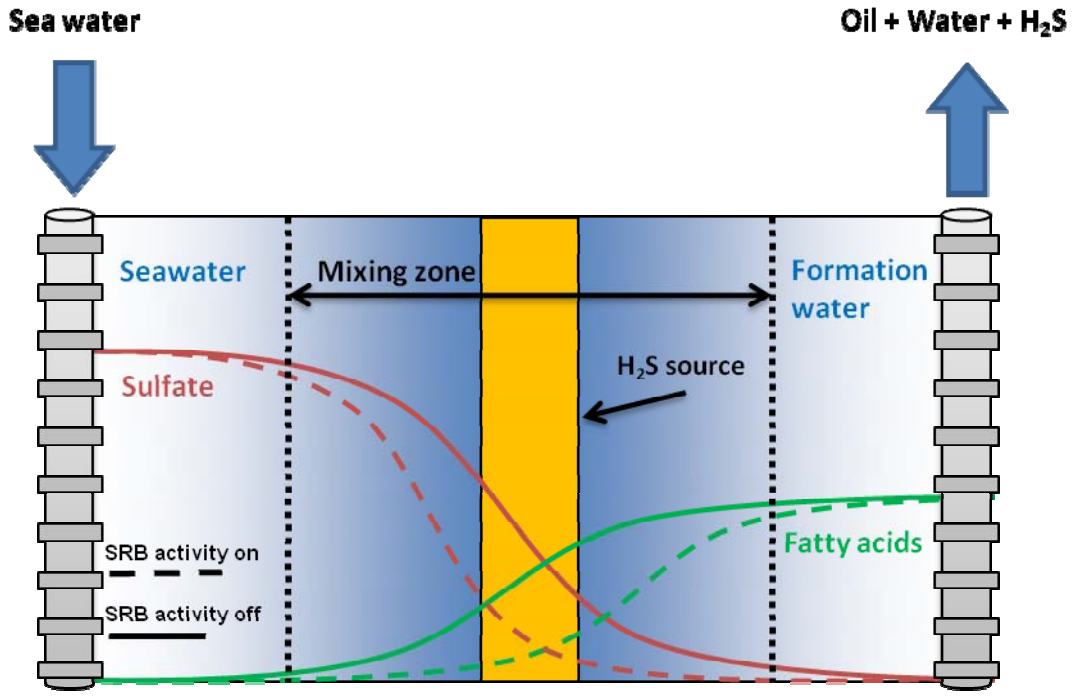

Figure 2.1: The schematic of the mixing model. Solid lines are the concentrations with no bacterial reaction and dashed lines are concentrations with bacterial reactions.

The mixing model by Ligthelm et al. is based on one-dimensional fluid flow in porous media. They derived a material balance equation with convection, dispersion, and source terms for hydrogen sulfide in three phases (water, oil and solid). The adsorption of H_2S on the rock surface and partitioning between oil and water are included in a retardation factor.

When there is no reaction, error function solution for convection/dispersion problems gives the concentration profiles. The mixing zone length is defined as $4\sqrt{Dt}$ where D is the dispersion coefficient and t is the displacement time. In case of microbial reactions, the reaction region length is defined as $2\sqrt{D\tau_b}$. τ_b is a measure of how long it takes to reach a balance in biological reactions. It is assumed that the bacteria population is large enough that this balance is reached very quickly and that τ_b is much smaller than t. Therefore, in the mixing model, the H_2S source moves with the same velocity as the water phase and has a constant width, which is assumed to be very small compared to the mixing zone width. It is assumed that generated H_2S is proportional to the width of the reaction region. Hence, the rate of H_2S generation is found to be

$$R_H^w = \left[\frac{C}{4\sqrt{\tau_b}}\right]\frac{1}{\sqrt{t}}, \qquad (2.5)$$

where C is an empirical constant that depends on the initial compositions of seawater and formation water; t is the displacement time. The bacterial reaction term is inversely proportional to the square root of time and becomes very high during very early time of water injection. Ligthelm et al. developed an analytical solution for the concentration profile of H_2S in a one-dimensional reservoir model (Lithelm et al., 1991).

The mixing model predicts that the H_2S production starts from small quantities after water breakthrough and gradually increases. It eventually stops after the mixing zone (i.e., bacterial reaction zone) is produced from a reservoir. However, this may not be consistent with field observations where H_2S production continues long after water breakthrough. Also,the mixing model does not incorporate the effects of temperature and limiting nutrients on SRB activity.

2.3.2. Biofilm Model

Sunde et al. (1993) developed a numerical model for reservoir souring considering the bacterial reactions that generate H_2S. The main approach of this model is that bacteria do not migrate deep into the reservoir and form a biofilm around the injectors. All the nutrients are available for bacterial activity in the biofilm zone. Therefore, hydrogen sulfide is generated in this area and transported toward the producers (Figure 2.2).

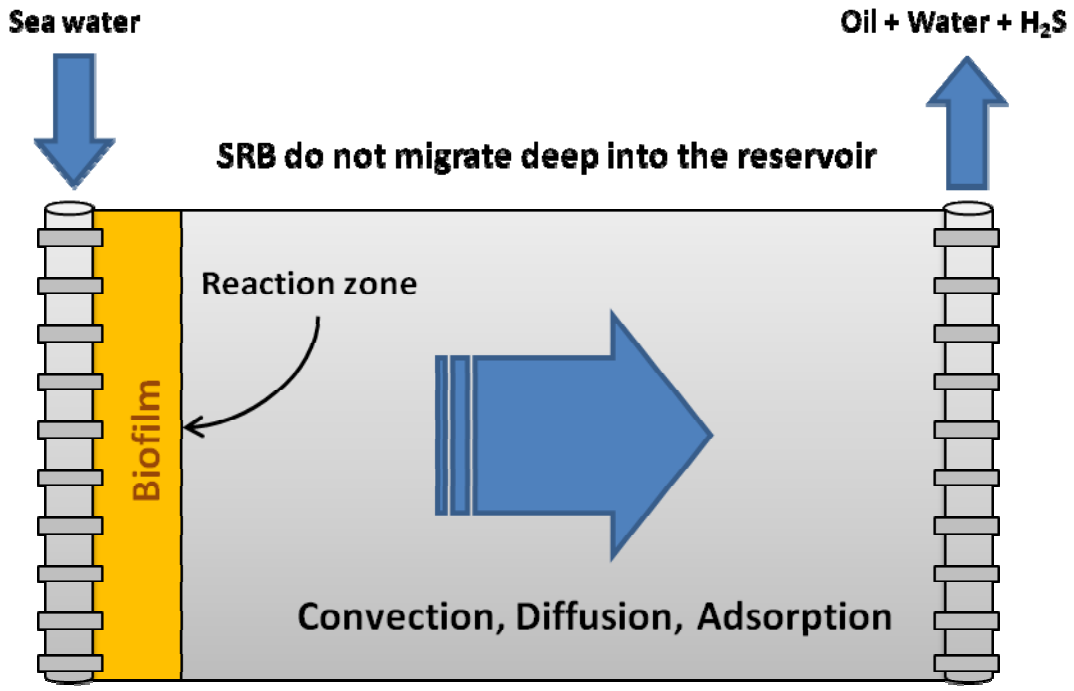

Figure 2.2: Schematic of the biofilm model. H_2S is generated in an area around the wellbore.

The biofilm model solves a material balance equation with convection, diffusion, reaction, and adsorption terms. The equation is solved numerically in a one-dimensional domain. The reaction term expresses the relationship between concentrations of sulfate, substrates and nutrients, and the maximum specific growth rate of SRB. In the case of one substrate, one electron acceptor (sulfate) and one nutrient, the bacteria growth rate is calculated from

$$\mu = \mu_{\max}\left(\frac{C_{Sulfate}}{K_{Sulfate}+C_{Sulfate}}\right)\left(\frac{C_{Substrate}}{K_{Substrate}+C_{Substrate}}\right)\left(\frac{C_{Nutrient}}{K_{Nutrient}+C_{Nutrient}}\right), \qquad (2.6)$$

where C is the concentration and K is the half-saturation coefficient. $\mu_{\max}$ is the maximum specific growth rate of SRB. Half-saturation coefficients and maximum specific growth rates are found from experimental data. The rate of consumption of sulfate is proportional to the bacteria growth rate.

The adsorption of hydrogen sulfide on the rock justifies the delay in the production of H_2S, which occurs long after water breakthrough. Sunde et al. (1993) incorporated an adsorption model in their simulation and matched the production data from the Gullfaks field in the North Sea. They stated that at a given H_2S production rate, the capacity of the reservoir to adsorb H_2S determines the number of pore volumes injected before the producer sours.

In the biofilm model, H_2S production is mainly limited by the injection water composition. When a mixture of seawater and produced water is injected in the reservoir, the biofilm model assumption is reasonable, as the injection water would contain sulfate from the seawater and organic acids from the produced water. However, this model does not explain reservoir souring when only seawater is injected into the reservoir and injection water does not have all the required organic material for SRB growth. It should also be noted that in the biofilm model, bacterial activity does not specifically depend on temperature or pressure.

2.3.3 Thermal Viability Shell (TVS) Model

The dynamic TVS model presented by Eden et al. (1993) emphasizes the effect of temperature and pressure on microbial activity. The basic idea of this model is that H_2S is produced in a portion of the reservoir that has a favorable temperature and pressure for bacterial growth. The thermal equilibrium between the low temperature injection

water and high temperature formation water establishes the so-called thermal viability shell which forms away from the injector. Eden et al. (1993) set temperature limits based on bacteria type to define and calculate the volume of the thermal viability shell (Figure 2.3). The production rate of H_2S is found from empirical correlations that relate sulfate consumption rate to environmental temperature and pressure. The amount of produced hydrogen sulfide is calculated by integrating the sulfide production rate over time in the reaction zone.

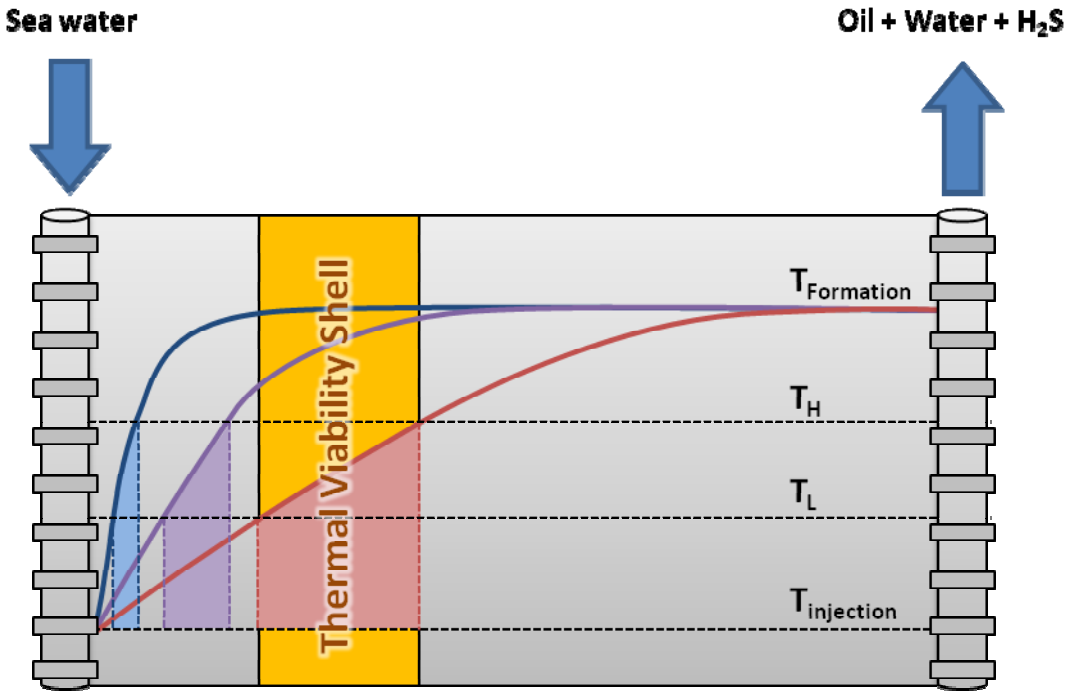

Figure 2.3: Schematic of the TVS model. Blue, purple, and red lines are temperature profiles at early life, mid life, and late life of waterflooding. The trend shows the establishment of the thermal viability shell. T_L and T_H are the lower and upper temperature limits for microbial activity.

The TVS model does not consider the nutrient effect in H_2S production. Yet, the H_2S production rate calculations do not depend on the composition of injection and

formation waters. The TVS model does not include the partitioning and adsorption of chemicals. In general, the TVS model gives an estimated measure of H_2S production for a simplified reservoir model. The reaction rate should be calculated for every reservoir specifically.

2.3.4 Mechanistic Model of Burger et al. (2005)

Burger et al. (2005 and 2006) published a series of work on modeling reservoir souring in different reservoirs. Their model includes fluid flow from an injector to a producer and H_2S production as well as partitioning and adsorption. The model should be adjusted for every reservoir. In this approach, the reservoir is divided into elements representing the total pore volume in the waterflooding pattern. The fluid flow between elements is matched with production data. Equation (2.7) is an empirical relationship which calculates the sulfide biogeneration as a function of pore volumes of seawater injected.

$$\text{moles} \quad H_2S\,|_{swi} = K_1\left\{1-\exp\left(-K_2/V_P\right)\right\}V_a\left[SO_4\right]_{swi}, \tag{2.7}$$

where K_1 and K_2 are coefficients tuned to match historical data. V_a is the water volume in the waterflooded portion of each element and $\left[SO_4\right]_{swi}$ is the sulfate concentration in the injected seawater (subscript swi stands for seawater injected). This relationship predicts an exponential decline in the sulfate reduction after an initial relatively flat period. For the case of production water re-injection, all the chemicals required for SRB activity are available in the injection water. The results of experimental studies lead to Equation (2.8) for hydrogen sulfide production:

$$\text{moles}\quad H_2S\,|_{pwri} = \left(\text{moles DOC}_{inj}\right)\mathrm{K}_{DOC}\,, \tag{2.8}$$

where K_{DOC} is stoichiometric metabolism of DOC_{inj} (dissolved organic carbon in the injected water) with sulfate and is determined from experiments (subscript pwri stands for produced water re-injected).

This model predicts the future production of hydrogen sulfide after history-matching with production data. However, the fluid flow and H_2S modeling are based on correlations that must be adapted from one reservoir to another.

2.3.5 Reservoir Souring Simulators

In this section, we give an overview of the reports regarding in-house reservoir simulators that predict reservoir souring. Most of the simulators are developed or adapted for specific fields. Al-Rasheedi et al. (1999) report the application of the BPOPE reservoir simulator to predict souring in the North Kuwait field. The generation of H_2S is based on the reaction of sulfate and nutrients in every gridblock that these chemicals are present. However, they do not give more details on the reaction equations.

Seto et al. (2000) propose a new mechanism for souring in the Caroline field in Alberta, Canada. This mechanism is not related to SRB activity and explains the H_2S concentration increase in already soured reservoirs. It is based on the changes in H_2S solubility in water with changes in pressure. As reservoir pressure decreases, H_2S is liberated from water phase into gas phase. They model this mechanism by assuming that water phase is the saturated oil phase and hydrocarbon is the dry gas phase in their

simulator to account for the partitioning of hydrogen sulfide from water to the hydrocarbon phase.

Reservoir souring in the Bonga field in Nigeria is simulated using an in-house simulator adapted to account for souring. Kuijvenhoven et al. (2007) stated that they used both the mixing model and the biofilm model in their simulations.

Evans and Dunsmore (2006) reported the development of a souring model coupled with a reservoir simulator with a one-way flow of simulation data to the souring model. This model uses transit flux maps from the simulator to control transport of the H_2S in the reservoir. Also, the generation of hydrogen sulfide is based on bacterial metabolisms (Evans and Dunsmore, 2006).

The Computer Modeling Group (CMG) has recently presented the development of a reservoir souring model in their STARS simulator (Coombe et al., 2010). They reported its application in souring control by nitrate in an Alberta heavy oil reservoir. They include stoichiometric reactions to represent the activity of SRB, NRB, and NR-SOB. Lastly, the model parameters are determined from up-flow column experiments.

2.3.6 Reservoir Souring Simulation with UTCHEM

UTCHEM is a three-dimensional compositional reservoir simulator developed at The University of Texas at Austin (Delshad et al., 1996). The biodegradation model in UTCHEM was used to simulate reservoir souring (Farhadinia et al., 2009 and 2010). This model accounts for biological sulfate reduction resulting in reservoir souring. UTCHEM is the first reservoir simulator with a comprehensive fully coupled souring model. Farhadinia et al. (2009 and 2010) present the application of UTCHEM to regenerate published results of different souring models. UTCHEM includes the effect of

temperature, partitioning and adsorption, media dispersion and reservoir properties on souring. To develop a biological model for GPAS we used the concept of the biodegradation model in UTCHEM. The details of biological model in GPAS are discussed in Chapter 4.

Chapter 3: General Purpose Adaptive Simulator (GPAS)

Performing accurate, efficient, and high-resolution simulations enables petroleum engineers to predict reservoir behavior and design conventional and enhanced oil recovery methods. The objective of GPAS is to simulate a variety of oil recovery processes with multi-million gridblock resolutions. In this chapter, we introduce the structure and different modules of GPAS. We describe the features and capabilities of this simulator that make it a proper candidate for the implementation of the biological model for reservoir souring simulation.

3.1 Overview of GPAS

GPAS is a fully-implicit compositional parallel processing simulator, which was initially developed for compositional miscible gas flooding simulations. The chemical module of GPAS was later added to model surfactant/polymer flooding. Further developments include dual porosity for modeling naturally fractured reservoirs, a geomechanics model for dynamic rock properties, and a thermal model for simulation of steam flooding and other thermal recovery methods. Ongoing developmental activities in GPAS include:

- Fully coupling the equation–of-state (EOS) gas and chemical phase behavior models
- Unstructured grid implementation using the element-based finite volume method with mixed elements
- Asphaltene precipitation modeling

- Coupled wellbore model
- Discrete fracture model
- Wettability alteration modeling

Parallel processing is performed by the Integrated Parallel Accurate Reservoir Simulation (IPARS) framework (Parashar et al., 1997; Wang et al., 1997). The physical model calculations are separated from parallel processing. Depending on the application, two separate modules in GPAS perform the physical model calculations: the equation–of-state compositional module solves phase behavior and mass balance equations for miscible gas flooding while the chemical module solves mass balance equations for aqueous phase components for surfactant/polymer flooding and biological souring simulations. Figure 3.1 shows the structure of GPAS and the connections between its modules.

We will explain the IPARS framework, EOS compositional, and chemical module in the following sections. For the purpose of reservoir souring simulation, we incorporated a biological model in the chemical module of GPAS. The dispersion model for transport of aqueous phase components is also developed in the chemical module of GPAS. Therefore, we discuss the derivation and formulation of chemical module in more detail.

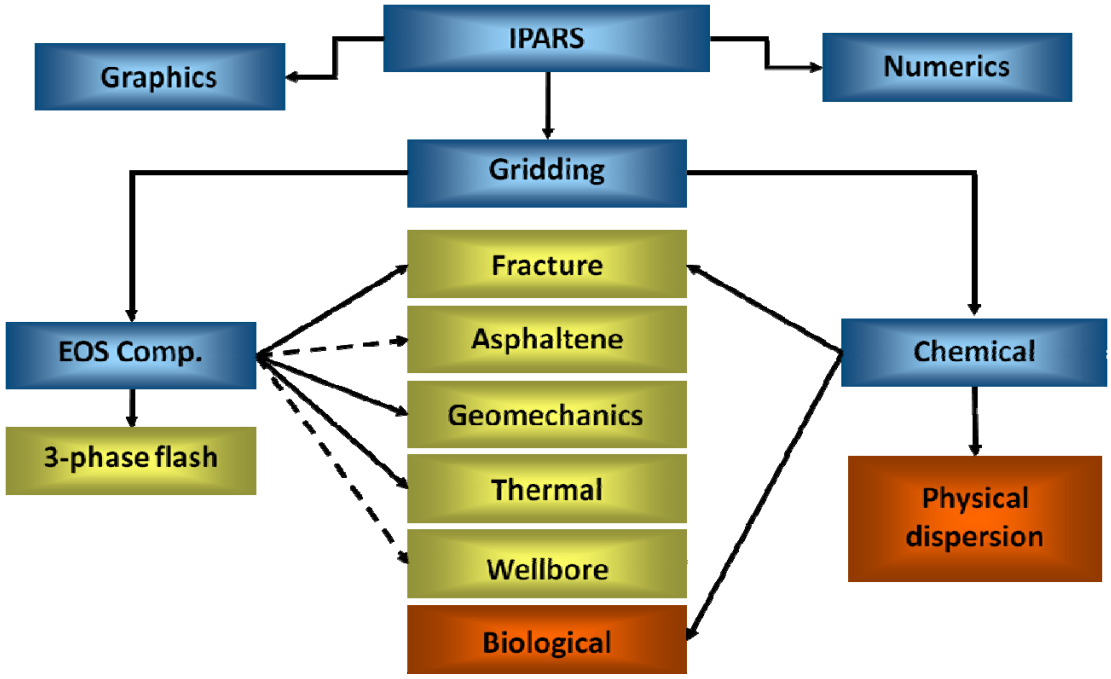

Figure 3.1: The structure of GPAS. The biological and the physical dispersion models are developed under the chemical module of GPAS.

3.2 FRAMEWORK

Integrated Parallel Accurate Reservoir Simulation (IPARS) is a framework for reservoir simulation models, developed for distributed memory, message-passing computers. GPAS is one of the simulators developed under this framework. The main functions of IPARS include: memory allocation and management, domain decomposition, and message passing between processors for parallel runs, and input/output processing.

- **Memory Allocation and Management:** The framework allocates memory for grid-element arrays such as porosity and permeability. These arrays store the grid-related properties and phase and component information. The memory management routines are written in C.

- **Domain Decomposition:** The reservoir is divided into several sub-domains equal to the number of processors. The division is over the y-direction. Every sub-domain is assigned to one processor that solves the physical model equations for that fragment of the reservoir.
- **Message Passing Between Processors:** The framework uses the message passing interface (MPI) to establish communication between processors. The routines that collect and distribute information among the processors are included in the framework.
- **Input/Output Processing:** The framework allows every processor to read the input file and collect the input data for the segment of the reservoir that is assigned to it. At the output times, the master processor gathers the data from all the processors and writes them into output files. The framework includes all the routines that read keywords and associated data from input files and write formatted data into output files.

3.3 EOS COMPOSITIONAL MODULE

Wang et al. (1997) implemented a fully-implicit equation-of-state (EOS) compositional module in GPAS for miscible gas flooding simulations. The EOS compositional module performs the material balance for hydrocarbon components and water, and the phase equilibrium calculations. In this model, each hydrocarbon phase is composed of n_c hydrocarbon components. The instantaneous local thermodynamic equilibrium between hydrocarbon phases is assumed. The EOS phase equilibrium calculations determine the number of stable hydrocarbon phases and their composition. The water phase has water as a single component. It is slightly compressible and its

viscosity is constant. Darcy's law describes the multi-phase flow in porous media. The governing equations of the EOS compositional model consist of n_c material balance equations, n_c phase equilibrium equations (equality of component fugacities), the water material balance equation, and the volume constraint equation. The equations are discretized using single point upstream weighted scheme and solved in a fully-implicit mode. The molar per unit pore volume of components, water phase pressure, and $\ln K_i$ are the primary variables for the system of equations (K_i is the k-value for component i). The Jacobian matrix representing the linear system is generated by computing the derivatives of the governing equations with respect to the independent variables. This linear system is then solved for the independent variables for all the gridblocks. The phase equilibrium calculations are performed to update the hydrocarbon phase's physical properties. This procedure is repeated using the Newton solution scheme until the convergence criteria based on the residual tolerances is met.

3.4 CHEMICAL COMPOSITIONAL MODULE

The EOS compositional module of GPAS does not take into account aqueous phase components. To simulate recovery processes that include the water phase component interactions such as chemical EOR, the chemical module of GPAS was developed. Nalla et al. (2002) implemented and tested the first chemical model for conservative tracers and polymers. John et al. (2003) extended Nalla's work for surfactant flooding by including partitioning traces, chemical species adsorption, and surfactant phase behavior. John et al. (2003) assumed that aqueous phase components are not volume-occupying and do not affect hydrocarbon phase behavior. This assumption is reasonable for typical chemical enhanced oil recovery processes. In this

model, they solved the material balance equations for hydrocarbon components implicitly (as in the EOS compositional module) but the material balance for aqueous phase components were solved explicitly after updating the saturations, densities, and phase fluxes. To take advantage of the larger time steps with the fully-implicit formulation to reduce the simulation time, Han et al. (2007) developed a fully-implicit chemical model in GPAS. In the new formulation, the material balance equations for aqueous phase components are solved implicitly as well as hydrocarbon components' material balance equations. The biological module of GPAS uses Han's chemical module for transport of biological species in the aqueous phase. In this section, we describe the assumptions, formulation, and solution procedure of the latest chemical module in GPAS.

3.4.1 Governing Equations

The chemical module was originally developed for chemical EOR simulations. It models up to three phases depending on the composition and phase behavior of water/oil/surfactant. Fathi et al. (2009) added the three-phase capability to Han's model. Because there is no surfactant in reservoir souring simulations, we use the original two-phase (oil and water) model with no dissolution of hydrocarbon components in the aqueous phase. We assume that aqueous phase biological components are not volume-occupying. We consider no gas phase in the chemical module; therefore, we do not include phase equilibrium equations. The governing equations in the chemical module are material balance equations and volume constraint equations.

3.4.1.1 Material Balance Equations

The original formulation of GPAS did not include a dispersion term in the material balance equations. Because dispersion effects are very significant in reservoir souring simulations, we implemented a diffusion/dispersion model in the chemical module of GPAS. The effect of dispersion on reservoir souring and the implementation of dispersion in the chemical module are covered in Chapters 6 and 7, respectively. For the hydrocarbon components, convection is the only transport mechanism that we model. The material balance equations for aqueous phase components are

$$V_b \frac{\partial}{\partial t}\left(\phi N_i\right) - V_b \bar{\nabla} \bullet \left(\xi_w \frac{\bar{\bar{k}} k_{rw}}{\mu_w} x_{iw} \left(\nabla P - \gamma_w \nabla h \right) \right) + V_b \bar{\nabla} \bullet \left(\xi_w \phi S_w \bar{\bar{D}}_{iw} \bullet \nabla x_{iw} \right) = q_i \;\; i = 1, \ldots, n_a \text{ , (3.1)}$$

and the material balance equations for the hydrocarbon components are

$$V_b \frac{\partial}{\partial t}\left(\phi N_i\right) - V_b \bar{\nabla} \bullet \left(\xi_o \frac{\bar{\bar{k}} k_{ro}}{\mu_o} x_{io} \left(\nabla P - \gamma_o \nabla h \right) \right) = q_i \quad i = 1, \ldots, n_c \text{ , } \qquad \text{(3.2)}$$

where subscript w refers to the aqueous phase and subscript o refers to the oleic phase. n_a is the number of aqueous phase components and n_c is the number of hydrocarbon components.

3.4.1.2 Volume Constraint Equation

The sum of volumes of volume occupying components (water and hydrocarbon components) should be equal to the pore volume in every gridblock. Therefore,

$$\frac{N_w}{\xi_w} + \frac{\sum_{i=1}^{n_c} N_i}{\xi_o} = 1. \tag{3.3}$$

We assume that water is slightly compressible and its molar density is calculated as

$$\xi_w = \xi_w^o (1 + c_w^o (P - P^o)). \tag{3.4}$$

3.4.2 Fully-Implicit Solution Procedure

We use a fully-implicit finite difference scheme to solve Equations (3.1) to (3.3). The mole per pore volume of components N_i and pressure P are selected as primary variables. Hence, we have $n_c + n_a + 2$ unknowns (hydrocarbon and aqueous phase components, water, and pressure) and the same number of equations for every gridblock. We use Newton's method to solve the non-linear equations as shown in Equation (3.5):

$$J \Delta X = -R. \tag{3.5}$$

The residual vector R consists of all the differentiated governing equations for all of the gridblocks. The unknown vector X contains the mole per pore volumes and

pressures for all gridblocks at the new time step. J is the Jacobian matrix that includes all the derivatives of the equations with respect to the primary variables. To search for the solution, we update X by

$$X^{new} = X^{old} + \Delta X \,, \tag{3.6}$$

where ΔX is found from Equation (3.5). We consider X as a solution when it satisfies $R(X^{new}) \approx \bar{0}$. Equation (3.5) can be rewritten in expanded form as

$$\begin{pmatrix} J_{1,1} & J_{1,2} & \dots & J_{1,n_b} \\ J_{2,1} & J_{2,2} & \dots & J_{2,n_b} \\ \vdots & & & \vdots \\ J_{n_b,1} & J_{n_b,2} & \dots & J_{n_b,n_b} \end{pmatrix} \begin{pmatrix} \Delta X_1 \\ \Delta X_2 \\ \vdots \\ \Delta X_{n_b} \end{pmatrix} = -\begin{pmatrix} R_1 \\ R_2 \\ \vdots \\ R_{n_b} \end{pmatrix}, \tag{3.7}$$

where

$$J_{i,j} = \begin{pmatrix} \frac{\partial R_{v_i}}{\partial N_{1,j}} & \cdots & \frac{\partial R_{v_i}}{\partial N_{n_c,j}} & \frac{\partial R_{v_i}}{\partial N_{n_c+1,j}} & \cdots & \frac{\partial R_{v_i}}{\partial N_{n_c+n_a,j}} & \frac{\partial R_{v_i}}{\partial P_j} & \frac{\partial R_{v_i}}{\partial N_{w,j}} \\ \frac{\partial R_{m_{1,i}}}{\partial N_{1,j}} & \cdots & \frac{\partial R_{m_{1,i}}}{\partial N_{n_c,j}} & \frac{\partial R_{m_{1,i}}}{\partial N_{n_c+1,j}} & \cdots & \frac{\partial R_{m_{1,i}}}{\partial N_{n_c+n_a,j}} & \frac{\partial R_{m_{1,i}}}{\partial P_j} & \frac{\partial R_{m_{1,i}}}{\partial N_{w,j}} \\ \vdots & & & & & & \vdots & \\ \frac{\partial R_{m_{n_c,i}}}{\partial N_{1,j}} & \cdots & \frac{\partial R_{m_{n_c,i}}}{\partial N_{n_c,j}} & \frac{\partial R_{m_{n_c,i}}}{\partial N_{n_c+1,j}} & \cdots & \frac{\partial R_{m_{n_c,i}}}{\partial N_{n_c+n_a,j}} & \frac{\partial R_{m_{n_c,i}}}{\partial P_j} & \frac{\partial R_{m_{n_c,i}}}{\partial N_{w,j}} \\ \frac{\partial R_{m_{n_c+1,i}}}{\partial N_{1,j}} & \cdots & \frac{\partial R_{m_{n_c+1,i}}}{\partial N_{n_c,j}} & \frac{\partial R_{m_{n_c+1,i}}}{\partial N_{n_c+1,j}} & \cdots & \frac{\partial R_{m_{n_c+1,i}}}{\partial N_{n_c+n_a,j}} & \frac{\partial R_{m_{n_c+1,i}}}{\partial P_j} & \frac{\partial R_{m_{n_c+1,i}}}{\partial N_{w,j}} \\ \vdots & & & & & & \vdots & \\ \frac{\partial R_{m_{n_c+n_a,i}}}{\partial N_{1,j}} & \cdots & \frac{\partial R_{m_{n_c+n_a,i}}}{\partial N_{n_c,j}} & \frac{\partial R_{m_{n_c+n_a,i}}}{\partial N_{n_c+1,j}} & \cdots & \frac{\partial R_{m_{n_c+n_a,i}}}{\partial N_{n_c+n_a,j}} & \frac{\partial R_{m_{n_c+n_a,i}}}{\partial P_j} & \frac{\partial R_{m_{n_c+n_a,i}}}{\partial N_{w,j}} \\ \frac{\partial R_{m_{H_2O,i}}}{\partial N_{1,j}} & \cdots & \frac{\partial R_{m_{H_2O,i}}}{\partial N_{n_c,j}} & \frac{\partial R_{m_{H_2O,i}}}{\partial N_{n_c+1,j}} & \cdots & \frac{\partial R_{m_{H_2O,i}}}{\partial N_{n_c+n_a,j}} & \frac{\partial R_{m_{H_2O,i}}}{\partial P_j} & \frac{\partial R_{m_{H_2O,i}}}{\partial N_{w,j}} \end{pmatrix}$$

$$\Delta X_i = (\Delta N_1, \ldots, \Delta N_{n_c}, \Delta N_{n_c+1}, \ldots, \Delta N_{n_c+n_a}, \Delta P, \Delta N_w) \qquad \text{for i}^{\text{th}} \text{ gridblock}$$

$$R_i = (R_v, R_{m_1}, \ldots, R_{m_{n_c}}, R_{m_{n_c+1}}, \ldots, R_{m_{n_c+n_a}}, R_{m_w}) \qquad \text{for i}^{\text{th}} \text{ gridblock}$$

A new criterion to check the convergence has been implemented in addition to $R(X^{new}) \approx \bar{0}$. The convergence is based on the changes in pressure and saturation being sufficiently small for a given change in X at any Newton iteration. This criterion is preferred, especially when large saturation changes may occur for very small changes in composition within Newton iterations.

3.5 CORNER POINT FORMULATION

Reservoir simulators normally use the Cartesian grid because the accumulation terms and fluxes are easily evaluated in this type of grid. On the other hand, the Cartesian grid does not represent several features of the reservoir such as faults, fractures, and irregular boundaries accurately. The alternative is to use non-orthogonal boundary-fitted meshes (Maliska et al., 1997; Marcondes et al., 2005). In this approach, the equations are transformed from the Cartesian system to a computational domain that accounts for non-orthogonal hexahedral grids. Then, the transformed equations are integrated in the regular system. Marcondes et al. (2005) developed and validated the corner point grid for GPAS. Similar to the original Cartesian formulation, they used Newton's method to solve non-linear equations. In order to not increase the number of non-zero elements in the Jacobian matrix of the Newton's method, they included the cross derivatives in the right-hand side of the residual function. This results in a semi-implicit procedure and a seven-diagonal Jacobian matrix. This procedure can reduce the convergence rate of the linear system if the mesh is highly distorted. However, this approach reproduces the exact mass flow rate along each interface of the control volume, no matter how distorted the mesh is. Marcondes et al. (2008) also investigated the effect of cross derivatives in discretization schemes in structured non-orthogonal meshes. The new formulation handles full tensor permeability. Hence, we adopted this capability for development of diffusion/dispersion model in GPAS. We explain the development of dispersion model and the full tensor formulation in Chapter 7.

3.6 PARALLEL PROCESSING

Parallel processing refers to dividing a problem into several fragments and executing the fragments on multiple processors simultaneously to reduce the run time. In reservoir simulation, we usually partition the reservoir domain. If we use *n* processors, the simulation time would be divided by *n*. In reality, as we increase the number of processors, the communication time between the processors increases. The communication is necessary, because the sub-domains are connected to each other and processors should receive the information from neighboring cells at every time step.

As mentioned in the framework description (Section 3.2), IPARS provides the parallel processing structure of GPAS. In GPAS multi-processor runs, the reservoir domain is divided in the y-direction into several sub-domains equal to the number of processors. Each processor reads the input data and assigns the properties to the cells that belong to it. A surrounding layer of cells (ghost layer) from the neighboring sub-domain is added to each sub-domain as a communication layer. A framework subroutine updates the data in the communication layers via a message passing interface (MPI). At output-reporting times, a master processor collects the data and sends them to output files under framework's control. We considered the parallel processing capability in the development of the biological model and the physical dispersion model in GPAS. The new models take advantage of the IPARS framework's options for parallel processing. We present the results of multi-processor simulations of reservoir souring in Chapter 8.

Chapter 4: Implementation of the Biological Model in GPAS

To develop a field-scale simulator for reservoir souring, we implemented a biological model in GPAS. In Chapter 3, we explained why GPAS is a good candidate for this implementation. The biological model of GPAS uses the concept of the UTCHEM biodegradation model developed by de Blanc for simulation of aquifer bioremediation (de Blanc, 1996; and de Blanc et al., 1998). Figure 4.1 illustrates how GPAS simulates reservoir souring and its remediation. The concentrations of chemical and biological species are found by solving the mass balance equations in a fully-implicit scheme (Chapter 3). GPAS includes both attached and free-floating bacteria that facilitate the souring reactions. We model these reactions with a set of ordinary differential equations. The details of mathematical modeling are explained in Section 4.1. At every time step and in each gridblock, we solve the reaction equations and update the concentrations. Section 4.2 describes the coupling of the biological model within the chemical module of GPAS. The effects of nitrate on bacterial activity are presented in Section 4.3. We modeled various mechanisms by which nitrate aids souring remediation.

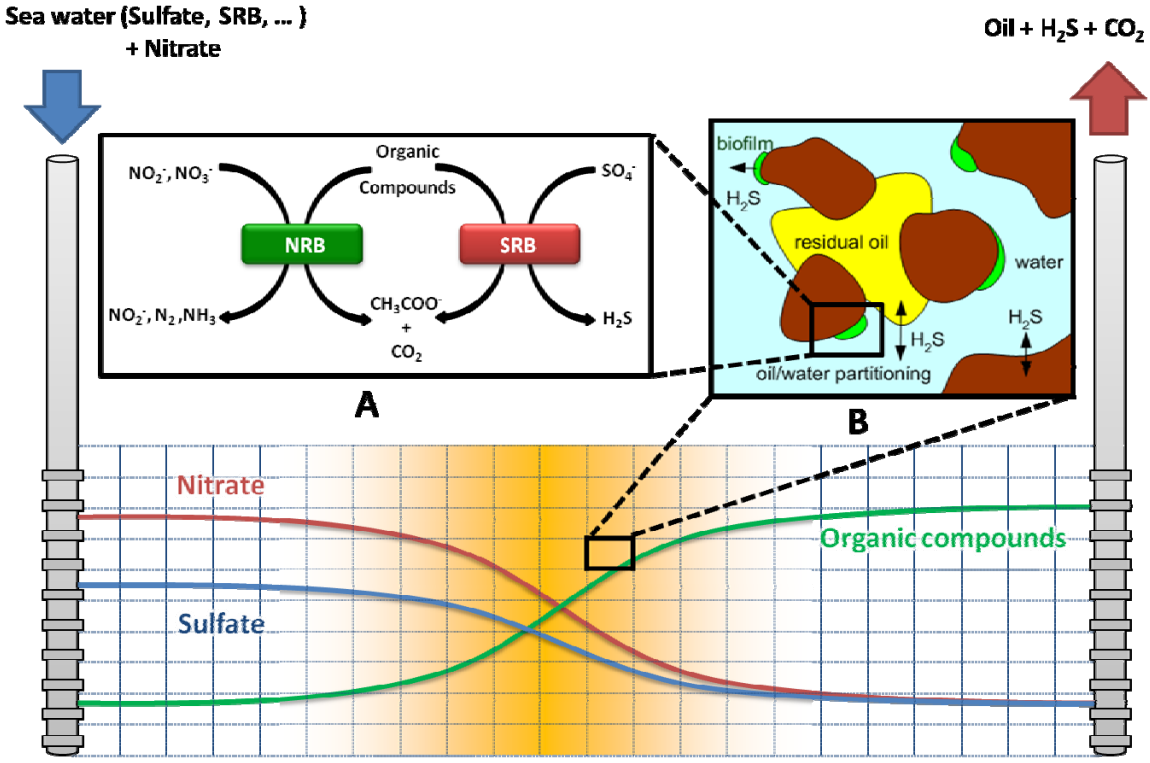

Figure 4.1: Schematic of reservoir souring simulations in GPAS. Material balance equations are solved for the chemical and biological component concentrations. The mathematical models represent bacterial reactions in the aqueous phase and attached biomass.

4.1 Overview of Biological Model

The biological model in GPAS simulates the biodegradation of organic compounds in the aqueous phase. The original purpose of model development in UTCHEM was to simulate the bioremediation of aquifers contaminated with non-aqueous phase liquids (NAPL). Biodegradation includes oxidation-reduction reactions facilitated by microbial activity. The reactions of reservoir souring and microbial EOR are very similar to the biodegradation of NAPL. With some improvements and adjustments, we can use the biodegradation model for reservoir souring simulations. This section

starts with the basic biodegradation concepts. Then we discuss the assumptions, features, and capabilities of UTCHEM's biodegradation model (UTCHEM Technical Documentation, 2003).

A biodegradation reaction is an oxidation-reduction reaction catalyzed by microorganisms' enzymes. It happens by transferring electrons from an electron donor (substrate) to an electron acceptor. The reaction provides energy and carbon for the growth and reproduction of bacteria. A generic biodegradation reaction can be described as

$$\textit{Substrate + Electron acceptor + Bacteria} \longrightarrow \textit{Products + Energy + More Bacteria.} \tag{4.1}$$

In the case of reservoir souring, sulfate-reducing bacteria are the microorganisms that aid the oxidation-reduction reactions. Sulfate acts as the electron acceptor. SRB can use a variety of organic compounds in the oil reservoirs as substrates. Acetate, propionate, naphthenic acids, n-alkanes, benzoate, benzene, toluene, and phenol are reported to act as substrates of souring reactions (Widdel, 1988; Aeckersberg et al., 1991; Heider et al., 1998; Lovly et al., 1995). In sulfate reduction, Equation (4.1) changes to the following form:

$$\textit{Substrate + Sulfate + SRB} \longrightarrow H_2S + \textit{Other products + Energy + More SRB}. \tag{4.2}$$

Hydrogen sulfide is produced from the reduction of sulfate. Depending on the substrate type and the degree of oxidation, products vary from carbon dioxide and acetate to other organic compounds.

Nitrate injection for souring remediation stimulates another type of bacteria known as nitrate-reducing bacteria (NRB). The corresponding reaction for nitrate reduction is

$$\textit{Substrate + Nitrate + NRB} \longrightarrow N_2\,,\ NO_2^-\ \textit{+Other products + Energy + more NRB}. \tag{4.3}$$

The substrates of NRB activity are also normally available in the reservoirs. The generation of nitrogen, nitrite or other products depends on the bacteria type and the redox conditions. Equations (2.3) and (2.4) from Chapter 2 show the stoichiometry of sulfate- and nitrate-reduction reactions.

The bacteria in an aqueous system could be attached to the rock surface or floating in the water. Figure 4.2 shows a representation of the bacteria environment in the pore space; the attached biomass form small microcolonies on the rock surface (Molz et al., 1986). We must measure or estimate the specific area of microcolonies to calculate the concentration equivalent of the attached biomass. A stagnant liquid film separates each microcolony from the aqueous phase. All the chemical species such as substrates, electron acceptors, and nutrients must diffuse across this liquid layer to become available to the attached microorganisms. This liquid film causes resistance in mass transfer between the chemicals in the aqueous phase and attached biomass. We assume that the concentrations of chemicals are uniform in the attached biomass.

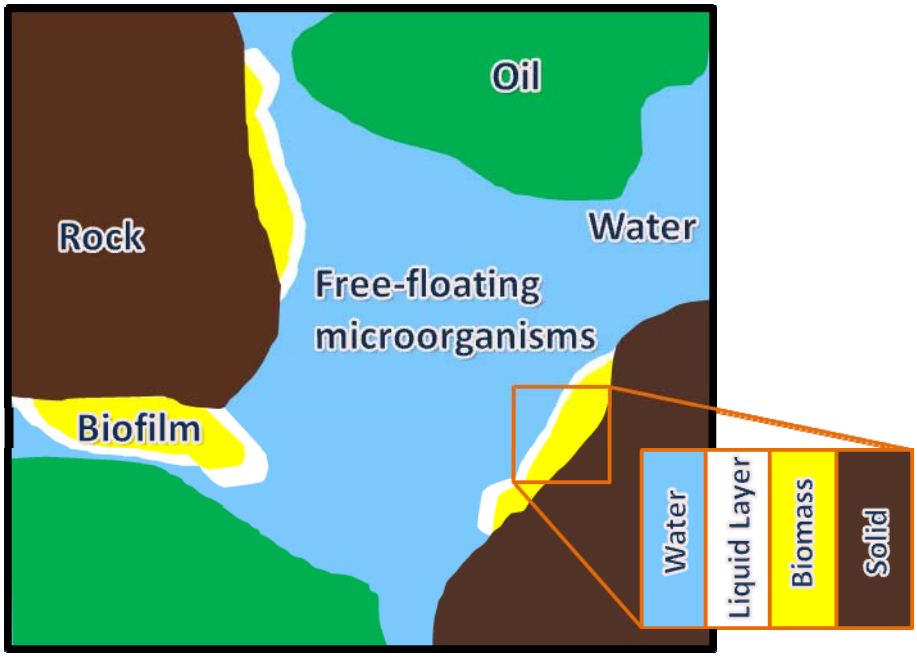

Figure 4.2: Pore-scale illustration of a microorganism environment showing the attached and free-floating microorganisms. The stagnant liquid film on the biomass forms a diffusion layer for mass transfer between the aqueous phase and biomass.

The GPAS biological model assumes that the intrinsic kinetics of substrate and electron acceptor consumption are the same in free-floating cells and in attached cells. In addition, biomass is initially uniformly distributed throughout the porous medium.

The biological model handles multiple substrates, electron acceptors and microorganisms. We define a metabolic combination as a reaction between one substrate and one electron acceptor in the presence of one microorganism. GPAS can solve problems with an unlimited number of metabolic combinations. We model the microbial growth and substrate consumption rate with Monod kinetic equations. In the simplest form of a single metabolic combination (one microorganism X, one substrate S, and one electron acceptor A), the biological model equations are

$$\frac{dS}{dt} = -\frac{\beta\kappa\bar{X}}{m_c}(S-\bar{S}) - \frac{\mu_{\max} X}{Y}\left(\frac{S}{K_S+S}\right)\left(\frac{A}{K_A+A}\right), \tag{4.4}$$

$$\frac{d\bar{S}}{dt} = \frac{\beta\kappa}{V_c}(S-\bar{S}) - \frac{\mu_{\max}\rho_X}{Y}\left(\frac{\bar{S}}{K_S+\bar{S}}\right)\left(\frac{\bar{A}}{K_A+\bar{A}}\right), \tag{4.5}$$

$$\frac{dA}{dt} = -\frac{\beta\kappa\bar{X}}{m_c}(A-\bar{A}) - \frac{\mu_{\max} XE}{Y}\left(\frac{S}{K_S+S}\right)\left(\frac{A}{K_A+A}\right), \tag{4.6}$$

$$\frac{d\bar{A}}{dt} = \frac{\beta\kappa}{V_c}(A-\bar{A}) - \frac{\mu_{\max}\rho_X E}{Y}\left(\frac{\bar{S}}{K_S+\bar{S}}\right)\left(\frac{\bar{A}}{K_A+\bar{A}}\right), \tag{4.7}$$

$$\frac{dX}{dt} = \mu_{\max} X\left(\frac{S}{K_S+S}\right)\left(\frac{A}{K_A+A}\right), \tag{4.8}$$

$$\frac{d\bar{X}}{dt} = \mu_{\max}\bar{X}\left(\frac{\bar{S}}{K_S+\bar{S}}\right)\left(\frac{\bar{A}}{K_A+\bar{A}}\right). \tag{4.9}$$

Table 4.1 describes the parameters of the biological model equations. Equations (4.4) and (4.6) calculate the consumption rates of substrate and electron acceptor in the aqueous phase. Equations (4.5) and (4.7) are the attached biomass consumption rates of the substrate and electron acceptor, respectively. The first term in these equations is the mass transfer between the aqueous phase and attached biomass through the liquid film. The last two equations ((4.8) and (4.9)) are the microbial growth rate expressions for free-floating and attached microorganisms. The attached bacteria concentration is initially calculated as

$$\overline{X} = \frac{C_c\rho_b m_c}{n\phi}, \tag{4.10}$$

where C_c is the number of cells per mass of solid, ρ_b is the bulk density of the porous medium, n is the number of cells per microcolony, and ϕ is the porosity.

Table 4.1: Definition of parameters in the biological equations.

Parameter	Dimension	Description
S	ML^{-3}	Aqueous phase substrate concentration
$\overline{S}$	ML^{-3}	Substrate concentration in attached biomass
A	ML^{-3}	Aqueous phase electron acceptor concentration
$\overline{A}$	ML^{-3}	Electron acceptor concentration in attached biomass
X	ML^{-3}	Aqueous phase biomass concentration
$\overline{X}$	ML^{-3}	Mass of attached cells per volume of aqueous phase
β	L^{2}	Surface area of a single microcolony
κ	LT^{-1}	Mass transfer coefficient
m_c	M	Mass of cells in a single microcolony
V_C	L^{3}	Volume of a single microcolony
ρ_X	ML^{-3}	Biomass density
$\mu_{\max}$	T^{-1}	Maximum specific growth rate
E	---	Mass of electron acceptor consumed per mass of substrate biodegraded
Y	---	Yield coefficient, mass of cells produces per mass of substrate biodegraded
K_S	ML^{-3}	Substrate half-saturation coefficient
K_A	ML^{-3}	Electron acceptor half-saturation coefficient
t	T	Time

If we assume that all of the biomass is attached and the rate of mass transfer of chemical species between the aqueous phase and biomass is instantaneous, then the system of equations is reduced to three equations consisting of Equation (4.9) (rewritten below) and the consumption rate equations of the substrate and electron acceptor (Equations (4.11) and (4.12), respectively). This simple form is used in Chapter 5 to simulate the core-flood experiments.

$$\frac{d\overline{X}}{dt} = \mu_{\max}\overline{X}\left(\frac{S}{K_S + S}\right)\left(\frac{A}{K_A + A}\right)$$

$$\frac{dS}{dt} = -\frac{\mu_{\max}\overline{X}}{Y}\left(\frac{S}{K_S + S}\right)\left(\frac{A}{K_A + A}\right) \quad (4.11)$$

$$\frac{dA}{dt} = -\frac{\mu_{\max}\overline{X}E}{Y}\left(\frac{S}{K_S + S}\right)\left(\frac{A}{K_A + A}\right) \quad (4.12)$$

Monod batch kinetics (Equations (4.8) and (4.9)) applies during the growth phase (cell multiplication), and thus, does not predict a limiting concentration of microbes. Therefore, the microbe population in the model described above grows without bounds as long as nutrients are available, and the reactions would continue as long as substrate and electron acceptors are available. In the subsurface, the growth of attached biomass is limited by several factors such as the surface area and pore size of the rock, biofilm thickness, limited access of underlying bacteria to nutrients, and the endogenous decay of the species. It is therefore crucial to account for the limitation on attached biomass concentration to model souring in reservoirs. A model proposed by Khan et al. (2008) accounts for limiting the microbe population and introduces a different specific growth rate when the microbe population reaches a critical value. The new specific growth rate corresponds to the resting metabolic requirement of the microbes. We assume that the attached biomass population is limited by an upper bound $\overline{X}_{\max}$. This maximum concentration is found from experimental data and is given to the simulator as an input parameter. At the maximum concentration, biomass growth stops, but nutrient consumption is assumed to continue at the same rate. The latter assumption is partially motivated by the experimental observations explained in Chapter 5. This scheme is described by Equations (4.13) to (4.15) that replace Equations (4.9) to (4.12) when the attached biomass concentration reaches its maximum ($\overline{X}_{\max}$):

$$\frac{d\bar{X}}{dt} = 0 \tag{4.13}$$

$$\frac{dS}{dt} = -\frac{\mu_{\max}\bar{X}}{Y}\left(\frac{S}{K_S + S}\right)\left(\frac{A}{K_A + A}\right) \tag{4.14}$$

$$\frac{dA}{dt} = -\frac{\mu_{\max}\bar{X}E}{Y}\left(\frac{S}{K_S + S}\right)\left(\frac{A}{K_A + A}\right) \tag{4.15}$$

4.1.1 Product Generation, Nutrition, and Inhibition Effects

In some biodegradation reactions, the by-products of metabolic reactions are more important than the substrates or the nutrients, especially in reservoir souring where H_2S is the product of sulfate-reduction. We model product generation by changing the product concentration with respect to the amount of consumed substrate. The product's stoichiometric ratio (mass of product generated per mass of substrate used) is an input parameter. We can define any number of products for every metabolic combination. The model calculates the amount of generated products after solving rate equations and updating the concentrations at every time step.

The assumption in multiplicative Monod kinetics formulation is that the substrate, electron acceptor, and other nutrients limit microbial growth. When chemical species such as nitrogen or phosphorous are the limiting nutrients, the substrate consumption rate equation is modified to include an additional limitation by nutrient concentration:

$$\frac{dS}{dt} = -k_{\max,S}X\left(\frac{S}{K_S + S}\right)\left(\frac{A}{K_A + A}\right)\left(\frac{N}{K_N + N}\right), \tag{4.16}$$

where N is the nutrient concentration and K_N is the nutrient half-saturation coefficient.

Toxic chemicals act as inhibitors in microbial processes. We model the inhibition effect by multiplying the reaction rates by a factor that limits the reactions as the inhibitor concentration increases:

$$\frac{I}{I + C_{inhibtor}}.$$

As an example, the substrate consumption rate is modified as

$$\frac{dS}{dt} = -k_{\max,S} X \left(\frac{S}{K_S + S} \right) \left(\frac{A}{K_A + A} \right) \left(\frac{I}{I + C_{inhibtor}} \right), \tag{4.17}$$

where $C_{inhibitor}$ is the inhibitor concentration and I is the inhibition constant determined from experimental data. With no inhibitor, this factor is one. As the inhibitor concentration increases the multiplier approaches zero and the bacteria growth and reaction rates are limited. The biological model can accommodate any number of inhibitors. For each inhibitor, a multiplier is included in the equations.

In the case of reservoir souring treatment by nitrate, the produced nitrite acts as an inhibitor for SRB activity. The effect of nitrite is modeled by including the inhibition term in metabolic combinations of SRB, sulfate, and substrates.

4.1.2 Solving the Biological Model Equations

The biological model equations form a system of ordinary differential equations with time as the independent variable and chemical and biological species concentrations as dependent variables. The size of the system depends on the number of metabolic combinations defined by the user. For every metabolic combination in the general form (both attached and aqueous phase bacterial activity), six equations are to be solved. We solve the system of equations for every gridblock at each time step after solving the governing equations of GPAS. The coupling of the biological model with the chemical module of GPAS is discussed in Section 4.3.

de Blanc (1998) performed a detailed study on the numerical characteristics of the system of biological equations in UTCHEM. He investigated the stiffness of the system of equations by calculating the eigenvalues of Jacobian matrix in different conditions. He concluded that equations were stiff under all conditions. Therefore, a stiff equation solver such as Gear's method (Gear, 1971) is required for the biological model. The numerical solver selected by de Blanc for UTCHEM is SDRIV2 (or DDRIV2 for double precision calculations). This FORTRAN code package was published by Kahaner et al. (1989). These subroutines use Gear's method to solve a stiff system of ordinary differential equations. Since the calculations in GPAS are mostly in double precision mode, we used DDRIV2 to solve the biological model equations in GPAS.

4.2 Modeling Nitrate Inhibition Mechanisms

Nitrate affects SRB activity in several different ways. Experimental study of reservoir souring enables microbiologists to explain the mechanisms by which nitrate

inhibits reservoir souring. We discussed the main four mechanisms in Section 2.2.3. In the following sections, we describe the mathematical modeling for each mechanism in the biological model of GPAS. No other simulators accommodate such a comprehensive model for reservoir souring remediation by nitrate.

4.2.1 Inhibitory Action of Nitrite

In Section 2.2.3 we discussed the inhibitory effect of nitrite on SRB activity. Figure 4.3 illustrates the generation of nitrite and its inhibiting effect on H_2S production. To model this effect in GPAS, we define nitrite as a product for nitrate reduction metabolic combinations and also as an inhibitor for SRB metabolic combinations. The inhibition effect is modeled by multiplying the bacteria growth and substrate/electron acceptor consumption rates by an inhibition term (Equation (4.17)). The inhibition constant is an input parameter and experimental data is required to accurately find the inhibition constant (I) in Equation (4.17).

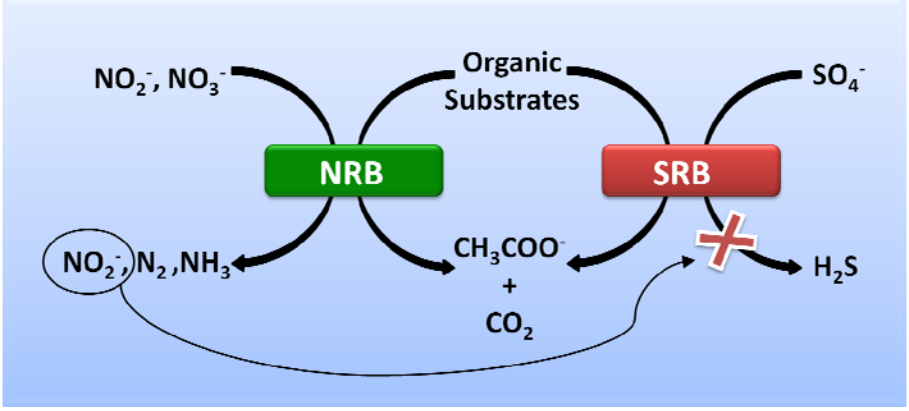

Figure 4.3: The inhibitory action of nitrite.

4.2.2 Bio-Competitive Exclusion

This mechanism involves the competition between NRB and SRB for a common substrate (Figure 4.4). As stated in Section 2.2.3, nitrate reduction has a significant thermodynamic advantage over sulfate reduction. Therefore, in a competition between NRB and SRB for available carbon sources, nitrate-reducing bacteria grow faster and eliminate sulfide production. To model this effect, it is speculated that $\mu_{\max,NRB} > \mu_{\max,SRB}$. The rate at which a microbe population grows exponentially depends on $\mu_{\max}$, known as the specific growth rate. It should be noted that an accurate estimation of the specific growth rates is critical. To model this mechanism, we add a new set of metabolic combinations in which nitrate acts as the electron acceptor instead of sulfate, and biological species for this reaction set are NRB with a higher specific growth rate than SRB.

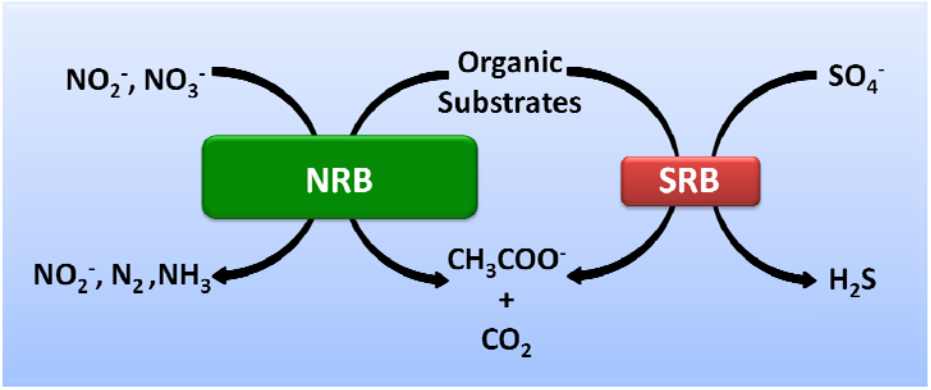

Figure 4.4: Bio-competitive exclusion of SRB by NRB.

4.2.3 Nitrate Utilization by SRB

It is known that some SRB can use nitrate as a terminal electron acceptor, thereby preventing sulfide production (Dalsgaard and Bak, 1994). The competition process of two electron acceptors may be represented very similarly to the substrate competition model proposed by Bailey and Ollis in 1986. According to their model, when substrate competition is considered, the half-saturation coefficient of each substrate Monod term is decreased based on the concentration and half-saturation coefficient of the other competing substrates. For example, if sulfate and nitrate compete for SRB (Figure 4.5), then the Monod expressions are the following:

For SO_4^{2-}:

$$\frac{dC_{SO_4^{2-}}}{dt} = -k_{\max,SO_4^{2-}} X_{SRB} \left(\frac{C_S}{K_S + C_S} \right) \left[\frac{C_{SO_4^{2-}}}{K_{SO_4^{2-}} \left(1 + \frac{C_{NO_3^-}}{K_{NO_3^-}} \right) + C_{SO_4^{2-}}} \right] \tag{4.18}$$

For NO_3^-:

$$\frac{dC_{NO_3^-}}{dt} = -k_{\max,NO_3^-} X_{SRB} \left(\frac{C_S}{K_S + C_S} \right) \left[\frac{C_{NO_3^-}}{K_{NO_3^-} \left(1 + \frac{C_{SO_4^{2-}}}{K_{SO_4^{2-}}} \right) + C_{NO_3^-}} \right] \tag{4.19}$$

When modeled in this manner, the competition reduces the effective rate of biodegradation compared to the rate that would exist in the absence of competition.

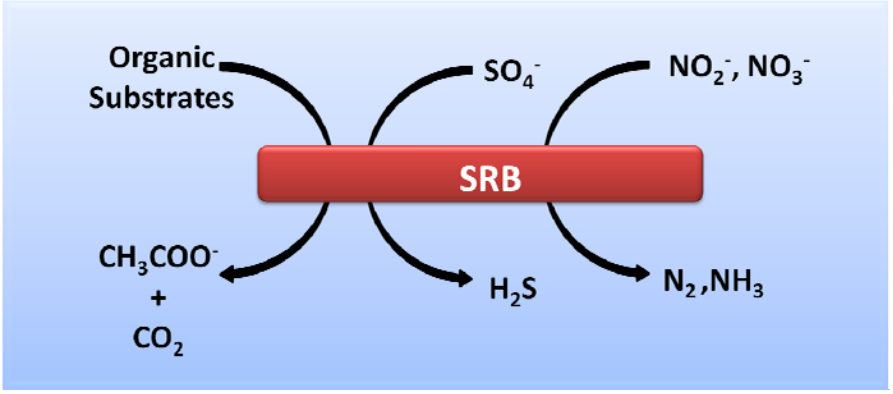

Figure 4.5: Nitrate utilization by SRB.

4.2.4 Nitrate-Reducing Sulfide-Oxidizing Bacteria Stimulation

As illustrated in Figure 4.6, NR-SOB oxidize the existing hydrogen sulfide back to sulfate and remediate reservoir souring. Introducing NR-SOB growth kinetics gives

$$\frac{dX_{NRSOB}}{dt} = \mu_{\max,NRSOB} X_{NRSOB} \left(\frac{C_{HS^-}}{K_{HS^-} + C_{HS^-}} \right) \left(\frac{C_{NO_3^-}}{K_{NO_3^-} + C_{NO_3^-}} \right). \tag{4.20}$$

In this reaction combination, sulfide acts as an electron donor for nitrate reduction. The nitrate reduction is given by the Monod expression:

$$\frac{dC_{NO_3^-}}{dt} = -k_{\max,NRSOB,NO_3^-} X_{NRSOB} \left(\frac{C_{HS^-}}{K_{HS^-} + C_{HS^-}} \right) \left(\frac{C_{NO_3^-}}{K_{NO_3^-} + C_{NO_3^-}} \right). \tag{4.21}$$

Since SRB reduce sulfate to sulfide and NR-SOB produce sulfate from sulfide, the rate expressions for sulfate can be described by

$$\frac{dC_{SO_4^{2-}}}{dt} = -k_{\max,SRB,SO_4^{2-}} X_{SRB} \left(\frac{C_{SO_4^{2-}}}{K_{SO_4^{2-}} + C_{SO_4^{2-}}} \right) \left(\frac{C_S}{K_S + C_S} \right) + k_{\max,NRSOB,SO_4^{2-}} X_{NRSOB} \left(\frac{C_{NO_3^-}}{K_{NO_3^-} + C_{NO_3^-}} \right) \left(\frac{C_{HS^-}}{K_{HS^-} + C_{HS^-}} \right) . \quad (4.22)$$

To model this mechanism, we introduce a new set of biological reactions with H_2S as the substrate and nitrate as the electron acceptor. The net rate of sulfide generation by these competing consortia is simply the rate of consumption of sulfate in Equation (4.22). Thus, if the NR-SOB have the same level of activity as the SRB, the two contributions on the right-hand side of Equation (4.22) negate each other out and the net rate of sulfide generation approaches zero.

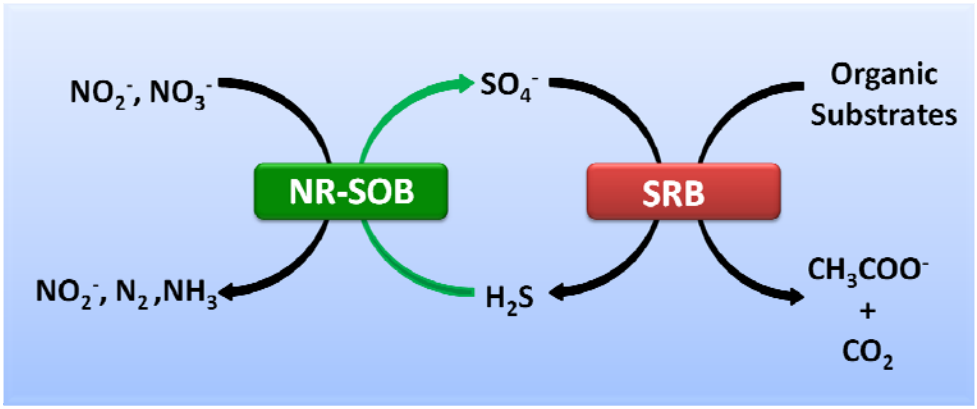

Figure 4.6: Nitrate-reducing sulfide-oxidizing bacteria stimulation.

4.3 IMPLEMENTATION IN GPAS

In this section, we explain the developmental work on the incorporation of the biological model in GPAS. Coupling the model in the chemical module of GPAS and the structure of the code are also discussed.

4.3.1 Solution of the Combined Transport and Biological Equations

The biological model forms a system of ordinary differential equations with concentrations as dependent variables. The chemical module comprises a system of partial differential equations for concentrations. We used an implicit discretization scheme for both models. We must couple two systems of implicit differential equations. We solve the combined transport and biological equations using an operator-splitting approach (Valocchi and Malmstead, 1992), meaning that the solution to mass balance equations is used as the initial condition for the biological equations. At every time step, GPAS solves the governing equations of the chemical module and finds the aqueous components' concentrations. Then it calls the main subroutine of the biological model. The biological model uses the concentrations as an initial condition and solves the reaction equations. The concentrations are subsequently updated and returned to the chemical module for the next time step calculations. The advantage of the operator-splitting method is that the biological model or the chemical module can be modified independent from each other.

4.3.2 GPAS Biological Model Code

The implementation of biological model in GPAS includes the modification of existing subroutines and adding new subroutines. The chemical module of GPAS was initially developed to simulate chemical EOR. The original code could accommodate only four aqueous phase components (surfactant, polymer, salt, and tracer). In reservoir souring, several aqueous phase components are present. The first step in coding was to develop the capability to simulate unlimited number of components in GPAS. We completed this task by modifying various subroutines in the framework and chemical module. Now, GPAS can solve material balance equations for any number of aqueous phase components.

The biological model code solves the system of ordinary differential equations that models the growth rates of biological species and the consumption rates of chemical species (Section 4.1). As illustrated in the workflow of Figure 4.7, the computer code consists of the following subroutines:

- BIOREAD reads the biological input data. This subroutine looks for **`InputFileName.bio`** where **`InputFileName`** is the name of the main GPAS input file. The biological file format keeps the format of UTCHEM biodegradation input data.
- BIOSTEP is the main subroutine of the biological model. It calculates the free-floating and attached biomass concentrations, initializes the equation terms, calls the ODE solver to solve the biological equations, and returns the concentration values to chemical module of GPAS.
- F calculates the derivatives of ODE system. This file is required by DDRIV2.
- G is required by DDRIV2.

- DDRIV2 is the ODE solver. We explained the solver selection criteria in Section 4.2.1. Supplementary information is published by Kahaner et al. (1989).

The next step was to integrate the biological model in GPAS. The driver subroutine of GPAS is XSTEP which is the main interface between the framework and chemical module. It carries out the fluid flow calculations over a time step. The call for BIOSTEP is placed in XSTEP after the convergence is achieved in every time step. The concentrations are updated inside BIOSTEP and XSTEP passes the values to the next time step.

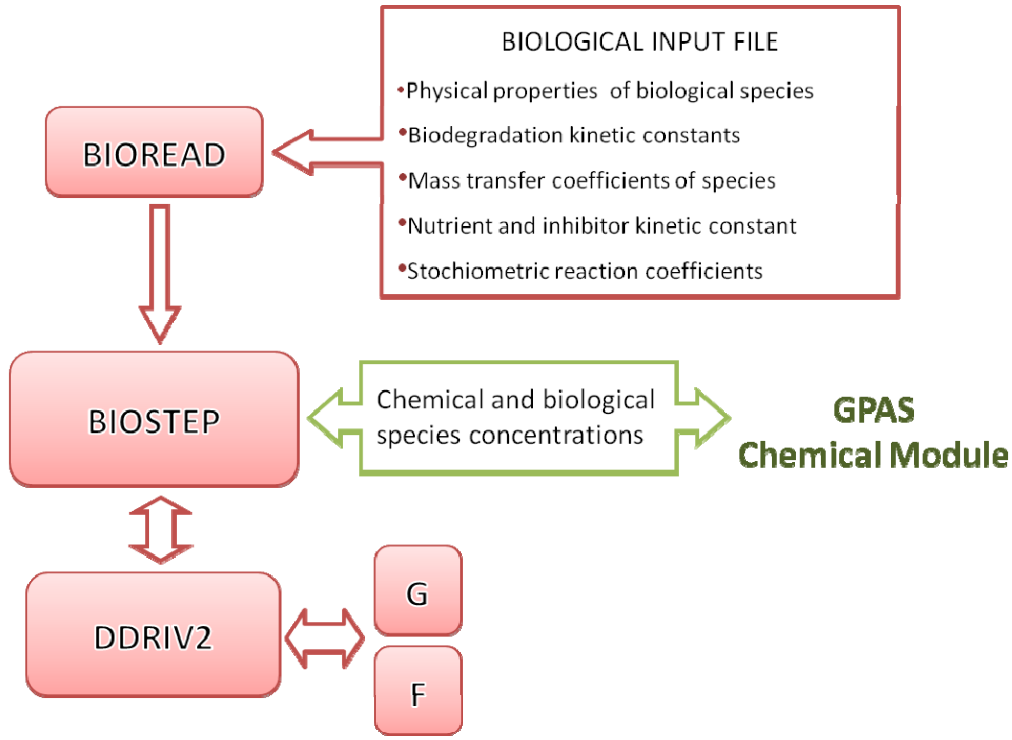

Figure 4.7: Structure of the GPAS biological model.

Chapter 5: Model Verification with Experimental Data

Experimental studies on microbial souring in batch reactors and porous media columns are considered for model validation. Each section in this chapter presents the simulation of a laboratory experiment. In the first two sections, we simulate two separate experiments performed at Montana State University. The first work is microbial souring in an up-flow porous media reactor (Chen et al., 1994). The second work, by the same group, studied the effect of nitrate injection on reservoir souring (Reinsel et al., 1996). In this experiment, the inhibitory action of nitrite is the dominant mechanism in souring mitigation. Section 5.3 presents the simulation of NR-SOB activity in batch reactors studied by Nemati et al. (2001) at The University of Calgary. Section 5.4 demonstrates the simulation results of experiments by Hubert et al. (2005). They studied the activity of NRB and NRSOB bacteria in porous media column reactors. For every experiment, we set up GPAS input based on the reported data and compared the simulation output to laboratory results.

5.1 Microbial Souring in Porous Media

Chen et al. (1994) investigated the microbial souring in a packed-bed porous media reactor. The reactor is a 50 cm long column and is equipped with four equally spaced sampling ports. The porosity of crushed Berea sandstone medium is approximately 50%. The injected fluid flows at a constant rate of 650 mL/day from the bottom of the column to the top. This flow rate equals an average pore velocity of 55 cm/day which is close to the flow speed for water injection in reservoirs. We model this

column with a one-dimensional grid with 20 cells with constant porosity of 0.5 and constant permeability of 300 md. Figure 5.1 shows a schematic of the experimental setup and the simulation model.

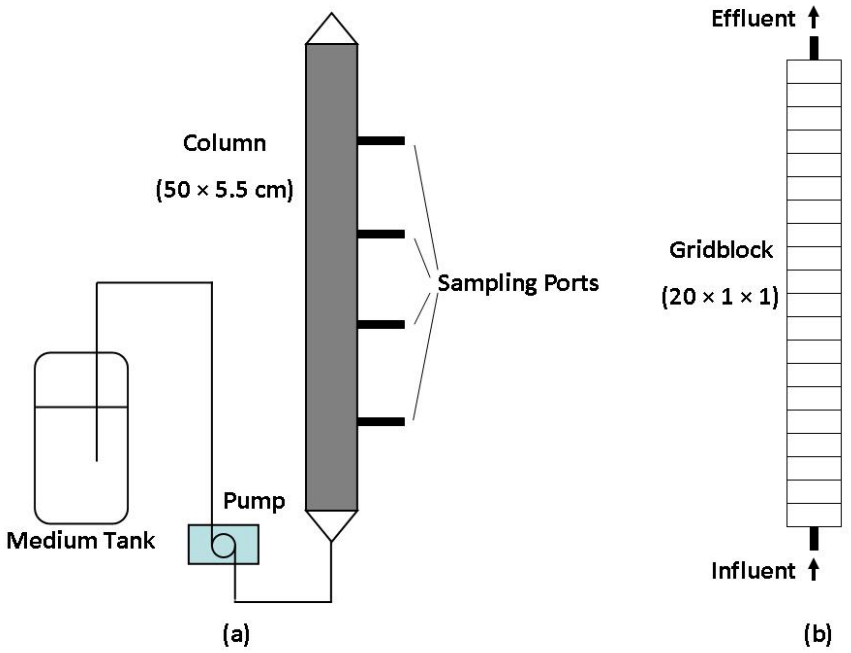

Figure 5.1: Schematics of (a) experimental setup (Chen et al., 1994) and (b) simulation model for souring in the porous media column.

Produced water from Kuparuk (Alaska) fields was used to establish the microbial consortia. In the simulator, all of the microbial species are lumped as a single type of SRB. As stated by Chen et al., the biomass attached to the surface of grains in the column is dominant over free-floating cells. Hence, in the simulation model for this case, only attached biomass is assumed to be active in oxidation-reduction reactions. Four short-chain acids (formic acid, propionic acid, n-butyric acid, and isobutyric acid) were used as the substrates in the model since they were the major carbon sources in the

experiment. Table 5.1 shows the feed concentration in our simulation; sulfate is the only electron acceptor and is available in excess to avoid electron acceptor limitation. The chemical and biological species and associated model parameters are shown in Table 5.2. The model consists of four metabolic combinations for SRB, sulfate, and each substrate (n-butyrate, isobutyrate, formate, and propionate). To find the maximum specific growth rates and half saturation coefficients, we started from values in the literature for SRB reactions (Vance and Thrasher, 2005) and adjusted the parameters to fit the concentration profiles reported in Chen et al. (1994). We calculated the substrate utilization and product generation coefficients from experiment data in Chen et al. (1994) and the reaction stoichiometry. For instance, experiment data provide how many moles of available sulfate are consumed and from reaction stoichiometry, we obtain the equivalent generated H_2S. The same approach is used to find the amount of substrate consumed per one mole of sulfate reduced (substrate utilization rate).

Figure 5.2 shows the simulation results of H_2S production against experimental data. H_2S production starts about 20 days after the injection starts. During this time, bacteria grow to an amount that is large enough to facilitate the oxidation-reduction reactions. After the initial indication of souring, H_2S concentration in the effluent increases steadily until it becomes relatively constant in about 60 days.

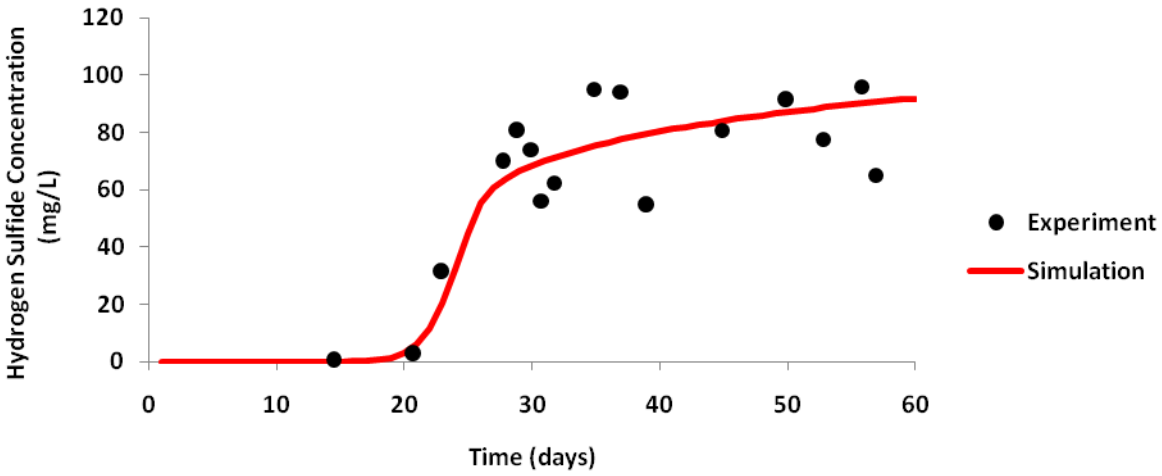

Figure 5.2: Simulation (this work) and laboratory results (Chen et al., 1994) of H_2S production for the souring case.

Table 5.1: Feed composition for the reservoir souring experiment simulation.

	Component	Concentration (mg/L)
Electron acceptor	Sulfate	320
Substrates	n-Butyrate	200
	Isobutyrate	250
	Formate	200
	Propionate	200

Table 5.2: Biological model parameters for the reservoir souring model.

Metabolic Combination	1	2	3	4
Substrate	N_Butyrate	Isobutyrate	Formate	Propionate
Biological species	SRB	SRB	SRB	SRB
Electron acceptor	Sulfate	Sulfate	Sulfate	Sulfate
Product	H_2S	H_2S	H_2S	H_2S
Maximum specific growth rate (1/day)	1	0.1	0.1	0.01
Yield coefficient	0.8	0.2	0.2	0.2
Substrate half saturation coefficient (mg/L)	180	600	600	600
Electron acceptor half saturation coefficient (mg/L)	10	10	10	10
Substrate utilization rate	0.1	0.8	0.8	0.8
Product generation coefficient	0.0375	0.3	0.3	0.3

Substrate utilization and the transformation of sulfate to sulfide along the column are shown in Figure 5.3 and Figure 5.4, respectively. These profiles show the concentrations at the end of the experiment (60 days). In the experimental setup, sampling ports provide measurements of chemicals along the column. Means and standard deviations of several measurements are reported in Figure 5.3 and Figure 5.4. As sulfate and substrates are consumed through the column, H_2S concentration increases (Figure 5.4). The produced hydrogen sulfide is transported toward the end of the column. The sulfate concentration decreases from 320 mg/L at the inlet to 75 mg/L at the outlet. The rate of consumption of sulfate is higher at the beginning part of the

column compared to the end region. This is consistent with the substrate utilization shown in Figure 5.3. The simulated profile of n-butyrate concentration shows that it is depleted within the first 10 cm of the column. This is because a larger reaction rate constant is set for the biological combination of n-butyrate, sulfate, and SRB. The concentration profiles of isobutyrate and formate are also shown in Figure 5.3. There is a good agreement between the simulation trend and laboratory data. In the model, all biological reactions proceed with a growth in biomass.

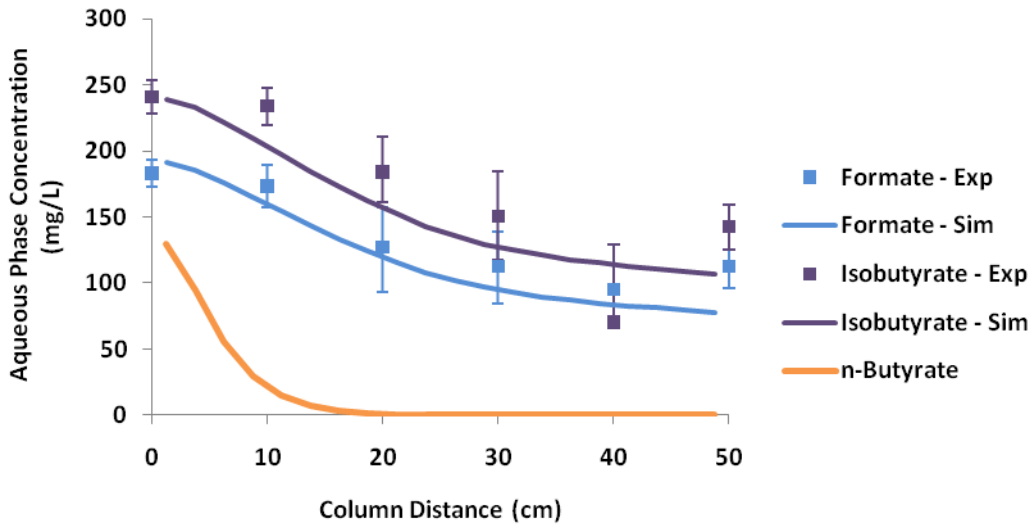

Figure 5.3: Substrates concentration profiles in the column for the souring case (curves: simulations in this work; points with error bars from Chen et al., 1994).

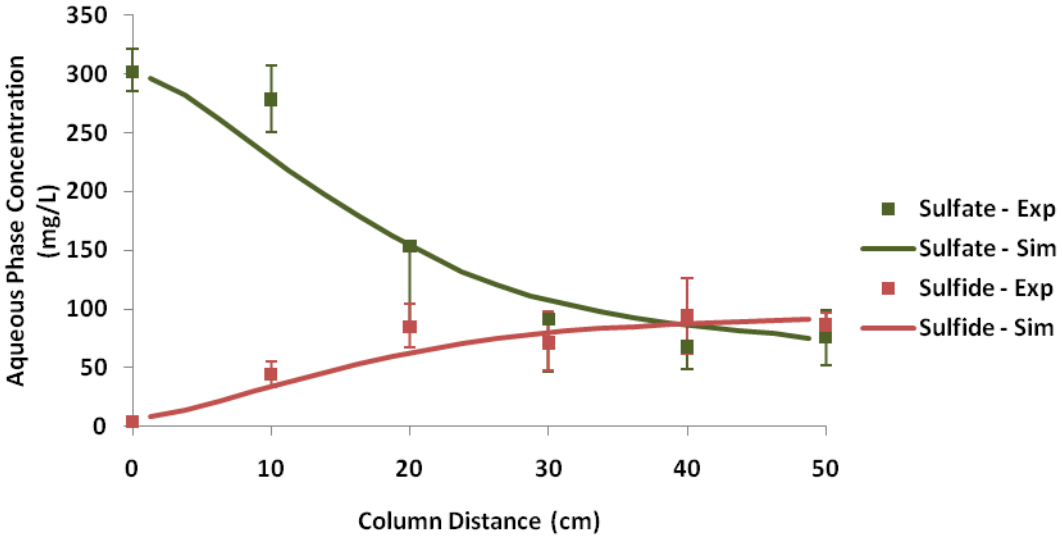

Figure 5.4: Hydrogen sulfide and sulfate concentration profiles in the column for the souring case (curves: simulations in this work; points with error bars from Chen et al., 1994).

Figure 5.5 shows simulated profiles of attached SRB. The exponential growth of the bacteria population can be observed in this figure. The biomass amount is insignificant for up to 18 days. However, the biomass increases and reaches the maximum concentration of 3000 mg/L. This maximum value is obtained from biomass accumulation data in the column experiment of Chen et al. (1994). At the end of the experiment, in the region from 0 to 30 cm of the core, the biomass amount has reached the maximum limit. As discussed in the model development (Section 4.1), the consumption of nutrients continues even after the biomass stops growing. Thus, the concentration of sulfide in the effluent remains high.

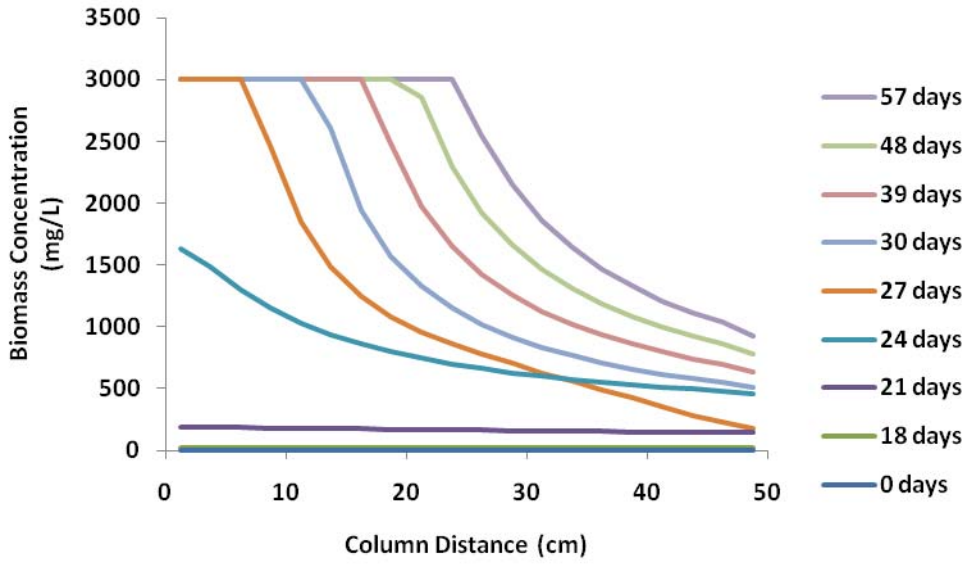

Figure 5.5: Simulated SRB profiles in the column at different times for the souring case.

5.2 Control of Microbial Souring by Nitrate

After testing and tuning our model for the basic microbial souring simulation, we consider simulation of nitrate injection for souring remediation. For this purpose, we simulate an experiment by Reinsel et al. (1996). The experimental setup is similar to the souring experiment described in Section 5.1. The microbial consortia and the substrate concentrations are also the same as before. Sulfate is injected at a much higher concentration of 1350 mg/L (Table 5.3) to avoid sulfate limitation. The experiment starts with no nitrate injection at the beginning. The process is given enough time for H_2S concentration to reach steady-state. Nitrate is then injected at a concentration of 300 mg/L.

Table 5.3: Feed composition for the reservoir souring control by nitrate.

	Component	Concentration (mg/L)
Electron acceptors	Sulfate	1350
	Nitrate (after 20 days)	300
Substrates	n-Butyrate	200
	Isobutyrate	250
	Formate	200
	Propionate	200

The simulation of this process requires adding another set of bacteria (NRB) and associated biological reactions to the previous model. NRB reduce nitrate to nitrite and consume the same available substrates. Rapid consumption of nitrate at the beginning of the column implies that NRB are more active than their competitors (SRB). This could affect the activity of SRB, but an adequate amount of substrates is available and the competition for substrates is not rigorous enough to stop SRB activity. In this experiment, the inhibitory action of nitrate is believed to be the main mechanism of souring remediation. We model this effect by introducing the inhibition factor in the substrate and electron acceptor utilization rates (Section 4.1.1). The inhibition constant (I) is tuned to a value of 1.0 to match the experimental data. The model parameters for NRB metabolic combinations are presented in Table 5.4. The SRB metabolic combination parameters are the same as the previous experiment (Table 5.3). Similar to the SRB parameters, we started with generic values for these types of bacteria and adjusted the parameters to fit the nitrate and nitrite concentration profiles.

Table 5.4: Biological model parameters for the reservoir souring control by nitrate.

Metabolic Combination	1	2	3	4
Substrate	N_Butyrate	Isobutyrate	Formate	Propionate
Biological species	NRB	NRB	NRB	NRB
Electron acceptor	Nitrate	Nitrate	Nitrate	Nitrate
Product	Nitrite	Nitrite	Nitrite	Nitrite
Maximum specific growth rate (1/day)	2	0.5	0.3	0.3
Yield coefficient	0.1	0.1	0.1	0.1
Substrate half saturation coefficient (mg/L)	150	250	250	250
Electron acceptor half saturation coefficient (mg/L)	20	20	20	20
Substrate utilization rate	1.2	1.2	1	1
Product generation coefficient	0.96	0.96	0.8	0.8

In the simulation, nitrate injection starts after 20 days when H_2S is being produced at a constant concentration of 195 mg/L (Figure 5.6). Nitrate injection stimulates NRB to take part in nitrate reduction. Once enough nitrite is produced to entirely inhibit SRB activity, the concentration of H_2S at the effluent becomes zero. Figure 5.6 shows that 30 days after the start of nitrate injection (day 50), all of the nitrate is consumed in the column and the nitrate concentration in the effluent is not a considerable amount. However, a stoichiometric equivalent amount of nitrite is produced. The experimental and simulation profiles of nitrate and nitrite along the column are shown in Figure 5.7. The transformation of nitrate to nitrite takes place at the first 5 cm of the column. The large reaction rate of the nitrate-substrate-NRB combination in the model explains the rapid consumption of nitrate.

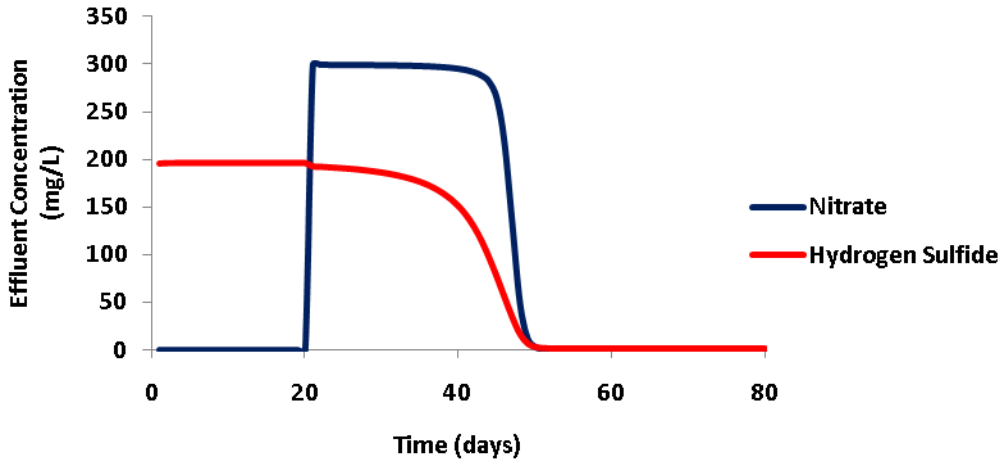

Figure 5.6: Simulated nitrate and H_2S concentrations at the effluent for the nitrate injection case.

The investigation of bacterial growth and accumulation after nitrate injection shows that the NRB population is at its maximum at the beginning section of the column. Since the nitrate concentration is not significant away from the beginning part of the reactor, the NRB population does not increase notably from its initial value. On the other hand, the SRB population develops, but the bacteria are not active in the reduction of sulfate because of the nitrite inhibition effect. The biomass profiles are plotted in Figure 5.8.

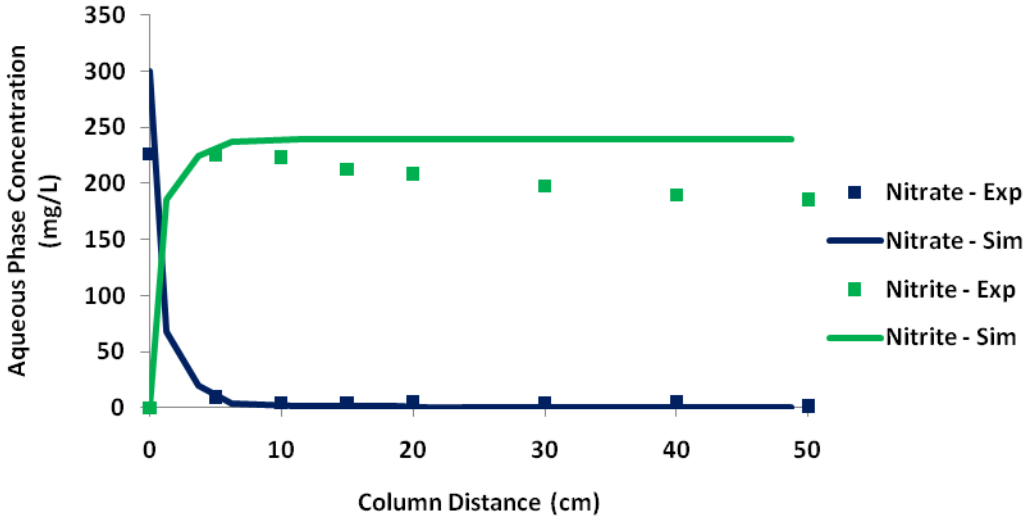

Figure 5.7: Nitrate and nitrite profiles in the column at time t = 80 days for the nitrate injection case (curves: simulations in this work; points from Reinsel et al., 1996).

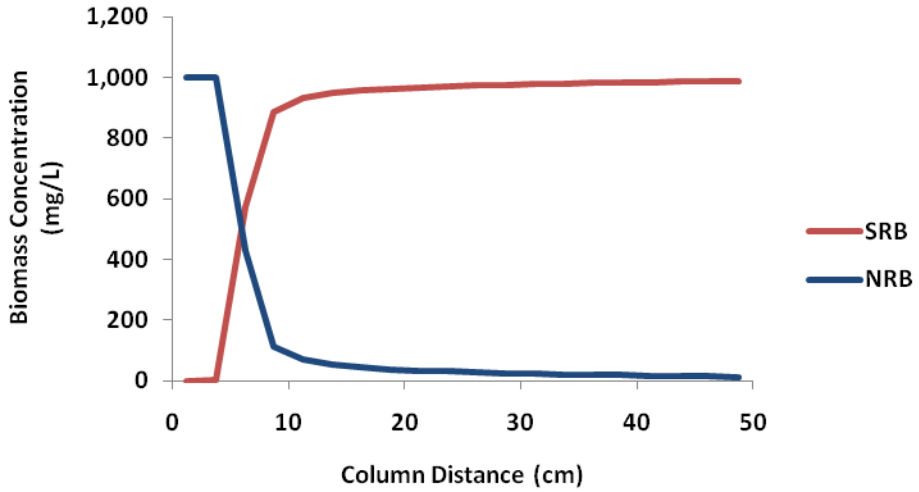

Figure 5.8: Simulated SRB and NRB profiles in the column for the nitrate injection case.

The effect of nitrate injection in reservoir souring is modeled with the assumption that nitrite is inhibiting the sulfate reduction activity of SRB. The comparison of simulation results (Figure 5.6) with experimental data (no H_2S production 30 days after nitrate addition) shows that this assumption is valid for this study. Reinsel et al. (1996) report other methods of souring control such as direct nitrite addition to the reactor, which has the same inhibitory effect on H_2S generation.

The laboratory experiment simulations demonstrate the capability of GPAS in modeling the reactions associated with reservoir souring. The maximum specific growth rate in reactions and other model parameters are found for this specific microbial system. These reaction parameters could be used for the field-scale simulation of a reservoir with similar bacterial culture and aqueous phase components.

5.3 NR-SOB Activity in a Batch Reactor

Nemati et al. (2001) studied the microbial control of biogenic H_2S production by nitrate-reducing sulfate-oxidizing bacteria. They made a model system consisting of pure cultures of the nitrate-reducing sulfate-oxidizing bacterium *Thiomicrospira sp*. strain CVO and the sulfate-reducing bacterium *Desulfovibrio sp.* strain Lac6. Using pure cultures of bacteria is an advantage of selecting this experiment for numerical modeling as there are fewer biological species and corresponding parameters in our model. Nemati et al. used serum bottles containing a synthetic brine medium as batch reactors. The medium contained 14 mM sulfate as the electron acceptor for SRB. In the experiments that we model, nitrate concentration was 10 mM. A separate experiment showed that this concentration had a slight effect on sulfate reduction even with no NR-

SOB in the system. The medium was initially inoculated with 3 mL of SRB culture (10^9 cell/mL).

In a second set of experiments to study the effect of NR-SOB on H_2S production, 3 mL of NR-SOB culture (10^8 cell/mL) was added during the exponential growth of SRB (after 50 hours). All the reactors with NR-SOB and without NR-SOB continued to operate for 400 hours. Lactate was the main substrate for bacterial activity, with different concentrations of Na-lactate ranging from 10 to 50 mM. The experiment results are presented in Figure 5.9. Column (a) shows the sulfide generation with no NR-SOB present. Sulfide production was observed after 24-48 hours in all the cultures. With 10 mM of Na-lactate only 50% of available sulfate was reduced to sulfide, because of the substrate limitation. In the culture containing 20 mM of Na-lactate, the extent of sulfate reduction reached 85%. A complete reduction of sulfate was achieved after 70-80 hours in the media with 30 and 50 mM of lactate. Column (b) in Figure 5.9 shows the effect of adding NR-SOB to the cultures after about 50 hours. NR-SOB inhibited the activity of SRB in all the cultures with different Na-lactate concentrations. Sulfide concentration decreased to zero and sulfate was generated. These results show the long-lasting inhibition of sulfide production by NR-SOB and nitrate. Increasing the lactate concentration did not revert the inhibition effect. Therefore, competition over substrate is not the main mechanism of souring remediation. Instead, the inactivity of SRB and regeneration of sulfate indicate that NR-SOB mitigates reservoir souring in two ways. It imposes a strong inhibition effect on sulfide production by SRB and also diminishes the level of H_2S by sulfide oxidation. We implemented formulation for modeling both effects in our simulator as explained in Section 4.2. To model the batch reactor experiments with a fluid flow simulator (GPAS), we built a single gridblock model with the same

volume as serum bottles in Nemati et al. (2001) experiments and a porosity and water saturation of one.

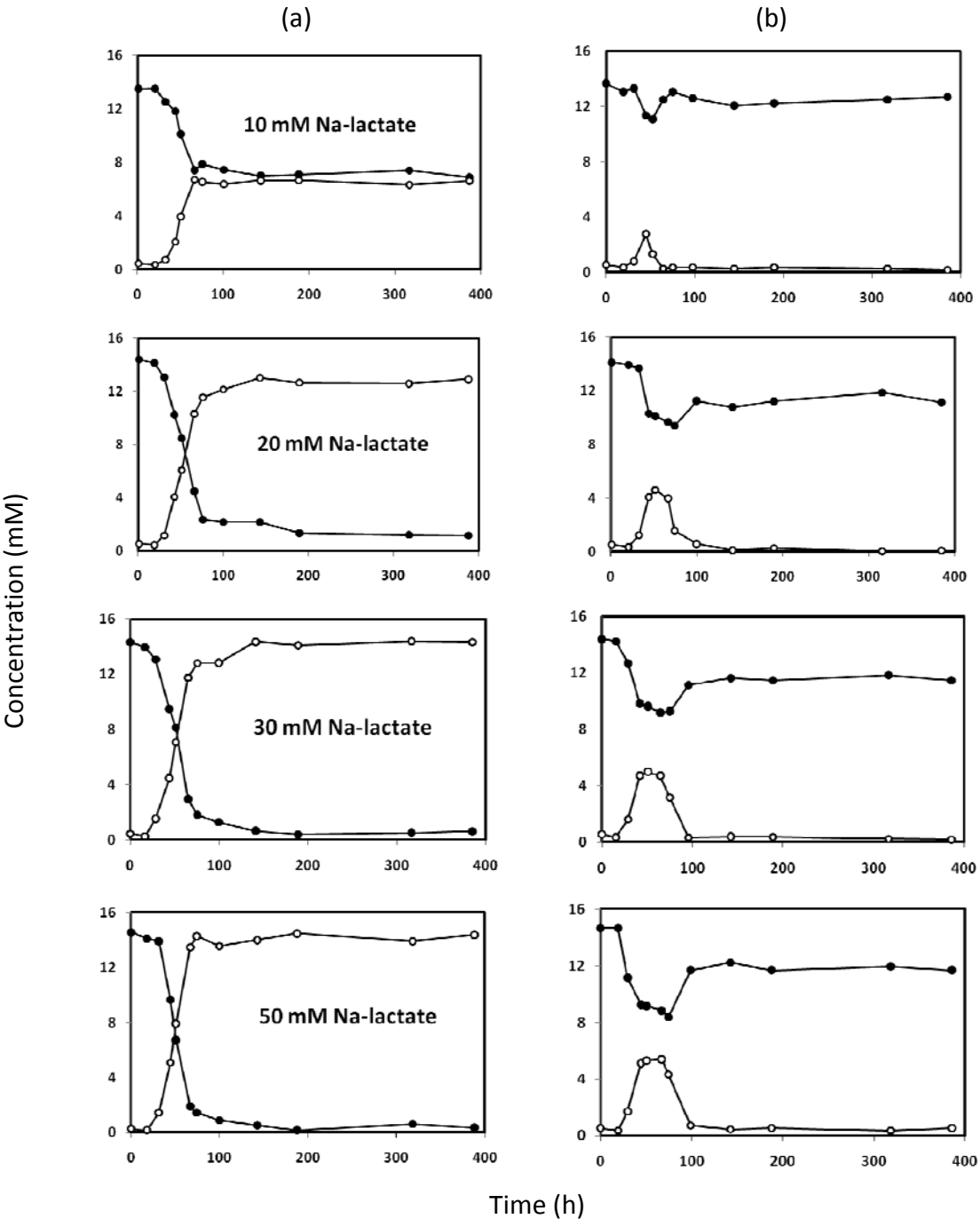

Figure 5.9: Concentrations of sulfate (●) and sulfide (○) in a culture of SRB in the presence of 10 mM nitrate and different Na-lactate concentrations (a) without NR-SOB and (b) with NR-SOB added after 50 hours (Nemati et al., 2001).

We explained the modeling of inhibitory action of nitrite in the previous section. This effect is also observed in the Nemati et al. (2001) experiments with NR-SOB. The additional effect of NR-SOB is sulfide oxidization. The model is therefore extended with a new set of reaction for the oxidization of sulfide to sulfate. Hence, we have three metabolic combinations. The first metabolic combination is the reduction of sulfate by SRB. H_2S is the product of this reaction. The second combination is the reduction of nitrate to nitrite by NR-SOB. The produced nitrite acts as an inhibitor for the SRB activity which is presented by the first metabolic combination. Lactate is the electron donor for both reactions. The third metabolic combination is sulfide oxidization by NR-SOB. Sulfide is the electron donor and sulfate is the product of this reaction. The equations being used in the model are

Sulfate reduction:

$$\text{Lactate} + \text{Sulfate} + \text{SRB} \rightarrow H_2S + CO_2 + H_2O + \text{SRB}$$

Nitrate reduction:

$$\text{Lactate} + \text{Nitrate} + \text{NR-SOB} \rightarrow \text{Nitrite} + CO_2 + H_2O + \text{NR-SOB}$$

Sulfide oxidization:

$$\text{Sulfide} + \text{Nitrate} + \text{NR-SOB} \rightarrow \text{Sulfate} + \text{Nitrite} + H_2O + \text{NR-SOB}$$

Since we are modeling a batch reactor, bacteria are free-floating in the aqueous phase. The model is set up and run for all of the cases in Figure 5.9. Table 5.5 presents the parameters of the biological model for this simulation case. The specific growth rates, yield coefficients, and half saturation coefficients are common values for SRB and NR-SOB from the literature (Vance and Thrasher, 2005). The product generation and electron acceptor utilization coefficients are calculated from the stoichiometric ratios and consumption rate data reported by Nemati et al. (2001). The reaction parameters

are adjusted to fit the experimental data for the case of 30 mM of Na-lactate. The same parameters are then used for other cases (10, 20, and 50 mM of Na-lactate). Figure 5.10 shows the simulation results against the experimental data points. The experimental data are the same as Figure 5.9. Simulation matches the experiment agreeably for 20 mM Na-lactate. With 10 mM Na-lactate, simulation results show more delay in sulfate reduction and sulfide generation. For the media with 50 mM of lactate, simulation predicts less sulfide oxidation than the experiment. It is because of the consumption of the nitrate before complete elimination of H_2S (shown in Figure 5.12). We will give further discussion on limiting compounds in each experiment later.

Column (a) in Figure 5.10 shows the basic H_2S generation by SRB for different values of substrate concentration. With 10 mM of Na-lactate, half of the initial sulfate concentration is reduced. This ratio gives the substrate utilization coefficient for our model. With 20 mM and more Na-lactate, the substrate amount is no longer a limiting factor and the entire sulfate is reduced. Column (b) shows the effect of adding NR-SOB after 50 hours from the beginning of the experiment. In all the cases, sulfate concentration decreases in the first 50 hours as SRB is the only active bacteria. Once NR-SOB is added to the system the sulfate reduction rate decreases. After a while, by increasing the NR-SOB population and further oxidation of sulfide, the sulfate concentration increases. However, the sulfate concentration at the end of the experiment is less than the original amount, indicating that sulfide is oxidized partly to sulfate and partly to elemental sulfur.

Table 5.5: Biological model parameters for the NR-SOB batch reactor simulation

Metabolic combination	Components		Parameters	
Sulfate reduction	Biological species	SRB	Maximum specific growth rate (1/day)	1.1
			Yield coefficient	0.15
	Substrate	Lactate	Substrate half saturation coefficient (mg/L)	1000
			Substrate utilization rate	0.89
	Electron acceptor	Sulfate	Electron acceptor half saturation coefficient (mg/L)	10
	Product	H_2S	Product generation coefficient	0.49
	Inhibitor	Nitrite	Inhibition constant (mg/L)	1
Nitrate reduction	Biological species	NR-SOB	Maximum specific growth rate (1/day)	1
			Yield coefficient	0.01
	Substrate	Lactate	Substrate half saturation coefficient (mg/L)	1000
			Substrate utilization rate	0.3
	Electron acceptor	Nitrate	Electron acceptor half saturation coefficient (mg/L)	10
	Product	Nitrite	Product generation coefficient	0.24
Sulfide oxidation	Biological species	NR-SOB	Maximum specific growth rate (1/day)	1
			Yield coefficient	0.05
	Substrate	Sulfide	Substrate half saturation coefficient (mg/L)	100
			Substrate utilization rate	0.2
	Electron acceptor	Nitrate	Electron acceptor half saturation coefficient (mg/L)	10
	Product	Sulfate	Product generation coefficient	0.91

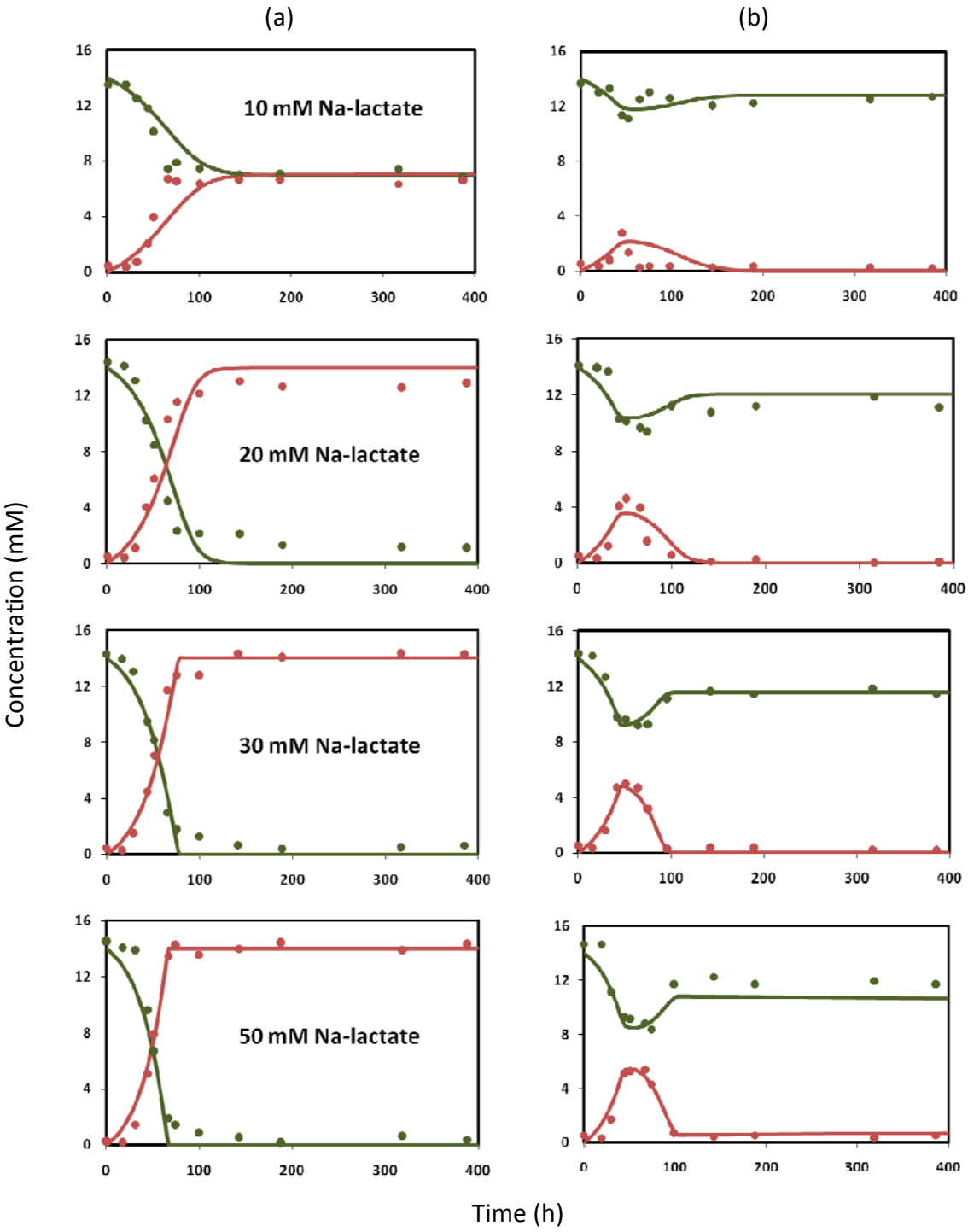

Figure 5.10: Simulation results (solid lines) and experimental data (dots) for the effect of NR-SOB on sulfide production with different Na-lactate concentrations. Sulfate concentration is shown in green and sulfide concentration is in red.

As stated before, three reactions of the NR-SOB simulation case are sulfate reduction, nitrate reduction, and sulfide oxidation. They occur simultaneously throughout the experiment. However, the dominant reaction at every phase of the experiment is determined by available chemical and bacterial species. Before adding NR-SOB, the only bacteria culture is SRB, which reduces sulfate to sulfide. Adding NR-SOB initiates the nitrate reduction and sulfide oxidation. The produced nitrite suppresses SRB activity, thereby inhibiting sulfate reduction. At the final stage of this experiment, sulfide oxidation is the main reaction.

To understand the mechanism of NR-SOB and the effect of substrate and electron acceptor limitation, we study the changes in chemical and biological species concentrations for experiments with 20 and 50 mM Na-lactate. Figure 5.11 shows the concentrations for the experiment with 20 mM lactate up to 150 hours when it has reached the steady-state. Shortly after adding NR-SOB, the SRB growth stops because of the inhibition effect of nitrite. The rise in the nitrite concentration, while the nitrate amount decreases, is evident. NR-SOB grow exponentially and the sulfide removal rate increases; at about 100 hours, sulfide is removed entirely. Nitrate reduction is continued until lactate is depleted. At that time, NR-SOB growth stops and steady-state is achieved. The amount of lactate is sufficient for sulfide removal but is a limiting factor for NR-SOB activity. Nemati et al. (2001) measured the composition of the bacteria culture at 140 hours following the complete oxidation of sulfide. They reported 73% NR-SOB and 27% SRB in the media. Figure 5.11 shows 3.4×10^{10} cells of NR-SOB (78%) and 1.2×10^{10} cells of SRB (22%) at 140 hours. Thus, the simulation result is in a good agreement with experimental data for the bacteria population growth.

Compared to the 20 mM of Na-lactate in Figure 5.11, sulfate and nitrate consumption rates increase in the case of 50 mM Na-lactate as shown in Figure 5.12.

Hence, SRB generate more sulfide in the early stages of the experiment with 50 mM Na-lactate than the 20 mM case. Sulfide removal is also faster than the case with less lactate. The plots of SRB and NR-SOB cell numbers show that bacteria population is much larger in the 50 mM Na-lactate experiment than the case with 20 mM Na-lactate. As expected, providing more sources of carbon and energy resulted in further bacteria growth. The NR-SOB population with 50 mM lactate increases to about 5×10^{10} cells compared to 3.4×10^{10} cells with 20 mM lactate. The large population of NR-SOB consumes the nitrate rapidly; hence, nitrate becomes the limiting component for NR-SOB activity in the media with 50 mM Na-lactate. When nitrate is depleted completely, steady-state occurs while extra amount of lactate remains in the reactor.

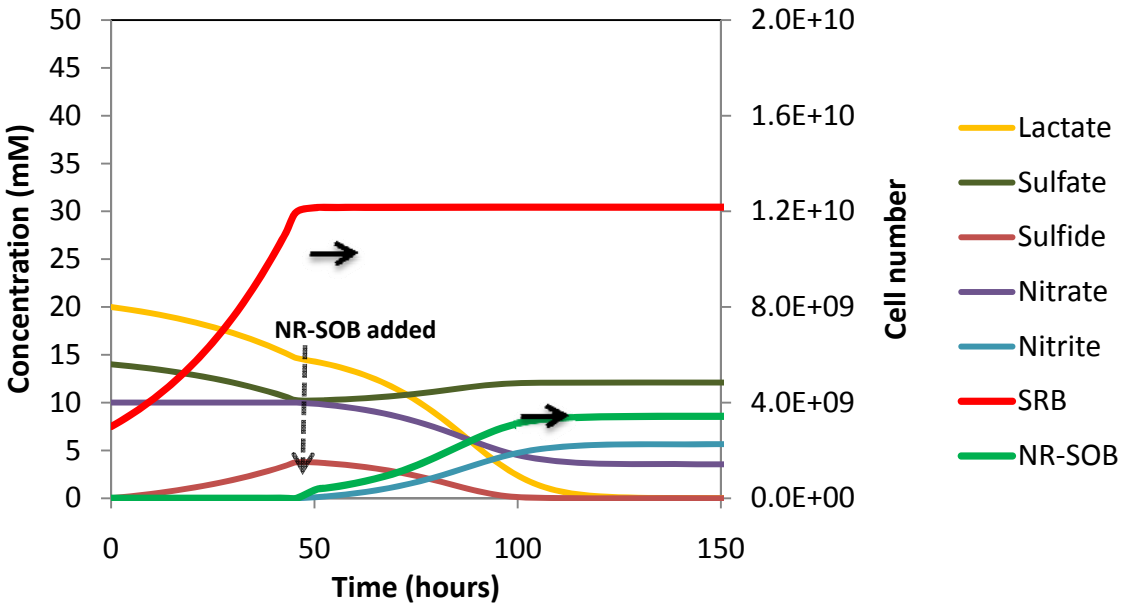

Figure 5.11: Simulated chemical and biological species concentrations in the media with 20 mM Na-lactate and NR-SOB (added at 50 hours).

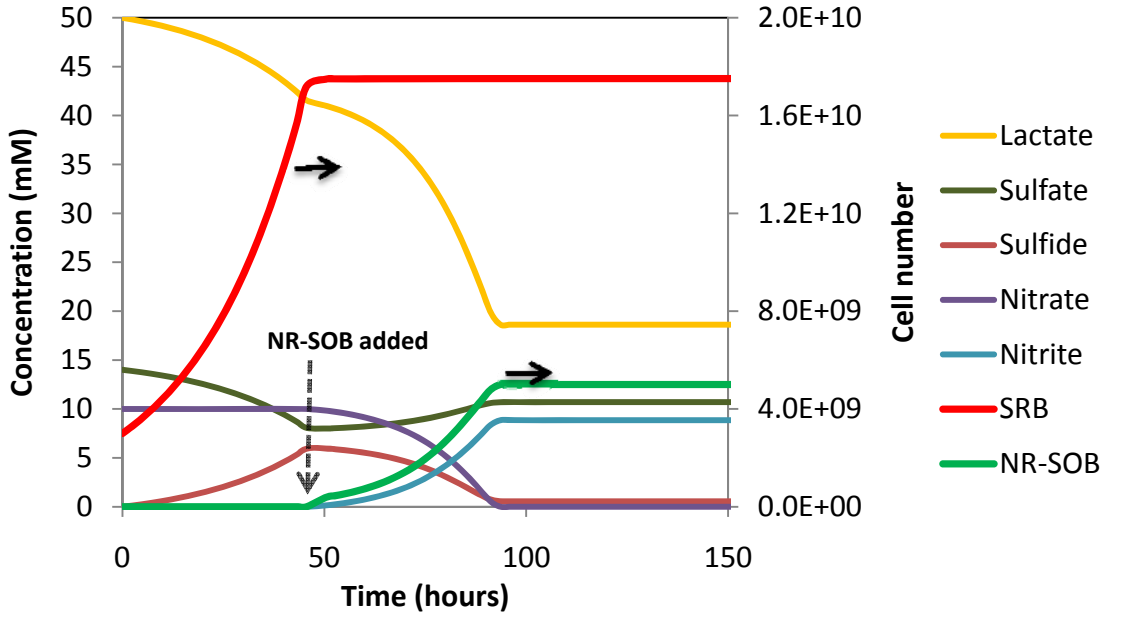

Figure 5.12: Simulated chemical and biological species concentrations in the media with 50 mM Na-lactate and NR-SOB (added at 50 hours).

5.4 NR-SOB ACTIVITY IN A COLUMN

Hubert et al. (2003 and 2005) studied the effect of nitrate-reducing sulfide-oxidizing bacteria on souring in sand-packed column reactors. We used their results (Hubert et al. 2005) to compare our simulations to experiments. Figure 5.13 illustrates the experimental setup and its equivalent simulation model. The bioreactor is an up-flow, packed-bed sand column of 4.5 cm in diameter and 64 cm in height. The sampling ports are installed at 14 cm intervals along the column. To simulate this experiment, we used a one-dimensional model with 20 cells and constant porosity and permeability of 0.21 and 300 md, respectively. Hubert et al. (2005) also installed carbon steel corrosion coupons to investigate the corrosion effects of souring and nitrate treatment. Produced water samples from the Coleville oil field in Saskatchewan, Canada was used as inocula. They set up 7 bioreactors to study souring and corrosion in different situations such as no treatment, nitrate treatment, nitrite treatment, and continuous and pulsed injection of nitrate or nitrite. We simulated the basic reservoir souring case with no treatment (bioreactor 1) and the continuous treatment by nitrate (bioreactor 2).

The medium that was used in the bioreactors consisted of 8 mM sulfate and 25 mM lactate. The bioreactors were filled with the medium and inoculated by injecting oil field produced water into sampling ports. The bioreactors operated batch-wise for 21-25 days to allow for microbial growth. Medium was then injected into the reactor at increasing flow rates from 0.5 mL/h to 9 mL/h for 20 days. The final injection rate of 9mL/h corresponds to 24 hour residence time. The injection continued at the constant rate for the first bioreactor for 70 days. For the second bioreactor, nitrate was added at 17.5 mM and injection continued for 67 days. The concentrations of sulfate, sulfide, nitrate, and nitrite were measured at the sampling ports.

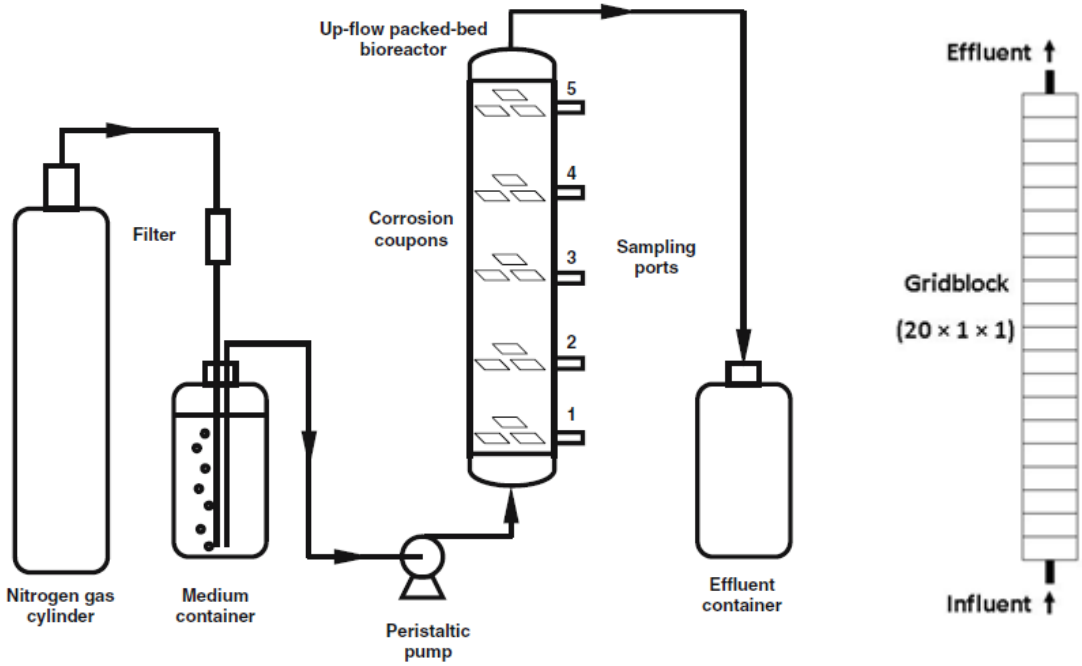

Figure 5.13: Schematics of (a) the experimental setup (Hubert et al. 2005) and (b) the simulation model.

Hubert et al. (2005) measured similar concentrations at ports 2-5; thus, they only reported measurements from ports 1 and 4. Figure 5.14 shows the concentrations of sulfate, sulfide, nitrate, and nitrite at the top and bottom of the column for both bioreactors (bioreactor 1 with no treatment and bioreactor 2 with continuous nitrate injection). Sulfide production started at the batch-wise reaction phase and increased as medium injection started. The complete reduction of sulfate was observed at the top of the column while the sulfate reduction at the bottom was not yet complete. Adding 17 mM nitrate to bioreactor 2 at the constant injection phase caused the sulfide

concentration to drop to 0-1 mM during the rest of the experiment. Nitrate reduction was completed after 10-15 days and nitrite was generated as the main product.

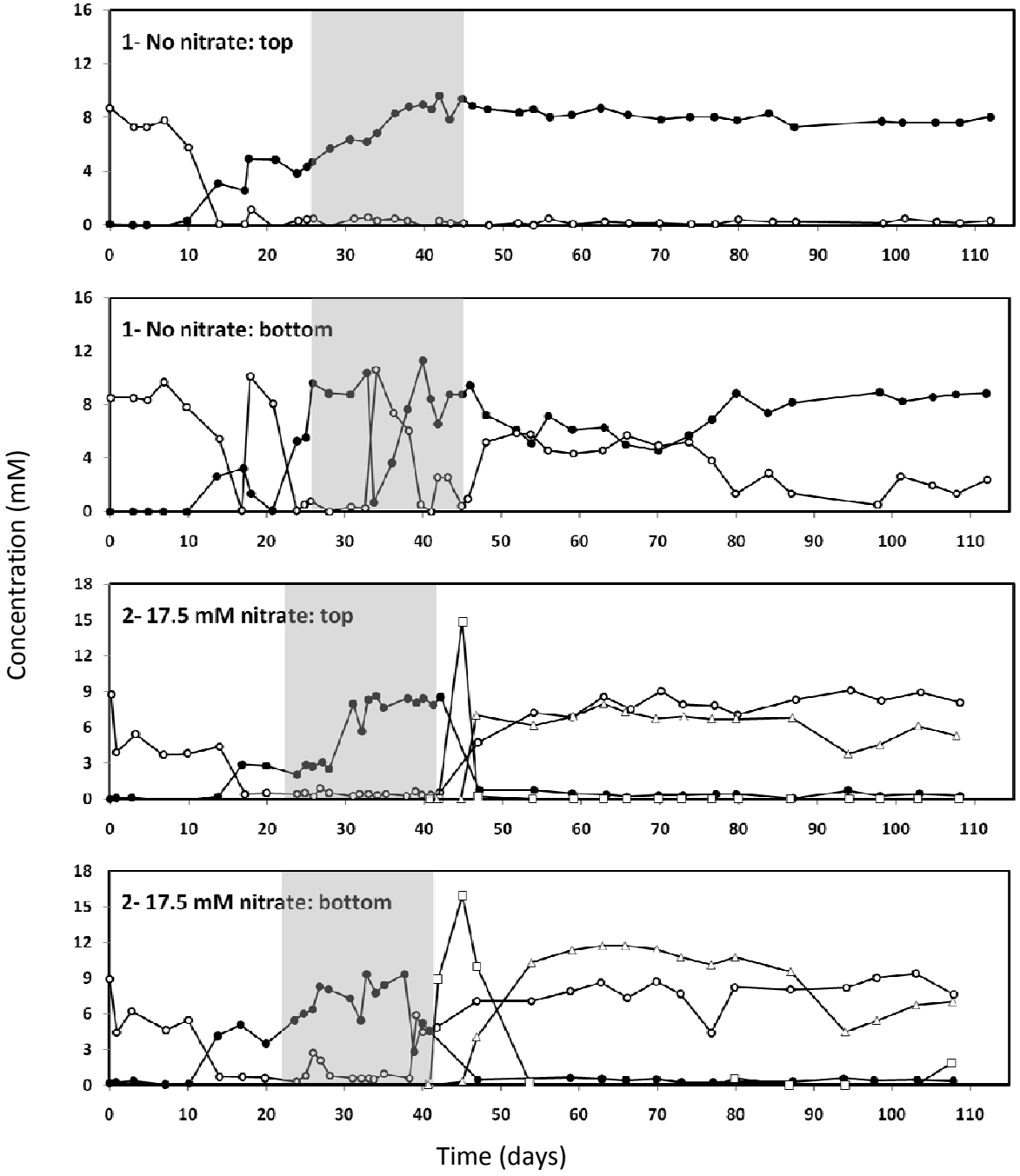

Figure 5.14: Concentrations of sulfate (○), sulfide (●), nitrate (□), and nitrite (Δ) at sampling ports 1 (bottom) and 4 (top). The time domain from left to right represent periods of batch-wise growth, increasing medium flow rates (gray boxes), and constant rate medium injection (Hubert et al., 2005).

This experiment shows the inhibition effect of nitrate when injected at adequate concentrations. The survey of nitrate-reducing bacteria in the water samples shows the presence of hNRB and NR-SOB species. Nitrate injection stimulates these bacteria and results in sulfide removal when nitrate-reducing bacteria are grown to an extensive population. The modeling of bacterial reactions is similar to the batch reactor discussed in the previous section. We include three metabolic combinations. The first metabolic combination is reduction of sulfate by SRB where H_2S is the product of this reaction. The second combination is reduction of nitrate to nitrite by NR-SOB. The produced nitrite acts as an inhibitor for the SRB activity which is presented by the first metabolic combination; lactate is the electron donor for both reactions. The third metabolic combination is sulfide oxidization by NR-SOB. Sulfide is the electron donor and sulfate is the product of this reaction. We assumed that the main active bacteria population is the attached biofilm. Table 5.6 shows the parameters of the biological model for this simulation case. We started with the specific growth rates, yield coefficients, and half saturation coefficients of the batch experiment (Section 5.3) and adjusted the values to fit the experimental results of Figure 5.14. Note that the bacteria culture in Hubert et al. (2005) is obtained from production waters and it is expected to have different characteristics from the pure cultures in Nemati et al. (2001) experiments (Section 5.3). The product generation and electron acceptor utilization coefficients are calculated from the stoichiometric ratios, and by the consumption rate data reported by Hubert et al. (2005).

Bioreactor 1 represents reservoir souring with no nitrate treatment. Hence, NR-SOB are not active. In this case, only the first metabolic combination (SRB-lactate-sulfate) is in effect. We set up the model with the biological model parameters listed in

Table 5.6 and ran the simulation for the three phases of the experiment (batch-wise growth, increasing injection rate, and constant injection rate).

Table 5.6: Biological model parameters for the NR-SOB column bioreactor simulation.

Metabolic combination	Components		Parameters	
Sulfate reduction	Biological species	SRB	Maximum specific growth rate (1/day)	1.1
			Yield coefficient	0.15
	Substrate	Lactate	Substrate half saturation coefficient (mg/L)	1000
			Substrate utilization rate	0.89
	Electron acceptor	Sulfate	Electron acceptor half saturation coefficient (mg/L)	10
	Product	H_2S	Product generation coefficient	0.49
	Inhibitor	Nitrite	Inhibition constant (mg/L)	0.05
Nitrate reduction	Biological species	NR-SOB	Maximum specific growth rate (1/day)	3.5
			Yield coefficient	0.01
	Substrate	Lactate	Substrate half saturation coefficient (mg/L)	2000
			Substrate utilization rate	0.6
	Electron acceptor	Nitrate	Electron acceptor half saturation coefficient (mg/L)	100
	Product	Nitrite	Product generation coefficient	0.18
Sulfide oxidation	Biological species	NR-SOB	Maximum specific growth rate (1/day)	3.5
			Yield coefficient	0.05
	Substrate	Sulfide	Substrate half saturation coefficient (mg/L)	100
			Substrate utilization rate	0.2
	Electron acceptor	Nitrate	Electron acceptor half saturation coefficient (mg/L)	100
	Product	Sulfate	Product generation coefficient	0.91

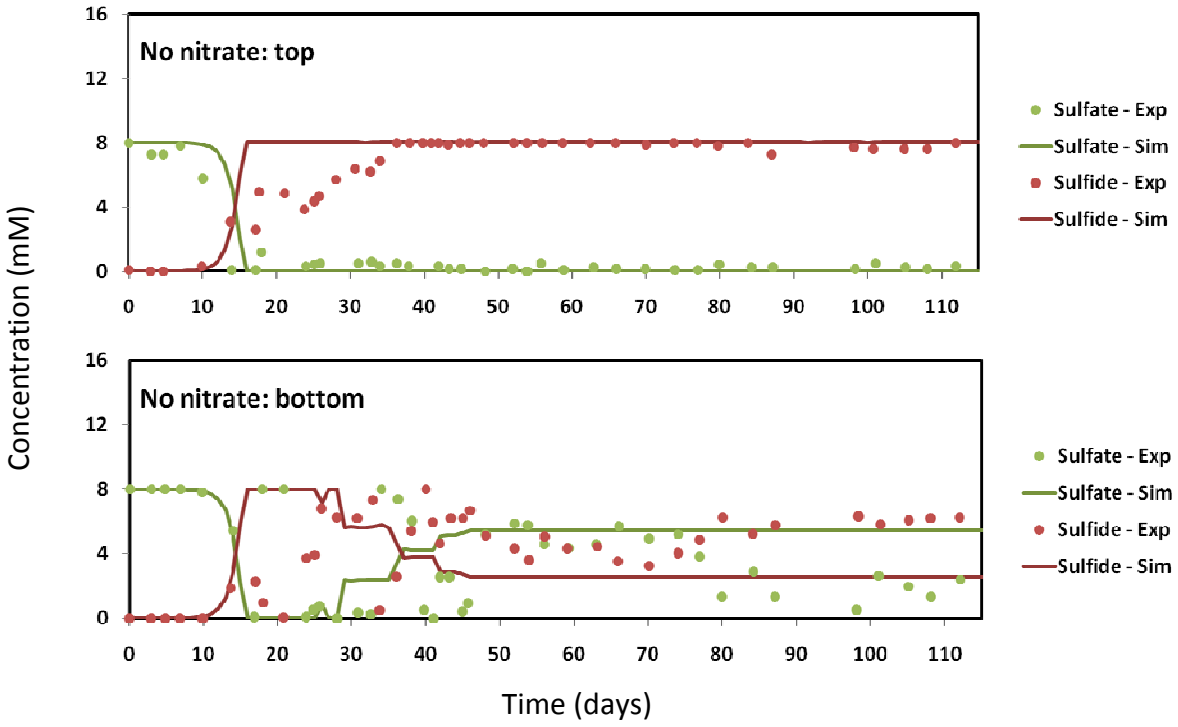

Figure 5.15: Concentrations of sulfate (green) and sulfide (red) at sampling ports 1 (bottom) and 4 (top) for the bioreactor 1 (souring with no treatment). The dots are experimental data points (Hubert et al., 2005) and the solid lines are simulation results (this work).

The simulation results of bioreactor 1 are plotted in Figure 5.15. Some experimental data points for sulfate and sulfide concentrations were above 8 mM, which is the initial sulfate concentration and cannot be exceeded. Those points show inaccurate analytical procedures that resulted in erroneous measurements. We adjusted those data points to a maximum of 8mM for sulfate and sulfide. There is a good match between simulation and experiment for the trend of sulfate consumption and sulfide production. The data points for concentrations at the bottom of the column show vast disorder and do not follow a trend. But the top part of the column shows complete depletion of sulfate as predicted by simulation. In our model, we assumed that for every

mole of sulfate reduced, one mole of sulfide is generated. However, the experiments show that at the early injection times, sulfide concentration is less than the reduced sulfate concentration (Figure 5.15 top). This implies that elemental sulfur is also generated from sulfate reduction. Because the production of elemental sulfur was not noted in the paper and no measurement was performed, we did not include that in the model. The difference between experimental and simulation data for sulfide concentration could be associated with the generation of elemental sulfur or other products of sulfate reduction.

Bioreactor 2 is subject to treatment with the introduction of 17.5 mM nitrate at day 41 when medium injection at a constant rate begins. The simulation results are presented in Figure 5.16 for the top and bottom of the bioreactor. Sulfide concentration drops to zero and sulfate concentration increases to its initial amount of 8 mM. The simulation and experiment results properly match. Nitrate reduction is complete after 5 days at the top of the column and after 15 days at the bottom of the column. Nitrite is the only product in our model; however, the moles of produced nitrite are less than the moles of consumed nitrate, indicating the generation of other products such as ammonia or nitrogen. Our simulator predicts the same nitrite concentration at the final stages of the experiment at the top and bottom of the bioreactor. But, the nitrite concentration at the bottom of the column is reported to be more than the concentration at the top. The authors offer no explanation for this observation; yet, it might be related to the different ratios of nitrite produced per nitrate consumed at the top and bottom of the core. In both cases (no treatment and nitrate addition), the top portion of the bioreactor shows a fairly steady trend which can be more accurately predicted by the simulator than the bottom part of the reactor.

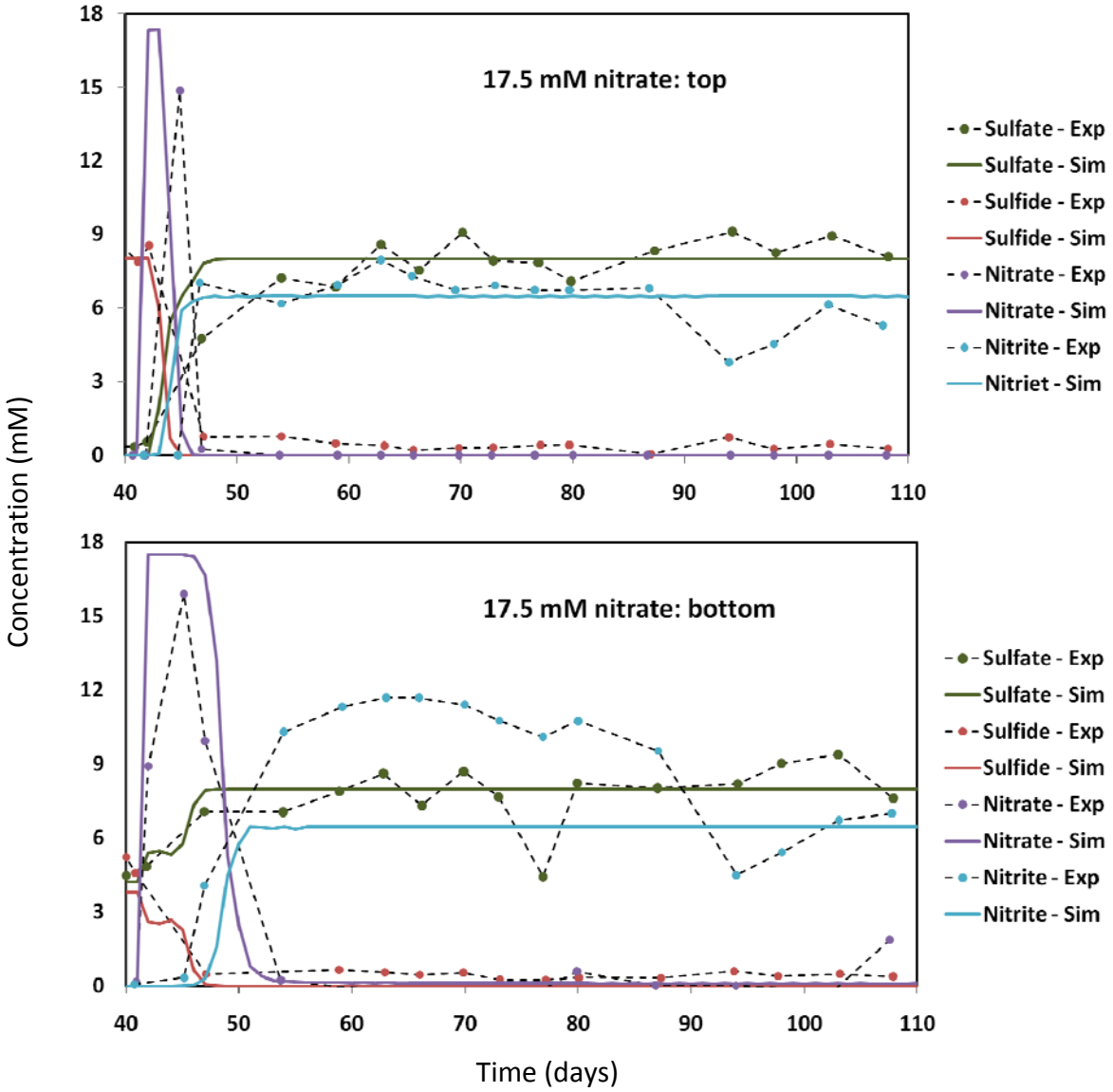

Figure 5.16: Concentrations of sulfate (green), sulfide (red), nitrate (purple), and nitrite (blue) at sampling ports 1 (bottom) and 4 (top) for the bioreactor 2 (souring treatment with 17.5 mM nitrate). The dots are experimental data points (Hubert et al., 2005) and the solid lines are the simulation results (this work).

The simulation of laboratory experiments demonstrates the capability of the biological model in GPAS to handle the full suite of biological pathways and reactions relevant for souring and inhibition of souring. However, microbial reaction parameters such as maximum specific growth rates and half saturation coefficients are used as fitting parameters for history matching of experiments. The obtained parameters are used to predict the results of similar experiments as shown in batch experiments of Section 5.3. This shows that our biological model can solve souring problems if enough experimental data are available to find the microbial reactions parameters. The simulation input data can be used for the field-scale modeling of reservoir souring. However, transport of chemical and biological species in the field-scale is more complex than at the laboratory-scale. Adsorption, partitioning, and dispersion affect the transport of chemical components in the reservoir. Attachment and free-floating movement of microorganisms are also important factors in field-scale simulations. It is necessary to use an accurate reservoir simulator to solve the transport equations in porous media along with biological reaction equations. The effect of biomass growth on porosity and permeability and the maximum volume occupied by bacteria in the pore space are other parameters that vary from laboratory to field applications. In the following chapters, we investigate the effect of dispersion on reservoir souring and discuss the development of the dispersion model in GPAS. Chapter 8 demonstrates the application of the GPAS biological model in the field-scale simulation of reservoir souring.

Chapter 6: Effect of Dispersion on Reservoir Souring

Microbial reservoir souring is the result of sulfate reduction by microorganisms that use organic compounds as sources of carbon and energy. Hence, sulfate-reducing bacteria are active where sulfate and all the required nutrients are available for their activity and growth. Formation water is usually rich with organic acids and other types of substrates. Sulfate, on the other hand, is introduced into the reservoir by water injection. In the case of produced water re-injection, injection water also contains organic acids. Nonetheless, the presence of all the chemical compounds in part of a reservoir establishes the reaction zone. Mixing due to physical dispersion is an important mechanism in the transport of aqueous phase components. The degree of mixing determines the area at which microbial reactions occur. Therefore, understanding the dispersion effect and considering it in fluid flow calculations is necessary in reservoir souring simulation. In the first section, we review mixing and physical dispersion in the transport of aqueous phase components. Then we study the effect of physical and numerical dispersion on reservoir souring predictions in Section 6.2. In addition, we investigate the formation of reaction zone with different water injection compositions.

6.1 Dispersion in Porous Media

Dispersion and convection are the main transport mechanisms in porous media. Physical dispersion in porous media originates from the interaction of molecular diffusion and mechanical dispersion.

6.1.1 Molecular Diffusion and Mechanical Dispersion

Molecular Diffusion refers to the spread of particles through random motions from regions of high concentration to regions of low concentration. Diffusion can occur when there is no concentration gradient; however, there will be no net flux. The diffusive flux is described by Fick's law (Bear, 1988):

$$J = -D_0 \frac{dC}{dx}, \tag{6.1}$$

where D_0 is diffusion coefficient and C is concentration. From mass conservation for the instantaneous diffusive flux we get

$$\frac{\partial C}{\partial t} = -\frac{\partial J}{\partial x}. \tag{6.2}$$

Plugging Equation (6.1) into Equation (6.2) gives Fick's second law as

$$\frac{\partial C}{\partial t} = D_0 \frac{\partial^2 C}{\partial x^2}. \tag{6.3}$$

Equation (6.3) describes how the component concentration varies with time and space because of diffusion. The Solution of Equation (6.3) gives a normal distribution of concentration across the contact area of two miscible fluids. In a porous medium, the tortuous path through the medium increases the path length for diffusion. Therefore, the diffusion coefficient in porous media is related to the tortuosity of the medium (τ) as

$$D = \frac{D_0}{\tau} = \frac{D_0}{F\phi}\ , \tag{6.4}$$

where F is formation resistivity factor and ϕ is porosity. The relation between the tortuosity and resistivity factor derives from electrical conductivity in porous media.

Mechanical dispersion is the additional mixing because of convection. Variations in magnitude and direction of local velocity along the tortuous flow paths cause solute particles to spread. Two solute particles starting close to each other become widely separated by mechanical dispersion. This mechanism is governed by the pore structure. α_L and α_T represent the longitudinal and transversal dispersivities, respectively. Longitudinal dispersivity is the coefficient of dispersion parallel to the convective flow and transversal dispersivity is the coefficient of dispersion perpendicular to the flow. Mechanical dispersion is treated in the same manner as diffusion with the conventional Fickian representation of Equation (6.1). The term "dispersion coefficient" (D_L) expresses the combined effects of molecular diffusion and mechanical dispersion.

6.1.2 Convection Diffusion Equation (CDE)

The convection-diffusion equation (CDE) describes the overall transport and mixing of fluids in porous media (Lake, 1989). For one-dimensional solute transport in porous media, CDE is in the form:

$$\phi\frac{\partial C}{\partial t} + u\frac{\partial C}{\partial x} = \phi D_L \frac{\partial^2 C}{\partial x^2}, \tag{6.5}$$

where u is the bulk fluid velocity and the diffusion coefficient in Equation (6.3) is replaced by the dispersion coefficient that includes mechanical dispersion as well as molecular diffusion. CDE assumes incompressible fluid, meaning no volume change upon mixing and spatially constant porosity.

Rewriting CDE in the dimensionless form gives

$$\frac{\partial C_D}{\partial t_D} + \frac{\partial C_D}{\partial x_D} = \frac{1}{N_{Pe}} \frac{\partial^2 C_D}{\partial x_D^2}, \tag{6.6}$$

where dimensionless parameters are defined as

$$C_D = \frac{C - C_I}{C_J - C_I}, \tag{6.7}$$

$$t_D = \frac{ut}{\phi L}, \tag{6.8}$$

$$x_D = \frac{x}{L}, \tag{6.9}$$

and

$$N_{Pe} = \frac{uL}{\phi D_L}, \tag{6.10}$$

where C_D is the dimensionless concentration normalized to the injection concentration (C_J) and the initial concentration (C_I). t_D is the dimensionless time (pore volume injected), x_D is the dimensionless distance, and N_{Pe} is the Peclet number. The Peclet number is the ratio of the characteristic time from the dispersive transport to the convective transport of a particle. Hence, a large Peclet number (low dispersion coefficient or high velocity) means that the convective transport dominates dispersive

mixing, and a small Peclet number (high dispersion coefficient or low velocity) indicates the domination of dispersive mixing over convection.

Depending on the initial and boundary conditions, analytical solutions can be offered for one-dimensional CDE. The most common solution is for the semi-infinite boundary condition as follows:

$$\begin{aligned} &C_D(x_D,0)=0 \qquad \text{for} \quad x_D \geq 0 \\ &C_D(\infty,t_D)=0 \qquad \text{for} \quad t_D \geq 0 \\ &C_D(0,t_D)=1 \qquad \text{for} \quad t_D \geq 0 \ . \end{aligned}$$

The analytical solution of Equation (6.6) with the above boundary condition (Lake, 1989) is

$$C_D(x_D,t_D)=\frac{1}{2}erfc\left(\frac{x_D-t_D}{2\sqrt{\frac{t_D}{N_{Pe}}}}\right)+\frac{e^{x_D N_{Pe}}}{2}erfc\left(\frac{x_D+t_D}{2\sqrt{\frac{t_D}{N_{Pe}}}}\right), \tag{6.11}$$

where error function (erf) and complementary error function ($erfc$) are defined as

$$\begin{aligned} &erf\left(x\right)=\frac{2}{\sqrt{\pi}}\int_0^x e^{-x^2}dx \\ &erfc(x)=1-erf\left(x\right) \ . \end{aligned} \tag{6.12}$$

For large t_D or x_D, the second term in Equation (6.11) becomes negligible and the solution to the CDE reduces to

$$C_D(x_D,t_D)=\frac{1}{2}erfc\left(\frac{x_D-t_D}{2\sqrt{\frac{t_D}{N_{Pe}}}}\right) \tag{6.13}$$

or Equation (6.14) in the dimensional form

$$C(x,t)=C_I+\frac{C_J-C_I}{2}erfc\left(\frac{x-ut}{2\sqrt{D_L t}}\right). \tag{6.14}$$

Applying the above solution to a simplified one-dimensional souring problem gives an understanding of the mixing zone formation. If we assume that formation water contains only one substrate and injection water contains only sulfate, the concentration distribution of substrate and sulfate are given as

$$C_{sulfate}(x,t)=\frac{C_{inj}}{2}\left(1-erf\left(\frac{x-ut}{2\sqrt{D_L t}}\right)\right) \tag{6.15}$$

$$C_{substrate}(x,t)=\frac{C_{init}}{2}\left(1+erf\left(\frac{x-ut}{2\sqrt{D_L t}}\right)\right), \tag{6.16}$$

where C_{inj} is the injection sulfate concentration and C_{init} is the initial substrate concentration. Figure 6.1 shows a schematic of the profiles of sulfate and substrate at half pore volume injected for different values of the Peclet number. In this illustration, we assume no reaction between components. The highlighted area in each image shows the region where both sulfate and substrate are available. With more physical

dispersion (a low Peclet number), more mixing occurs; therefore, we expect a wider reaction zone, and thus, higher H_2S production.

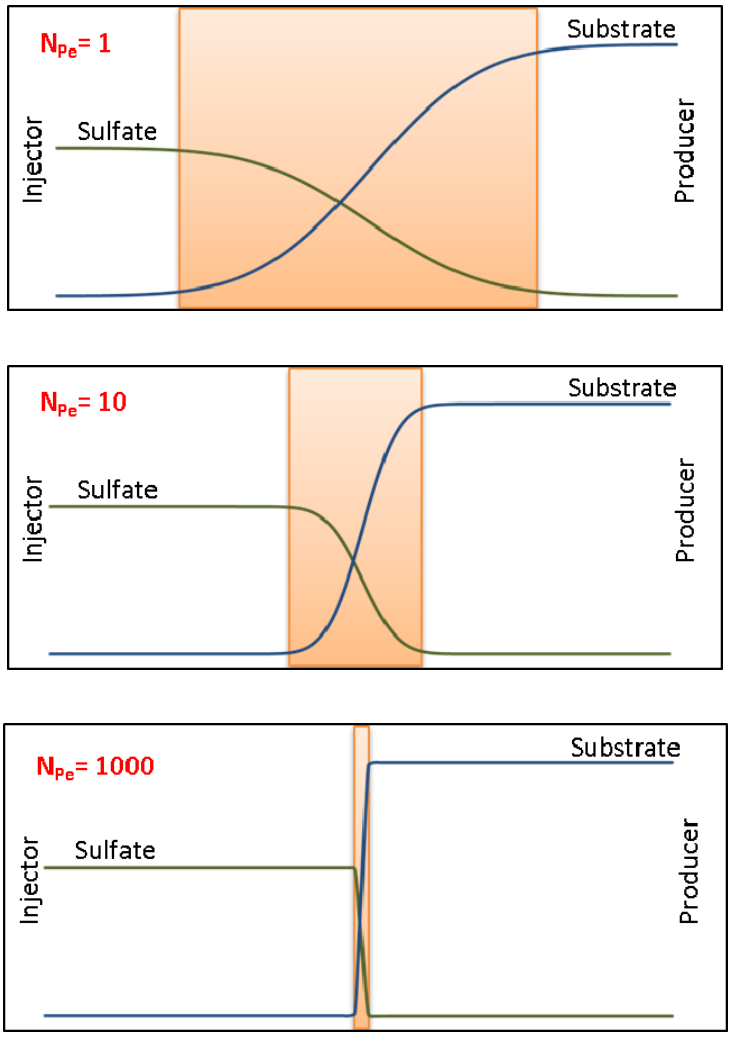

Figure 6.1: Schematic of sulfate and substrate concentration profiles along a one-dimensional model at half pore volume injected obtained from the analytical solution of CDE.

6.2 Investigation of Dispersion Effects by UTCHEM

The area of the reservoir in which microbial reactions occur depends on the availability of reaction components. If the injection water contains organic compounds (as in produced water re-injection), then all the components of reservoir souring reactions will be available in the injection water. Therefore, souring takes place around the injector and the reaction zone develops in the wellbore vicinity. As the bacteria grow, they consume more substrates and nutrients. Hence, the injection water leaves behind the substrates and carries only the H_2S and other products into the reservoir. In this situation, the amount of dispersion does not have a significant effect on reaction zone formation. This is the basic theory of the biofilm model explained in Section 2.3.2 which assumes that bacteria are attached to the rock surface and grow in the reaction zone around the injector. On the other hand, If injection water does not comprise considerable organic acids (as in seawater injection), the reactions will happen in the mixing zone between injection water and formation water. This is the basic concept of the mixing model discussed in Section 2.3.1. The mixing zone moves along the reservoir as the water front advances. The extent of the mixing zone depends on the dispersion properties of porous media.

To quantify the effect of dispersion on reservoir souring we set up several simulation cases with different injection water compositions and dispersion properties. We chose UTCHEM for dispersion investigations because it has a high-order finite difference approximation and a flux-limiting total variation diminishing (TVD) scheme to minimize numerical dispersion. This differencing scheme is third-order in space to minimize numerical dispersion and grid-orientation effects. Harten (1983) developed the TVD scheme that includes a limiting procedure to obtain oscillation-free, high-

resolution, high-order results. Liu et al. (1994) developed a limiter which constraints the gradient of the flux function and varies as a function of time step and gridblock size. By using this feature in UTCHEM, the dispersion effects in simulation are mostly limited to physical dispersion which is controlled via input data.

We examined the effect of dispersion in two reservoir models. A one-dimensional homogeneous reservoir model and a three-dimensional, more complex reservoir are studied with different dispersion coefficients. We present the details of the models and simulation results in the following sections.

6.2.1 One-Dimensional Homogeneous Reservoir

This model represents a one-dimensional reservoir with one injector and one producer. We used a 200×1×1 grid with constant porosity and permeability. Table 6.1 shows the reservoir properties. We run the model with three values of longitudinal dispersivity (α_L=0.1, 1, and 5 ft). Other properties are the same for all the cases. To minimize the numerical dispersion, we used the higher order TVD scheme in UTCHEM and small gridblock size in the direction of flow. Because we are eliminating the numerical dispersion, permeability is homogeneous, and reservoir model is one-dimensional, all of the mixing is associated with physical dispersion which is controlled by dispersivity coefficient (α_L).

Figure 6.2 shows the profiles of H_2S concentration at different times for α_L=1. This figure illustrates the development of the reaction zone and its advancement toward the producer. As the injection front proceeds, the mixing zone grows and more H_2S is generated. The generated H_2S moves toward the producer with convection and dispersion transport mechanisms. We can also observe the development of the reaction

zone by studying the bacteria population at different times as the injection front moves in the reservoir. Figure 6.3 shows the biofilm bacteria growth with time after 150, 175, and 200 days.

Table 6.1: Properties of the one-dimensional homogeneous model.

Grid	200×1×1
Grid Size	5×100×100 (ft)
Porosity	0.3
Permeability	100 md
Initial S_w	0.3
Initial substrate concentration	1000 mg/L
Injected sulfate concentration	1400 mg/L
Wells	one injector at grid 1 Q1 = 2672 BPD
	one producer at grid 200 Pwf = 1500 psi
Longitudinal Dispersivity	Case1: 0.1 ft
	Case2: 1 ft
	Case3: 5 ft
Simulation time	500 days (≈1.5 PV)

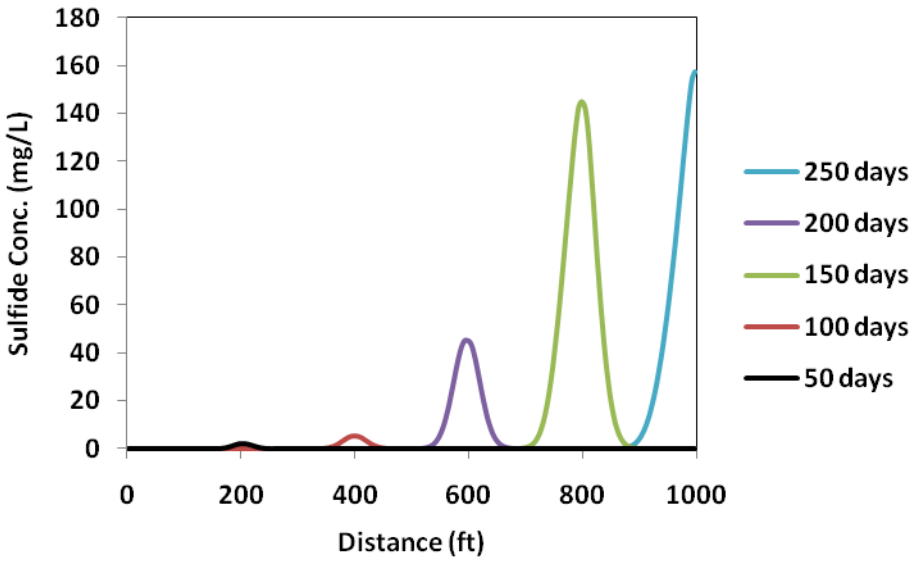

Figure 6.2: Concentration profiles of H_2S along the reservoir after 50, 100, 150, 200, and 250 days for the one-dimensional reservoir model with longitudinal dispersivity of 1 ft.

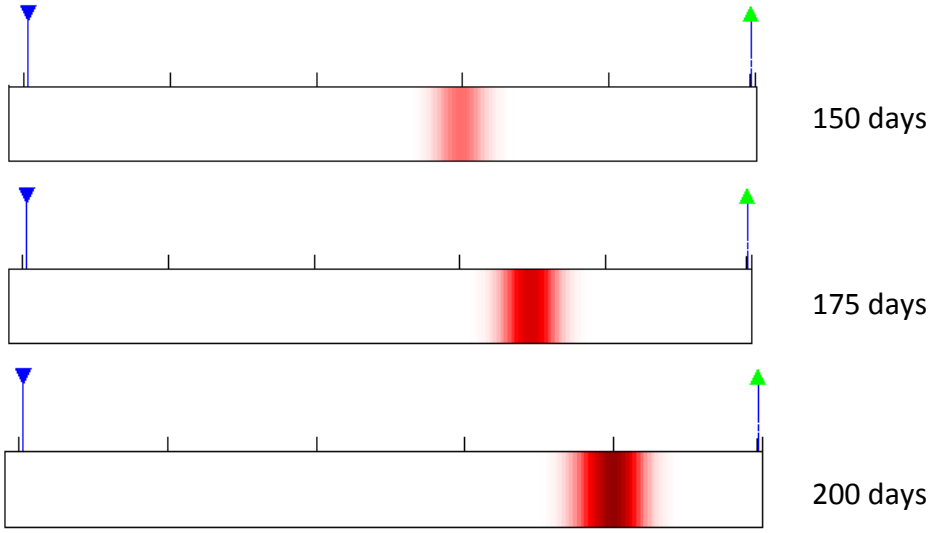

Figure 6.3: Sulfate-reducing bacteria population at 150, 175, and 200 days along the reservoir.

Figure 6.4 shows the concentration profiles of substrate, sulfate, and produced sulfide along the reservoir after 140 days. Longitudinal dispersivity is the variable parameter that changes the amount of dispersion in the simulation cases of Figure 6.4. With a higher dispersivity coefficient, we have a larger mixing zone, thus more H_2S production. The maximum amount of sulfide concentration in the last two cases is approximately the same. However, the wider distribution of sulfide indicates more H_2S production in the case with α_L=5 than in the case with α_L=1. As expected, dispersion has a significant effect on reservoir souring when mixing is the governing mechanism.

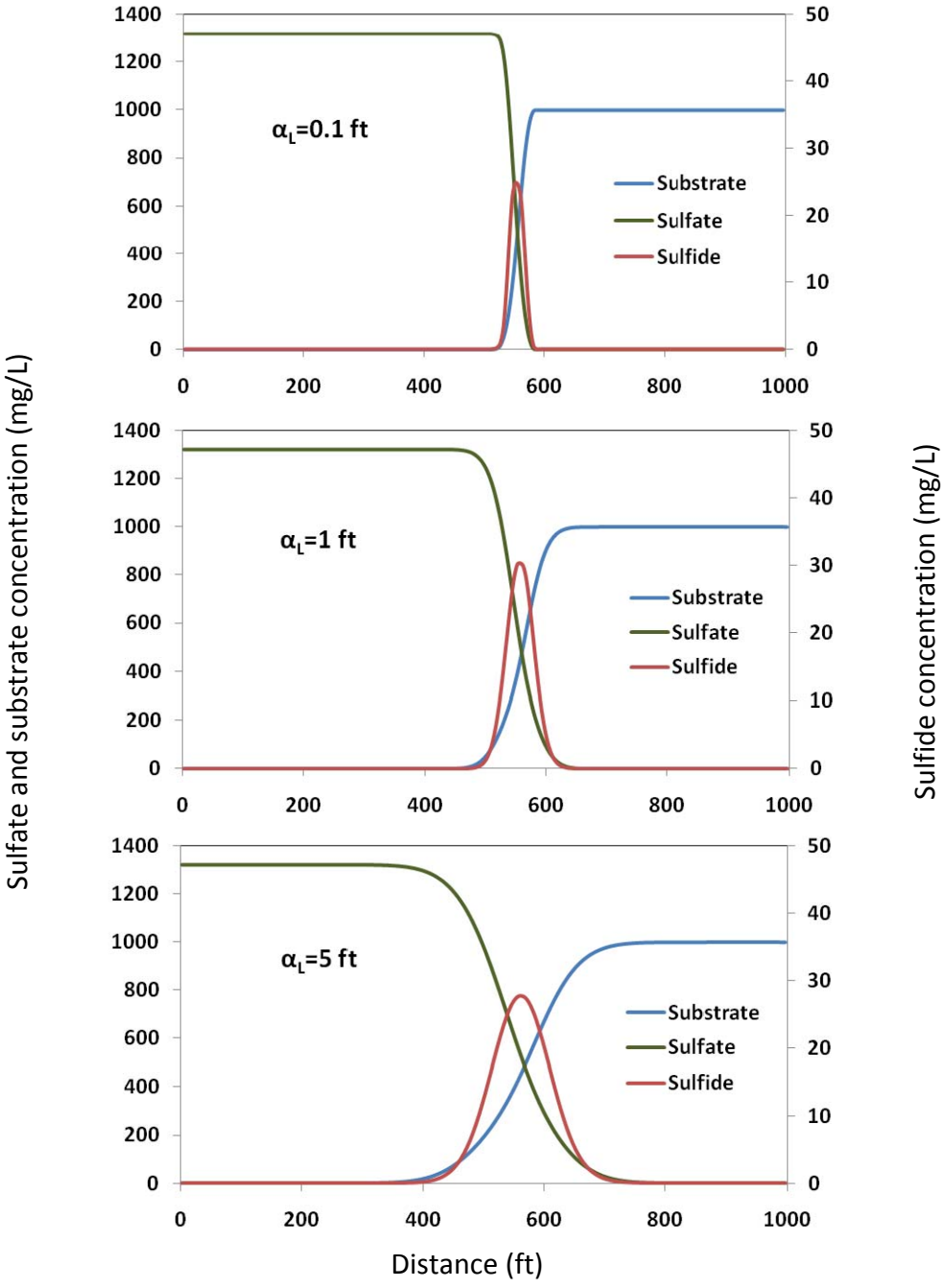

Figure 6.4: Concentration profiles of substrate, sulfate, and sulfide along the reservoir after 140 days (0.42 pore volume injected) for the one-dimensional reservoir model with longitudinal dispersivities of 0.1, 1, and 5 ft.

Dispersion affects the onset souring; as high dispersion expedites the production of H_2S. Figure 6.5 shows H_2S production versus pore volume of injected water. For the high dispersivity case (α_L=5), sulfide production starts at about 0.6 pore volume injected. With lower dispersivities, the onset of reservoir souring happens at a later time. This secondary effect of dispersion can also be observed in the biofilm model. In the case of produced water re-injection, mixing between formation water and injection water is not important, but the effect of dispersion on H_2S transport is considerable. Dispersion smears the front of H_2S and causes faster breakthrough compared to the non-dispersed sharp front.

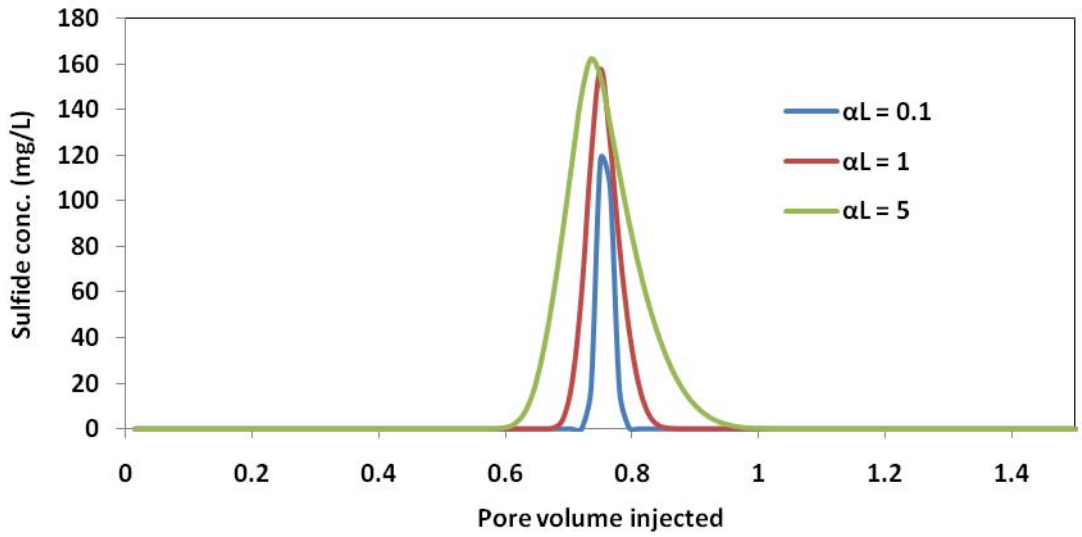

Figure 6.5: H_2S production for the one-dimensional reservoir model with longitudinal dispersivities of 0.1, 1, and 5 ft.

6.2.2 Three-Dimensional Heterogeneous Reservoir Model

To study the effect of dispersion on reservoir souring in a field case, we built a three-dimensional reservoir model with three injectors and five producers. Figure 6.6 illustrates the permeability distribution and well locations. The irregular shaped reservoir is composed of 1237 active cells of 40′×40′×20′. A Cartesian 25×25×3 mesh is used for simulation. This model presents waterflooding in a two-phase (water-oil) reservoir. Water is injected at 356 bbl/day (2000 ft^3/day) from each injector and injection starts from the first day and continues for 3960 days (two pore volumes injected). Producers operate at a constant bottom-hole pressure of 1500 psi. The reservoir has a constant porosity of 0.3 and a heterogeneous permeability distribution. The average permeability is 75 md and the Dykstra-Parson coefficient is 0.7, indicating high heterogeneity. Table 6.2 shows the reservoir properties and well constraints.

It is assumed that all the biomass is attached to the rock surface and that free-floating biomass is negligible. The biological model parameters and concentrations of aqueous components are similar to the laboratory experiment simulation detailed in Section 5.1. We run the simulation for two cases; the first case is a seawater injection where injection water does not contain any substrates. The second case is produced water re-injection. In this case, injection water has substrates but in smaller amounts than the formation water. The assumption that injection water contains organic acids is appropriate when produced water is mixed with the seawater and injected back into the reservoir. Recycling the produced water is very common, especially in offshore reservoirs. The concentrations of sulfate and substrates in the formation water and injection water for both cases are presented in Table 6.3. We discuss the effect of

dispersion on H_2S production for seawater injection (SWI) and produced water re-injection (PWRI) in the following sections.

Table 6.2: Properties of the three-dimensional reservoir model.

Grid	25×25×3
Active cells	1237
Grid size	40×40×20 (ft)
Porosity	0.3
Permeability	Mean = 75 md Dykstra-Parson coef. = 0.7
Initial S_w	0.3
Wells	3 injectors Q1 = 623 BPD Q2 = 712 BPD Q3 = 623 BPD
	5 producers Pwf = 1500 psi

Table 6.3: Injection and formation water compositions for SWI and PWRI cases in the three-dimensional reservoir model.

	Component	Injection water concentration (mg/L)		Formation water concentration (mg/L)
		Seawater Injection	Produced Water Re-Injection	
Electron acceptor	Sulfate	300	300	0
Substrates	n-Butyrate	0	100	200
	Isobutyrate	0	125	250
	Formate	0	100	200
	Propionate	0	100	200

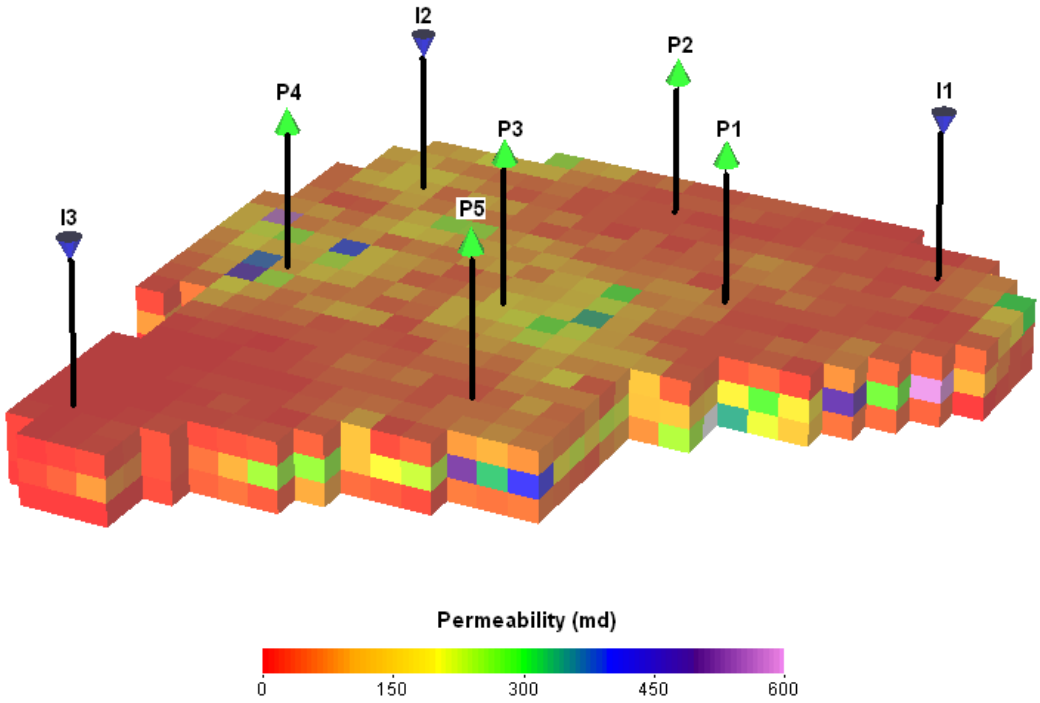

Figure 6.6: Permeability distribution of the three-dimensional reservoir model with 3 injectors and 5 producers.

6.2.2.1 Seawater Injection (SWI)

Seawater introduces sulfate into the reservoir but normally does not have an adequate amount of organic acids for SRB activity. On the other hand, these organic compounds are abundant in the formation water. The mixing zone that forms between formation water and injection water provides the environment for bacterial activity. The effect of dispersion on mixing zone size and H_2S production is investigated by setting up two different cases. In the first case, the diffusion and dispersion coefficients are set to zero. However, the heterogeneity and three-dimensional flow forms mixing in the

reservoir. Clearly, some mixing is generated by numerical dispersion, although we are using the higher order differencing option in UTCHEM. We refer to this case as the base case. For the second case, longitudinal dispersivity and transversal dispersivity are set to 20 ft and 0.5 ft, respectively.

Formation of mixing zone provides sulfate and carbon sources for SRB activity. This results in the growth of biomass and the reduction of sulfate to sulfide. Figure 6.7 shows the biomass amounts at different times in the reservoir. The reaction zone develops and progresses toward the producers as water injection continues. Figure 6.8 shows the H_2S concentrations at 0.5, 1, and 2 pore volume injected. The produced H_2S moves along the water front and reaches the producers. In this realistic reservoir model, we can observe the formation of reaction zones at different regions of reservoir and merging of these areas as they develop and move. The production histories of H_2S for all the producers are plotted in Figure 6.9. The distance from injectors, reservoir heterogeneity, and various flow paths result in different times for H_2S breakthrough.

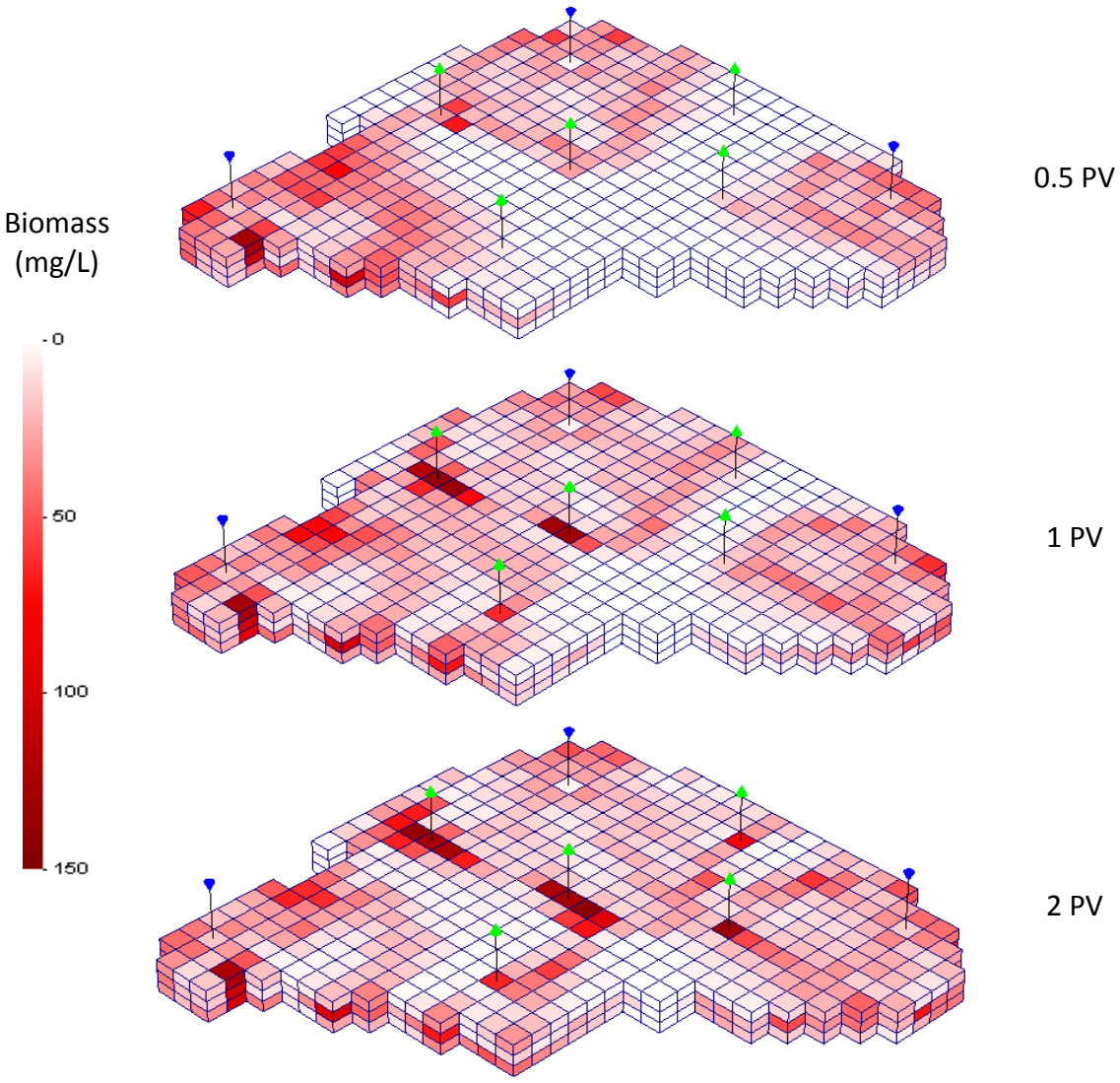

Figure 6.7: SRB concentration at 0.5, 1, and 2 pore volume injected in the three-dimensional reservoir model for the base case of SWI.

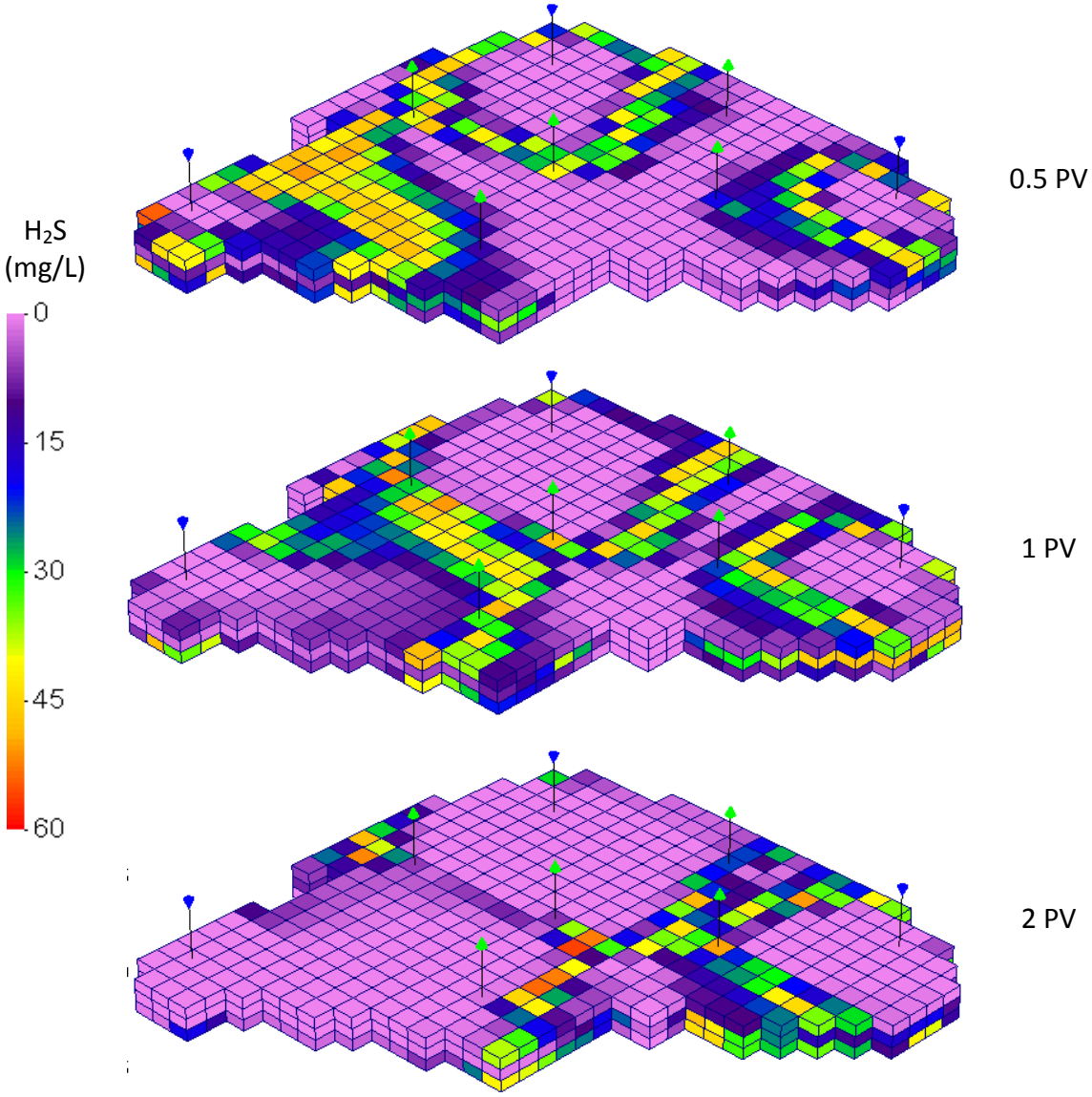

Figure 6.8: H_2S concentration at 0.5, 1, and 2 pore volume injected in the three-dimensional reservoir model for the base case of SWI.

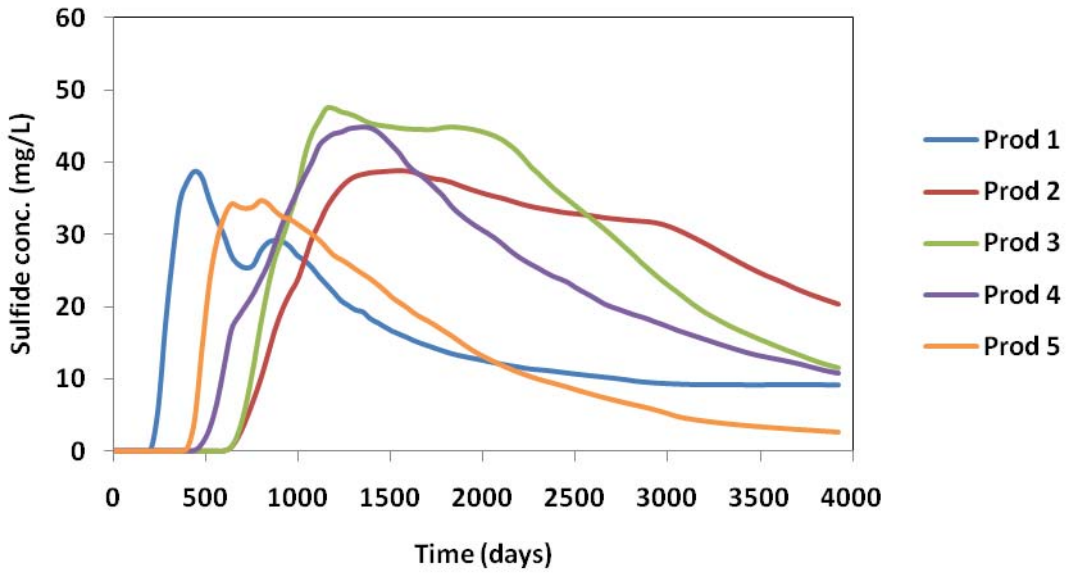

Figure 6.9: H_2S production concentration for producers in the three-dimensional reservoir model for the base case of SWI.

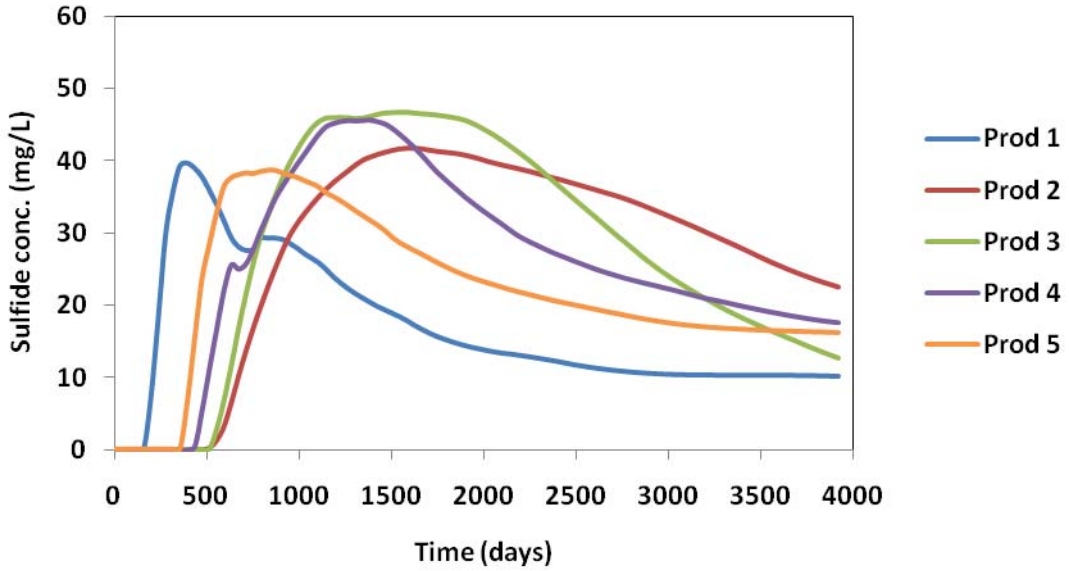

Figure 6.10: H_2S production concentration for producers in the three-dimensional reservoir model for the high dispersivity case (α_L = 20 ft) of SWI.

The second case has a relatively high dispersivity compared to the base case. We chose longitudinal dispersivity of 20 ft and transverse dispersivity of 0.5 ft to examine the effect of dispersion on sulfide generation. Figure 6.10 shows the H_2S production from all the producers for the high dispersivity case. Comparing the plots of Figure 6.9 and Figure 6.10 indicates higher levels of hydrogen sulfide in the high dispersivity case than the base case. To better see the effect of dispersion, the H_2S production from producers 2 and 5 in both cases are plotted on the same graph (Figure 6.11). With high dispersion, H_2S production in producer 2 started after 500 days which is earlier than the base case where souring started after 590 days. The maximum H_2S concentration increased with dispersion. In producer 2, the maximum H_2S concentration increased from 38.8 mg/L with no dispersion to 41.7 mg/L with α_L=20. After 4000 days (2 PV) of water injection, the H_2S level at producer 5 is around 16 mg/L in the high dispersivity case. This is drastically higher than the final H_2S levels for the same well in the base case (2.5 mg/L). Considering the continuous H_2S production at high levels and high water production rates, the extra amount of H_2S is substantial. Hence, dispersion significantly increases reservoir souring when mixing is the dominant mechanism.

Figure 6.12 and Figure 6.13 compare the SRB and H_2S distribution in two cases. As shown in Figure 6.12, the reaction zone in the high dispersivity case is wider than the base case. Figure 6.13a is the concentration map of H_2S for the base case. Figure 6.13b is the H_2S concentration at the same time for the high dispersivity case. As can be seen, the H_2S front is smeared because of dispersion and the total H_2S amount is higher than the base case as discussed above.

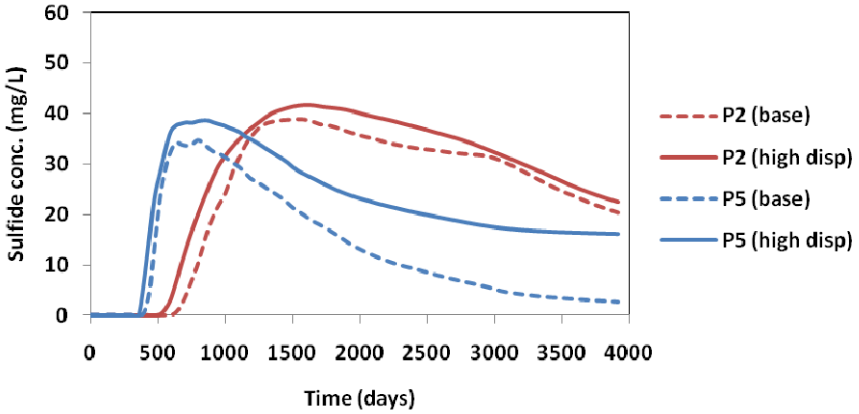

Figure 6.11: H_2S production concentration for producers 2 and 5 for the base case and the high dispersivity case (α_L = 20 ft) in the three-dimensional reservoir model with SWI.

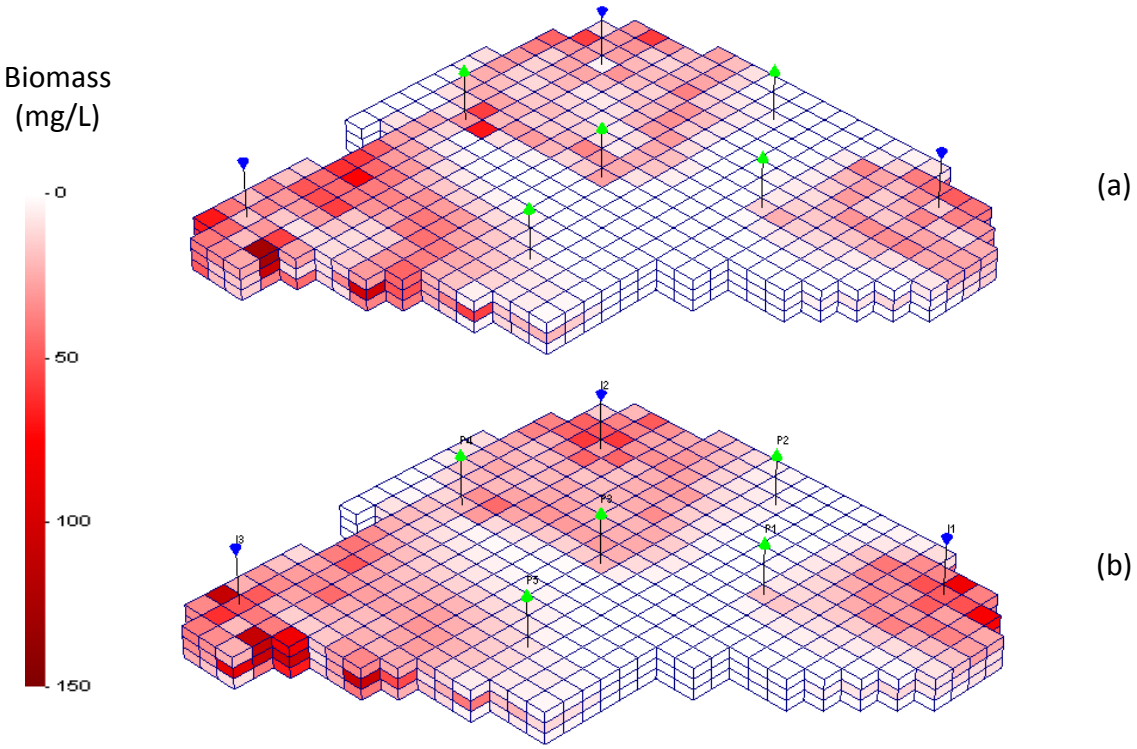

Figure 6.12: SRB concentration at 0.5 pore volume injected in the three-dimensional reservoir model for (a) the base case and (b) the high dispersivity case of SWI.

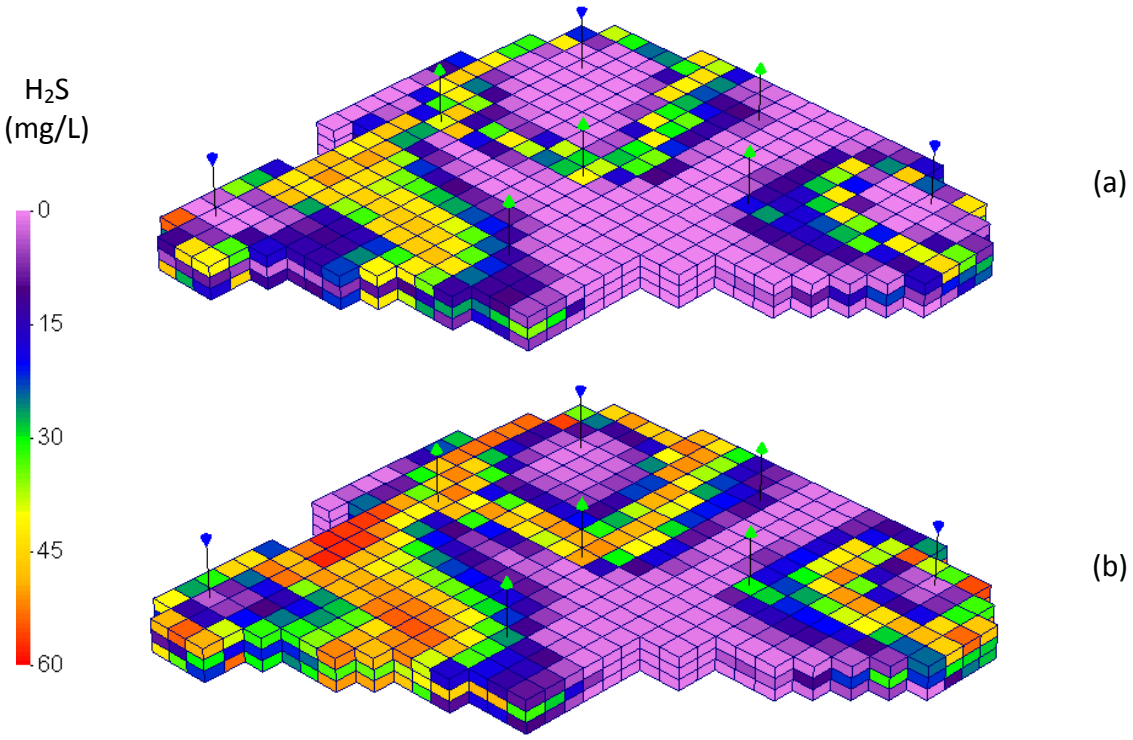

Figure 6.13: H_2S concentration at 0.5 pore volume injected in the three-dimensional reservoir model for (a) the base case and (b) the high dispersivity case of SWI.

6.2.2.2 Produced Water Re-Injection (PWRI)

When produced water is recycled, the injection water includes organic components from the formation water or partitioned from oleic phase. The composition of injection water in our model is presented in Table 6.3. In this situation, most of the microbial activities are in the vicinity of the wellbore where all of the chemicals are available for the bacteria. This results in biomass growth around the injection wells (Figure 6.14) as explained in the biofilm model by Sunde et al. (1993). The biofilm forms

at the early stages of water injection and does not change considerably throughout the process. In the produced water re-injection, souring continues as long as water is injected, because sulfate and substrates are continuously being provided by the injection water. Therefore, higher levels of hydrogen sulfide are observed in the producers (Figure 6.16) than the seawater injection case (Figure 6.9). The distribution of H_2S shown in Figure 6.15 indicates the nonstop H_2S generation as well.

All the components of bacterial reaction exist at a fairly small area around the injectors. Hence, mixing of injection water and formation water is not vital for souring. Therefore, we did not expect to have many different results when applying higher dispersion coefficients. Figure 6.17 shows the H_2S production from producers in the PWRI case with high dispersivity (α_L=20). Except for minor changes, the plots are very similar to the base case with no dispersion. The comparison of H_2S production from wells 2 and 5 is illustrated in Figure 6.18. The maximum concentration and the general trend are quite similar. However, souring starts earlier in the high dispersivity situation than in the base case. The expedited souring is associated with the smeared front of H_2S because of high dispersion. The effect of dispersion on reservoir souring is considerable when mixing is playing a significant role in providing the components for bacterial activity. This happens when injection water is not rich with organic acids. Otherwise, the effect of dispersion is mostly limited to the onset of souring.

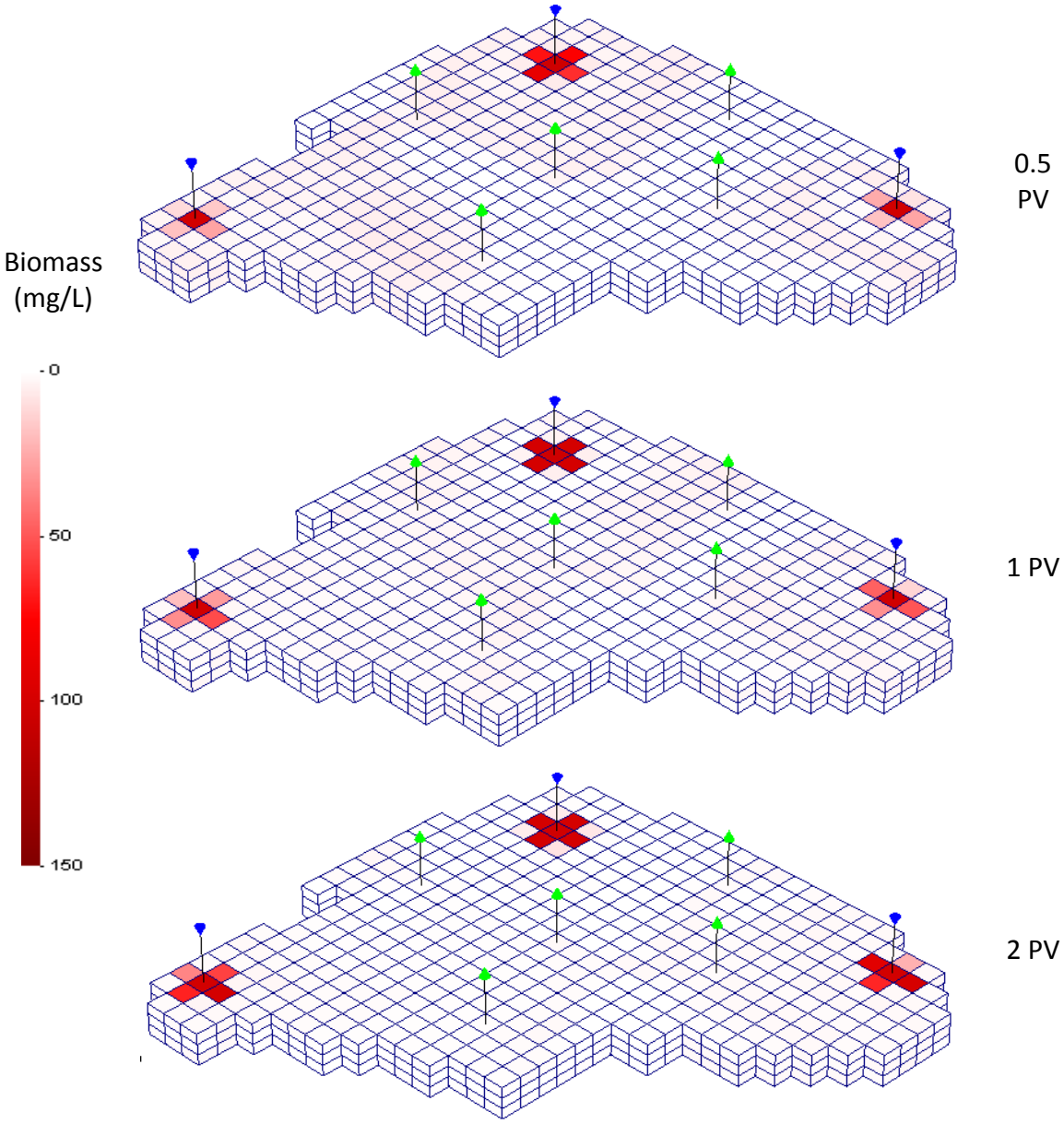

Figure 6.14: SRB concentration at 0.5, 1, and 2 pore volume injected in the three-dimensional reservoir model for the base case of PWRI.

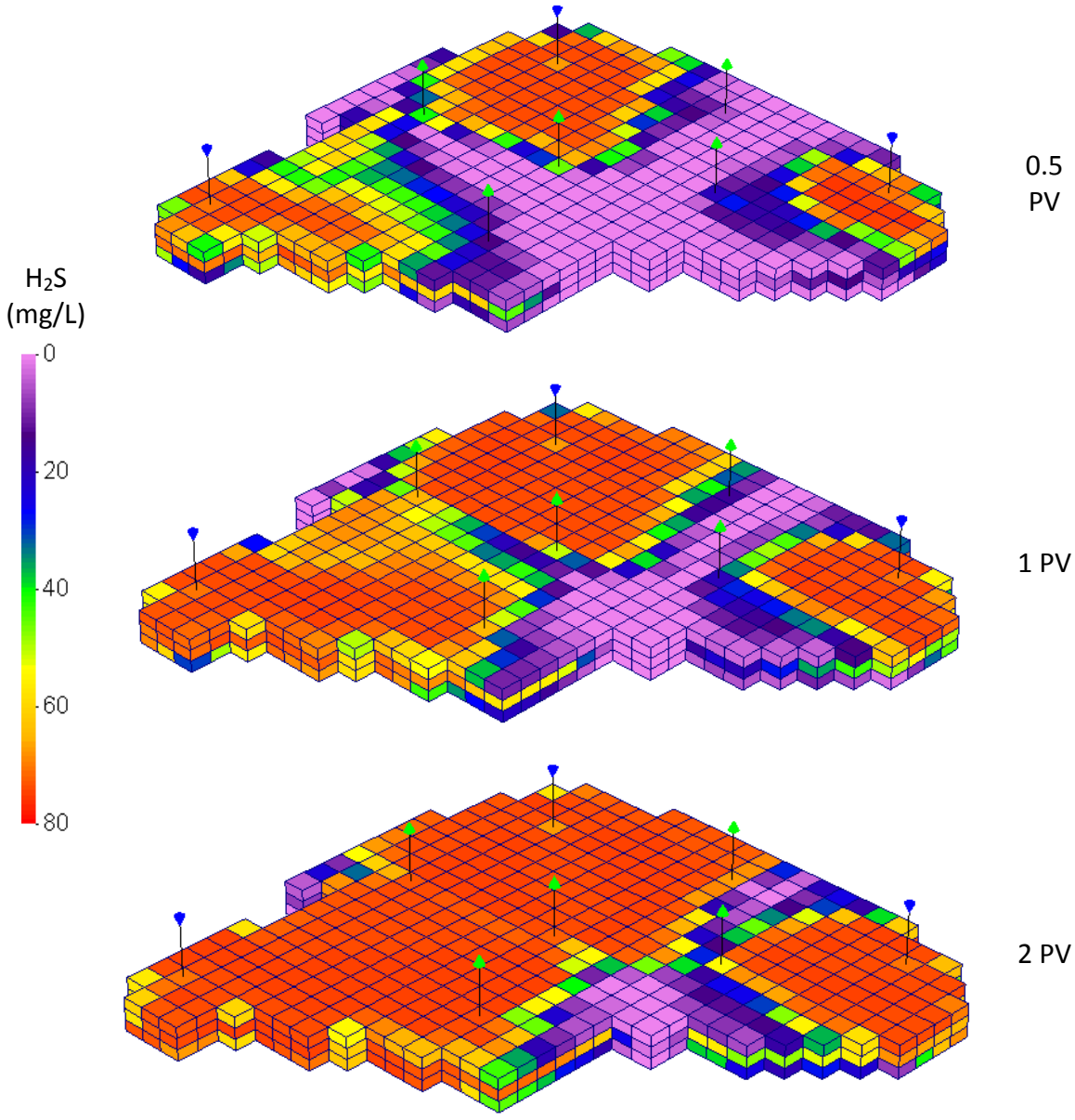

Figure 6.15: H_2S concentration at 0.5, 1, and 2 pore volume injected in the three-dimensional reservoir model for the base case of PWRI.

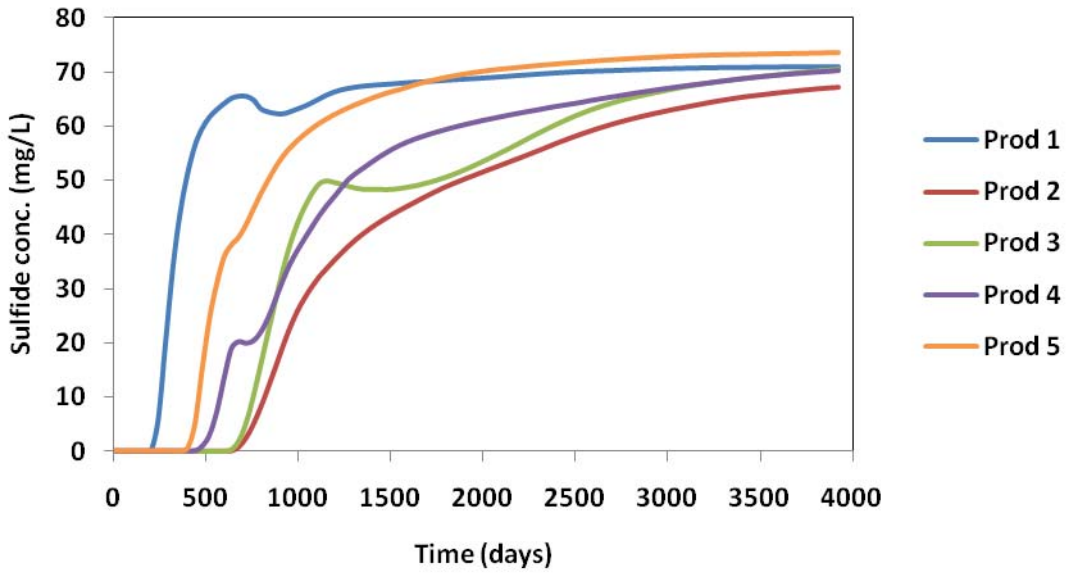

Figure 6.16: H_2S production concentration for producers in the three-dimensional reservoir model for the base case of PWRI.

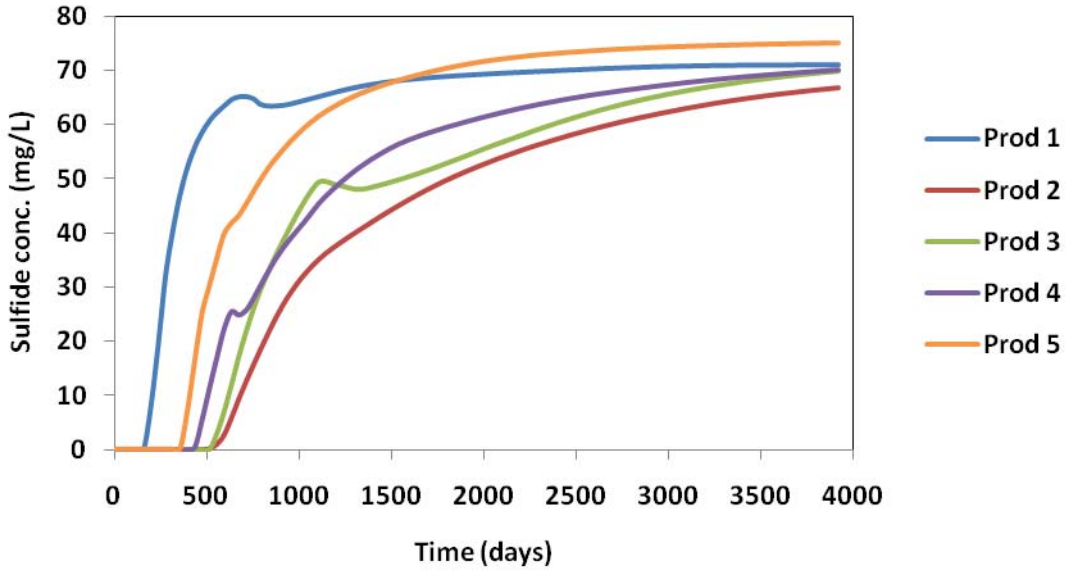

Figure 6.17: H_2S production concentration for producers in the three-dimensional reservoir model for the high dispersivity case (α_L = 20 ft) of PWRI.

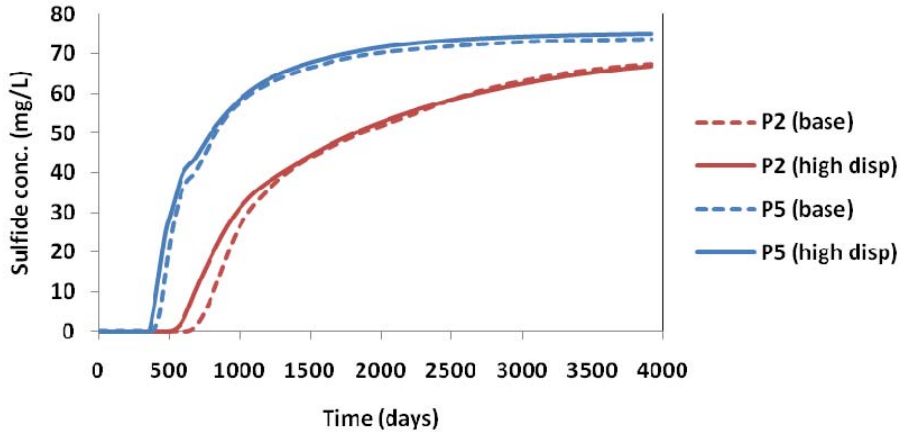

Figure 6.18: H_2S production concentration for producers 2 and 5 for the base case and the high dispersivity case (α_L = 20 ft) in the three-dimensional reservoir model with PWRI.

6.2.2.3 Effect of Heterogeneity

To evaluate the effect of heterogeneity on reservoir souring, we set up the same reservoir model as Section 6.2.2.1 with a homogeneous permeability distribution. The constant permeability in the homogeneous model is equal to the average permeability of the heterogeneous model (75 md). We ran the simulation with the conditions of seawater injection described in Section 6.2.2.1 and compared the H_2S production results for the homogeneous case to the heterogeneous case with high and low dispersivities. Figure 6.19 shows the produced H_2S concentration from producer number 5 for the homogeneous reservoir, the low dispersivity heterogeneous reservoir, and the high dispersivity heterogeneous reservoir. Changing permeability distribution affects waterflooding progress as well as mixing zone formation. Therefore, the differences we observe in H_2S production in homogeneous and heterogeneous cases are a result of changes in both the water saturation distribution and the mixing zone formation. However, the effect of heterogeneity on H_2S breakthrough is significant. In the

homogeneous case souring occurs later. But, the amount of produced H_2S (area under the curve) in the homogeneous case and the low dispersion heterogeneous case are analogous. The high dispersion case shows more total H_2S production compared to the other two cases. In conclusion, heterogeneity expedites reservoir souring but does not change the total amount of produced H_2S considerably, in the seawater injection conditions. On the other hand, physical dispersion increases the extent of H_2S production significantly as discussed in Section 6.2.2.1.

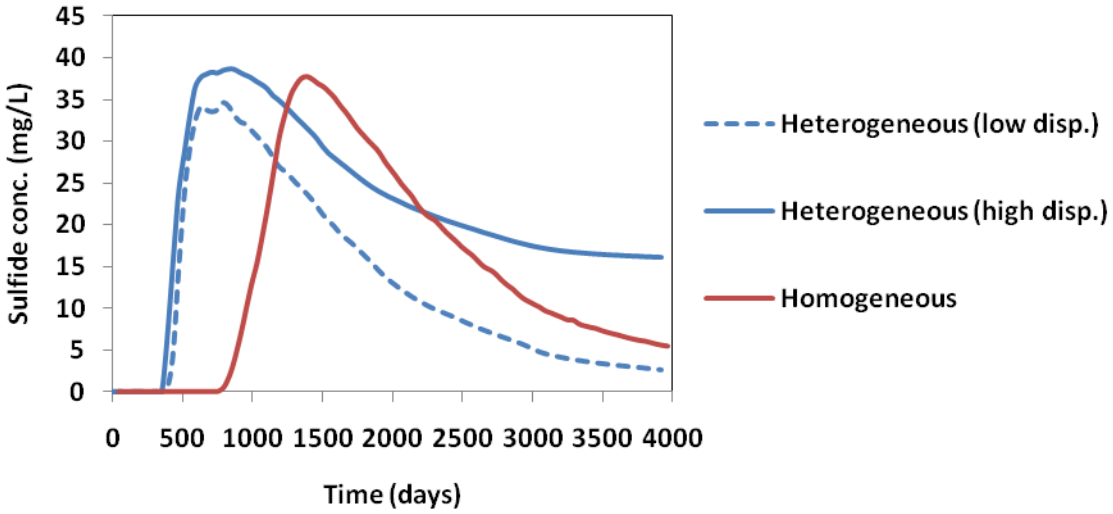

Figure 6.19: H_2S production concentration for producer 5 for the homogeneous case (red line) and the heterogeneous case with high dispersivity (solid blue line) and low dispersivity (dashed blue line) in the three-dimensional reservoir model with SWI.

Chapter 7: Physical Dispersion Model in GPAS

The implementation of physical dispersion is mainly considered for miscible gas flooding simulators, as mixing is the main mechanism in a miscible displacement. Many compositional simulators include a physical dispersion model for miscible gas flooding (Shrivastava et al., 2005a, b). However, dispersion in the aqueous phase becomes important when we have mixing of components during waterflooding. Water injection into reservoirs results in the mixing of chemical components in injection water and formation water, and chemical reactions take place in the mixing area. Reservoir souring is an example of an aqueous phase reaction in waterflooding. In Chapter 6, we described the components of physical dispersion and their effect on mixing zone development. We also discussed the effect of dispersion on reservoir souring. Another example of chemical interaction between injection water and formation water is the precipitation of chemicals because of ion exchange. Dispersion effects are also important in chemical flooding for enhanced oil recovery. In all the cases, the size of the mixing zone determines the area at which reactions occur. Hence, considering dispersion effects is essential in the simulation of aqueous phase processes. Therefore, we implemented a physical dispersion term in GPAS to accurately model the transport of aqueous phase components.

UTCHEM incorporates physical dispersion in the transport of aqueous phase components. The material balance equations in UTCHEM are solved explicitly. However, fully-implicit implementation of dispersion in GPAS adds a great deal of complexity, because dispersion is represented as full-tensor. This is similar to full-tensor

permeability formulation. Therefore, we used hexahedron corner point grids that handle the flows, which are not necessarily parallel to the principal axes. The mass balance equation is transformed into a computational space with non-orthogonal boundary-fitted grids. Both permeability and dispersion are expressed with symmetric full tensors. The dispersion term, comprised of molecular diffusion and mechanical dispersion, is incorporated in the mass balance equations of aqueous phase components. Then, the equations are solved in an implicit scheme. We validated the dispersion model in GPAS with the analytical solution for one-dimensional problems and with comparison to UTCHEM for multi-dimensional problems. Considering the physical dispersion and minimizing the numerical dispersion enables us to accurately model the mixing of chemical components in water flooding and chemical flooding simulations. GPAS is the first fully-implicit simulator with a physical dispersion model for reactive aqueous components. We will explain the full tensor formulation and discretization of material balance equations below.

7.1 Full Tensor Formulation in GPAS

We explained the chemical module of GPAS in Section 3.4. This model assumes that aqueous phase components do not partition in the oleic phase. The gas phase is not yet considered in the chemical module of GPAS. In this section, we detail the implementation of dispersion term in the material balance equation of aqueous components. The material balance equation for the aqueous phase component i in the chemical module of GPAS is given by

$$\frac{\partial}{\partial t}\left(\phi N_i\right) - \nabla\bullet\left(\xi_w \lambda_w x_{iw} k \bullet \nabla\Phi_w\right) + \nabla\bullet\left(\xi_w \phi S_w D_{iw} \bullet \nabla x_{iw}\right) - \frac{q_i}{V_b} = 0 \qquad i = 1, 2, ..., n_a, \qquad (7.1)$$

where n_a is the number of aqueous phase components, ϕ is the porosity, N_i is the moles of component i per unit of pore volume, S_w, ξ_w and λ_w are saturation, molar density and relative mobility of water, respectively; x_{iw} is the molar fraction of component i in water, and k is the absolute permeability tensor. Φ_w is the potential of water phase and is given by

$$\Phi_w = P_w - \gamma_w h. \tag{7.2}$$

In Equation (7.2), P_w denotes the water phase pressure and h is depth, which is positive in downward direction. The molar dispersive flux is assumed to be in the form of Fick's first law of diffusion:

$$J_{iw} = -\phi S_w D_{iw} \bullet \nabla x_{iw}. \tag{7.3}$$

The dispersion tensor D_{iw} consists of molecular diffusion and mechanical dispersion. It can be shown in the matrix form as

$$D_{iw} = \begin{bmatrix} D_{iw,xx} & D_{iw,xy} & D_{iw,xz} \\ D_{iw,yx} & D_{iw,yy} & D_{iw,yz} \\ D_{iw,zx} & D_{iw,zy} & D_{iw,zz} \end{bmatrix}. \tag{7.4}$$

The elements of dispersion tensor are calculated as follows:

$$D_{iw,mn} = \frac{D_{0iw}}{\tau}\delta_{mn} + \frac{\alpha_{Tw}}{\phi S_w}\left|\bar{u}_w\right|\delta_{mn} + \frac{\left(\alpha_{Lw} - \alpha_{Tw}\right)}{\phi S_w}\frac{u_{wm}u_{wn}}{\left|\bar{u}_w\right|} \qquad m,n = x,y,z\,, \quad (7.5)$$

where α_{Lw} and α_{Tw} are water phase longitudinal and transversal dispersivities, respectively; τ is the tortuosity factor with the definition of being a value greater than one; u_{wm} and u_{wn} are the components of Darcy flux of aqueous phase in m and n directions; and δ_{mn} is the Kronecker delta function defined as

$$\delta_{mn} = \begin{cases} 1 & \text{for m=n} \\ 0 & \text{otherwise} \end{cases} . \quad (7.6)$$

The magnitude of vector flux for water phase is calculated as

$$\left|u_w\right| = \sqrt{\left(u_{xw}\right)^2 + \left(u_{yw}\right)^2 + \left(u_{zw}\right)^2} . \quad (7.7)$$

The material balance equation (Equation (7.1)) for full symmetric permeability and dispersion tensors can be written in a Cartesian system as

$$\frac{\partial(\varphi N_i)}{\partial t}-\frac{\partial}{\partial x}\left(\xi_w\, x_{iw}\,\lambda_w K_{xx}\frac{\partial\Phi_w}{\partial x}+\xi_j\, x_{ij}\,\lambda_j K_{xy}\frac{\partial\Phi_w}{\partial y}+\xi_j\, x_{ij}\,\lambda_j K_{xz}\frac{\partial\Phi_w}{\partial z}\right)$$
$$-\frac{\partial}{\partial y}\left(\xi_w\, x_{iw}\,\lambda_w K_{xy}\frac{\partial\Phi_w}{\partial x}+\xi_w\, x_{iw}\,\lambda_w K_{yy}\frac{\partial\Phi_w}{\partial y}+\xi_w\, x_{iw}\,\lambda_w K_{yz}\frac{\partial\Phi_w}{\partial z}\right)$$
$$-\frac{\partial}{\partial z}\left(\xi_w\, x_{iw}\,\lambda_w K_{xz}\frac{\partial\Phi_w}{\partial x}+\xi_w\, x_{iw}\,\lambda_w K_{yz}\frac{\partial\Phi_w}{\partial y}+\xi_w\, x_{iw}\,\lambda_w K_{zz}\frac{\partial\Phi_w}{\partial z}\right)$$
$$+\frac{\partial}{\partial x}\left(\xi_w\,\phi\, S_w D_{iw,xx}\frac{\partial x_{iw}}{\partial x}+\xi_w\,\phi\, S_w D_{iw,xy}\frac{\partial x_{iw}}{\partial y}+\xi_w\,\phi\, S_w D_{iw,xz}\frac{\partial x_{iw}}{\partial z}\right)$$
$$+\frac{\partial}{\partial y}\left(\xi_w\,\phi\, S_w D_{iw,xy}\frac{\partial x_{iw}}{\partial x}+\xi_w\,\phi\, S_w D_{iw,yy}\frac{\partial x_{iw}}{\partial y}+\xi_w\,\phi\, S_w D_{iw,yz}\frac{\partial x_{iw}}{\partial z}\right)$$
$$+\frac{\partial}{\partial z}\left(\xi_w\,\phi\, S_w D_{iw,xz}\frac{\partial x_{iw}}{\partial x}+\xi_w\,\phi\, S_w D_{iw,yz}\frac{\partial x_{iw}}{\partial y}+\xi_w\,\phi\, S_w D_{iw,zz}\frac{\partial x_{iw}}{\partial z}\right)-\frac{q_i}{V_b}=0\ ;\ i=1,2,..,n_a. \tag{7.8}$$

In the approach used in this work, the equations are transformed from the Cartesian system to a computational domain. The transformed equations are then integrated into the regular system. Figure 7.1 (a) shows the physical and computational domain. Equation (7.1) can be written in a boundary-fitted coordinate system using the following transformation:

$$\xi=\xi(x,y,z)\ ;\ \eta=\eta(x,y,z)\ ;\ \gamma=\gamma(x,y,z). \tag{7.9}$$

The transformed material balance equation for the *i*-th aqueous component is given by

$$
\begin{aligned}
&\frac{\partial}{\partial t}\left(\frac{\varphi N_i}{J_t}\right)-\frac{\partial}{\partial \xi}\left(T_{11ij}\frac{\partial \Phi_w}{\partial \xi}\right)-\frac{\partial}{\partial \xi}\left(T_{12ij}\frac{\partial \Phi_w}{\partial \eta}\right)-\frac{\partial}{\partial \xi}\left(T_{13ij}\frac{\partial \Phi_w}{\partial \gamma}\right)\\
&-\frac{\partial}{\partial \eta}\left(T_{21ij}\frac{\partial \Phi_w}{\partial \xi}\right)-\frac{\partial}{\partial \eta}\left(T_{22ij}\frac{\partial \Phi_w}{\partial \eta}\right)-\frac{\partial}{\partial \eta}\left(T_{23ij}\frac{\partial \Phi_w}{\partial \gamma}\right)\\
&-\frac{\partial}{\partial \gamma}\left(T_{31ij}\frac{\partial \Phi_w}{\partial \xi}\right)-\frac{\partial}{\partial \gamma}\left(T_{32ij}\frac{\partial \Phi_w}{\partial \eta}\right)-\frac{\partial}{\partial \gamma}\left(T_{33ij}\frac{\partial \Phi_w}{\partial \gamma}\right)\\
&+\frac{\partial}{\partial \xi}\left(M_{11ij}\frac{\partial x_{iw}}{\partial \xi}\right)+\frac{\partial}{\partial \xi}\left(M_{12ij}\frac{\partial x_{iw}}{\partial \eta}\right)+\frac{\partial}{\partial \xi}\left(M_{13ij}\frac{\partial x_{iw}}{\partial \gamma}\right)\\
&+\frac{\partial}{\partial \eta}\left(M_{21ij}\frac{\partial x_{iw}}{\partial \xi}\right)+\frac{\partial}{\partial \eta}\left(M_{22ij}\frac{\partial x_{iw}}{\partial \eta}\right)+\frac{\partial}{\partial \eta}\left(M_{23ij}\frac{\partial x_{iw}}{\partial \gamma}\right)\\
&+\frac{\partial}{\partial \gamma}\left(M_{31ij}\frac{\partial x_{iw}}{\partial \xi}\right)+\frac{\partial}{\partial \gamma}\left(M_{32ij}\frac{\partial x_{iw}}{\partial \eta}\right)+\frac{\partial}{\partial \gamma}\left(M_{33ij}\frac{\partial x_{iw}}{\partial \gamma}\right)-\frac{q_i}{V_b J_t}=0,
\end{aligned}
\tag{7.10}
$$

where J_t is the Jacobian of the transformation and the tensors T and M involve fluid, reservoir, and geometric information. It is worthwhile to mention that K, D, T, and M tensors are symmetric; T and M tensors are always full tensors with nine entries while K and D can be represented as diagonal tensors. The entries of T are given by

$$T_{11ij} = \frac{\xi_w x_{iw} \lambda_w}{J_t}\left(\xi_x^2 K_{xx} + \xi_y^2 K_{yy} + \xi_z^2 K_{zz} + 2\xi_x\xi_y K_{xy} + 2\xi_x\xi_z K_{xz} + 2\xi_y\xi_z K_{yz}\right)$$

$$T_{12ij} = \frac{\xi_w x_{iw} \lambda_w}{J_t}\begin{pmatrix}\xi_x\eta_x K_{xx} + \xi_y\eta_y K_{yy} + \xi_z\eta_z K_{zz} + (\xi_x\eta_y + \xi_y\eta_x)K_{xy} + \\ (\xi_x\eta_z + \xi_z\eta_x)K_{xz} + (\xi_y\eta_z + \xi_z\eta_y)K_{xz}\end{pmatrix}$$

$$T_{13ij} = \frac{\xi_w x_{iw} \lambda_w}{J_t}\begin{pmatrix}\xi_x\gamma_x K_{xx} + \xi_y\gamma_y K_{yy} + \xi_z\gamma_z K_{zz} + (\xi_x\gamma_y + \xi_y\gamma_x)K_{xy} + \\ (\xi_x\gamma_z + \xi_z\gamma_x)K_{xz} + (\xi_y\gamma_z + \xi_z\gamma_y)K_{yz}\end{pmatrix}$$

$$T_{22ij} = \frac{\xi_w x_{iw} \lambda_w}{J_t}\left(\eta_x^2 K_{xx} + \eta_y^2 K_{yy} + \eta_z^2 K_{zz} + 2\eta_x\eta_y K_{xy} + 2\eta_x\eta_z K_{xz} + 2\eta_y\eta_z K_{yz}\right)$$

$$T_{23ij} = \frac{\xi_w x_{iw} \lambda_w}{J_t}\begin{pmatrix}\eta_x\gamma_x K_{xx} + \eta_y\gamma_y K_{yy} + \eta_z\gamma_z K_{zz} + (\eta_x\gamma_y + \eta_y\gamma_x)K_{xy} + \\ (\eta_x\gamma_z + \eta_z\gamma_x)K_{xz} + (\eta_y\gamma_z + \eta_z\gamma_y)K_{yz}\end{pmatrix}$$

$$T_{33ij} = \frac{\xi_w x_{iw} \lambda_w}{J_t}\left(\gamma_x^2 K_{xx} + \gamma_y^2 K_{yy} + \gamma_z^2 K_{zz} + 2\gamma_x\gamma_y K_{xy} + 2\gamma_x\gamma_z K_{xz} + 2\gamma_y\gamma_z K_{yz}\right).$$

(7.11)

A similar approach is used to find entries of M from dispersion coefficient tensor as follows:

$$M_{11ij} = \frac{\xi_w \phi S_w}{J_t}\left(\xi_x^2 D_{xx} + \xi_y^2 D_{yy} + \xi_z^2 D_{zz} + 2\xi_x\xi_y D_{xy} + 2\xi_x\xi_z D_{xz} + 2\xi_y\xi_z D_{yz}\right)$$

$$M_{12ij} = \frac{\xi_w \phi S_w}{J_t}\begin{pmatrix}\xi_x\eta_x D_{xx} + \xi_y\eta_y D_{yy} + \xi_z\eta_z D_{zz} + (\xi_x\eta_y + \xi_y\eta_x)D_{xy} + \\ (\xi_x\eta_z + \xi_z\eta_x)D_{xz} + (\xi_y\eta_z + \xi_z\eta_y)D_{xz}\end{pmatrix}$$

$$M_{13ij} = \frac{\xi_w \phi S_w}{J_t}\begin{pmatrix}\xi_x\gamma_x D_{xx} + \xi_y\gamma_y D_{yy} + \xi_z\gamma_z D_{zz} + (\xi_x\gamma_y + \xi_y\gamma_x)D_{xy} + \\ (\xi_x\gamma_z + \xi_z\gamma_x)D_{xz} + (\xi_y\gamma_z + \xi_z\gamma_y)D_{yz}\end{pmatrix}$$

$$M_{22ij} = \frac{\xi_w \phi S_w}{J_t}\left(\eta_x^2 D_{xx} + \eta_y^2 D_{yy} + \eta_z^2 D_{zz} + 2\eta_x\eta_y D_{xy} + 2\eta_x\eta_z D_{xz} + 2\eta_y\eta_z D_{yz}\right)$$

$$M_{23ij} = \frac{\xi_w \phi S_w}{J_t}\begin{pmatrix}\eta_x\gamma_x D_{xx} + \eta_y\gamma_y D_{yy} + \eta_z\gamma_z D_{zz} + (\eta_x\gamma_y + \eta_y\gamma_x)D_{xy} + \\ (\eta_x\gamma_z + \eta_z\gamma_x)D_{xz} + (\eta_y\gamma_z + \eta_z\gamma_y)D_{yz}\end{pmatrix}$$

$$M_{33ij} = \frac{\xi_w \phi S_w}{J_t}\left(\gamma_x^2 D_{xx} + \gamma_y^2 D_{yy} + \gamma_z^2 D_{zz} + 2\gamma_x\gamma_y D_{xy} + 2\gamma_x\gamma_z D_{xz} + 2\gamma_y\gamma_z D_{yz}\right).$$

(7.12)

Integrating Equation (7.10) in the control volume of Figure 7.1 (b) and time results in the following approximate equation:

$$\left(\frac{\varphi N_i}{J_t}\right)_P^{n+1}\frac{\Delta V}{\Delta t}-\left(\frac{\varphi N_i}{J_t}\right)_P^{n}\frac{\Delta V}{\Delta t}-$$

$$T_{11ij,e}^{n+1}\frac{\partial\Phi_w}{\partial\xi}\bigg|_e^{n+1}\Delta\eta\,\Delta\gamma+T_{11ij,w}^{n+1}\frac{\partial\Phi_w}{\partial\xi}\bigg|_w^{n+1}\Delta\eta\,\Delta\gamma-T_{12ij,e}^{n+1}\frac{\partial\Phi_w}{\partial\eta}\bigg|_e^{n}\Delta\eta\,\Delta\gamma$$

$$+T_{12ij,w}^{n+1}\frac{\partial\Phi_w}{\partial\eta}\bigg|_w^{n}\Delta\eta\,\Delta\gamma-T_{13ij,e}^{n+1}\frac{\partial\Phi_w}{\partial\gamma}\bigg|_e^{n}\Delta\eta\,\Delta\gamma+T_{13ij,w}^{n+1}\frac{\partial\Phi_w}{\partial\gamma}\bigg|_w^{n}\Delta\eta\,\Delta\gamma$$

$$-T_{21ij,n}^{n+1}\frac{\partial\Phi_w}{\partial\xi}\bigg|_n^{n}\Delta\xi\,\Delta\gamma+T_{21ij,s}^{n+1}\frac{\partial\Phi_w}{\partial\xi}\bigg|_s^{n}\Delta\xi\,\Delta\gamma-T_{22ij,n}^{n+1}\frac{\partial\Phi_w}{\partial\eta}\bigg|_n^{n+1}\Delta\xi\,\Delta\gamma$$

$$+T_{22ij,s}^{n+1}\frac{\partial\Phi_w}{\partial\eta}\bigg|_s^{n+1}\Delta\xi\,\Delta\gamma-T_{23ij,n}^{n+1}\frac{\partial\Phi_w}{\partial\gamma}\bigg|_n^{n}\Delta\xi\,\Delta\gamma+T_{23ij,s}^{n+1}\frac{\partial\Phi_w}{\partial\gamma}\bigg|_s^{n}\Delta\xi\,\Delta\gamma$$

$$-T_{31ij,f}^{n+1}\frac{\partial\Phi_w}{\partial\xi}\bigg|_f^{n}\Delta\xi\,\Delta\eta+T_{31ij,b}^{n+1}\frac{\partial\Phi_w}{\partial\xi}\bigg|_b^{n}\Delta\xi\,\Delta\eta-T_{32ij,f}^{n+1}\frac{\partial\Phi_w}{\partial\eta}\bigg|_f^{n}\Delta\xi\,\Delta\eta$$

$$+T_{32ij,b}^{n+1}\frac{\partial\Phi_w}{\partial\eta}\bigg|_b^{n}\Delta\xi\,\Delta\eta-T_{33ij,f}^{n+1}\frac{\partial\Phi_w}{\partial\gamma}\bigg|_f^{n+1}\Delta\xi\,\Delta\eta+T_{33ij,b}^{n+1}\frac{\partial\Phi_w}{\partial\gamma}\bigg|_b^{n+1}\Delta\xi\,\Delta\eta$$

$$+M_{11ij,e}^{n+1}\frac{\partial x_{iw}}{\partial\xi}\bigg|_e^{n+1}\Delta\eta\,\Delta\gamma-M_{11ij,w}^{n+1}\frac{\partial x_{iw}}{\partial\xi}\bigg|_w^{n+1}\Delta\eta\,\Delta\gamma+M_{12ij,e}^{n+1}\frac{\partial x_{iw}}{\partial\eta}\bigg|_e^{n}\Delta\eta\,\Delta\gamma$$

$$-M_{12ij,w}^{n+1}\frac{\partial x_{iw}}{\partial\eta}\bigg|_w^{n}\Delta\eta\,\Delta\gamma+M_{13ij,e}^{n+1}\frac{\partial x_{iw}}{\partial\gamma}\bigg|_e^{n}\Delta\eta\,\Delta\gamma-M_{13ij,w}^{n+1}\frac{\partial x_{iw}}{\partial\gamma}\bigg|_w^{n}\Delta\eta\,\Delta\gamma$$

$$+M_{21ij,n}^{n+1}\frac{\partial x_{iw}}{\partial\xi}\bigg|_n^{n}\Delta\xi\,\Delta\gamma-M_{21ij,s}^{n+1}\frac{\partial x_{iw}}{\partial\xi}\bigg|_s^{n}\Delta\xi\,\Delta\gamma+M_{22ij,n}^{n+1}\frac{\partial x_{iw}}{\partial\eta}\bigg|_n^{n+1}\Delta\xi\,\Delta\gamma$$

$$-M_{22ij,s}^{n+1}\frac{\partial x_{iw}}{\partial\eta}\bigg|_s^{n+1}\Delta\xi\,\Delta\gamma+M_{23ij,n}^{n+1}\frac{\partial x_{iw}}{\partial\gamma}\bigg|_n^{n}\Delta\xi\,\Delta\gamma-M_{23ij,s}^{n+1}\frac{\partial x_{iw}}{\partial\gamma}\bigg|_s^{n}\Delta\xi\,\Delta\gamma$$

$$+M_{31ij,f}^{n+1}\frac{\partial x_{iw}}{\partial\xi}\bigg|_f^{n}\Delta\xi\,\Delta\eta-M_{31ij,b}^{n+1}\frac{\partial x_{iw}}{\partial\xi}\bigg|_b^{n}\Delta\xi\,\Delta\eta+M_{32ij,f}^{n+1}\frac{\partial x_{iw}}{\partial\eta}\bigg|_f^{n}\Delta\xi\,\Delta\eta$$

$$-M_{32ij,b}^{n+1}\frac{\partial x_{iw}}{\partial\eta}\bigg|_b^{n}\Delta\xi\,\Delta\eta+M_{33ij,f}^{n+1}\frac{\partial x_{iw}}{\partial\gamma}\bigg|_f^{n+1}\Delta\xi\,\Delta\eta-M_{33ij,b}^{n+1}\frac{\partial x_{iw}}{\partial\gamma}\bigg|_b^{n+1}\Delta\xi\,\Delta\eta-\frac{q_{i,P}^{n+1}\Delta V}{J_{t,P}}=0\ .$$

(7.13)

In Equations (7.11) and (7.12), ξ_x, ξ_y, ... are the direct metrics of the transformation which are evaluated numerically. All of the derivatives in Equation (7.13) are evaluated using a central difference scheme and fluid and phase properties that are grouped into D and M tensors are evaluated by an upstream difference scheme. Finally, Newton's method is used to linearize the equations.

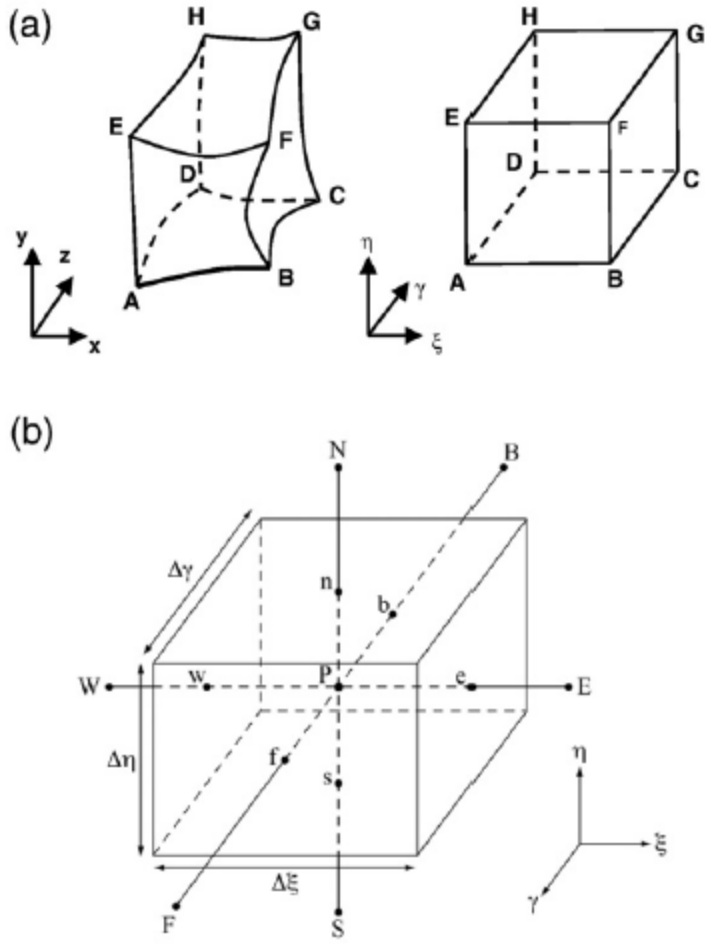

Figure 7.1: (a) Physical and computational domain (b) control volume.

7.2 SEMI-IMPLICIT IMPLEMENTATION

GPAS solves the material balance equations by Newton's method as described in Section 3.4.2. The fully-implicit scheme allows for large time steps, thus fast runs. However, the fully-implicit method requires including the derivates of equations with respect to the primary variables in the Jacobian matrix. The full tensor formulation requires a 27-point template in three dimensions. The flux of each cell is a function of pressure and molar concentration of components at all the neighboring nodes. In order to not increase the number of non-zero diagonals in the coefficient matrix of the linear system of equations, the cross derivatives were included in the right-hand side of the residual function resulting in a semi-implicit procedure. This procedure can reduce the convergence rate of the linear system if the mesh is highly distorted. However, this procedure reproduces the exact mass flow rate along each interface of the control volume. It is important to mention that this procedure results in a seven diagonal Jacobian matrix similar to the corner point procedures used in most commercial codes, but in this procedure all mass fluxes are correctly evaluated, no matter how distorted the mesh is.

The implementation of the physical dispersion model in GPAS includes adding new subroutines and applying related changes to existing subroutines. The input data for the physical dispersion model are molecular diffusion coefficients for all the components, and longitudinal and transversal dispersivity of the aqueous phase. Their keywords in the input file are DIFF, ALPL, and ALPT, respectively. Figure 7.2 shows a schematic of interactions between the physical dispersion model and other GPAS subroutines. The main subroutines of physical dispersion model are listed as follows:

- RES is the main subroutine of the physical dispersion model. It calculates the dispersion term in the aqueous phase material balance equations of GPAS (Equation (7.1)). RES is called at every Newton's iteration in XSTEP which is the driver subroutine of GPAS. The dispersion term calculated by RES is added to the convection term, and source term and form the residual vector of the Newton's method.
- JXDISP, JYDISP, and JZDISP calculate the derivatives of the dispersion term with respect to the primary variables. The derivatives are then added to the corresponding elements of the Jacobian matrix.
- DISPERSIVITY calculates the dispersion tensor components (matrices D and M in Equation (7.12)).
- POTENK, POTENE, and POTENG calculate the derivatives of the water phase potential (pressure and gravity) in the ξ, η, and γ directions, respectively. Equation (7.2) shows the potential term and Equation (7.13) contains the potential derivatives.
- VELK, VELE, and VELG calculate the velocities in the ξ, η, and γ directions, respectively. These velocities are used in the computation of the dispersion tensor as it appears in Equation (7.5).
- DIFFXK, DIFFXE, and DIFFXG calculate the derivatives of molar densities of components in the ξ, η, and γ directions, respectively. These derivatives appear in Equation (7.13).

After adding these subroutines, we applied subsequent changes in XSTEP and other GPAS subroutines (such as memory allocation and input/output subroutines) to incorporate the physical dispersion model.

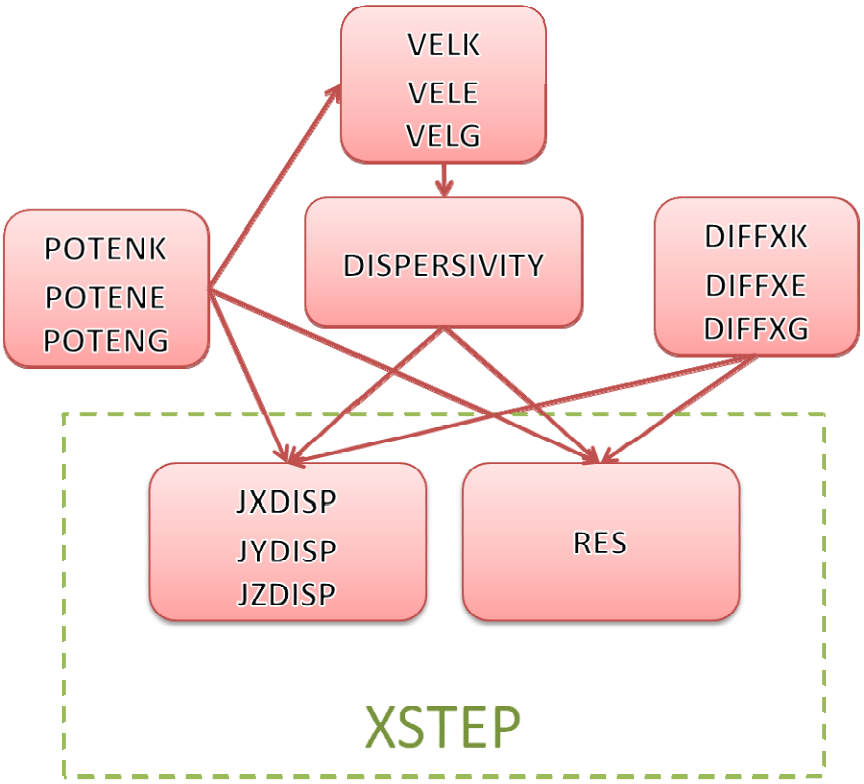

Figure 7.2: Schematic of physical dispersion model subroutines in GPAS.

7.3 Physical Dispersion Model Verification

We presented the error function solution for the one-dimensional convection diffusion equation (CDE) in Section 6.1. We used this analytical solution for the validation of GPAS results for a one-dimensional model. The second verification study is for a two-dimensional model of a quarter five-spot waterflooding. We verified GPAS results for the two-dimensional reservoir with UTCHEM.

7.3.1 Validation with One-Dimensional Analytical Solution

To validate the dispersion model in GPAS, we compare the simulation results of a one-dimensional convection diffusion problem to the analytical solution. Since we use one-point upstream differencing in GPAS, the numerical dispersion is inevitable. Thus, we use small gridblock sizes in the direction of flow to minimize numerical dispersion. We offer a comprehensive study of numerical dispersion in GPAS in Section 4 of this chapter.

Table 7.1: Properties of the one-dimensional model.

Grid	4000×1×1
Grid size	0.0125×4×4 (ft)
Porosity	0.136
Permeability	540 md
Initial S_w	1
Wells	one injector at grid 1 Q = 1 BPD
	one producer at grid 4000 Pwf = 200 psi
Longitudinal dispersivity	Case 1: 0.1 ft
	Case 2: 0.05 ft
	Case 3: 0.1 ft
	Case 4: 1 ft
Simulation time	5 days (≈0.5 PV)

The one-dimensional model properties are listed in Table 7.1. It represents a single-phase water injection with one tracer. Longitudinal dispersivity is the variable parameter. First of all, we must quantify the numerical dispersion. Although we used very small gridblock sizes, the tracer front is slightly smeared. Figure 7.3 shows the normalized concentration profile with no physical dispersion compared to the analytical solution with no dispersion and with α_L=0.01. The observed dispersion is merely associated with the numerical dispersion. The equivalent longitudinal dispersivity for analytical solution to match the simulation is 0.01 ft. This gives us an idea of how much numerical dispersion we have for this case study.

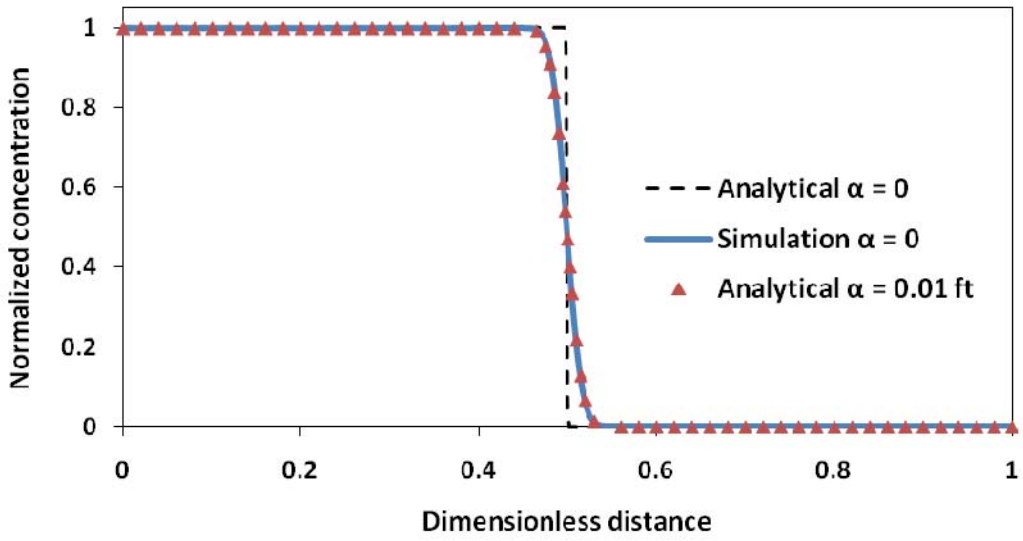

Figure 7.3: Quantifying the numerical dispersion in GPAS by comparing the simulation to the analytical solution for the one-dimensional model.

If dispersivity of the medium is considerably greater than 0.01 ft, then the numerical dispersion is negligible. Figure 7.4 shows the simulation results for several dispersion coefficients compared to the analytical solution. As the dispersion coefficient increases, the numerical dispersion becomes negligible and the concentration profiles from GPAS match the analytical solution perfectly.

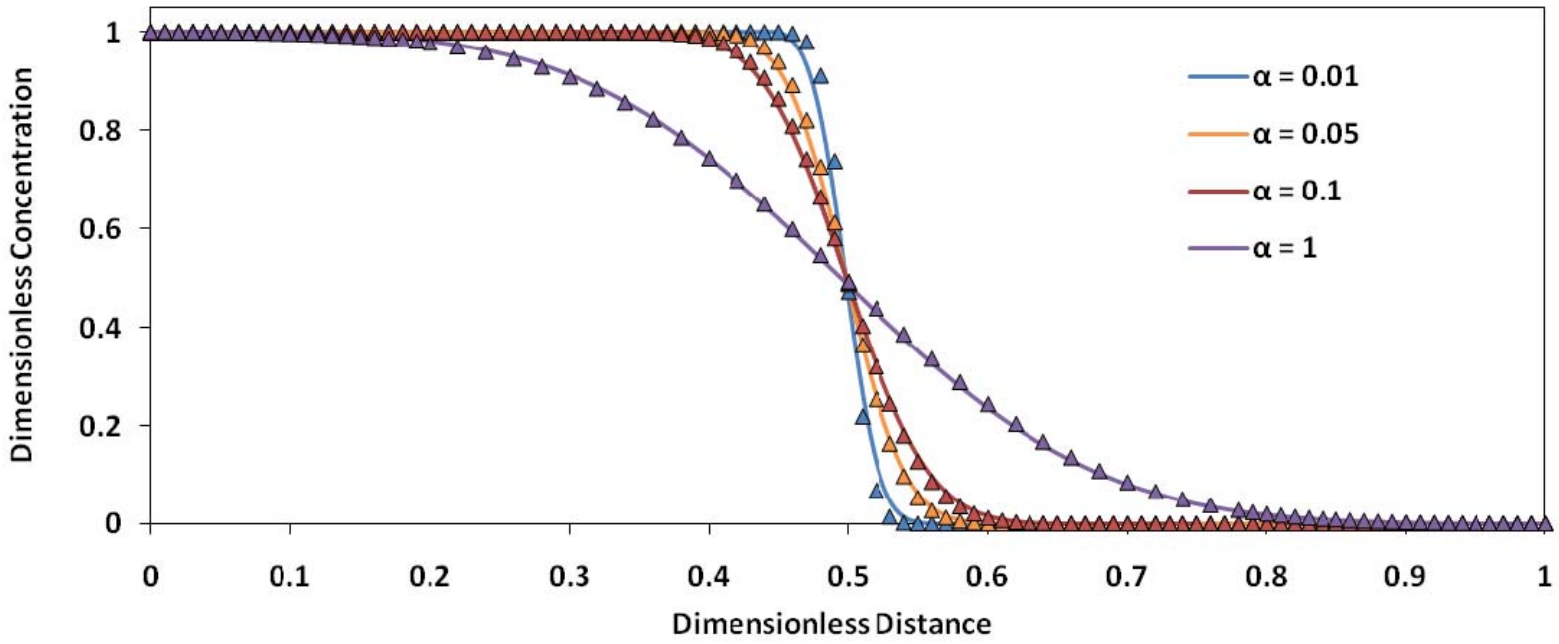

Figure 7.4: Simulation results (lines) and analytical solutions (Δ) for concentration profiles after 0.5 pore volume injected for longitudinal dispersivities of 0.01, 0.05, 0.1, and 1 ft.

7.3.2 Comparison of Two-Dimensional Simulations with UTCHEM

The results of two-dimensional simulations are compared against UTCHEM. The 2D case is a quarter five-spot water injection with a non-reactive tracer. It is assumed that water is the only phase. Table 7.2 presents the properties of the reservoir model. We used a single point upwind differencing scheme and a constant time step of 0.1 day in both simulators. Starting from the base case without any physical dispersion, we applied different values of molecular diffusion and longitudinal dispersion coefficients. The normalized concentration distributions are plotted as contours in Figure 7.5. The dotted lines are UTCHEM results and the solid lines are GPAS results. The results correspond perfectly as can be seen in the plots of Figure 7.5.

Table 7.2: Properties of the two-dimensional quarter five-spot reservoir model.

Grid	15×15×1
Grid size	32×32×50 (ft)
Porosity	0.136
Permeability	540 md
Initial Sw	1
Wells	injector Q1 = 534 BPD
	producer Pwf = 200 psi

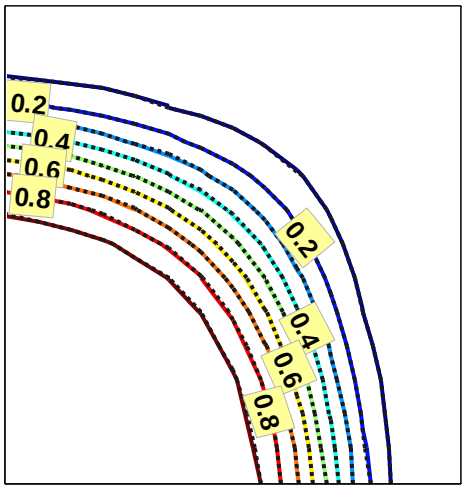

D=0, α=0

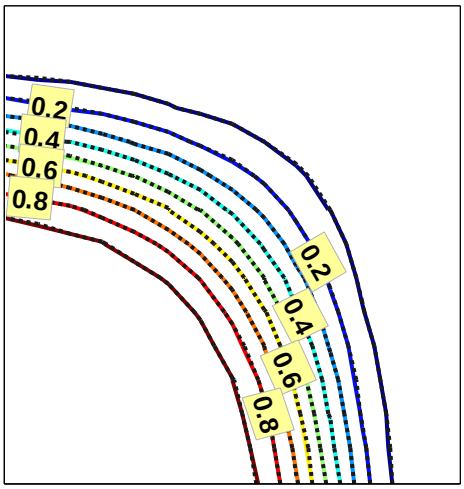

D=0, α=1 ft

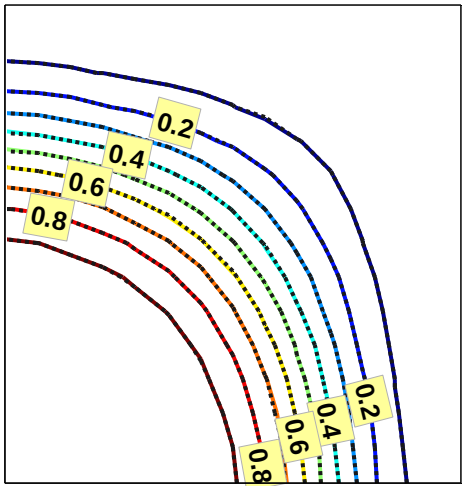

D=10 ft^2/day, α=0

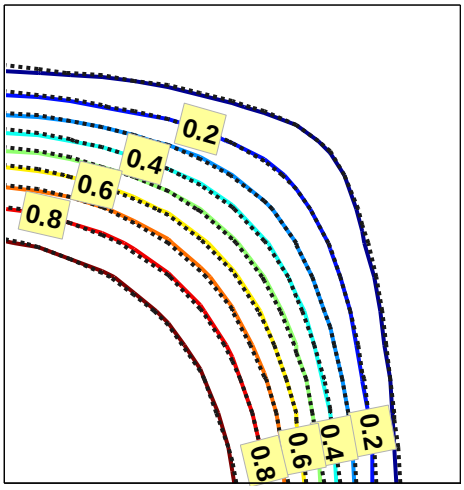

D=0, α=10 ft

Figure 7.5: Normalized concentration profiles of GPAS (solid lines) and UTCHEM (dotted lines) with different values of molecular diffusion and mechanical dispersion.

7.3.3 Non-Orthogonal Grid

The corner point option in GPAS solves the problems with non-orthogonal meshes. The advantage of non-orthogonal meshes is their flexibility to handle important features of reservoirs, as oil-bearing formations do not have regular shapes. Figure 7.6 shows a highly distorted non-orthogonal and an orthogonal 16×16×10 mesh. We used these meshes to validate the formulation for non-orthogonal gridblocks. Model properties are presented in Table 7.3 . We ran the cases with no physical dispersion and with a longitudinal dispersivity of 50 ft. Figure 7.7 compares the normalized production tracer concentrations. The plots of non-orthogonal mesh match the orthogonal mesh results for both cases of with and without physical dispersion.

Table 7.3: Properties of the three-dimensional quarter five-spot reservoir model.

Grid	16×16×10
Reservoir size	560×560×100 (ft)
Porosity	0.136
Permeability	540 md
Initial Sw	1
Wells	injector Q1 = 1069 BPD
	producer Pwf = 200 psi
Longitudinal dispersivity	Case 1: 0
	Case 2: 50 ft
Injection time	1044 days (≈1.4 PV)

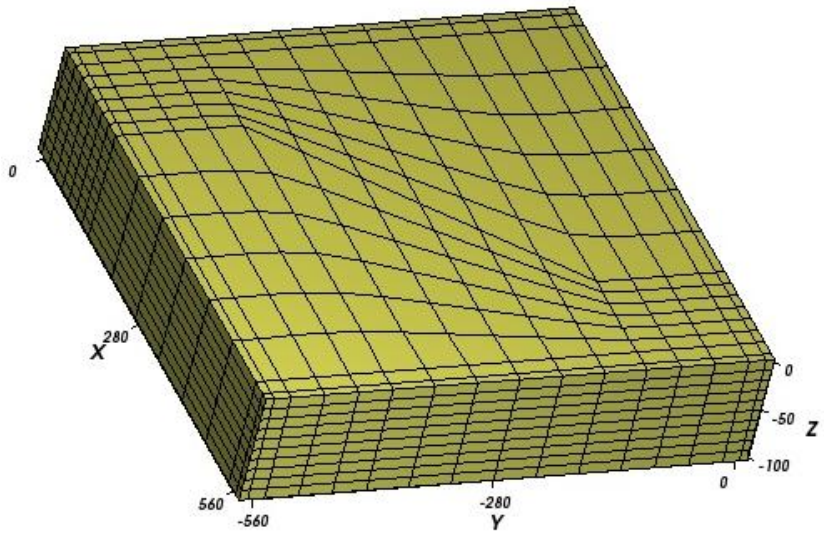

(a)

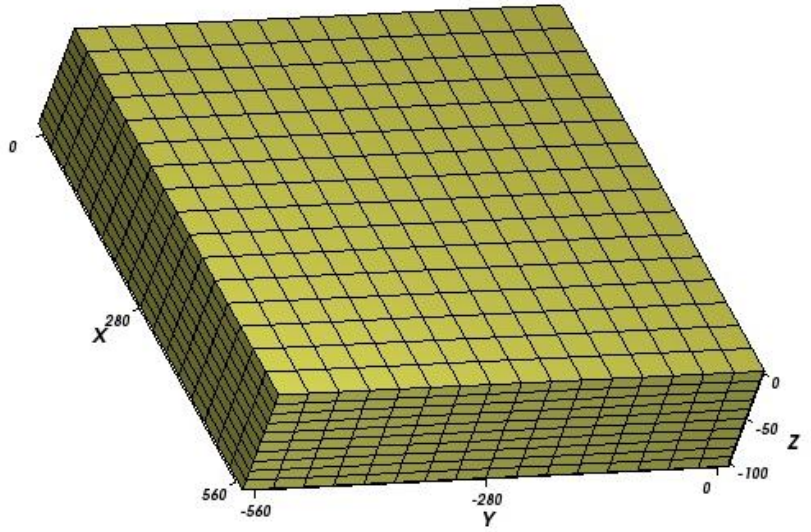

(b)

Figure 7.6: (a) Non-orthogonal and (b) orthogonal meshes for a quarter five-spot reservoir model.

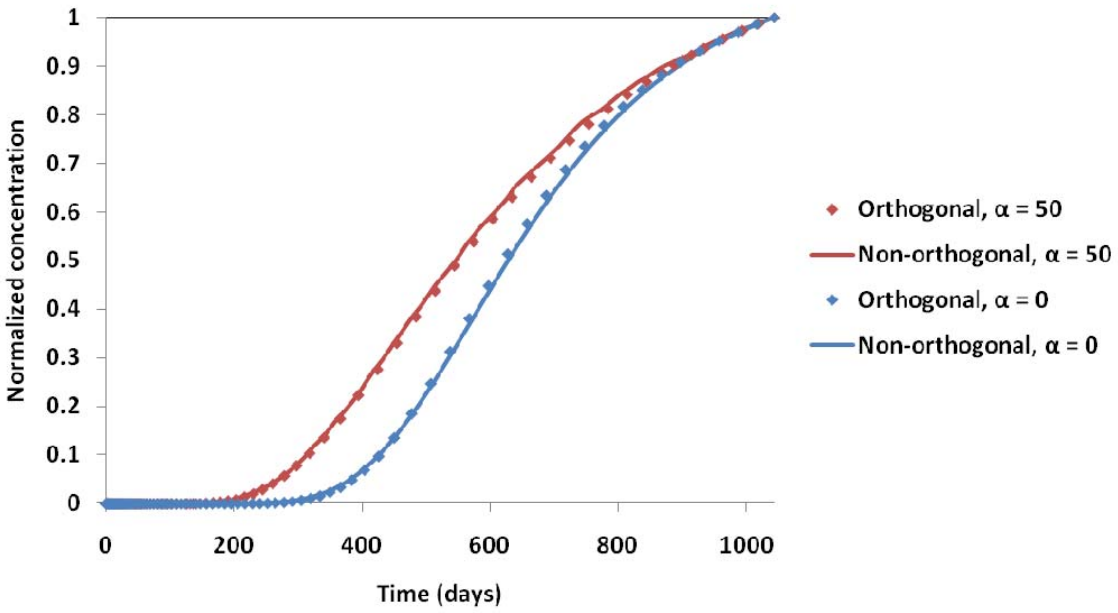

Figure 7.7: Normalized tracer concentration at the producer for orthogonal and non-orthogonal grids with and without physical dispersion.

7.4 Investigation of Numerical Dispersion in GPAS

Most reservoir simulators replace derivatives of partial differential equations by finite difference approximations (Peaceman, 1977; Aziz and Settari, 1979). These approximations are derived from truncated Taylor series. Finite difference approach introduces a truncation error which comes from neglecting the higher order terms in Taylor series. Truncation error smears the fronts of saturation and concentration as if additional physical dispersion existed. This smearing of front is called numerical dispersion, which can be of the same order of magnitude as physical dispersion. Because of numerical dispersion, simulations may produce erroneous results, especially when physical dispersion has an important role in the process. A number of techniques are suggested to reduce numerical dispersion. These techniques include variably timed flux-

updating methods (Larson, 1982a, b), high-order Godunov schemes (Thiele and Edwards, 2001), and the total variation diminishing (TVD) scheme (Edwards and Rubin, 1991). UTCHEM uses a higher order differencing with flux-limiting TVD scheme to minimize numerical dispersion (Harten, 1983; Liu et al., 1994). The magnitude of numerical dispersion in a simulator depends on the spatial and temporal differencing methods. GPAS uses backward differencing in space and implicit time differencing. We investigate numerical dispersion in GPAS with analytical and numerical studies.

7.4.1 Truncation Error Analysis

The extent of numerical dispersion can be obtained from the truncation error generated from the finite difference discretization of the convection diffusion equation (Peaceman and Rachford, 1962; Lantz, 1971; and Peaceman, 1977). We assume no physical dispersion and calculate the equivalent dispersion introduced by the truncation error. The one-dimensional convection equation for one component in a single phase fluid is

$$\phi \frac{\partial C}{\partial t} + u \frac{\partial C}{\partial x} = 0, \tag{7.14}$$

where C is the concentration, ϕ is porosity, and u is Darcy velocity. Discretization of Equation (7.14) using upwind implicit scheme gives

$$\phi \frac{C_i^{n+1} - C_i^n}{\Delta t} + u \frac{C_i^{n+1} - C_{i-1}^{n+1}}{\Delta x} = 0. \tag{7.15}$$

To find the truncation error resulted from the approximation, we made to obtain Equation (7.15), we expand the Taylor series around C_i^{n+1} for time and space differences:

$$C_i^{n+1} = C_{i-1}^{n+1} + \Delta x \frac{\partial C}{\partial x} - \frac{(\Delta x)^2}{2} \frac{\partial^2 C}{\partial x^2} + HOT \,, \tag{7.16}$$

where HOT represents the higher order terms. Therefore,

$$\frac{C_{i-1}^{n+1} - C_i^{n+1}}{\Delta x} = \frac{\partial C}{\partial x} - \frac{\Delta x}{2} \frac{\partial^2 C}{\partial x^2} + HOT \,. \tag{7.17}$$

The same approach for the time derivative results in

$$C_i^{n+1} = C_i^n + \Delta t \frac{\partial C}{\partial t}\Big|_{n+1} - \frac{(\Delta t)^2}{2} \frac{\partial^2 C}{\partial t^2}\Big|_{n+1} + HOT \,. \tag{7.18}$$

Hence,

$$\frac{C_i^{n+1} - C_i^n}{\Delta t} = \frac{\partial C}{\partial t} - \frac{\Delta t}{2} \frac{\partial^2 C}{\partial t^2} + HOT \,. \tag{7.19}$$

To find a relationship between second order terms ($\frac{\partial^2 C}{\partial t^2}$ and $\frac{\partial^2 C}{\partial x^2}$), we take the derivative of Equation (7.14) with respect to time, assuming that Darcy velocity and porosity are time-independent:

$$\frac{\partial^2 C}{\partial t^2} = -\frac{u}{\phi}\frac{\partial}{\partial t}\left(\frac{\partial C}{\partial x}\right) = -\frac{u}{\phi}\frac{\partial}{\partial x}\left(\frac{\partial C}{\partial t}\right),$$

$$\frac{\partial^2 C}{\partial t^2} = -\frac{u}{\phi}\frac{\partial}{\partial x}\left(-\frac{u}{\phi}\frac{\partial C}{\partial x}\right) = \frac{u^2}{\phi^2}\frac{\partial^2 C}{\partial x^2}. \tag{7.20}$$

Combining Equations (7.17), (7.19), and (7.20), while neglecting the higher order terms, provides

$$\phi\frac{C_i^{n+1} - C_i^n}{\Delta t} + u\frac{C_i^{n+1} - C_{i-1}^{n+1}}{\Delta x} = u\frac{\partial C}{\partial x} + \phi\frac{\partial C}{\partial t} - \left(\frac{\Delta t}{2}\frac{u^2}{\phi} + \frac{\Delta x}{2}u\right)\frac{\partial^2 C}{\partial x^2}. \tag{7.21}$$

Therefore, the truncation error has the form

$$Error = -\left(\frac{\Delta t}{2}\frac{u^2}{\phi^2} + \frac{\Delta x}{2\phi}u\right)\phi\frac{\partial^2 C}{\partial x^2}. \tag{7.22}$$

This implies that an equivalent dispersion coefficient that accounts for numerical dispersion is

$$D_{num} = \frac{\Delta x}{2}\frac{u}{\phi} + \frac{\Delta t}{2}\frac{u^2}{\phi^2} = \frac{u\Delta x}{2\phi}\left(1 + \frac{u\Delta t}{\phi\Delta x}\right) = \frac{u\Delta x}{2\phi}\left(1 + N_{Co}\right), \tag{7.23}$$

where $N_{Co} = \frac{u\Delta t}{\phi\Delta x}$ is the Courant number. Using the same approach for explicit formulation will result in a numerical diffusion coefficient of (Lantz, 1971; Fanchi, 1983):

$$D_{num} = \frac{u\Delta x}{2\phi}\left(1 - \frac{u\Delta t}{\phi \Delta x}\right) = \frac{u\Delta x}{2\phi}\left(1 - N_{Co}\right). \tag{7.24}$$

Comparing Equations (7.23) and (7.24) shows that time step size has different effects on the numerical dispersion in implicit and explicit formulations. Using large time steps reduces the numerical dispersion in an explicit simulator. On the other hand, using large time steps in an implicit simulator adds to the numerical dispersion. However, for small Courant numbers ($u\Delta t \ll \Delta x$), both Equations (7.23) and (7.24) reduce to

$$D_{num} \approx \frac{u\Delta x}{2\phi} \quad \Rightarrow \quad \alpha_{num} \approx \frac{\Delta x}{2} \ . \tag{7.25}$$

Hence, in the simulation of one-dimensional cases with small time steps, $\alpha_{num} \approx \Delta x/2$ provides an estimation of numerical dispersion.

In solving a multi-dimensional convection diffusion equation, numerical dispersion coefficient appears as a tensor. In Equation (7.26), D_{ij} is the corresponding dispersion tensor element and v_i is the interstitial velocity.

$$\frac{\partial C}{\partial t} = \sum_{i=1}^{3}\left(\sum_{j=1}^{3} D_{ij}\frac{\partial^2 C}{\partial x_i \partial x_j} - v_i \frac{\partial C}{\partial x_i}\right). \tag{7.26}$$

Fanchi (1983) derived the numerical dispersion tensor for a variety of finite-differencing schemes in multi-dimensional reservoirs. The two-dimensional numerical dispersion tensor for single-point backward spatial differencing and implicit time differencing becomes

$$D_{num} = \frac{1}{2}\begin{bmatrix} v_x\left(\Delta x + v_x \Delta t\right) & v_x v_y \Delta t \\ v_x v_y \Delta t & v_y\left(\Delta x + v_y \Delta t\right) \end{bmatrix}. \tag{7.27}$$

Expanding Equation (7.27) to a 3D problem, gives the numerical dispersion tensor in three dimensions as follows:

$$D_{num} = \frac{1}{2}\begin{bmatrix} v_x\left(\Delta x + v_x \Delta t\right) & v_x v_y \Delta t & v_x v_z \Delta t \\ v_x v_y \Delta t & v_y\left(\Delta x + v_y \Delta t\right) & v_y v_z \Delta t \\ v_x v_z \Delta t & v_y v_z \Delta t & v_z\left(\Delta x + v_z \Delta t\right) \end{bmatrix}. \tag{7.28}$$

In Equations (7.27) and (7.28), v_x, v_y, and v_z are interstitial velocities ($v = u/\phi$). When we solve the convection-diffusion equation with actual physical dispersion, numerical dispersion effect is added to the physical dispersion and results in additional smearing of the fronts. As shown in Equation (7.28), increasing time step and gridblock size increases the numerical dispersion in a fully implicit simulator.

7.4.2 Gridblock Size Effect

We used the one-dimensional reservoir model of Section 7.3.1 with a variety of gridblock sizes and without any physical dispersion to examine the effect of gridblock size on the numerical dispersion in GPAS. We used a very small time step of Δt=0.001 day to minimize the contribution of time step size in the numerical dispersion. The normalized concentration profiles are plotted in Figure 7.8 for different gridblock sizes and the same time step. As expected, increasing gridblock size increases the numerical dispersion. We calculated the associated numerical dispersivity (α_{num}) for every case from Equation (7.23) and plotted the analytical solution on the same figure. The

simulation cases and corresponding dispersivity values are presented in Table 7.14. Comparing gridblock size and numerical dispersivities shows that $\alpha_{num} \approx \Delta x/2$, which we derived in the previous section, is a valid approximation for one-dimensional cases with relatively large gridblock sizes.

Table 7.4: Effect of gridblock size on numerical dispersion.

Case no.	Number of Grids	Δx	α_{num}
1	200	0.25	0.1275
2	400	0.125	0.065
3	1000	0.05	0.0275
4	2000	0.025	0.015
5	4000	0.0125	0.00875

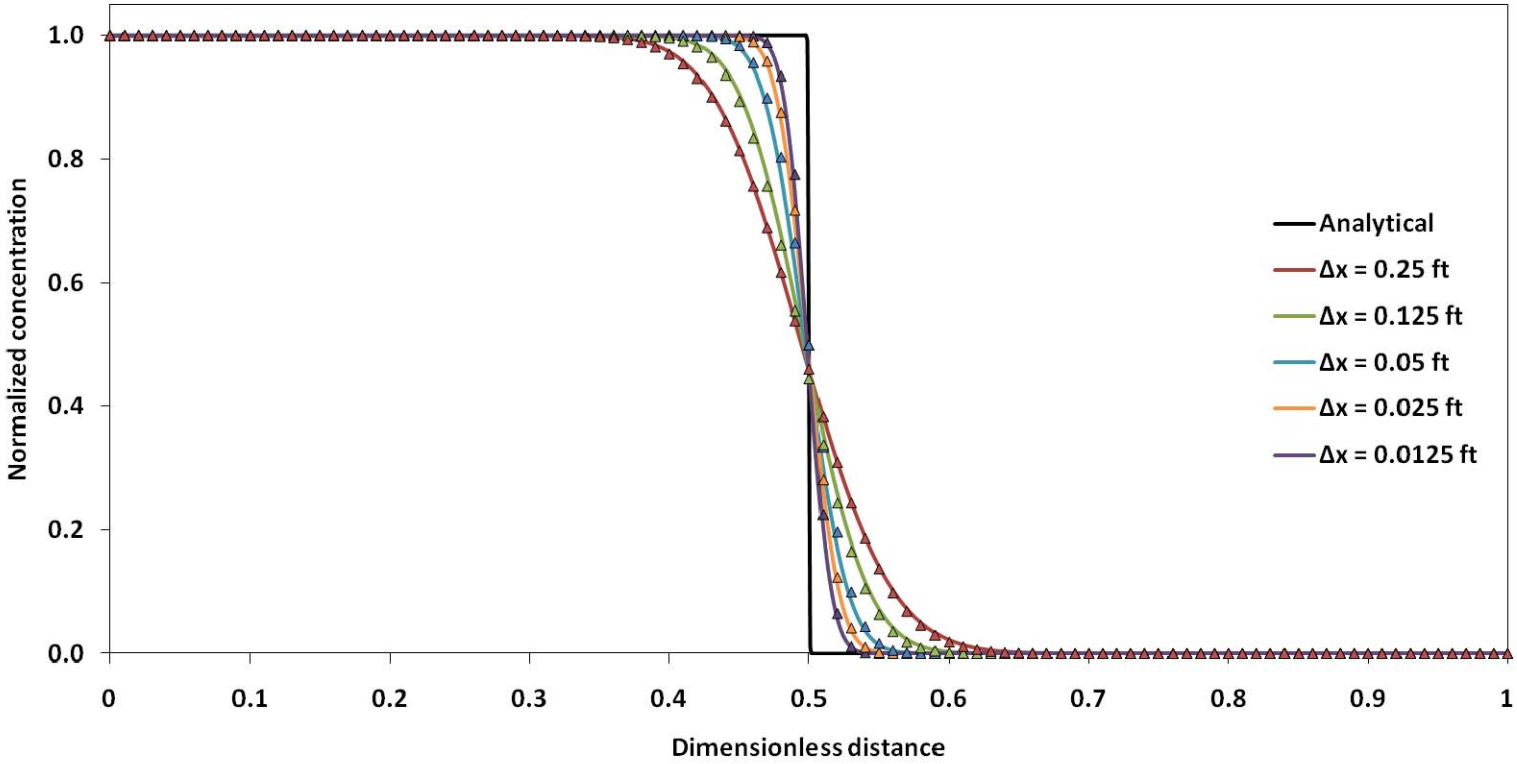

Figure 7.8: Normalized concentration profiles after 0.5 pore volume injected with no physical dispersion for gridblock sizes of 0.25, 0.125, 0.05, 0.025, and 0.0125 ft. The solid colored lines are simulation results. The triangular markers are analytical solution with dispersivities calculated from Equation (7.23).

7.4.3 Time Step Effect

We started from Case 2 of the previous section (Nx=400, Δx=0.125) and ran that case with different time step sizes to investigate the effect of time step on numerical dispersion in GPAS. Figure 7.9 shows the concentration profiles for cases with different time steps listed in Table 7.5. For every case, we calculated the numerical dispersivity from Equation (7.23) and used the analytical solution to plot concentration profiles for the corresponding dispersivities. For the first case, the numerical dispersion is mainly from the first term in Equation (7.23). As Δt increases, the second term becomes dominant and adds to the numerical dispersion.

Table 7.5: Effect of time step size on numerical dispersion.

Case no.	Δt	α_{num}	α from Equation (7.23)
1	0.001	0.065	0.065
2	0.01	0.09	0.0875
3	0.1	0.32	0.3125
4	0.2	0.55	0.5625

The effects of time step and gridblocks on numerical dispersion can be estimated by the analytical approaches of Section 7.6.1. We presented one-dimensional examples that show these effects. Note that these cases represent extreme situations with high numerical dispersions for study purposes. In typical reservoir simulations, Courant numbers and Darcy velocities are much smaller than the cases that we showed here.

However, understanding the consequence of numerical inaccuracies and having an estimate of their effect is essential in reservoir simulation. In field-scale simulation, physical dispersivities are normally much higher than the numerical dispersivity. Proper selection of time steps and gridblocks assures accurate numerical calculations while performing fast and robust simulations.

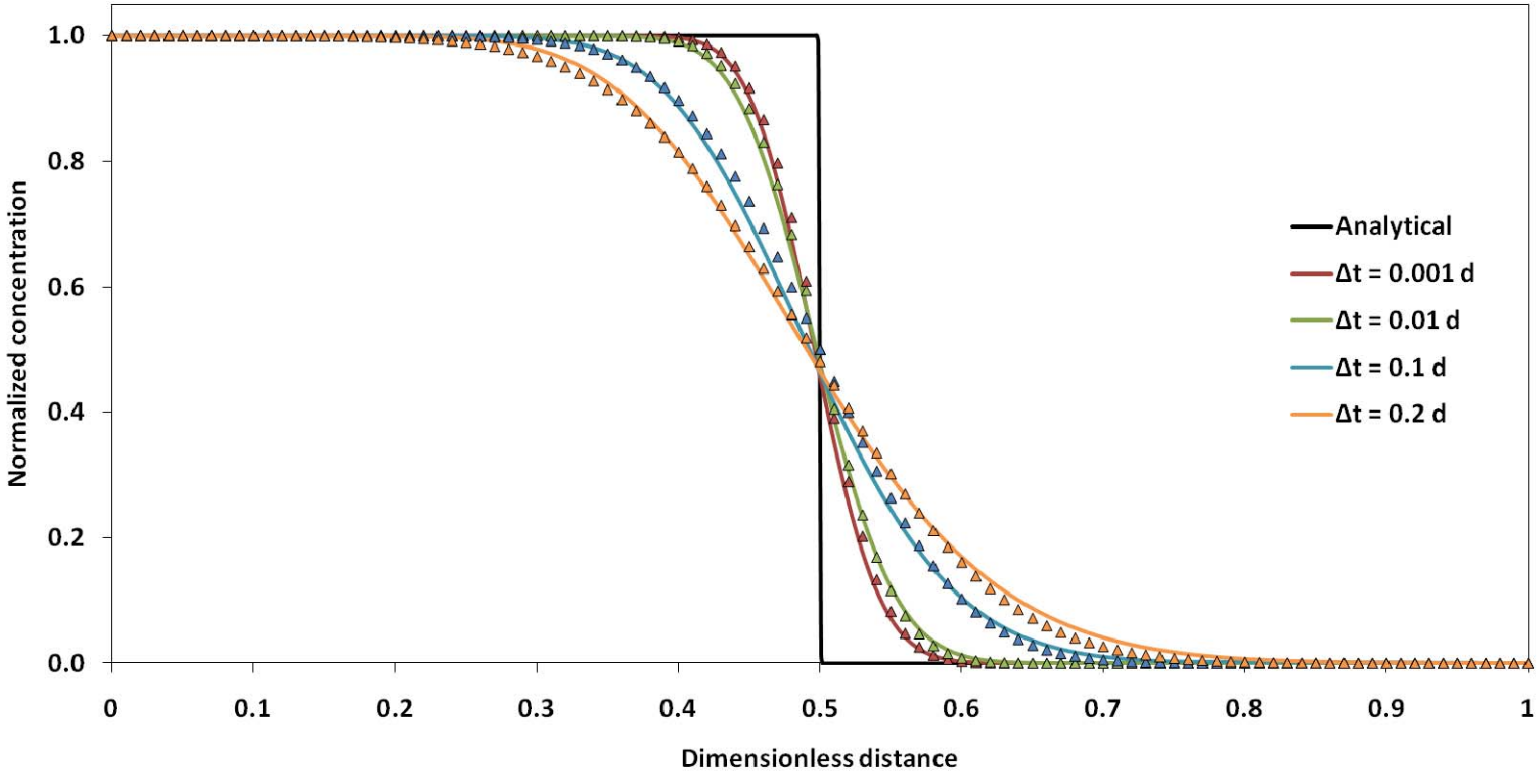

Figure 7.9: Normalized concentration profiles after 0.5 pore volume injected with no physical dispersion for time step sizes of 0.001, 0.01, 0.1, and 0.2 d. The solid colored lines are simulation results. The triangular markers are analytical solution with dispersivities calculated from Equation (7.23).

Chapter 8: Field Application of GPAS Reservoir Souring Model

The implementation of the biological model in GPAS enables us to perform field-scale simulations of reservoir souring and its remediation. In this chapter, we show the capabilities of GPAS in modeling complex reservoirs and simulating reservoir souring reactions. The first field case example is a hypothetical reservoir model with a non-orthogonal mesh and heterogeneous porosity and permeability. We perform simulations of different injection strategies to study the effect of nitrate injection on reservoir souring. In the second reservoir model, we demonstrate the parallel processing feature of GPAS for the biological model and the physical dispersion model.

8.1 Non-Orthogonal Reservoir Model

Figure 8.1 shows the corner point mesh of our hypothetical reservoir model from several views. We use a 40x32x3 non-orthogonal grid. This reservoir has 6 producers and 8 injectors. The permeability and porosity distributions for the top layer of the reservoir are shown in Figure 8.2 and Figure 8.3, respectively. The average permeability is 540 md and the Dykstra-Parson coefficient is 0.6. The average porosity is 0.2 and the Dykstra-Parson coefficient for porosity is 0.2. Figure 8.4 shows the water-oil relative permeability curves. Reservoir has a total pore volume of 5.2×10^7 ft^3. Producers operate with constant bottom-hole pressures and injectors operate at constant water injection rates which remain the same during the simulation. Table 8.1 presents the reservoir model properties and well constraints. Initial water saturation is 0.5 and water injection

continues for 10 years, which is equivalent to about 1.55 pore volume injected. Oil production rates and water production rates from all of the producers are plotted in Figure 8.5 and Figure 8.6, respectively. Figure 8.7 shows the water saturation maps for the top layer of the reservoir after 0.2, 1, and 1.5 pore volume injected.

Table 8.1: Properties of the non-orthogonal reservoir model.

Number of cells	3840 (40×32×3)
Number of vertices	5412
Pore volume	5.2×10^{7} ft^3
Porosity	Mean = 0.2 Dykstra-Parson coef. = 0.2
Permeability	Mean = 540 md Dykstra-Parson coef. = 0.6
Initial Sw	0.5
Initial Pressure	3300 psi
Water properties	Density = 62.4 lb/ft^3 Viscosity = 1 cp
Initial substrate concentration	1000 mg/L
Oil properties	One component T_C = 652 ^oF P_C = 304 psi V_C = 12.087 ft^3 Acentric factor = 0.488 MW = 200.3 Oil viscosity = 2.6 cp
Wells	7 injectors Q1to Q7 = 500 STBD Q8 = 300 STBD
	6 producers Pwf = 3000 psi

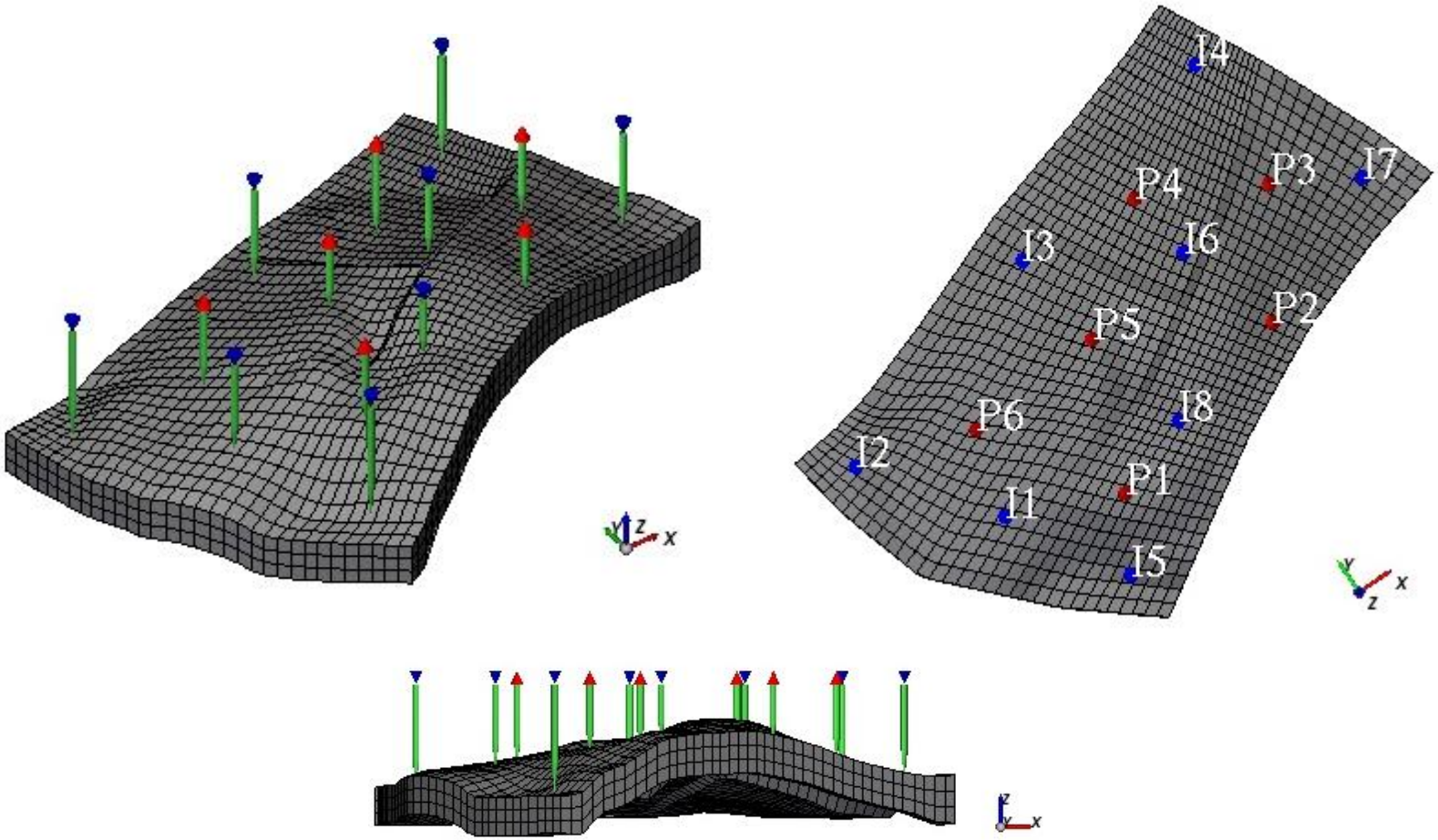

Figure 8.1: Grid geometry and well locations for the non-orthogonal reservoir model from different angles. The reservoir is enlarged in the z-direction by a factor of 10. The injectors are displayed with blue wellheads and producers with red wellheads.

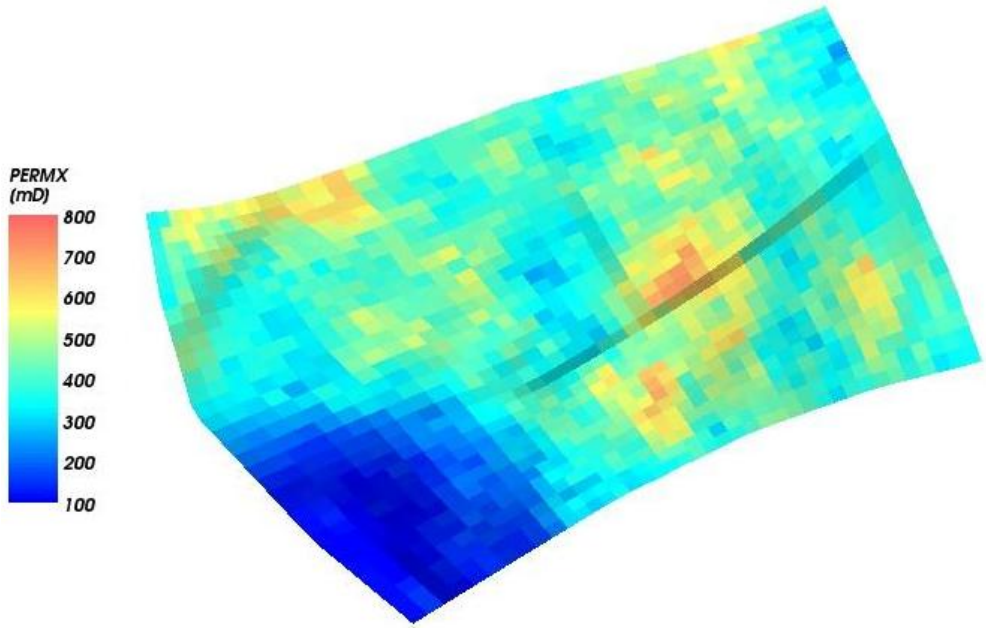

Figure 8.2: Permeability distribution for the top layer of the reservoir. The Dykstra-Parson coefficient is 0.6 and the average permeability is 540 md.

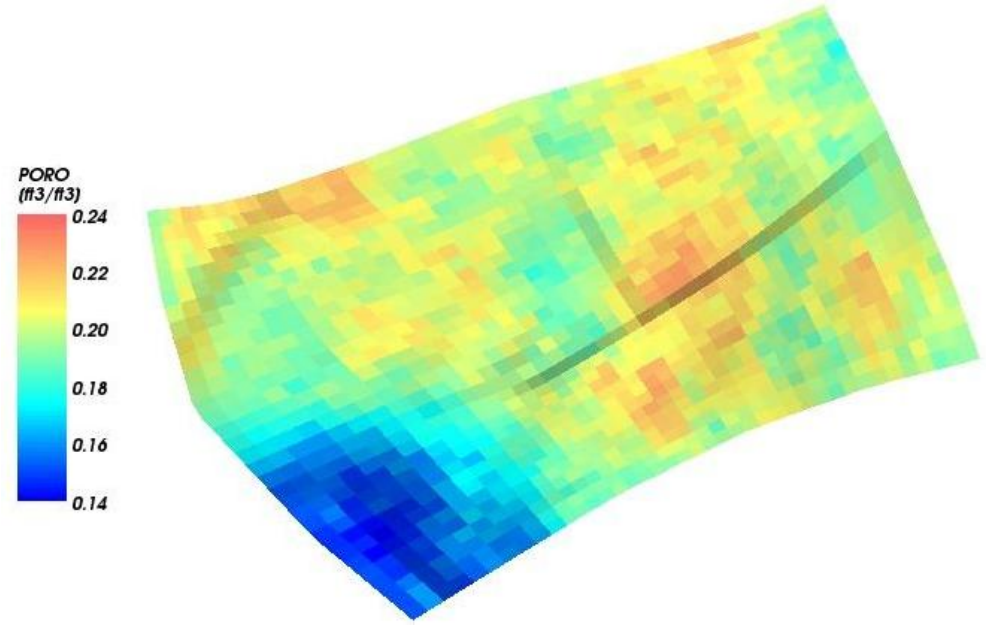

Figure 8.3: Porosity distribution for the top layer of the reservoir. The Dykstra-Parson coefficient is 0.2 and the average porosity is 0.2.

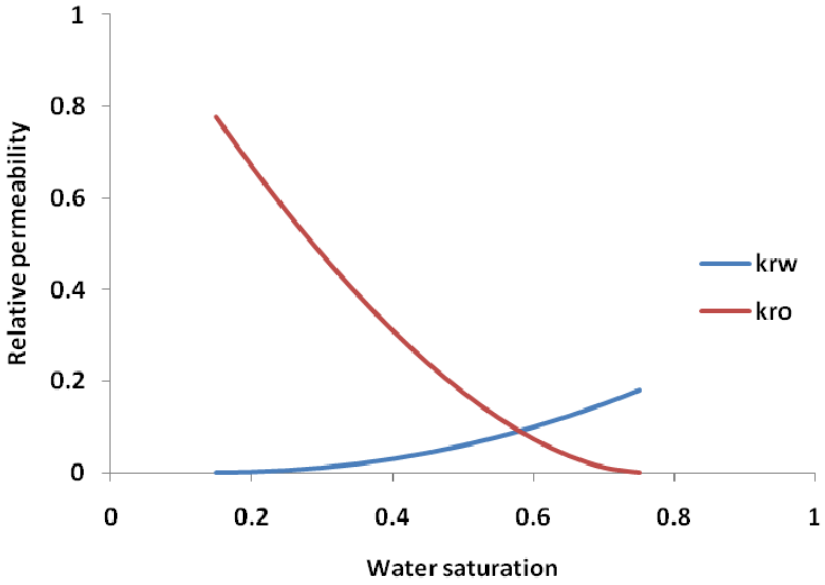

Figure 8.4: Relative permeability curves for the non-orthogonal reservoir model.

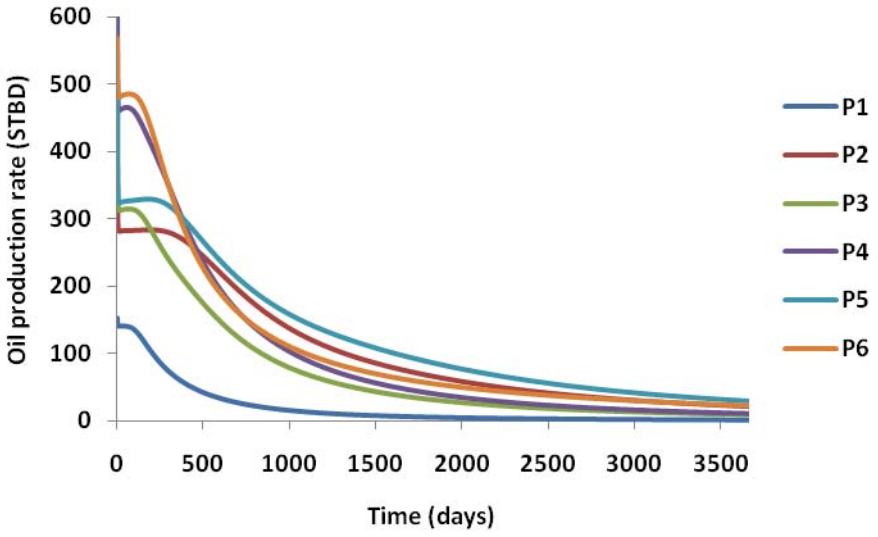

Figure 8.5: Oil production rates from all of the producers of the non-orthogonal reservoir model.

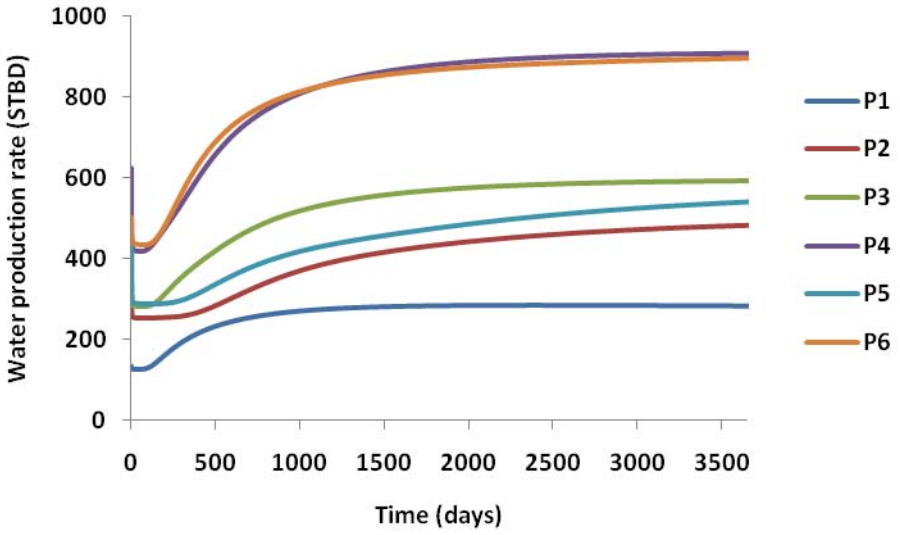

Figure 8.6: Water production rates from all of the producers of the non-orthogonal reservoir model.

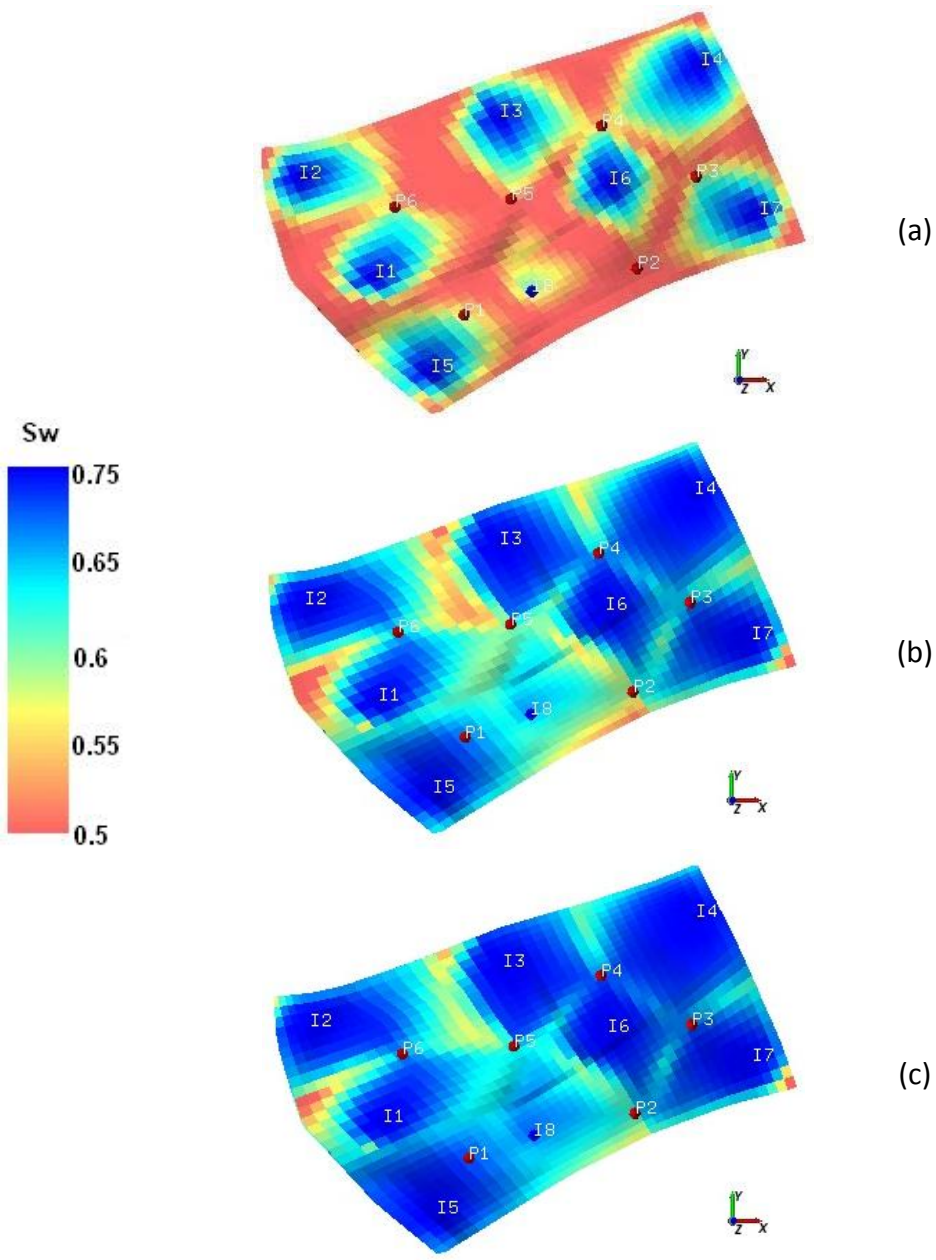

Figure 8.7: Water saturation maps of the top layer of the non-orthogonal reservoir model after (a) 468 days (0.2 PV), (b) 2346 days (1 PV), and (c) 3508 days (1.5 PV).

The biological species in our model are SRB and NR-SOB which exist in attached biofilm and as free-floating biomass in the aqueous phase. The biological model parameters are obtained from the simulation of NR-SOB activity in a porous media column reactor presented in Section 5.4. We also consider the free-floating bacteria in field-scale simulations assuming that free-floating bacteria have the same maximum specific growth rate as the attached biomass. Similar to the experiment model, we have three metabolic combinations. The first metabolic combination is the reduction of sulfate by SRB; H_2S is the product of this reaction. The second combination is the reduction of nitrate to nitrite by NR-SOB. The produced nitrite acts as an inhibitor for the SRB activity which is presented by the first metabolic combination. The third metabolic combination is sulfide oxidization by NR-SOB. Sulfide is the electron donor and sulfate is the product of this reaction. Biological model parameters for all of the simulation cases of this section are listed in Table 8.2. However, in the basic reservoir souring case without nitrate injection, the nitrate reduction and sulfide oxidation reactions do not occur.

The aqueous phase components in the biological reactions are sulfate, sulfide, nitrate, nitrite, and a substrate which represents all of the fatty acids and other organic compounds that provide carbon and energy for bacterial activity. Substrate concentration in the formation water is 1000 mg/L. We assumed that there is no sulfate, sulfide, nitrate, or nitrite in the formation water. As we discussed in Section 6.2.2, the abundance of organic compounds in the injection water determines the area at which reservoir souring takes place. In real field applications, produced water is normally injected back into the reservoir. Therefore, we assume that water injection starts with low substrate concentration (30 mg/L); but, after 200 days, we increase the injection

substrate concentration to 200 mg/L to account for organic compounds that are re-injected into the reservoir with recycled water. After 700 days, when water cut is very high, almost all of the injection water is provided by the produced water and is rich in organic compounds. Hence, we increase the injection substrate concentration to 400 mg/L.

To study the effect of nitrate, we consider three injection scenarios. First, we run the reservoir model for souring with no nitrate injection. SRB are the only active bacteria and souring is not inhibited. Then, we examine two souring treatment cases: nitrate injection after H_2S breakthrough and nitrate injection from the beginning of waterflooding. The injection concentration and simulation results for each case are presented in the following sections.

Table 8.2: Biological model parameters for simulation cases of the non-orthogonal reservoir model.

Metabolic combination	Components		Parameters	
Sulfate reduction	Biological species	SRB	Maximum specific growth rate (1/day)	1.1
			Yield coefficient	0.15
	Substrate	Substrate	Substrate half saturation coefficient (mg/L)	1000
			Substrate utilization rate	0.89
	Electron acceptor	Sulfate	Electron acceptor half saturation coefficient (mg/L)	10
	Product	H_2S	Product generation coefficient	0.49
	Inhibitor	Nitrite	Inhibition constant (mg/L)	0.05
Nitrate reduction	Biological species	NR-SOB	Maximum specific growth rate (1/day)	3.5
			Yield coefficient	0.01
	Substrate	Substrate	Substrate half saturation coefficient (mg/L)	2000
			Substrate utilization rate	0.6
	Electron acceptor	Nitrate	Electron acceptor half saturation coefficient (mg/L)	100
	Product	Nitrite	Product generation coefficient	0.18
Sulfide oxidation	Biological species	NR-SOB	Maximum specific growth rate (1/day)	3.5
			Yield coefficient	0.05
	Substrate	Sulfide	Substrate half saturation coefficient (mg/L)	100
			Substrate utilization rate	0.2
	Electron acceptor	Nitrate	Electron acceptor half saturation coefficient (mg/L)	100
	Product	Sulfate	Product generation coefficient	0.91

8.1.1 Souring without Nitrate Injection

In this case, we do not inject any nitrate for souring treatment. The composition of the injection water is presented in Table 8.3. Injection sulfate concentration is 2700 mg/L and substrate concentration increases in two steps (30 mg/L to 200 mg/L after 200 days and 200 mg/L to 400 mg/L after 700 days) as explained in the previous section to account for the produced water re-injection. Figure 8.8 shows the concentration maps of H_2S at three different times. The high concentrations at the water front indicate the souring reactions at the mixing zone where injection and formation waters meet. Behind the mixing zone, H_2S concentration is associated with the souring in the biofilm around the injectors. Figure 8.9 shows the formation of SRB biofilm in the vicinity of injectors, after we start injecting considerable amount of substrate (note the concentration of substrate in Table 8.3 after 200 days). Figure 8.10 shows the aqueous concentration of H_2S from all of the producers. As we expected, H_2S production continues, because substrate and sulfate are continuously provided by the injection water. The higher concentrations at the beginning (300-350 mg/L) are associated with the production of H_2S generated in the mixing zones. After the mixing zones pass the producers (Figure 8.8c), the H_2S that is generated around the injectors reaches the producers.

In this case, substrate is the limiting component in the souring reactions. All of the substrate is consumed in the reaction zone and the stoichiometric equivalent of sulfate reduces to sulfide. Figure 8.11 shows the concentration maps of substrate and sulfate at the end of the simulation (1.5 PV). Although a large amount of sulfate is available in the reservoir, souring is limited by the substrate amount which is almost entirely used.

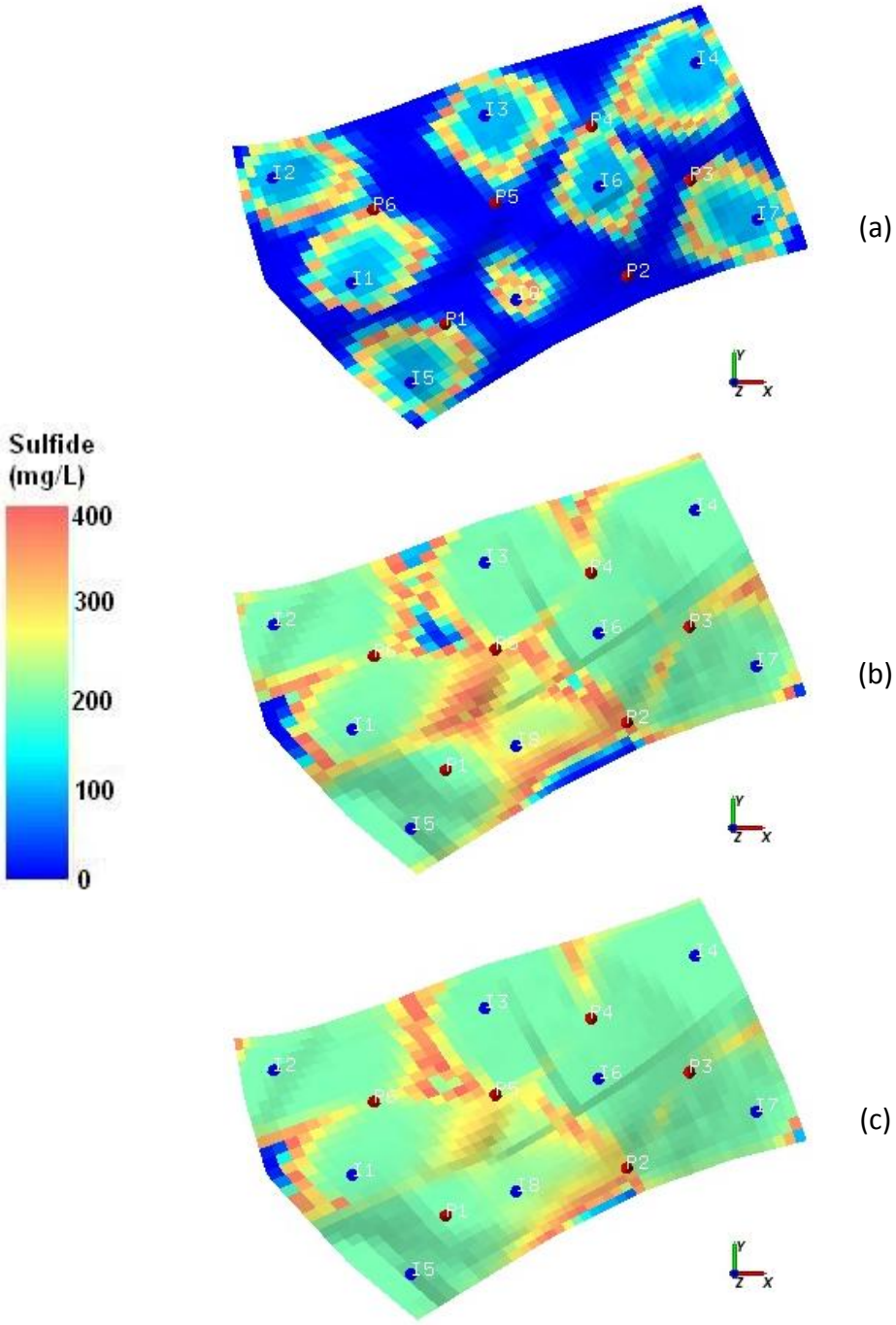

Figure 8.8: H_2S concentration maps of the top layer of the non-orthogonal reservoir model after (a) 468 days (0.2 PV), (b) 2346 days (1 PV), and (c) 3508 days (1.5 PV) with no nitrate injection.

Table 8.3: Composition of the injection water for the case of souring without nitrate injection.

Component	Injection water concentration (mg/L)		
	0-200 days	200-700 days	700-3650 days
Substrate	30	200	400
Sulfate	2700	2700	2700
Sulfide	0	0	0
Nitrate	0	0	0
Nitrite	0	0	0
SRB	1	1	1
NR-SOB	1	1	1

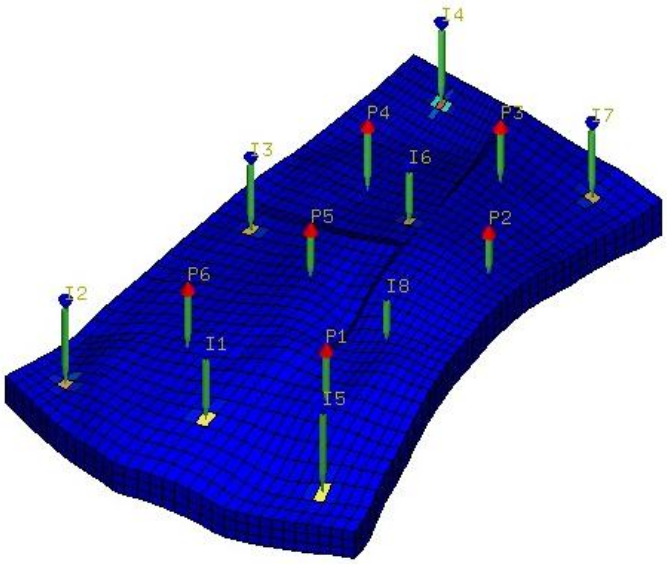

Figure 8.9: Formation of SRB biofilm in the injector gridblocks after increase in the substrate concentration in the injection water for the non-orthogonal reservoir model with no nitrate injection.

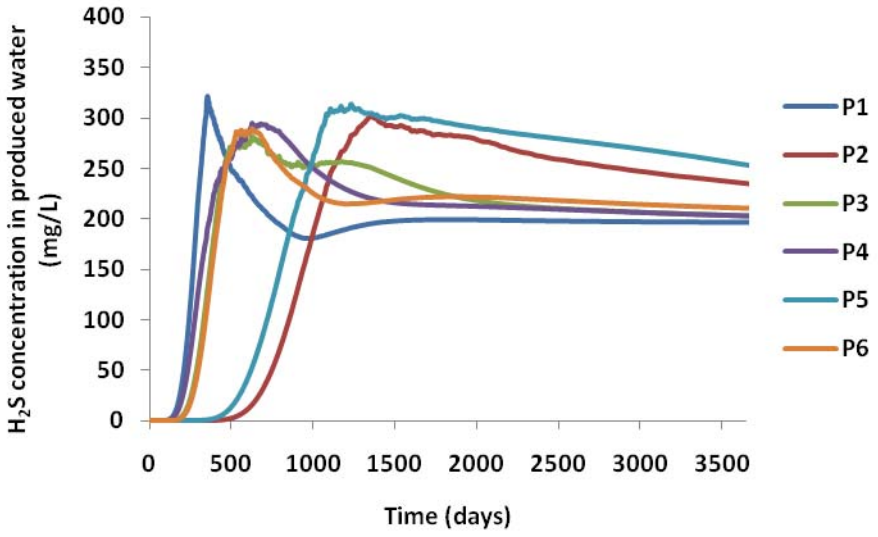

Figure 8.10: Aqueous phase H_2S concentration from all of the producers of the non-orthogonal reservoir model with no nitrate injection.

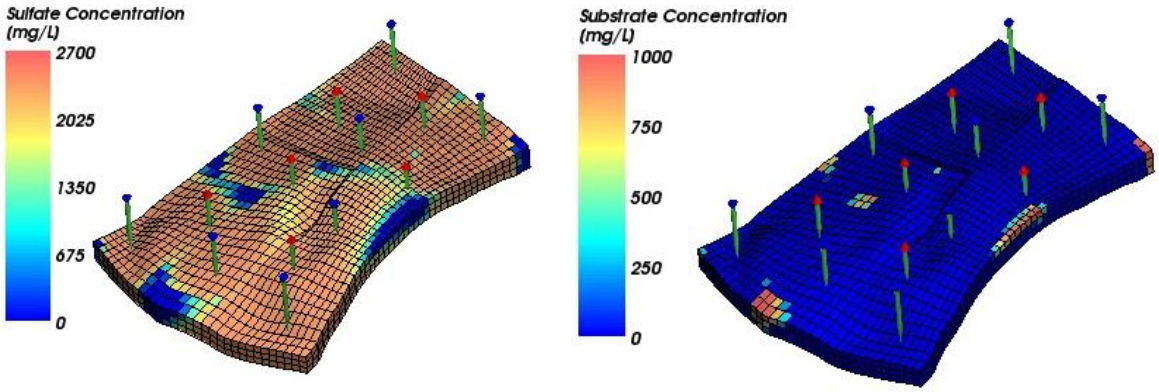

(a) (b)

Figure 8.11: Concentration maps of (a) sulfate and (b) substrate after 1.5 PV injected for the non-orthogonal reservoir model.

8.1.2 Nitrate Injection after H_2S Breakthrough

In this case, we assume that nitrate injection starts at 400 mg/L of injected water after one year. At this time, all of the producers have already started to produce H_2S. Injected nitrate inhibits reservoir souring by stimulating NR-SOB. The nitrite produced by NR-SOB stops the SRB activity. Figure 8.12 shows the concentration maps of nitrite at 0.2, 1, and 1.5 pore volume injected. Nitrite generation starts at 365 days when we start nitrate injection. At this time, H_2S generation at the biofilm around injectors stops. However, nitrite affects only the areas that it reaches; therefore, H_2S that is already generated and moves ahead of nitrite toward producers will not be removed. Figure 8.13 shows the concentration maps of sulfide at 0.2, 1, and 1.5 pore volume injected. As can be observed in this figure, the H_2S produced before nitrate injection moves toward the producers, but it is not followed by any further produced H_2S. Figure 8.14 shows the concentration of H_2S in the produced water form all of the producers. The H_2S production at the beginning is similar to the previous case (Figure 8.10), but after the start of nitrate injection, H_2S concentrations reduce to almost zero.

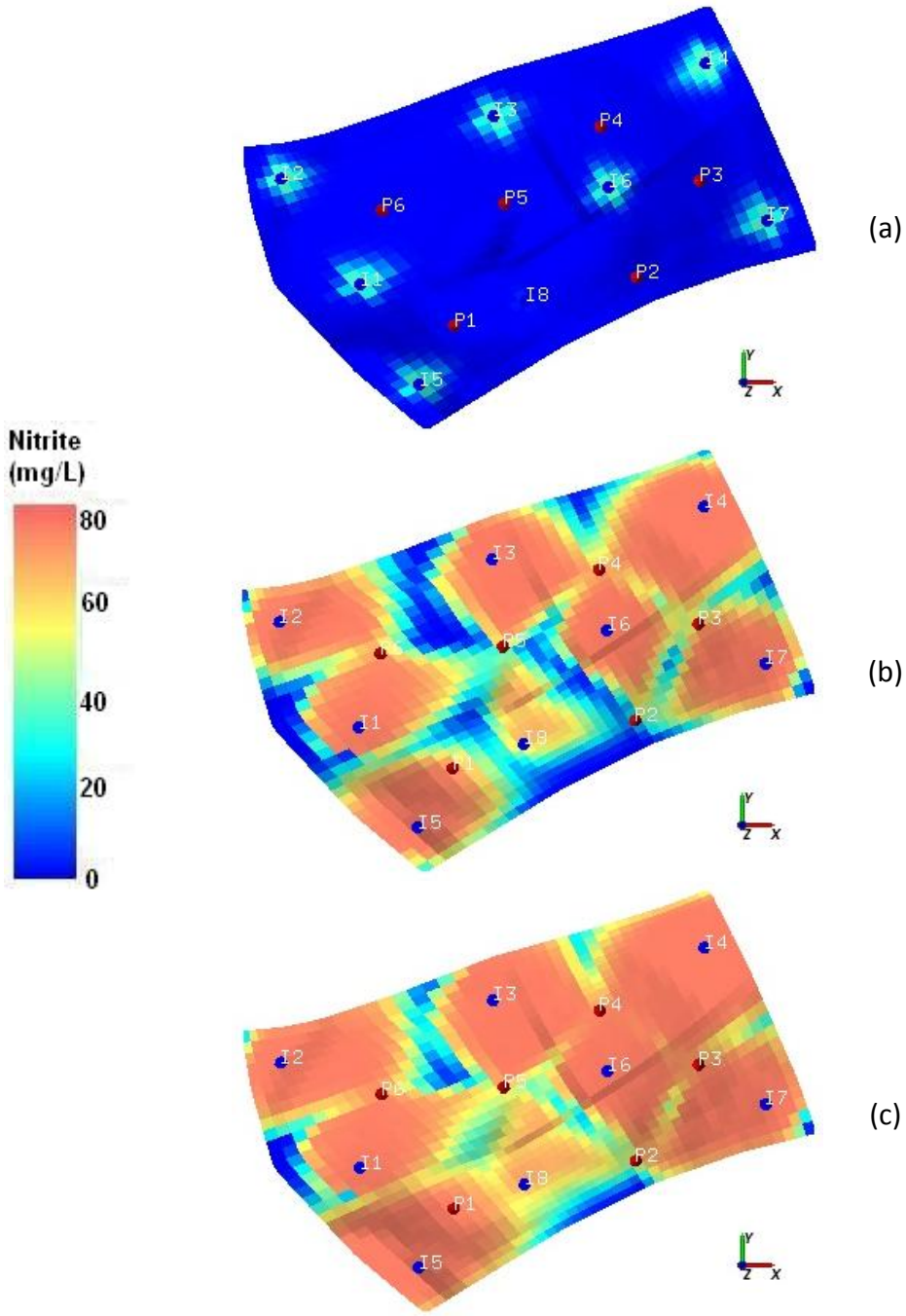

Figure 8.12: Nitrite concentration maps of the top layer of the non-orthogonal reservoir model after (a) 468 days (0.2 PV), (b) 2346 days (1 PV), and (c) 3508 days (1.5 PV) for nitrate injection after H_2S breakthrough.

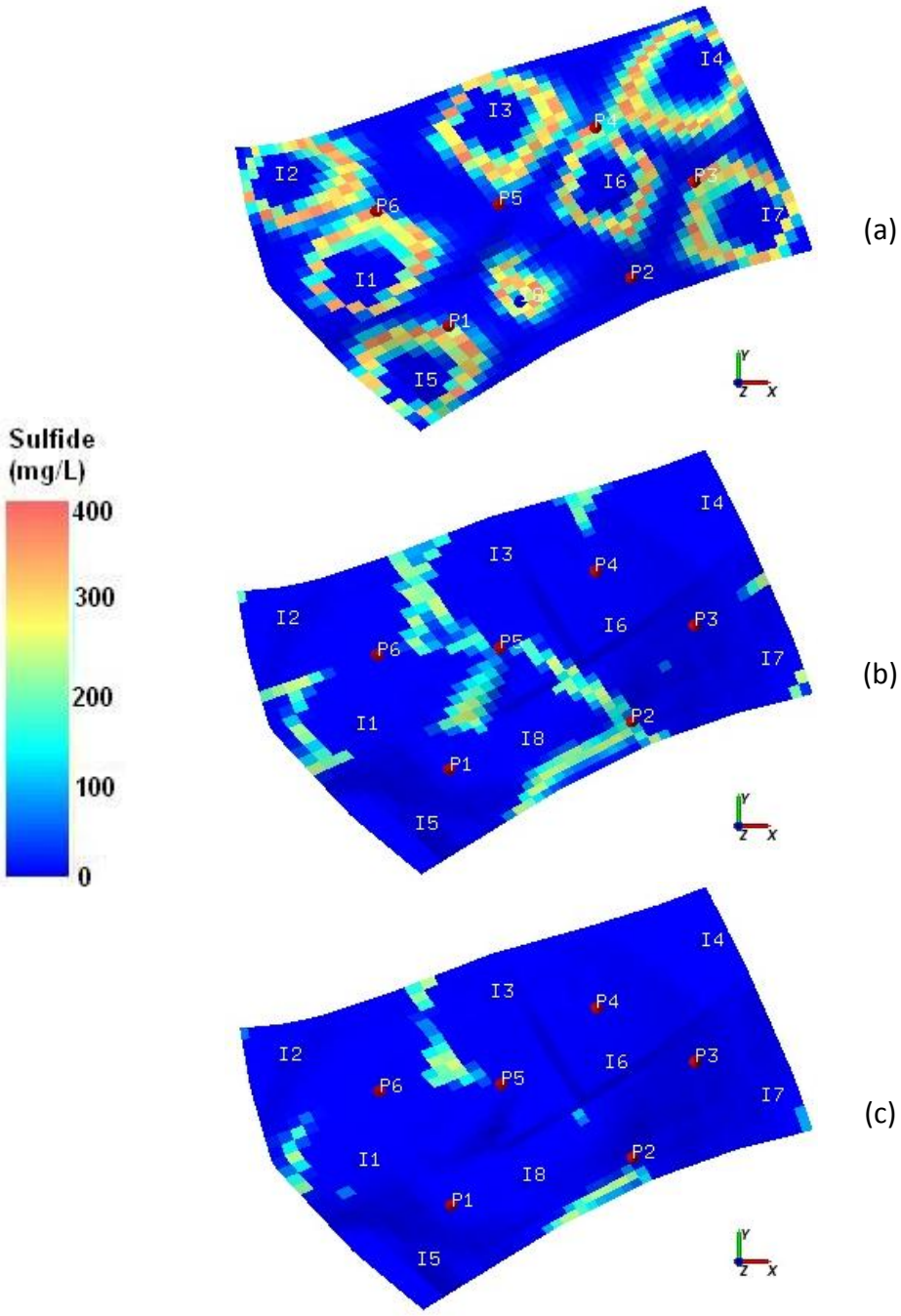

Figure 8.13: H_2S concentration maps of the top layer of the non-orthogonal reservoir model after (a) 468 days (0.2 PV), (b) 2346 days (1 PV), and (c) 3508 days (1.5 PV) for nitrate injection after H_2S breakthrough.

Table 8.4: Composition of the injection water for the case of nitrate injection after H_2S breakthrough.

Component	Injection water concentration (mg/L)			
	0-200 days	200-365 days	365-700 days	700-3650 days
Substrate	30	200	200	400
Sulfate	2700	2700	2700	2700
Sulfide	0	0	0	0
Nitrate	0	0	400	400
Nitrite	0	0	0	0
SRB	1	1	1	1
NR-SOB	1	1	1	1

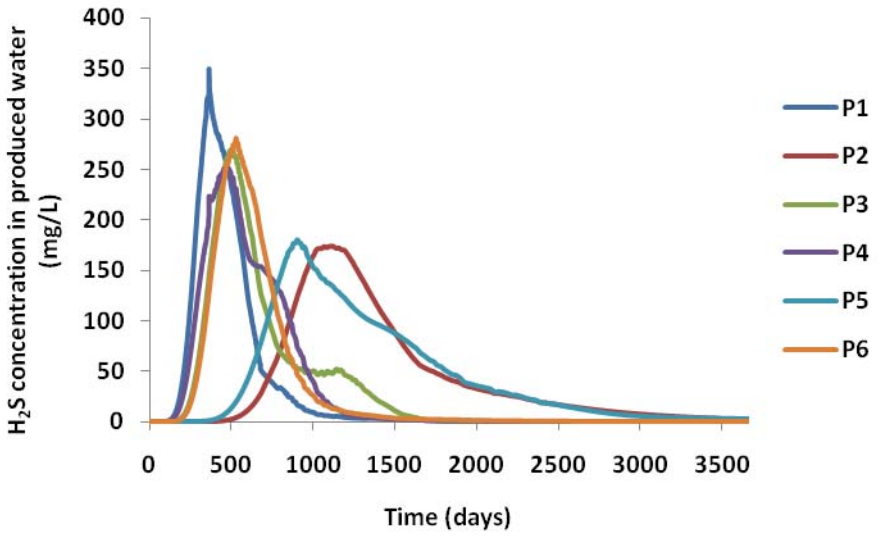

Figure 8.14: Aqueous phase H_2S concentration from all of the producers of the non-orthogonal reservoir model with nitrate injection after H_2S breakthrough.

8.1.3 Initial Nitrate Injection

The previous case showed the effectiveness of nitrate injection in souring remediation. However, if operators examine the reservoir water and the injection water compositions, they could predict the occurrence of souring and take preventive measures from the start. In this case, we study the effect of nitrate injection from the beginning of waterflooding. The same amount of nitrate as the previous case (400 mg/L of injected water) is injected. Other injection compositions remain the same as listed in Table 8.5. Nitrite generation starts from the first day and inhibits SRB activity. H_2S production is reduced to very small amounts (maximum of approximately 10 mg/L) as shown in Figure 8.15. Note the scale on the vertical axes of Figure 8.15 compared to Figure 8.10 and Figure 8.14. Analyzing the results of three cases, we can conclude that nitrate injection is most effective if it starts from the beginning of water injection. However, injection of nitrate at any time reduces SRB activity, but the H_2S that is propagated through reservoir will not be affected by nitrate. Figure 8.16 shows the H_2S production from producer number 6 in three cases for comparison.

Table 8.5: Composition of the injection water for the case of nitrate injection from the beginning.

Component	Injection water concentration (mg/L)		
	0-200 days	200-700 days	700-3650 days
Substrate	30	200	400
Sulfate	2700	2700	2700
Sulfide	0	0	0
Nitrate	400	400	400
Nitrite	0	0	0
SRB	1	1	1
NR-SOB	1	1	1

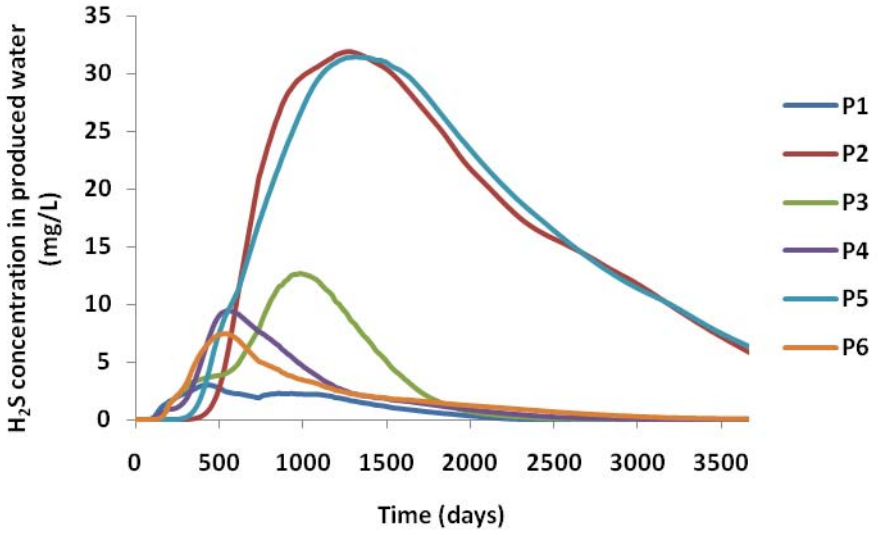

Figure 8.15: Aqueous phase H_2S concentration from all of the producers of the non-orthogonal reservoir model with initial nitrate injection.

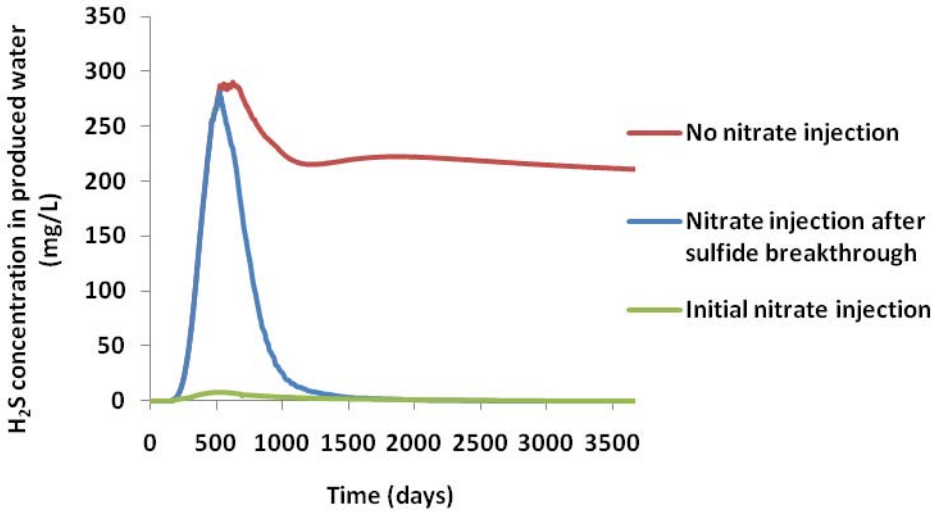

Figure 8.16: Aqueous phase H_2S concentration from producer number 6 in the non-orthogonal reservoir model for three cases: 1) No nitrate injection, 2) Nitrate injection after H_2S breakthrough, and 3) Initial nitrate injection.

8.2 PARALLEL PROCESSING

As we explained in Section 3.6, GPAS uses a domain decomposition approach for parallel processing. In this method, the reservoir model is divided into fragments in the y-direction and each fragment is assigned to a processor for solving the associated equations. The domain decomposition and communication between processors are managed by a framework named IPARS (Parashar et al., 1997). To demonstrate the parallel processing performance of GPAS, we built a relatively large reservoir model with multiple wells and carried out simulations with different number of processors. First, we describe the reservoir model and single-processor simulation results, and then we show the speed-up in multi-processor runs.

8.2.1 Model Description

The reservoir model has an orthogonal corner point mesh with 80×64×3 gridblocks. Model properties are listed in Table 8.6. We simply call this model "parallel model." The reservoir dimensions of 11000'×5500'×70' and constant porosity of 0.3 provide a total pore volume of 1.26×10^{9} ft^3. The mean value of the heterogeneous permeability distribution is 386 md and the Dykstra-Parson coefficient is 0.34. Figure 8.17 shows the permeability distribution and well locations in the reservoir. The reservoir model has 11 injectors that inject water at constant volumetric rates and 9 producers that operate at a constant bottom-hole pressure. The well constraints remain constant during the simulation. The injection starts at an initial water saturation of 0.5 and continues for 15 years, which is equivalent to 0.94 pore volume injected. Relative permeability curves are the same as the relative permeability curves of the non-orthogonal reservoir model shown in Figure 8.4.

Table 8.6: Properties of the parallel reservoir model.

Number of cells	15360 (80×64×3)
Number of vertices	21060
Reservoir size	11000'×5500'×70'
Single grid size	137.5'×85.9'×23.3'
Porosity	0.3
Permeability	Mean = 386 md Dykstra-Parson coef. = 0.34
Initial Sw	0.5
Initial Pressure	5000 psi
Water properties	Density = 62.4 lb/ ft^3 Viscosity = 1 cp
Oil properties	One components T_C = 652 ^oF P_C = 304 psi V_C = 12.087 ft^3 Acentric factor = 0.488 MW = 200.3 Oil viscosity = 2.6 cp
Wells	11 injectors Q1 = 3000 STBD Q2 = 1500 STBD Q3 = 4500 STBD Q4 = 5000 STBD Q5 = 2500 STBD Q6 = 3200 STBD Q7 = 4500 STBD Q8 = 4000 STBD Q9 = 3500 STBD Q10 = 3500 STBD Q11 = 3500 STBD
	9 producers Pwf = 3500 psi

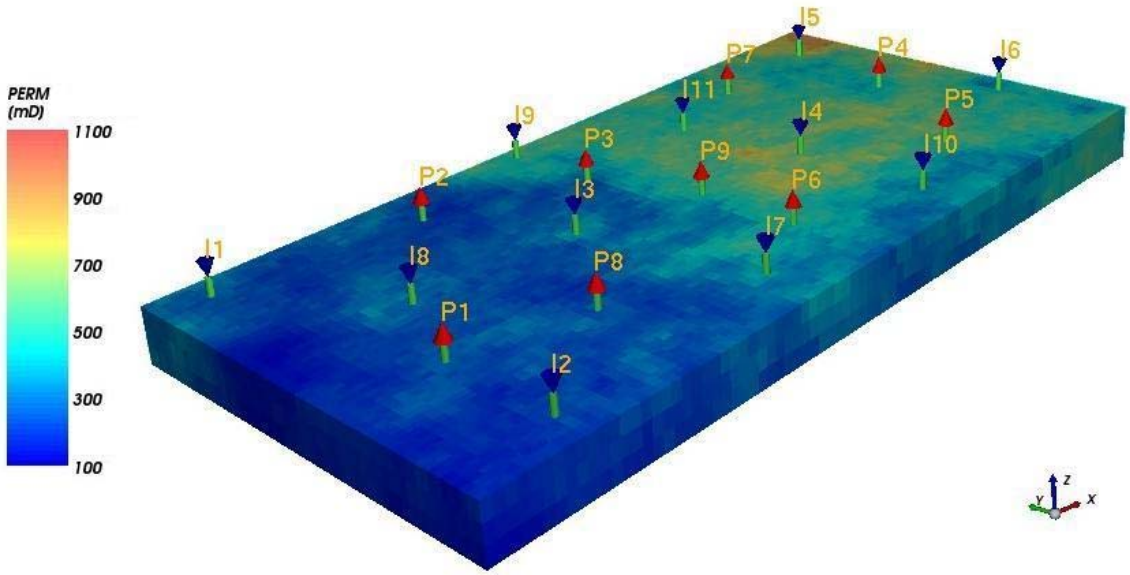

Figure 8.17: Permeability distribution and well locations for the parallel reservoir model. The Dykstra-Parson coefficient is 0.34 and the average permeability is 386 md. The reservoir is enlarged in the z-direction by a factor of 10.

The biological model parameters are obtained from the simulation of souring in a porous media column reactor presented in Section 5.1. The biological species in this model are SRB, which exist in attached biofilm and as free-floating biomass in the aqueous phase. We assume that free-floating bacteria have the same maximum specific growth rate as the attached biomass. Similar to the experiment model, we have a metabolic combination with sulfate as the electron acceptor, but all of the organic acids are combined into one substrate. H_2S is the product of the biological reaction. Biological model parameters are listed in Table 8.7.

Table 8.7: Biological model parameters for the parallel reservoir model.

Metabolic Combination	3
Maximum specific growth rate (1/day)	0.1
Yield coefficient	0.2
Substrate half saturation coefficient (mg/L)	600
Electron acceptor half saturation coefficient (mg/L)	10
Substrate utilization rate	0.8
Product generation coefficient	0.3

Substrate concentration in the formation water is 850 mg/L. We assumed that there is no sulfate or sulfide in the formation water. Similar to the case study of Section 8.1, we consider the produced water re-injection. Therefore, we assume that water injection starts with zero substrate concentration. After 500 days, we increase the injection substrate concentration to 400 mg/L to account for the organic compounds that are re-injected into the reservoir with recycled water. Table 8.8 presents the injection water composition.

Table 8.8: Composition of the injection water for the parallel model.

Component	Injection water concentration (mg/L)	
	0-500 days	500-5475 days
Substrate	0	400
Sulfate	320	320
Sulfide	0	0
SRB	1	1

8.2.2 Simulation Results

Oil production rates and water production rates from all of the producers are plotted in Figure 8.18 and Figure 8.19, respectively. Figure 8.20 shows the water saturation maps for the top layer of the reservoir after 0.1, 0.5, and 0.9 pore volume injected. At the start of the process, mixing model conditions apply and reaction zones propagate in the reservoir along with the water front. This is observed in parts (a) and (b) of Figure 8.21, which show the generation of H_2S in the mixing zones. After the start of substrate injection (500 days), the reactions take place in the vicinity of the injectors and H_2S generation continues (Figure 8.21, (c), (d), and (e)). Figure 8.22 shows the producers' aqueous phase H_2S concentrations. A maximum H_2S concentration of about 120 mg/L is consistent with the experiment simulation results of Section 5.1 presented in Figure 5.2. Figure 8.23 shows the attached and free-floating biomass concentrations at the end of the simulation (PV=0.9). This figure shows the growth of bacteria around the injectors. Attached biomass accumulates in near wellbore area (Figure 8.23a); but free-floating bacteria propagate in the reservoir after multiplying in the reaction zone (Figure 8.23b). We assumed a high injection concentration for the free-floating bacteria (1 mg/L), which resulted in higher concentrations than for the attached biofilm.

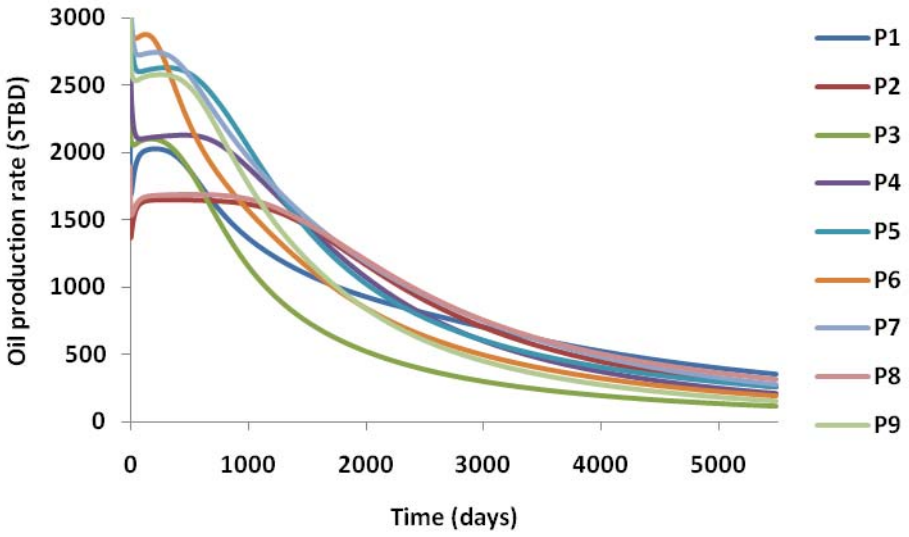

Figure 8.18: Oil production rates from all of the producers of the parallel model.

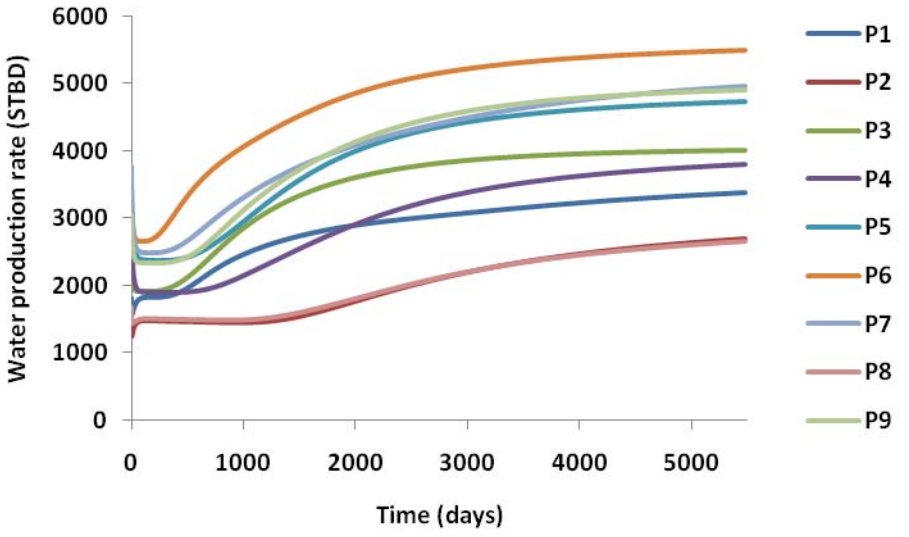

Figure 8.19: Water production rates from all of the producers of the parallel model.

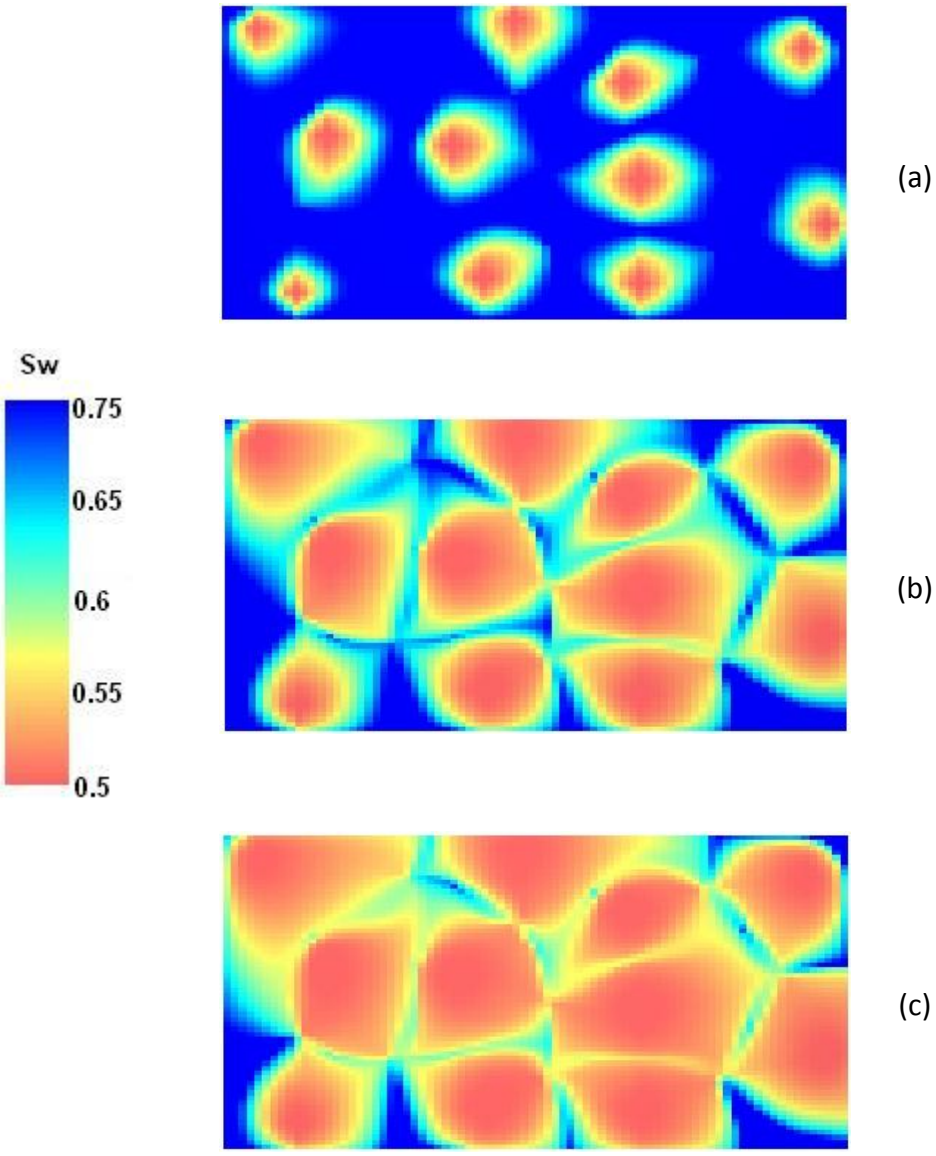

Figure 8.20: Water saturation maps of the top layer of the parallel model after (a) 588 days (0.1 PV), (b) 2944 days (0.5 PV), and (c) 5254 days (0.9 PV).

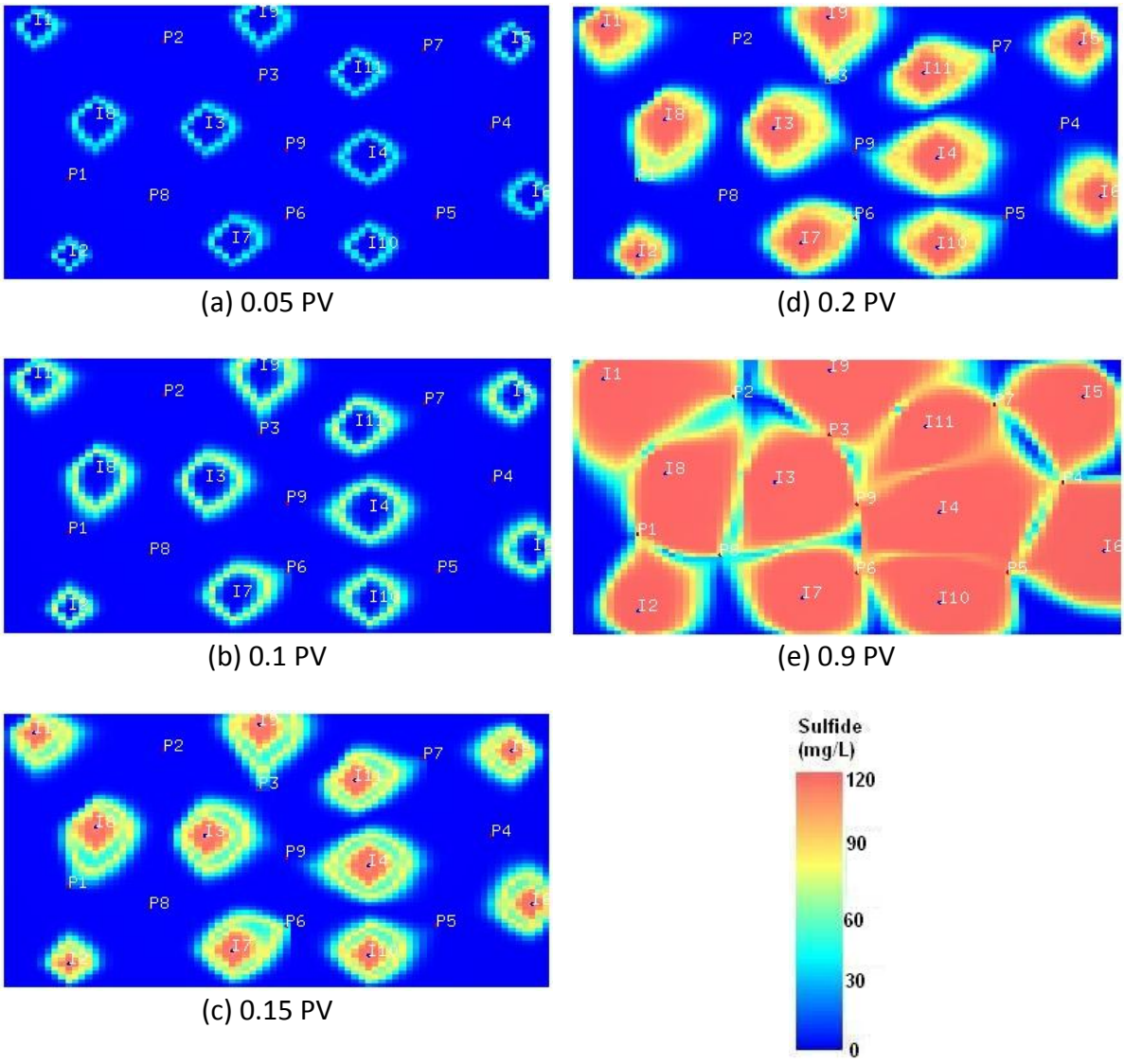

Figure 8.21: H_2S concentration maps of the top layer of the parallel model after (a) 0.05 PV, (b) 0.1 PV, (c) 0.15 PV, (d) 0.2 PV, and (e) 0.9 PV.

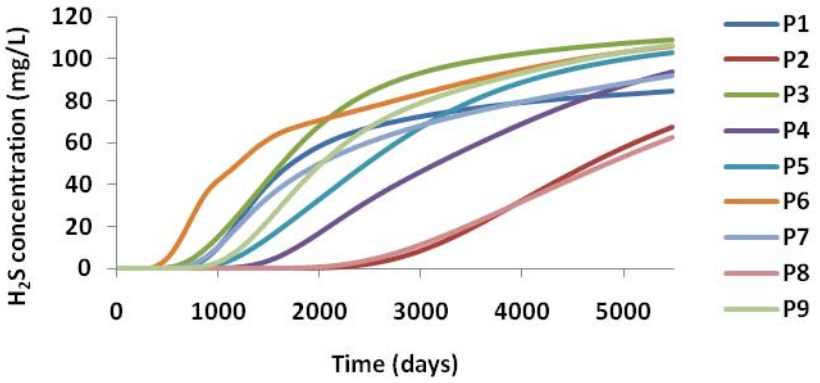

Figure 8.22: Aqueous phase H_2S concentration from all of the producers of the parallel model.

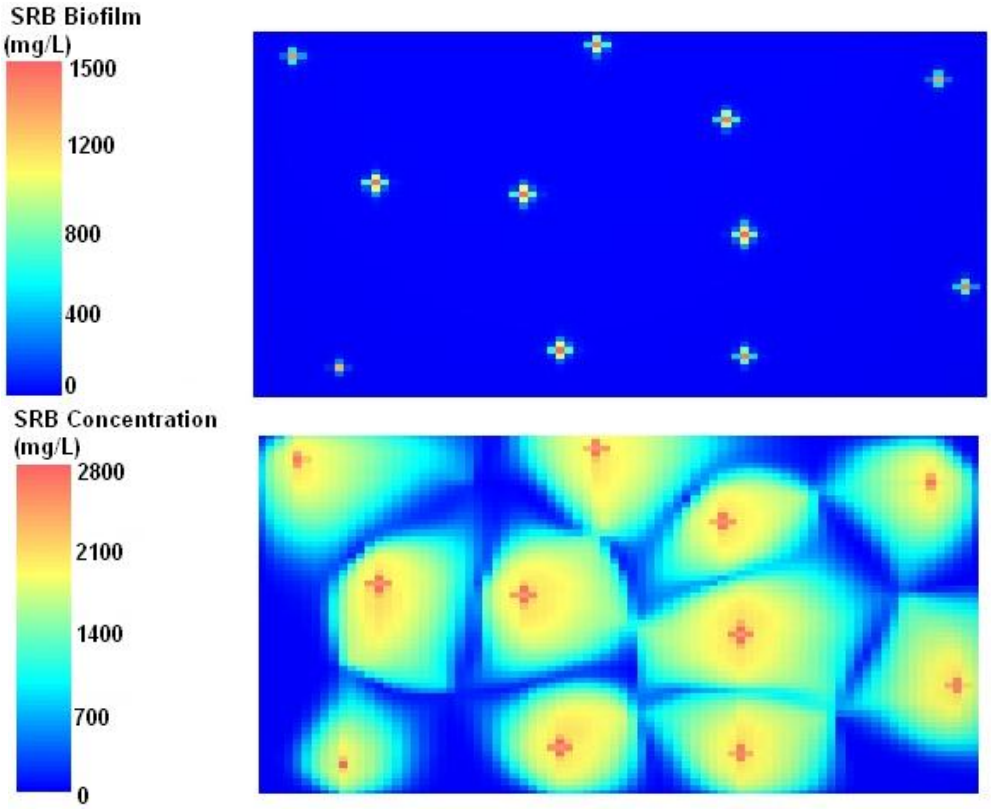

Figure 8.23: (a) Attached and (b) free-floating SRB concentration maps of the top layer of the parallel model after 0.9 PV injected.

8.2.3 Multi-Processor Runs

One way to evaluate the parallel processing performance is to measure the speed-up parameter defined as

$$S_p = \frac{T_1}{T_p}, \tag{8.1}$$

where, T_1 is the single processor run-time and T_p is the parallel processing run-time using p processors. The ideal speed-up is $S_p = p$. However, in practice, some time is spent on communication and synchronization and the achieved speed-up is less than ideal. For parallel runs, we used a cluster of PCs at the Petroleum and Geosystems Engineering Department at The University of Texas at Austin. The cluster consists of eight nodes of dual processors at 3.02 GHz speed and each node has 2 GB of memory. We executed GPAS for the parallel model described in Section 8.1 on 1, 2, 4, 8, and 16 processors. Table 8.9 presents the simulation time and speed-up for each number of processors. For this particular case, the speed-up of 6.31 is achieved with 8 processors and the speed-up of 8.43 is achieved with 16 processors. As the number of processors increases, the time spent on communication and synchronization between processors increases. Moreover, the addition of ghost layers increases the size of problem; hence, the speed-up does not increase as one might expect in an ideal situation. Figure 8.24 shows the ideal speed-up and the actual speed-up we obtained with 1 to 16 processors for our reservoir model. However, with increasing the problem size, the communication time becomes less dominant compared to the problem-solving time and the speed-up with a high number of processors reaches the ideal speed-up.

Table 8.9: Execution time and speed-up for parallel processing.

No. of processors	Execution time (s)	Speed-up
1	24600	1
2	14177	1.74
4	7421	3.31
8	3898	6.31
16	2909	8.46

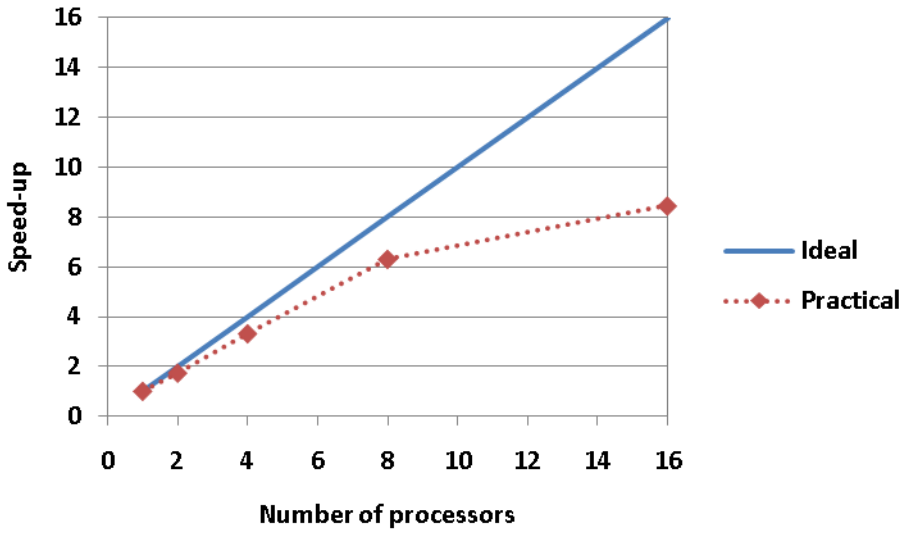

Figure 8.24: Ideal speed-up and achieved speed-up in simulation of the parallel model with GPAS using 1, 2, 4, 8, and 16 processors.

8.2.4 Grid Refinement

To study the speed-up for a larger simulation case we performed a mesh refinement on the parallel case of Section 8.2.1. Each cell is divided into 8 cells by splitting each side in half. This increased the total number of gridblocks to 122,860. We ran this case on 4, 8, and 16 processors and calculated the speed-up for each case as plotted in Figure 8.25. In this case, the obtained speed-up is closer to the ideal speed-up compared to the previous case (Figure 8.24).

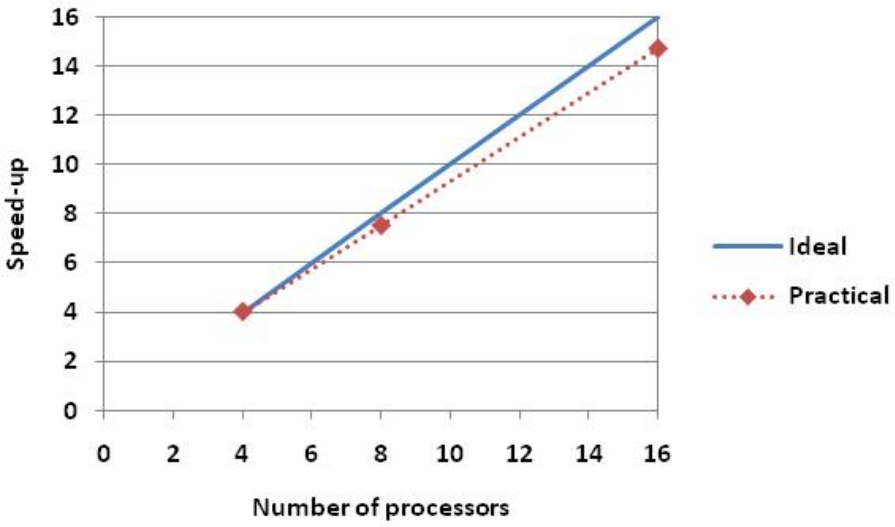

Figure 8.25: Ideal speed-up and achieved speed-up in simulation of the refined parallel model with GPAS using 1, 2, 4, 8, and 16 processors.

Chapter 9: Summary, Conclusions, and Recommendations

9.1 Summary and Conclusions

1. We developed a biological model in a fully-implicit, parallel, compositional reservoir simulator (GPAS). This model is capable of simulating reservoir souring and its remediation by modeling the microbial growth and reactions in porous media. Incorporating a comprehensive biological model in a field-scale reservoir simulator enables us to predict reservoir souring and design the remediation process for field applications.
2. We studied different mechanisms by which nitrate injection eliminates reservoir souring and developed mathematical models to represent each mechanism. These mechanisms include inhibitory action of nitrite, bio-competitive exclusion, nitrate utilization by SRB, and NR-SOB stimulation. The mechanism models are incorporated in the biological model of GPAS.
3. We used the results of the batch reactor and packed-bed column reactor experiments to verify the development of the biological model in GPAS (Chapter 5). The simulation input data such as bacteria properties and reaction parameters are obtained from experimental data. Simulation results match the experimental data in all of the reaction phases including the bacteria growth and the steady-state. The reported experiments show that the dominant mechanism by which nitrate injection inhibits reservoir souring is different in different cases, depending on the bacteria type and availability of chemical components. We simulated the inhibitory action of nitrite, the NRB-SRB competition and sulfide

oxidization mechanisms. The consistent results of simulation and experiments show that proposed models are reliable representatives of the actual biological reactions.

4. We investigated the effect of physical dispersion in the development of reaction zones in reservoir souring. We considered different water injection compositions that result in the formation of reaction zones in different regions of the reservoir. If the injection water is rich in fatty acids and nutrients, then bacteria multiply in biofilm around the injectors as explained in the biofilm model (Sunde et al., 1993). This is expected when produced water is re-injected into the reservoir. On the other hand, when injection water does not contain enough organic compounds for bacteria growth and activity, as in seawater injection, the reactions occur in a mixing zone between injection water and formation water, as all the required chemicals are available in the mixing zone. This is the basic concept of mixing model by Ligthelm et al. (1991). In this situation, dispersion intensely affects the amount of produced hydrogen sulfide, because the extent of the mixing zone strongly depends on the physical dispersion. Moreover, in both the mixing model and the biofilm model, once H_2S is generated, it is transported to the producer and dispersion determines the smearing of the H_2S front and the onset of reservoir souring.
5. After studying the effect of dispersion on reservoir souring by UTCHEM, we developed a physical dispersion model in the chemical module of GPAS. To implement the dispersion term in the aqueous component mass balance equations, we used a full-tensor corner point grid formulation. This model performs simulation of arbitrary-shaped reservoirs with non-orthogonal grids. The dispersion model is verified with an analytical solution and UTCHEM.

6. Using a finite difference scheme introduces numerical dispersion in the solution of convection dispersion equations. We derived analytical solutions to estimate numerical dispersion in one-dimensional models with variable gridblock sizes and time steps. We also investigated the effect of gridblock size and time steps on numerical dispersion in GPAS and observed that increasing the time step and gridblock increases the numerical dispersion as evaluated by analytical solutions. Therefore, when we use a fully-implicit simulator to take advantage of large time steps, we should consider the effect of numerical dispersion on the accuracy of the solution. Nevertheless, in most field-scale applications the physical dispersion is sufficiently large that the numerical dispersion becomes negligible.
7. We demonstrated the capability of GPAS to perform fast and robust simulations of reservoir souring and remediation processes in field-scale applications. We perform simulations for reservoirs souring without nitrate injection, with nitrate injection after H_2S breakthrough, and with initial nitrate injection. As expected, nitrate injection from the beginning eliminates H_2S generation. Therefore, in field applications when injection and formation water compositions and reservoir temperature are favorable for SRB activity, it is recommended to start nitrate treatment from the beginning of waterflooding.
8. The developed models (biological and dispersion) are implemented to work on multiple processors for parallel simulations. We evaluated the parallel performance of GPAS by measuring the speed-up when running on several processors. As the number of processors increases, the communication time increases and the speed-up rate decreases.

9.2 Recommendations for Future Work

1. It is advisable to validate the biological model of GPAS with the actual field data. The model parameters for generation and transport of H_2S in a real reservoir could be different from laboratory-scale simulations.
2. Adsorption on the rock and partitioning between aqueous and oleic phases affect the transport of H_2S. Incorporating adsorption and partitioning models for aqueous phase components in GPAS would provide more accurate models to simulate reservoir souring. The simulations presented in this work are conservative in that they underestimate the time required for H_2S to arrive at a producer.
3. The porous media environment limits the bacteria growth and activity in different ways. Developing comprehensive models to predict the maximum growth of bacteria and the changes in their growth rate and substrate utilization rate is necessary for accurate simulation of reservoir souring. In this work, we assumed an upper bound for the volume fraction of biomass in the pore space.
4. The corner point formulation in GPAS uses a semi-implicit scheme as off-diagonal terms are not included in the Newton's method Jacobian matrix. We used the same approach in implementing the dispersion model. We expect that considering the derivatives of off-diagonal elements reduces the Newton iterations and increases the simulation speed.
5. We assumed that reservoir souring reactions occur in the aqueous phase and H_2S remains in the water phase in the reservoir. However, it is worthwhile to investigate the possibility of H_2S partitioning in the hydrocarbon phases and also investigate its effect on phase behavior. Since GPAS has both chemical and

equation-of-state compositional modules, it is the most suitable simulator for this study.

Appendix: Sample Input Files

A.1 Microbial Souring in Porous Media (Section 5.1)

Main GPAS Input File:

```
TITLE(2) = "MICROBIAL SOURING IN POROUS MEDIA"
$SECTION 5.1

COMPOSITIONAL_MODEL

TIMEEND = 80

$ I/O OPTIONS
OUTLEVEL = 1
OUTPUT_PRE
OUTPUT_SAT
OUTPUT_VIS
OUTPUT_HIS
OUTPUT_AQ

OUTPUT_TIME() = 5 10 15 20 25 30 35 40 45 50 55 60 65 70 75 80

ISTEP(,,) = 1
JSTEP(,,) = 1
KSTEP(,,) = 1

$ FAULT BLOCK AND MESH DATA
METHOD = 2
DOWN() = 0 0 1
NX(1) = 20  NY(1) = 1  NZ(1) = 1

MES = "corn"
GEN = "gpasmesh"

Include orth20x1x1

$ COMPOUND NAMES
COMPOUND(1) = "C10"

$ COMPOUND CRITICAL TEMPERATURES
CRIT() 652.0

$ COMPOUND CRITICAL PRESSURES
CRIP() 304.0

$ COMPOUND CRITICAL VOLUMES
CRIV() 12.087

$ COMPOUND ACEN
ACEN() 0.488

$ COMPOUND MOL WEIGHTS
MOLW() 200

$ COMPOUND PARA
PARA() 431.0
```

```
$ MAX NUMBER OF PHASES
NPHASE = 3

$ Initial rock & water properties
ROCKZ = 0.00000  ROCKP = 14.7
H2OZ = 0.000003  H2OP = 14.7  H2OD = 3.467
SURTF = 60.0  SURPS = 14.7
RESTF = 60.0

$ TOLERANCE
CVGOPT = 1
TOL_FLASH = 0.000001
TOL_VOLUME = 0.000001
TOL_MASS = 0.000001
TOL_WATER = 0.000001
MAXNEWT = 25

$ POROSITY
POROSITY1() = 0.5

$ PERMEABILITY
PERMX() = 300
PERMY() = 300
PERMZ() = 300

$ INITIAL WATER SATURATION
SWINI1() = 1

$ INITIAL WATER CELL PRESSURE
PINI1() = 14.7

$ INITIAL PHASE VISCOSITIES AT EACH CELL
VIS1() = 1.00

$ INITIAL COMPOSITIONS
ZXY1(,,,1) = 1.000

$ TRACER DATA
IOILVIS
OILVIS 2.6

$ NUMERICAL METHOD
IMPAQCOMP
IBIO

NBIOS 2
NAQCOMP 8
AQCOMPNAM() = "SRB" "NBUTYRATE" "ISOBUTYRATE" "FORMATE" "PROPIONATE" "SULFATE" "H2S"
"DUMMY"
AQCOMPDEN() = 62.4 62.4 62.4 62.4 62.4 62.4 62.4 62.4
AQCOMPMW() = 74 102 102 74 108 142 34
AQCOMPTYPE() = 1 1 1 1 1 1 1 1
AQCOMPINIT() = 0. 0. 0. 0. 0. 0. 0. 0.

D() = 0. 0. 0. 0. 0. 0. 0. 0.
ALPHAL() = 0 0 0 0 0 0 0 0
ALPHAT() = 0. 0. 0. 0. 0. 0. 0. 0.

$ SURFACTANT PARAMETERS
EPSME 0.0001
HBNC70 0.07
HBNC71 0.04
CSEL7 0.177
CSEU7 0.25
AD31 1.5
AD32 0.5
```

```
B3D 1000.

$ IFT PARAMETERS
AHUH 9
CHUH 0.2
XIFTW 1.3

$ POLYMER PARAMETERS
AP1 81
AP2 2700
AP3 2500
SLOPP 0
AD41 0.0
AD42 0.0
B4D 100.

$ RELPERM DATA
RELP 2
NRELFUN 1
ITRAP

ENDPTLOW() = 0.18 0.800 0.000
ENDPTHIGH() = 1.000 1.000 0.000
SRLOW() = 0.140 0.250 0.000
SRHIGH() = 0.000 0.000 0.000
EXPNLOW() = 2.100 1.700 0.000
EXPNHIGH() = 0.480 1.500 0.000
TL() = 364 59074 364
TAUL() = 1 1 1

$ ============== WELL SPECIFICATIONS ==============

NUMWELL = 2

WELLNAME(1) = "INFLUENT"
KINDWELL(1) = 1
WELLTOP(1 TO 3,1,1) =  0.1. 0.1 0.
WELLBOTTOM(1 TO 3,1,1) = 0.1. 0.1 0.1
DIAMETER(1,1) = 0.05
WELLPQ(1) Block
  Interpolation Linear
  Extrapolation Constant
  Data  0.0  0.0041
EndBlock

WELLNAME(2) = "EFFLUENT"
KINDWELL(2) = 3
WELLTOP(1 TO 3,1,2) =  1.5 0.1 0.
WELLBOTTOM(1 TO 3,1,2) = 1.5 0.1 0.1
DIAMETER(1,2) = 1.0
WELLPQ(2) Block
  Interpolation Linear
  Extrapolation Constant
  Data  0.0  14.7
EndBlock

EndInitial

$ TRANSIENT DATA INPUT BLOCKS

BeginTime  0.0
TIME_CONTROL = 2
DELTIM = 0.01  DTIMMUL = 1  DTIMMAX = 1  DTIMMIN = 0.01
TUNE = 1
DCMAX =0.9   DAQCMAX =0.9   DPMAX = 100. DSMAX =0.5
WZ(,1) = 0.0 1.0
```

```
AQCOMP_WFINJ(,1) =  0.  200 250 200 200 320 0. 0.
EndTime
```

Biological Model Input File:

```
CC
CC    BULK DENSITY
*----  DENBLK
       1.64
CC
CC MINIMUM CONCENTRATIONS, CONVERGENCE TOLERANCE, TYPE FOR TIME STEP CONTROL
*---- CMIN      EPSBIO    IBTIM  BVOLMAX
      0.001     0.00001    0      0.003
CC
CC CHEMICAL AND BIOLOGICAL,METABOLIC COMBINATIOS, FLAGS FOR BIODEGRADATION
KINETICS,POROSITY AND PERMEABILITY
*---- NBC   NMET   IBKIN   IBPP
       8    4      2       0
CC
CC INITIAL AQEUOUS PHASE CONCENTRATIOS
*----  KC(I)       ITYPE(I)      CINIT(I)   RABIO(I)     NPABIO(I)
        1             2          0.           0.           0.
        2             1          0.           0.           0.
        3             1          0.           0.           0.
        4             1          0.           0.           0.
        5             1          0.           0.           0.
        6             1          0.           0.           0.
        7             1          0.           0.           0.
        8             2          0.           0.           0.
CC
CC  BIOLOGICAL SPECIES PARAMETERS
*----  KC(I)   DENBIO(I)   RCOL(I)    TCOL(I)    COLNUM(I)   EDDOG(I)  EDDOGB(I)  CBI(I)
CBIOMN(I)  ADSBIO(I)
       1        1          0.000615   0.00005      100        0          0          10
0          0
       8        1          0.000615   0.00005      100        0          0          0
0          0
CC
CC  METEBOLIC COMBINATION INFORMATION
*---- ISUB(I)   IEA(I)  IBS(I)  BRMAX(I)  BRMAXB(I)  YXS(I)  AKS(I)  AKA(I)  FEA(I)
       2       6       1       0.        3         0.8      100    100    0.1
       3       6       1       0.        0.1       0.2      200    200    0.8
       4       6       1       0.        0.1       0.2      200    200    0.8
       5       6       1       0.        0.01      0.2      200    200    0.8
CC
CC  COMPETITION, INHIBITION, PRODUCT GEN., NUTRIENT LIM., COMETEBOLISM INFORMATION
*---- ISUB(I)   IEA(I)  IBS(I)  NCOMPS(I)  NIHB(I)   NPROD(I)   NNUT(I)  ICOMET(I)
       2       6       1       3          0          1          0         0
       3       6       1       1          0          1          0         0
       4       6       1       1          0          1          0         0
       5       6       1       1          0          1          0         0
CC
CC COMPETITION
*---- ISUB(I)   IEA(I)   IBS(I)  ICSUB(I)
       2       6       1       3   4    5
       3       6       1       2
       4       6       1       2
       5       6       1       2
CC
CC  PRODUCT GENERATION BY METABOLIC COMBINATION I
```

```
*---- ISUB(I)   IEA(I)   IBS(I)  IPR(I)    FPR(I)
       2       6       1       7          0.0375
       3       6       1       7          0.3
       4       6       1       7          0.3
       5       6       1       7          0.3
```

A.2 PARALLEL RESERVOIR MODEL (SECTION 8.2)

Main GPAS Input File:

```
TITLE(2) = "3 DIMENSIONAL RESERVOIR SOURING FOR PARALLEL SIMULATION"
$SECTION 8.2

COMPOSITIONAL_MODEL

TIMEEND = 5475

$ I/O OPTIONS
OUTLEVEL = 1
OUTPUT_PRE
OUTPUT_SAT
OUTPUT_VIS
OUTPUT_HIS
OUTPUT_AQ

TDPVOPT
OUTPUT_TIME() = 0.05 0.1 0.15 0.2 0.5 0.9 5

ISTEP(,,) = 1
JSTEP(,,) = 1
KSTEP(,,) = 1

$ FAULT BLOCK AND MESH DATA
METHOD = 2
DOWN() = 0 0 1
NX(1) = 80  NY(1) = 64  NZ(1) = 3

MES = "corn"
GEN = "gpasmesh"

Include orth80x64x3
Include perm80x64x3.txt

$ COMPOUND NAMES
COMPOUND(1) = "C10"

$ COMPOUND CRITICAL TEMPERATURES
CRIT() 652.0

$ COMPOUND CRITICAL PRESSURES
CRIP() 304.0

$ COMPOUND CRITICAL VOLUMES
CRIV() 12.087

$ COMPOUND ACEN
ACEN() 0.488

$ COMPOUND MOL WEIGHTS
```

```
MOLW() 200

$ COMPOUND PARA
PARA() 431.0

$ MAX NUMBER OF PHASES
NPHASE = 3

$ Initial rock & water properties
ROCKZ = 0.00000  ROCKP = 14.7
H2OZ = 0.000003  H2OP = 14.7  H2OD = 3.467
SURTF = 60.0  SURPS = 14.7
RESTF = 60.0

$ TOLERANCE
CVGOPT = 1
TOL_FLASH = 0.000001
TOL_VOLUME = 0.000001
TOL_MASS = 0.000001
TOL_WATER = 0.000001
MAXNEWT = 25

$ POROSITY
POROSITY1() = 0.3

$ INITIAL WATER SATURATION
SWINI1() = 0.5

$ INITIAL WATER CELL PRESSURE
PINI1() = 5000

$ INITIAL PHASE VISCOSITIES AT EACH CELL
VIS1() = 1.00

$ INITIAL COMPOSITIONS
ZXY1(,,,1) = 1.000

$ TRACER DATA
IOILVIS
OILVIS 2.6

$ NUMERICAL METHOD
IMPAQCOMP
IBIO

NBIOS 2
NAQCOMP 5
AQCOMPNAM() = "Substrate" "Sulfate" "Sulfide" "SRB" "DUMMY"
AQCOMPDEN() = 62.4 62.4 62.4 62.4 62.4
AQCOMPMW() = 74 74 74 74 74
AQCOMPTYPE() = 1 1 1 1 1
AQCOMPINIT() = 850. 0. 0. 0. 0.

D() = 0. 0. 0. 0. 0.
ALPHAL() = 0 0 0 0 0
ALPHAT() = 0. 0. 0. 0. 0.

$ SURFACTANT PARAMETERS
EPSME 0.0001
HBNC70 0.07
HBNC71 0.04
CSEL7 0.177
CSEU7 0.25
AD31 1.5
AD32 0.5
B3D 1000.
```

```
$ IFT PARAMETERS
AHUH 9
CHUH 0.2
XIFTW 1.3

$ POLYMER PARAMETERS
AP1 81
AP2 2700
AP3 2500
SLOPP 0
AD41 0.0
AD42 0.0
B4D 100.

$ RELPERM DATA
RELP 2
NRELFUN 1
ITRAP

ENDPTLOW() = 0.18 0.800 0.000
ENDPTHIGH() = 1.000 1.000 0.000
SRLOW() = 0.140 0.250 0.000
SRHIGH() = 0.000 0.000 0.000
EXPNLOW() = 2.100 1.700 0.000
EXPNHIGH() = 0.480 1.500 0.000
TL() = 364 59074 364
TAUL() = 1 1 1

$ ============== WELL SPECIFICATIONS ==============

NUMWELL = 20

WELLNAME(1) = "P1"
KINDWELL(1) = 3
WELLTOP(1 TO 3,1,1) =  1238. 3523. 0.
WELLBOTTOM(1 TO 3,1,1) = 1238. 3523. 70.
DIAMETER(1,1) = 1.0
WELLPQ(1) Block
  Interpolation Linear
  Extrapolation Constant
  Data  0.0  3500.
EndBlock

WELLNAME(2) = "P2"
KINDWELL(2) = 3
WELLTOP(1 TO 3,1,2) =  3163. 773. 0.
WELLBOTTOM(1 TO 3,1,2) = 3163. 773. 70.
DIAMETER(1,2) = 1.0
WELLPQ(2) Block
  Interpolation Linear
  Extrapolation Constant
  Data  0.0  3500.
EndBlock

WELLNAME(3) = "P3"
KINDWELL(3) = 3
WELLTOP(1 TO 3,1,3) =  5088. 1461. 0.
WELLBOTTOM(1 TO 3,1,3) = 5088. 1461. 70.
DIAMETER(1,3) = 1.0
WELLPQ(3) Block
  Interpolation Linear
  Extrapolation Constant
  Data  0.0  3500.
EndBlock
```

```
WELLNAME(4) = "P4"
KINDWELL(4) = 3
WELLTOP(1 TO 3,1,4) =  9763. 2492. 0.
WELLBOTTOM(1 TO 3,1,4) = 9763. 2492. 70.
DIAMETER(1,4) = 1.0
WELLPQ(4) Block
  Interpolation Linear
  Extrapolation Constant
  Data  0.0  3500.
EndBlock

WELLNAME(5) = "P5"
KINDWELL(5) = 3
WELLTOP(1 TO 3,1,5) =  8663. 4211. 0.
WELLBOTTOM(1 TO 3,1,5) = 8663. 4211. 70.
DIAMETER(1,5) = 1.0
WELLPQ(5) Block
  Interpolation Linear
  Extrapolation Constant
  Data  0.0  3500.
EndBlock

WELLNAME(6) = "P6"
KINDWELL(6) = 3
WELLTOP(1 TO 3,1,6) =  5638. 4211. 0.
WELLBOTTOM(1 TO 3,1,6) = 5638. 4211. 70.
DIAMETER(1,6) = 1.0
WELLPQ(6) Block
  Interpolation Linear
  Extrapolation Constant
  Data  0.0  3500.
EndBlock

WELLNAME(19) = "P7"
KINDWELL(19) = 3
WELLTOP(1 TO 3,1,19) =  8525. 860. 0.
WELLBOTTOM(1 TO 3,1,19) = 8525. 860. 70.
DIAMETER(1,19) = 1.0
WELLPQ(19) Block
  Interpolation Linear
  Extrapolation Constant
  Data  0.0  3500.
EndBlock

WELLNAME(18) = "P8"
KINDWELL(18) = 3
WELLTOP(1 TO 3,1,18) =  3025. 3953. 0.
WELLBOTTOM(1 TO 3,1,18) = 3025. 3953. 70.
DIAMETER(1,18) = 1.0
WELLPQ(18) Block
  Interpolation Linear
  Extrapolation Constant
  Data  0.0  3500.
EndBlock

WELLNAME(20) = "P9"
KINDWELL(20) = 3
WELLTOP(1 TO 3,1,20) =  5638. 2838. 0.
WELLBOTTOM(1 TO 3,1,20) = 5638. 2838. 70.
DIAMETER(1,20) = 1.0
WELLPQ(20) Block
  Interpolation Linear
  Extrapolation Constant
  Data  0.0  3500.
EndBlock
```

```
WELLNAME(7) = "I1"
KINDWELL(7) = 2
WELLTOP(1 TO 3,1,7) =  687. 429. 0.
WELLBOTTOM(1 TO 3,1,7) = 687. 429. 70.
DIAMETER(1,7) = 1.0
WELLPQ(7) Block
  Interpolation Linear
  Extrapolation Constant
  Data  0.0  3000.
EndBlock

WELLNAME(8) = "I2"
KINDWELL(8) = 2
WELLTOP(1 TO 3,1,8) =  1238. 5070. 0.
WELLBOTTOM(1 TO 3,1,8) = 1238. 5070. 70.
DIAMETER(1,8) = 1.0
WELLPQ(8) Block
  Interpolation Linear
  Extrapolation Constant
  Data  0.0  1500.
EndBlock

WELLNAME(9) = "I3"
KINDWELL(9) = 2
WELLTOP(1 TO 3,1,9) =  3988. 2492. 0.
WELLBOTTOM(1 TO 3,1,9) = 3988. 2492. 70.
DIAMETER(1,9) = 1.0
WELLPQ(9) Block
  Interpolation Linear
  Extrapolation Constant
  Data  0.0  4500.
EndBlock

WELLNAME(10) = "I4"
KINDWELL(10) = 2
WELLTOP(1 TO 3,1,10) =  7288. 3008. 0.
WELLBOTTOM(1 TO 3,1,10) = 7288. 3008. 70.
DIAMETER(1,10) = 1.0
WELLPQ(10) Block
  Interpolation Linear
  Extrapolation Constant
  Data  0.0  5000.
EndBlock

WELLNAME(11) = "I5"
KINDWELL(11) = 2
WELLTOP(1 TO 3,1,11) =  10310. 773. 0.
WELLBOTTOM(1 TO 3,1,11) = 10310. 773. 70.
DIAMETER(1,11) = 1.0
WELLPQ(11) Block
  Interpolation Linear
  Extrapolation Constant
  Data  0.0  2500.
EndBlock

WELLNAME(12) = "I6"
KINDWELL(12) = 2
WELLTOP(1 TO 3,1,12) =  10710. 3867. 0.
WELLBOTTOM(1 TO 3,1,12) = 10710. 3867. 70.
DIAMETER(1,12) = 1.0
WELLPQ(12) Block
  Interpolation Linear
  Extrapolation Constant
  Data  0.0  3200.
EndBlock
```

```
WELLNAME(13) = "I7"
KINDWELL(13) = 2
WELLTOP(1 TO 3,1,13) =  4538. 4727. 0.
WELLBOTTOM(1 TO 3,1,13) = 4538. 4727. 70.
DIAMETER(1,13) = 1.0
WELLPQ(13) Block
  Interpolation Linear
  Extrapolation Constant
  Data  0.0  4500.
EndBlock

WELLNAME(14) = "I8"
KINDWELL(14) = 2
WELLTOP(1 TO 3,1,14) =  1788. 2320. 0.
WELLBOTTOM(1 TO 3,1,14) = 1788. 2320. 70.
DIAMETER(1,14) = 1.0
WELLPQ(14) Block
  Interpolation Linear
  Extrapolation Constant
  Data  0.0  4000.
EndBlock

WELLNAME(15) = "I9"
KINDWELL(15) = 2
WELLTOP(1 TO 3,1,15) =  5088. 257. 0.
WELLBOTTOM(1 TO 3,1,15) = 5088. 257. 70.
DIAMETER(1,15) = 1.0
WELLPQ(15) Block
  Interpolation Linear
  Extrapolation Constant
  Data  0.0  3500.
EndBlock

WELLNAME(16) = "I10"
KINDWELL(16) = 2
WELLTOP(1 TO 3,1,16) =  7288. 4898. 0.
WELLBOTTOM(1 TO 3,1,16) = 7288. 4898. 70.
DIAMETER(1,16) = 1.0
WELLPQ(16) Block
  Interpolation Linear
  Extrapolation Constant
  Data  0.0  3500.
EndBlock

WELLNAME(17) = "I11"
KINDWELL(17) = 2
WELLTOP(1 TO 3,1,17) =  7013. 1290. 0.
WELLBOTTOM(1 TO 3,1,17) = 7013. 1290. 70.
DIAMETER(1,17) = 1.0
WELLPQ(17) Block
  Interpolation Linear
  Extrapolation Constant
  Data  0.0  3500.
EndBlock

EndInitial

$ TRANSIENT DATA INPUT BLOCKS

BeginTime  0.0
TIME_CONTROL = 2
DELTIM = 0.5  DTIMMUL = 1  DTIMMAX = 30  DTIMMIN = 0.5
TUNE = 1
DCMAX =0.9   DAQCMAX =0.9   DPMAX = 100. DSMAX =0.5
$MAXMOL = 1  MAXP = 10000  ERRLIMIT = 0.2
WZ(,7) = 0.0 1.0
```

```
WZ(,8) = 0.0 1.0
WZ(,9) = 0.0 1.0
WZ(,10) = 0.0 1.0
WZ(,11) = 0.0 1.0
WZ(,12) = 0.0 1.0
WZ(,13) = 0.0 1.0
WZ(,14) = 0.0 1.0
WZ(,15) = 0.0 1.0
WZ(,16) = 0.0 1.0
WZ(,17) = 0.0 1.0
AQCOMP_WFINJ(,7) = 0. 320. 0. 0. 0.
AQCOMP_WFINJ(,8) = 0. 320. 0. 0.  0.
AQCOMP_WFINJ(,9) = 0. 320. 0. 0. 0.
AQCOMP_WFINJ(,10) = 0. 320. 0. 0. 0.
AQCOMP_WFINJ(,11) = 0. 320. 0. 0. 0.
AQCOMP_WFINJ(,12) = 0. 320. 0. 0. 0.
AQCOMP_WFINJ(,13) = 0. 320. 0. 0. 0.
AQCOMP_WFINJ(,14) = 0. 320. 0. 0. 0.
AQCOMP_WFINJ(,15) = 0. 320. 0. 0. 0.
AQCOMP_WFINJ(,16) = 0. 320. 0. 0. 0.
AQCOMP_WFINJ(,17) = 0. 320. 0. 0. 0.
EndTime

BeginTime  500.0
TIME_CONTROL = 2
DELTIM = 5  DTIMMUL = 1  DTIMMAX = 30  DTIMMIN = 0.5
TUNE = 1
DCMAX =0.9   DAQCMAX =0.9   DPMAX = 100. DSMAX =0.5
$MAXMOL = 1  MAXP = 10000  ERRLIMIT = 0.2
WZ(,7) = 0.0 1.0
WZ(,8) = 0.0 1.0
WZ(,9) = 0.0 1.0
WZ(,10) = 0.0 1.0
WZ(,11) = 0.0 1.0
WZ(,12) = 0.0 1.0
WZ(,13) = 0.0 1.0
WZ(,14) = 0.0 1.0
WZ(,15) = 0.0 1.0
WZ(,16) = 0.0 1.0
WZ(,17) = 0.0 1.0
AQCOMP_WFINJ(,7) = 400. 320. 0. 0. 0.
AQCOMP_WFINJ(,8) = 400. 320. 0. 0.  0.
AQCOMP_WFINJ(,9) = 400. 320. 0. 0. 0.
AQCOMP_WFINJ(,10) = 400. 320. 0. 0. 0.
AQCOMP_WFINJ(,11) = 400. 320. 0. 0. 0.
AQCOMP_WFINJ(,12) = 400. 320. 0. 0. 0.
AQCOMP_WFINJ(,13) = 400. 320. 0. 0. 0.
AQCOMP_WFINJ(,14) = 400. 320. 0. 0. 0.
AQCOMP_WFINJ(,15) = 400. 320. 0. 0. 0.
AQCOMP_WFINJ(,16) = 400. 320. 0. 0. 0.
AQCOMP_WFINJ(,17) = 400. 320. 0. 0. 0.
EndTime
```

Biological Model Input File:

```
CC
CC    BULK DENSITY
*----  DENBLK
       1.64
CC
CC MINIMUM CONCENTRATIONS, CONVERGENCE TOLERANCE, TYPE FOR TIME STEP CONTROL
*---- CMIN      EPSBIO    IBTMIN  BVOLMAX
      0.001     0.00001    0      0.003
CC
```

```
CC CHEMICAL AND BIOLOGICAL,METABOLIC COMBINATIOS, FLAGS FOR BIODEGRADATION
KINETICS,POROSITY AND PERMEABILITY
*---- NBC   NMET   IBKIN   IBPP
       5    1      2       0
CC
CC INITIAL AQEUOUS PHASE CONCENTRATIOS
*----  KC(I)       ITYPE(I)      CINIT(I)   RABIO(I)     NPABIO(I)
        1             1          0.           0.            0.
        2             1          0.           0.            0.
        3             1          0.           0.            0.
        4             2          0.           0.            0.
        5             2          0.           0.            0.
CC
CC  BIOLOGICAL SPECIES PARAMETERS
*----  KC(I)   DENBIO(I)   RCOL(I)    TCOL(I)    COLNUM(I)   EDDOG(I)  EDDOGB(I)  CBI(I)
CBIOMN(I)  ADSBIO(I)
       4        1          0.000615   0.000084   100        0          0          10
0   0
       5        1          0.000615   0.000084   100        0          0          0
0   0
CC
CC  METEBOLIC COMBINATION INFORMATION
*---- ISUB(I)   IEA(I)  IBS(I)  BRMAX(I)  BRMAXB(I)  YXS(I)  AKS(I)  AKA(I)  FEA(I)
       1         2        4       0.1       0.1       0.2    600     10       0.8
CC
CC  COMPETITION, INHIBITION, PRODUCT GEN., NUTRIENT LIM., COMETEBOLISM INFORMATION
*----  ISUB(I)   IEA(I)   IBS(I)   NCOMPS(I)   NIHB(I)   NPROD(I)   NNUT(I)  ICOMET(I)
       1       2       4          0          0          1          0         0
CC
CC  PRODUCT GENERATION BY METABOLIC COMBINATION I
*----  ISUB(I)    IEA(I)   IBS(I)   IPR(I)    FPR(I)
         1       2       4       3       0.3
```

Nomenclature

A	Aqueous phase electron acceptor concentration, mg/L
$\bar{A}$	Electron acceptor concentration in attached biomass, mg/L
C_c	Number of cells per mass of solid, lb^{-1}
$\overline{\overline{D}}_{iw}$	Aqueous phase dispersion tensor for component i, ft^2/day
F	Formation resistivity factor
h	Depth, ft
I	Inhibition constant, mg/L
K_A	Electron acceptor half saturation coefficient, mg/L
K_S	Substrate half saturation coefficient, mg/L
$\overline{\overline{k}}$	Absolute permeability tensor, md
k_{rw}	Water relative permeability
k_{ro}	Oil relative permeability
m_c	Mass of cells in a single microcolony, $m_c = \rho_x V_C$
N_i	Moles of component *i* per unit pore volume, lb-mole/cu ft
N_w	Moles of water per unit pore volume, lb-mole/cu ft
N_{Pe}	Peclet number
N_{Co}	Courant number
n	Number of cells per microcolony
n_c	Total number of hydrocarbon components
n_a	Total number of aqueous components
P	Water phase pressure, psi

q_i	Molar injection (positive) or production (negative) rate for component i, lb-mole/day
S	Aqueous phase substrate concentration, mg/L
$\bar{S}$	Substrate concentration in attached biomass, mg/L
S_o	Oil saturation
S_p	Speed-up with p processors
S_w	Water saturation
T_1	Run-time, s
t	Time, day
u	Bulk fluid velocity, ft/day
V_b	Bulk volume, ft^3
V_c	Volume of a single microcolony, ft^3
X	Aqueous phase biomass concentration, mg/L
$\bar{X}$	Attached biomass concentration, mg/L
$\bar{X}_{\max}$	Maximum attached biomass concentration, mg/L
x	Distance, ft
x_{iO}	Molar concentration of component i in oleic phase, lb-mole/ft^3
x_{iw}	Molar concentration of component i in water phase, lb-mole/ft^3
α_{Lw}	Longitudinal dispersivity, ft
α_{Tw}	Transversal dispersivity, ft
β	Surface area of a single microcolony, ft^2
Φ_w	Water phase potential, psi
ϕ	Porosity
κ	Mass transfer coefficient, ft/day
$\mu_{\max}$	Maximum specific growth rate, 1/day

μ_w	Water viscosity, cp
μ_o	Oil viscosity, cp
ξ_w	Molar density of water phase, lb-mole/ft^3
ξ_o	Molar density of oil phase, lb-mole/ft^3
ρ_b	Bulk density of the porous medium, lb/ft^3
ρ_X	Biomass density, mg/L
τ	Tortuosity factor

Subscripts

i	Component index
w	Water phase
o	Oil phase

References

Aeckersberg, F., Bak, F., and Widdel, F. 1991. Anaerobic Oxidation of Saturated Hydrocarbons to CO_2 by a New Type of Sulfate-Reducing Bacterium. Archives of Microbiology. 156 (1): 5–14.

Al-Rasheedi, S., Kalli, C., Thrasher, D., and Al-Qabandi, S. 1999. Prediction and Evaluation of the Impact of Reservoir Souring in North Kuwait, a Case Study. presented at the MEOS 99 : managing the future : challenges for people, resources and technology, Bahrain, 20-23 February.

Aziz, K., and Settari, A. 1979. Petroleum Reservoir Simulation. Applied Science Publishers.

Bailey, J.E. and Ollis, D.F. 1986. Biochemical Engineering Fundamentals, 2nd edition. New York: McGraw-Hill.

Barth, T. 1991. Organic and Inorganic Ions in Water from Petroleum Reservoirs, Norwegian Continental Shelf : a Multivariate Statistical Analysis and Comparison with American Reservoir Formation Waters. Applied Geochemistry. 6 (1):1–15.

Barton, L.L. (ed) 1995. Sulfate-Reducing Bacteria. New York: Plenum Publishing Corp.

Bastin, E.S., Greer, F.E., Merritt, C.A., and Moulton, G. 1926. The Presence of Sulphate Reducing Bacteria in Oil Field Waters. Science. 63 (1618): 21-24. DOI: 10.1126/science.63.1618.21.

Bear, J. 1988. Dynamics of Fluids in Porous Media. Courier Dover Publications.

Beeder, J., Nilsen, R.K., Rosnes, J.T., Torsvik, T., and Lien, T. 1994. Archaeoglobus fulgidus Isolated from Hot North Sea Oil Field Waters. Applied Environmental Microbioly. 60 (4):1227-1231.

Beeder, J., Torsvik, T., and Lien, T. 1995. Thermodesulforhabdus norvegicus gen. nov., sp. nov., a Novel Thermophilic Sulfate-Reducing Bacterium from Oil Field Water. Archived Microbiology. 164 (5): 331-336.

Burger, E.D., Jenneman, G.E., Bache, Ø., Jensen, T.B., and Soerensen, S. 2005. A Mechanistic Model to Evaluate Reservoir Souring in the Ekofisk Field. Paper SPE 93297 presented at the SPE International Symposium on Oilfield Chemistry, The Woodlands, Texas, 2-4 February 2005. DOI: 10.2118/93297-MS.

Burger, E.D., Vedvik, A.D., Bache, O.D., Voldum, K.D., and Jenneman, G.E. 2006. Forecasting the Effect of Produced Water Reinjection on Reservoir Souring in the

Ekofisk Field. presented at the Corrosion 2006, San Diego, California, 12-16 March.

Chen, C.I., Reinsel, M.A., and Mueller, R.F. 1994. Kinetic Investigation of Microbial Souring in Porous Media Using Microbial Consortia from Oil Reservoirs. Biotechnology and Bioengineering. 44 (3): 263-269.

Christensen, B., Torsvik, T., and Lien, T. 1992. Immunomagnetically Captured Thermophilic Sulfate-Reducing Bacteria from North Sea Oil Field Waters. Applied and Environmental Microbiology. 58 (4): 1244-1248.

Coombe, D., Jack, T., Voordouw, J., Zhang, F., Clay, B., and Miner, K. 2010. Simulation of Bacterial Souring Control in an Alberta Heavy-Oil Reservoir. Journal of Canadian Petroleum Technology. 49 (5): 19-26. SPE-137046-PA. DOI: 10.2118/137046-PA.

Dalsgaard, T., and Bak, F. 1994. Nitrate Reduction in a Sulphate-Reducing Bacterium, Desulfovibrio Desulfuricans, Isolated from Rice Paddy Soil: Sulfide Inhibition, Kinetics, and Regulation. Applied Environmental Microbiology. 60 (1): 291-297.

de Blanc, P.C., McKinney, D.C., Speitel, G.E. Jr., Sepehrnoori, K., and Delshad, M. 1996. A Three-Dimensional, Multi-Component Model of Non-Aqueous Phase Liquid Flow and Biodegradation in Porous Media. In: Reddi., L.N. (ed) Non-Aqueous Phase Liquids (NAPLs) in the Subsurface Environment: Assessment and Remediation, American Society of Civil Engineers, New York.

de Blanc, P.C. 1998. Development and Demonstration of a Biodegradation Model for Non-Aqueous Phase Liquids in Groundwater. PhD dissertation, The University of Texas at Austin, Texas.

Delshad, M., Pope, G.A., Sepehrnoori, K. 1996. A compositional simulator for modeling surfactant enhanced aquifer remediation, 1 formulation. Journal of Contaminant Hydrology. 23(4): 303-327.

Eckford, R.E. and Fedorak, P.M. 2004. Using Nitrate to Control Microbially-Produced Hydrogen Sulfide in Oil Field Waters. In: Vazquez-Duhalt, R. and Quintero-Ramirez, R. (eds) Petroleum Biotechnology, Developments and Perspectives. Elsevier.

Eden, B., Laycock, P.J., and Fielder, M. 1993. Oilfield Reservoir Souring. HSE Books.

Evans, P. and Dunsmore, B. 2006. Reservoir Simulation of Sulfate Reducing Bacteria Activity in the Deep Sub-Surface. presented at the Corrosion 2006, San Diego, California, 12-16 March.

Edwards, M.G. and Rubin, B. 1991. Total Variation Diminishing Schemes and the Two-Point Upstream Mobility Weighting Scheme. Unsolicited paper SPE 23947.

Fanchi, J. R. 1983. Multidimensional Numerical Dispersion. SPE Journal. 23(1): 143-151.

Farhadinia, M.A. 2008. Development and Implementation of a Multi-Dimensional Reservoir Souring Module in a Chemical Flooding Simulator (UTCHEM). PhD Dissertation, The University of Texas at Austin.

Farhadinia, M.A., Bryant, S.L., Sepehrnoori, K., and Delshad, M. 2009. Development of a Reservoir Simulator for Souring Predictions. paper 118951-MS presentd at the SPE Reservoir Simulation Symposium, The Woodlands, Texas, 2-4 February. DOI: 10.2118/118951-MS.

Farhadinia, M.A., Bryant, S.L., Sepehrnoori, K., and Delshad, M. 2010. Development and Implementation of a Multidimensional Reservoir Souring Module in a Chemical Flooding Simulator. Petroleum Science and Technology, 28 (6): 535-546.

Fathi Najafabadi, N., Han, C., Delshad, M., and Sepehrnoori, K. 2009. Development of a Three Phase Fully Implicit Parallel Chemical Flooding Simulator. Paper SPE 119002 presented at the SPE Reservoir Simulation Symposium, The Woodlands, TX, 2-4 February. DOI: 10.2118/119002-MS.

Gear, C.W. 1971. Numerical Initial Value Problems in Ordinary Differential Equations. Upper Saddle River: Printice Hall.

GPAS, Technical Documentation for GPAS-3.5. 2005. Reservoir Engineering Research Program, Center for Petroleum and Geosystems Engineering, The University of Texas at Austin.

Greene, E.A., Hubert, C., Nemati, M., Jenneman, G.E., and Voordouw, G. 2003. Nitrite Reductase Activity of Sulphate-Reducing Bacteria Prevents Their Inhibition by Nitrate-Reducing, Sulphide-Oxidizing Bacteria. Environmental Microbiology. 5 (7): 607-617.

Han, C., Delshad, M., Sepehrnoori, K., and Pope, G.A. 2007. A Fully Implicit Parallel Compositional Chemical Flooding Simulator. SPE Journal. 12 (3): 322-338. DOI: 10.2118/97217-PA.

Harten, A. 1983. High Resolution Schemes for Hyperbolic Conservation Laws. SIAM Review. 25(1): 35-67.

Heatherly, M.W., Howell, M.E., and McElhiney, J.E. 1994. Sulfate Removal Technology For Seawater Waterflood Injection. Paper SPE 38768 presented at the SPE Offshore Technology Conference, Houston, Texas, 2-5 May. DOI: 10.4043/7593-MS

Heider, J., Spormann, A.M., Beller, H.R., and Widdel, F. 1998. Anaerobic Bacterial Metabolism of Hydrocarbons. FEMS Microbial Rev. 22 (5): 459–473.

Herbert, B.F. 1987. Reservoir Souring. In: Hill, E.C., Shennan, J.L., and Watkinson, R.J. (eds) Microbial Problems in the Off-shore Oil Industry. New York: John Wiley & Sons. pp 63-71.

Hitzman, D.O. and Dennis, D.M. 1997. Sulfide Removal and Prevention in Gas Wells. Paper SPE 37438 presented at the SPE Production Operations Symposium, Oklahoma City, Oklahoma, 9-11 March. DOI: 10.2118/37438-MS.

Hubert, C., Nemati, M., Jenneman, G., and Voordouw, G. 2003. Containment of Biogenic Sulfide Production in Continuous Up-Flow Packed-Bed Bioreactors with Nitrate or Nitrite. Biotechnology Progress. 19(2): 338-345.

Hubert, C., Nemati, M., Jenneman, G., and Voordouw, G. 2005. Corrosion Risk Associated with Microbial Souring Control Using Nitrate or Nitrite. Applied Microbiology and Biotechnology. 68(2): 272-282.

Hubert, C. and Voordouw, G. 2007. Oil Field Souring Control by Nitrate-Reducing Sulfurospirillum spp. That Outcompete Sulfate-Reducing Bacteria for Organic Electron Donors. Applied and environmental microbiology. 73 (8): 2644-2652.

Jenneman, G.E., McInerney, M.J., Knapp, R.M. 1986. Effect of Nitrate on Biogenic Sulfide Production. Applied Environmental Microbiology. 51(6):1205–1211.

Jenneman, G.E., Gevertz, D., Wright, M. 1996. Sulfide Bioscavenging of Soured Produced Water by Natural Microbial Populations. paper presented at the International Petroleum Environmental Conference, Albuquerque, New Mexico.

Jenneman, G.E., Moffitt, P.D., Bala, G.A., and Webb, R.H. 1997. Field Demonstration of Sulfide Removal in Reservoir Brine by Bacteria Indigenous to a Canadian Reservoir. Paper SPE 38768 presented at the SPE Annual Technical Conference and Exhibition, San Antonio, Texas, 5-8 October. DOI: 10.2118/38768-MS.

Jenneman, G.E., Moffitt, P.D., Bala, G.A., and Webb, R.H. 1997. Sulfide Removal in Reservoir Brine by Indigenous Bacteria. SPE Journal of Production and Facilities. 14 (3): 219-225. DOI: 10.2118/57422-PA.

John, A.K. 2003. Development of a Hybrid Approach to Couple Chemical and Compositional Model in an Implicit Parallel Simulator. M.S. Thesis, The University of Texas at Austin, Texas.

Kahaner, D., Moler, C., and Nash, S. 1989. Numerical Methods and Software. Englewood Cliffs: Prentice Hall.

Khan, H.A., Gbosi, A., Britton, L.N., and Bryant, S.L. 2008. Mechanistic Models of Microbe Growth in Heterogeneous Porous Media. paper SPE 113462 presented at the SPE Symposium on Improved Oil Recovery, Tulsa, Oklahoma, 20-23 April. DOI: 10.2118/113462-MS.

Kuijvenhoven, C., Noirot, J.C., Hubbard, P., and Oduola, L. 2007. One Year Experience with the Injection of Nitrate to Control Souring in Bonga Deepwater Development Offshore Nigeria. Paper SPE 105784 presented at the International Symposium on Oilfield Chemistry, Houston, Texas, 28 February-2 March. DOI: 10.2118/105784-MS.

Lake, L.W. 1989. Enhanced Oil Recovery. Englewood Cliffs: Prentice Hall.

Lantz, R.B. 1971. Quantitative Evaluation of Numerical Diffusion (Truncation Error). SPE Journal. 11(3): 315-320.

Larsen, J., Sanders, P.F., and Talbot, R.E. 2000. Experience with the use of Tetrakishydroxymethyl Phosphonium Sulfate (THPS) for the Control of Downhole Hydrogen Sulfide. Paper SPE 00123 presented at Corrosion 2000, Orlando, Florida, March 26-31.

Larsen, J. 2002. Downhole Nitrate Applications to Control Sulfate Reducing Bacteria Activity and Reservoir Souring. presented at the Corrosion 2002, Denver, Colorado, 7-11 April.

Larsen, J., Rod, M.H., and Zwolle, S. 2004. Prevention of Reservoir Souring in the Halfdan Field by Nitrate Injection. presented at the Corrosion 2004, New Orleans, Louisiana, March 28 - April 1.

Larson, R.G. 1982. Controlling Numerical Dispersion by Variably Timed Flux Updating in One Dimension. Journal of Petroleum Technology. 22(3): 399-408. Larson, R.G. 1982. Controlling Numerical Dispersion by Variably Timed Flux Updating in Two Dimensions. Journal of Petroleum Technology. 22(3): 409-419.

Ligthelm, D.J., deBoer, R.B., Brint, J.F., and Schulte, W.M. 1991. Reservoir Souring: An Analytical Model for H_2S Generation and Transportation in an Oil Reservoir Owing to Bacterial Activity. Paper SPE 23141 presented at the Offshore Europe, Aberdeen, United Kingdom, 3-6 September. DOI: 10.2118/23141-MS.

Liu, J., Delshad, M., Pope, G.A., and Sepehrnoori, K. 1994. Application of Higher-Order Flux-Limited Methods in Compositional Simulations. Journal of Transport in Porous Media. 16 (1): 1-29.

Lovley, D.R., Woodward, J.C., and Chapelle, F.H. 1996. Rapid Anaerobic Benzene Oxidation with a Variety of Chelated Fe(III) Forms. Applied Environmental Microbiology. 62 (1):288–291.

Maliska, C.R., da Silva, A.F.C., Czesnat, A.O., Lucianetti, R.M., Maliska Jr., C.R., 1997. Three Dimensional Multiphase Flow Simulation in Petroleum Reservoirs Using the Mass Fractions as Dependent Variables. Paper SPE 39067-MS presented at

the Latin American and Caribbean Petroleum Engineering Conference, 30 August – 3 September, Rio de Janeiro, Brazil.

Marcondes, F., Han, C., and Sepehrnoori, K., 2005. Implementation of Corner Point Mesh into a Parallel Fully Implicit Equation of State Compositional Reservoir Simulator. Presented at the 18th International Congress of Mechanical Engineering, Ouro Preto, Brazil, 6-11 November.

Marcondes, F., Han, C., and Sepehrnoori, K., 2008. Effect of Cross-Derivatives in Dicretization Schemes in Structured Non-Orthogonal Meshes for Compositional Reservoir Simulation. Journal of Petroleum Science and Technology. 63 (1): 53-60.

Maxwell, S., Charlton, P., Badalek, P., Hellings, G., and Mutch, K. 2002. In-Field Biocide Optimization for Magnus Water Injection Systems. presented at the Corrosion 2002, Denver, Colorado, 7-11 April.

McKinley, V. L., Costerton, J. W., and White, D. C. 1988. Microbial Biomass, Activity, and Community Structure of Water and Particulates Retrieved by Backflow from a Waterflood Injection Well. Applied Environmental Microbiology. 54 (6): 1383-1393.

McInerney, M.J., Bhupathiraju, V.K., Sublette, K.L. 1992. Evaluation of a Microbial Method to Reduce Hydrogen Sulfide Levels in a Porous Rock Biofilm. Journal of Industrial Microbiology. 11 (1): 53-58.

Molz, F.J., Widowson, M.A., and Benefield, L.D., 1986. Simulation of Microbial Growth Dynamic Coupled to Nutrient and Oxygen Transport in Porous Media. Water Resources Research. 22 (8): 1207–1216.

Mueller, R.F., Nielsen, P.H. 1996. Characterization of Thermophilic Consortia from Two Souring Oil Reservoirs. Applied Environmental Microbiology. 62 (9): 3083–3087.

Myhr, S., Lillebø, B.L.P., Sunde, E., Beeder, J., and Torsvik, T. 2002. Inhibition of Microbial H_2S Production in an Oil Reservoir Model Column by Nitrate Injection. Applied Microbiology and Biotechnology. 58 (3): 400-408.

Nalla, G. 2002. Implementation of Chemical Flooding Module into the General Purpose Adaptive Simulator. M.S. Thesis, The University of Texas at Austin, Texas.

Nemati, M., Jenneman, G.E., and Voordouw, G. 2001. Mechanistic Study of Microbial Control of Hydrogen Sulfide Production in Oil Reservoirs. Biotechnology and Bioengineering. 74 (5): 424-434.

Parashar, M., Wheeler, J.A., Pope, G.A., Wang K., and Wang, P. 1997. A New Generation EOS Compositional Reservoir Simulator: Part II - Framework and Multiprocessing.

Paper 37979-MS presented at the SPE Reservoir Simulation Symposium, Dallas, Texas, 8-11 June. DOI: 10.2118/37979-MS.

Peaceman, D.W. 1977. Fundamentals of Numerical Reservoir Simulation. New York: Elsevier Scientific Publishing Company.

Peaceman, D.W., Rachford, H.H. 1962. Numerical Calculation of Multi-Dimensional Miscible Displacement. SPE Journal. 2(4): 327-339.

Pfennig, N., Widdel, F., and Trüper, H.G. 1981. The Prokaryotes, A Handbook on the Habitat, Isolation and Identification of Bacteria. In: Stolp, M.P., Trüper, H.G., Balows, A., and Schlegel, H. (eds) Berlin: Springer-Verlag. pp. 926–947.

Postgate, J.R. 1984. Sulfate-Reducing Bacteria. 2nd edition, New York: Cambridge University Press.

Rees, G., Grassia, G.N., Sheehy, A.J, Dwivedi, P.P., and Patel, B.K.C. 1995. Desulfacinum Infernum gen. nov., sp. nov., a Thermophilic Sulfate-Reducing Bacterium from a Petroleum Reservoir. International Journal of Systematic Bacteriology. 45 (1): 85-89.

Reinsel, M.A., Sears, J.T., Stewart, P.S., and McInerney, M.J. 1996. Control of Microbial Souring by Nitrate, Nitrite or Glutaraldehyde Injection in a Sandstone Column. Journal of Industrial Microbiology and Biotechnology. 17 (2): 128-136.

Rizk, T., Stott, J.F., Eden, R., McElhiney, J.E., Hardy, J.A., Davis, R.A., Di Lorio, C. 1998. The Effect of Desulphuated Seawater Injection on Microbiological Hydrogen Sulphide Generation and Implication for Corrosion Control. SPE paper 98287 presented at Corrosion 98, San Diego, California, 22-27 March.

Rosnes, J., T., Torsvik, T., and Lien, T. 1991. Spore-FormingTthermophilic Sulfate-Reducing Bacteria Isolated from North Sea Oil Field Waters. Applied Environmental Microbiology. 57 (8): 2302–2307.

Seland, A., Bilstad, T., Mehan, S., and Bakke, R., 1992. Membrane Filtration of Seawater for Oil Reservoir Injection. Paper SPE 24805 presented at the SPE Annual Technical Conference and Exhibition, Washington, D.C., 4-7 October. DOI: 10.2118/24805-MS.

Seto, C. and Beliveau, D. 2000. Reservoir Souring in the Caroline Field. Paper SPE 59778 presented at the SPE/CERI Gas Technology Symposium, Calgary, Alberta, Canada, 3-5 April. DOI: 10.2118/59778-MS.

Shrivastava, V.K., Nghiem, L.X., Moore, R.G., and Okazawa, T. 2005. Modeling Physical Dispersion in Miscible Displacements-Part 1: Theory and the Proposed Numerical Scheme. 44 (5): 25-33.

Shrivastava, V.K., Nghiem, L.X., Moore, R.G., and Okazawa, T. 2005. Modeling Physical Dispersion in Miscible Displacements-Part 2: Validation, Numerical Tests, and Applications. Journal of Canadian Petroleum Technology. 44(5): 34-43.

Sturman, P.J. and Goeres, D.M. 1999. Control of Hydrogrn Sulfide in Oil and Gas Wells with Nitrate Injection. Paper SPE 56772 presented at the SPE Annual Technical Conference and Exhibition, Houston, Texas, 3-6 October. DOI: 10.2118/56772-MS.

Sunde, E., Thorstenson, T., Torsvik, T., Vaag, J.E., and Espedal, M.S. 1993. Field-Related Mathematical Model to Predict and Reduce Reservoir Souring. Paper SPE 25197 presented at the SPE International Symposium on Oilfield Chemistry, New Orleans, Louisiana, 2-5 March. DOI: 10.2118/25197-MS.

Sunde, E., Thorstenson, T., Lillebo, B.L., and Bodtker, G. 2004. H_2S Inhibition by Nitrate Injection on the Gullfaks Field. presented at the Corrosion 2004, New Orleans, Louisiana, March 28 - April 1.

Telang, A., Ebert, S., Foght, J., Westlake, D., Jenneman, G., Gevertz, D., and Voordouw, G. 1997. Effect of Nitrate Injection on the Microbial Community in an Oil Field as Monitored by Reverse Sample Genome Probing. Applied and environmental microbiology. 63 (5): 1785-1793.

Telang, A.J., Ebert, S., Foght, J.M., Westlake, D.W.S., and Voordouw, G. 1998. Effects of Two Diamine Biocides on the Microbial Community of an Oil Field. Canadian Journal of Microbiology 44 (11): 1060-1065.

Thiele, M.R. and Edwards, M.G. 2001. Physically Based Higher Order Godunov Schemes for Compositional Simulation. Paper SPE 66403 presented at the SPE Reservoir Simulation Symposium, Houston, Texas. February 11–14.

Thorstenson, T., Bødtker, G., Sunde, E., and Beeder, J. 2002. Biocide Replacement by Nitrate in Sea Water Injection Systems. Paper 02033 presented at Corrosion 2002, Denver, Colorado, 7-11 April.

UTCHEM. 2003. Technical Documentation for UTCHEM-10. Center for Petroleum and Geosystems Engineering, The University of Texas at Austin, Texas.

Valocchi, A.J. and Malmstead, M. 1992. Accuracy of the Operator Splitting for Advection–Dispersion Reaction Problems. Water Resources Research. 28 (5): 1471–1476.

Vance, I. and Brink, D.E. 1994. Propionate-Driven Sulphate-Reduction by Oil-Field Bacteria in a Pressurised Porous Rock Bioreactor. Applied Microbiology and Biotechnology, 40 (6): 920-925.

Vance, I. and Thrasher, R. 2005. Reservoir Souring Mechanisms and Prevention. In: Ollivier, B. and Magot, M. (eds) Petroleum Microbiology. Washington D.C.: ASM Press.

Wang, P., Yotov, I., Wheeler, M., Arbogast, T., Dawson, C., Parashar, M., Sepehrnoori, K. 1997. A New Generation EOS Compositional Reservoir Simulator: Part I - Formulation and Discretization. Paper 37979-MS presented at the SPE Reservoir Simulation Symposium, Dallas, Texas, 8-11 June. DOI: 10.2118/37979-MS.

Wang, P., Balay, S., Sepehrnoori, K., Wheeler, J., Abate, J., Smithe, B. and Pope, G.A. 1999. A Fully Implicit Parallel EOS Compositional Simulator for Large Scale Reservoir Simulation. Paper SPE 51885 presented at the Fifteenth Symposium on Reservoir Simulation, Houston, Texas, February 14-17.

Widdel, F. 1988. Microbiology and Ecology of Sulfate- and Sulfur-Reducing Bacteria. In: Zehnder, A.J.B. (ed) Biology of Anaerobic Microorganisms. New York: John Wiley & Sons. pp 469–585.